

JOINT INSTITUTE FOR LABORATORY ASTROPHYSICS



UNIVERSITY OF COLORADO

UNIVERSITY OF COLORADO
BOULDER, COLORADO 80309



NATIONAL BUREAU OF STANDARDS

AD A 097 563

LEVEL

91 FINAL REPORT.

⑥ RESEARCH IN LASER PROCESSES.

Research Sponsored by
Advanced Research Projects Agency

and

Office of Naval Research



ARPA Order No. 2683, Amendment 8
Program Code No. 8E20
Contractor: University of Colorado
Effective Date of Contract: 1 July 1975
Contract Expiration Date: 15 May 1980
Amount of Contract: \$580,000
Period Covered: 1 July 1975 to
15 May 1980

Contract No. N00014-76-C-0123
Principal Investigators:
A. V. Phelps
Telephone: (303) 492-7850
A. C. Gallagher
Telephone: (303) 492-7841
Scientific Officer: Director,
Physics Program, ONR
Short Title of Work: Laser Processes

DISTRIBUTION STATEMENT A

Approved for public release;
Distribution Unlimited

The views and conclusions contained in this document
are those of the authors and should not be interpreted
as necessarily representing the official policies,
either expressed or implied, of the Defense Advanced
Research Projects Agency or the U.S. Government.

⑪ 15 January 1981

⑫ 177

81 2 13 025

192700

Cable Address: JILA

Telephone Number: 492-7789

tpp

**Best
Available
Copy**

REPORT DOCUMENTATION PAGE		READ INSTRUCTIONS BEFORE COMPLETING FORM
1. REPORT NUMBER None	2. GOVT ACCESSION NO. <i>AD-A097563</i>	3. RECIPIENT'S CATALOG NUMBER
4. TITLE (and Subtitle) Final Report - Research in Laser Processes		5. TYPE OF REPORT & PERIOD COVERED Final Report 1 July 1975 - 15 May 1980
		6. PERFORMING ORG. REPORT NUMBER
7. AUTHOR(s) A. V. Phelps and A. C. Gallagher	8. CONTRACT OR GRANT NUMBER(s) N00014-76-C-0123 ✓	
9. PERFORMING ORGANIZATION NAME AND ADDRESS University of Colorado Joint Institute for Laboratory Astrophysics Boulder, CO 80309		10. PROGRAM ELEMENT, PROJECT, TASK AREA & WORK UNIT NUMBERS NR 393-506/3-21/79, Code 421 ARPA Ord. No. 2683 Prog. Cd. 8E20
11. CONTROLLING OFFICE NAME AND ADDRESS Office of Naval Research Department of the Navy 800 North Quincy Street, Arlington, VA 22217		12. REPORT DATE 15 January 1981
14. MONITORING AGENCY NAME & ADDRESS(if different from Controlling Office)		13. NUMBER OF PAGES 175
		15. SECURITY CLASS. (of this report) Unclassified
		16a. DECLASSIFICATION/DOWNGRADING SCHEDULE
16. DISTRIBUTION STATEMENT (of this Report) DISTRIBUTION STATEMENT A Approved for public release: Distribution Unlimited		
17. DISTRIBUTION STATEMENT (of the abstract entered in Block 20, if different from Report)		
18. SUPPLEMENTARY NOTES		
19. KEY WORDS (Continue on reverse side if necessary and identify by block number) Laser processes, sodium vapor, rare gas, electrical discharge, stability, high pressure, molecules, metastables, neon, absorption, dye laser, metastables, oxygen, nitrogen, sodium, excimer, cathode fall, resonance radiation, non-radiative, diffusion		
20. ABSTRACT (Continue on reverse side if necessary and identify by block number) Measurements at very high rare gas densities have yielded the contribution of trimer molecules, e.g., NaXe ₂ , to the absorption and stimulated emission continuum of metal vapor-rare gas excimers. Attempts to obtain a sufficiently high electron and excited state temperature in a pulsed discharge in high pressure metal vapor-rare gas mixtures were unsuccessful because of the approach of the system to local thermodynamic equilibrium and the limited peak electrical energy available. A model was developed to describe (continued)		

the temporal growth of the cathode fall in an electron-beam initiated electric discharge. The electron drift tube technique for the measurement of electron excitation coefficients was applied to the A^{3D} and b^{1D} metastable states of N_2 and O_2 , respectively, and was extended to make possible laser absorption measurements of excitation coefficients for the $3P_2$ metastable and $3P_1$ resonance states of Ne. Experimental measurements of fluorescent intensities from the resonance state of Na with white light and laser excitation, show agreement with theory when the theory is modified to include hyperfine structure and the non-radiative transport of resonance excitation.

sigma

Accession For	
NTIS GRA&I	<input checked="" type="checkbox"/>
DTIC TAB	<input type="checkbox"/>
Unannounced	<input type="checkbox"/>
Justification	
By _____	
Distribution/	
Availability Codes	
Dist	Avail and/or Special
A	

FINAL REPORT

This Final Report contains descriptions of work carried out under ONR Contract No. N00014-76-0123 and ARPA Order No. 2683. It covers the period from 1 July 1975 to 15 May 1980. Section I is the Final Report Summary, of which Sections IA through IE are summaries of work carried out under the projects supported by this contract. Section II contains copies of the papers published or submitted for publication under this contract.

	<u>Page</u>
I. Final Report Summary	
A. Generation and Interpretation of Molecular Continuum Radiation	3
B. Metal Vapor-Rare Gas Discharges	4
C. Stability of Discharges in Weakly Ionized Gases	6
D. Electron Excitation of Molecular and Atomic Metastables	7
E. Scattering and Transport of Resonance Radiation in Gases	9
F. References	11
II. Reprints and Preprints of Published Papers	13

I. FINAL REPORT SUMMARY

The projects carried out under this contract are summarized below.

The publications describing these results in detail are given in Section II of this report. All references in this section are to publications in Section II or, in the case of as yet unpublished results, to papers presented at various conferences.

A. Generation and Interpretation of Molecular Continuum Radiation (Project Leader - Dr. A. C. Gallagher)

The objective of this project was to extend previous measurements and analyses of the continuum radiation emitted by metal atom-rare gas excimers to the highest rare gas densities of proposed lasers and to extend the measurements to a metal vapor, Mg, characteristic of column II of the periodic table.

Measurements at very high rare gas densities¹⁻⁴ demonstrated the importance of trimer molecules, such as NaXe₂, and led to the development of a successful model for predicting the fluorescent intensity and the stimulated emission coefficients for the continuum radiation emitted by these molecules. This model makes possible extrapolation of the data obtained for various metal atom-rare gas atom systems at relatively low rare gas densities to the higher gas densities of potential lasers.

In the course of measurements at very high rare gas densities it was necessary to measure and interpret the spectral distribution of intensity near the cores of the resonance lines of thallium² and sodium.^{3,4} This data provides a means of normalizing the continuum data to the gas density and the resonance line transition probability.

The continuum spectra of the MgXe molecule⁵ was measured in order to characterize the spectra of molecules formed when rare gas atoms collide with excited atoms of the light elements of Column II of the periodic table. The moderate stimulated emission coefficient for MgXe and the higher excitation potential of the Mg atom mean that a higher excitation temperature is required for laser gain for Mg-Xe than for Na-Xe. The trends among the possible metal vapor-rare gas molecular excimers and the excitation conditions required for efficient laser operation were summarized in a review paper on metal vapor excimers.⁶

On the basis of the measurements and analyses of metal vapor excimer spectra completed under this project, it was concluded that the NaXe system offered many advantages for further investigation as the working medium for an efficient, high power laser. Among these advantages were the requirement of a relatively low excitation temperature of about 0.6 eV for the Na(3P) resonance state in order to obtain population inversion in the high gain portion of the A-X band of NaXe, a relatively high vapor pressure at workable temperatures, and the availability of a relatively large body of collision cross section and rate coefficient data for electrons, excited atoms and ions in the Na-Xe mixture. It was also concluded that electric discharge excitation of the Na-Xe molecules offered the possibility of an efficient, high power laser system.

B. Metal Vapor-Rare Gas Discharges
(Project Leader - Dr. A. C. Gallagher)

On the basis of our measurements and analyses of the continuum spectra of metal vapor-rare gas molecules, see Section IA, attempts were made to operate electrical discharges in metal vapor-rare gas mixtures with the

characteristics needed for efficient, high power lasers. The Na-Xe system was chosen for the initial studies because of the relatively low excitation and gas temperatures required and because of the possibilities for extensive modeling of these discharges. The experimental results for the Na-Xe discharges⁷ showed the existence of a stable, pulsed discharge mode lasting several microseconds at the desired Na densities of 10^{15} - 10^{16} cm^{-3} and Xe densities of 19^{19} - 10^{20} cm^{-3} at input powers of 10-100 Mw/liter. However, the excitation temperatures for the Na(^2P) state and the presumed electron temperatures were only about 0.4 eV compared to the value of about 0.6 eV needed for successful laser operation. These experiments showed that the higher excited states of the Na atoms and the Na⁺ ions were populated at concentrations near those expected for local thermodynamic equilibrium.

Similar experiments were carried out with the MgXe mixtures.⁵ In addition to providing the data on the MgXe excimer continuum referred to in Section IA, these experiments showed that one can obtain stable, pulsed discharges in Mg-Xe mixtures at Mg and Xe densities and electrical input powers of laser interest. However, as in the case of Na-Xe discharges, the excitation and electron temperatures were too low to yield optical gain at wavelengths of laser interest.

An extensive model of electrical discharges in Na-Xe mixtures was developed⁸ for use in understanding and extrapolating our experimental data.⁷ The model includes sixteen excited states of Na, three ions (Na⁺, NaXe⁺ and Na₂⁺), and the excimer levels of NaXe and Na₂. The degree of ionization is determined by a balance between collisional multistep

excitation and ionization of excited Na and dissociative recombination of electrons with Na_2^+ . The relative excited state densities predicted by this model can be brought into agreement with our experiments⁷ by choosing an unexpectedly high state of Na as the product of the dissociative recombination of electrons and Na_2^+ . We were unable to obtain satisfactory agreement between the calculated and measured electrical energy inputs for given densities of Na, Xe and electrons. The model suggests that successful NaXe excimer laser operation might be obtained by using sufficiently high Na and Xe densities and a short (< 100 ns), high current density electric discharge.

C. Stability of Discharges in Weakly Ionized Gases
(Project Leader - A. V. Phelps)

The objective of this project was to extend our previous calculations of the growth of radial constrictions in a weakly ionized gas discharge to include calculations of effect of axial inhomogeneities. When the three-dimensional solutions proved too difficult because of the large computer resources required to solve the cathode fall region of the discharge, we decided to concentrate on obtaining solutions for the one-dimensional cathode region to be used in future three-dimensional models. The geometry chosen for these calculations⁹ corresponded to that of an electron beam initiated, electric discharge laser. The model shows that after a period of reduced electric field near the peak of the initial ionization, the field at the cathode increases as the electrons are swept toward the anode. This increased field causes an ionization wave to move toward the cathode to form the cathode flow. The field and charge distributions in

the cathode region are essentially independent of the gap length. A potentially serious problem with this model occurs as the electric fields near the cathode increase toward their large, steady-state values. It is our use of ionization rate coefficients depending only on the local electric field strength. This problem is currently being investigated under another contract in connection with calculation of ionization coefficients at high electric fields.

D. Electron Excitation of Molecular and Atomic Metastables
(Project Leader - A. V. Phelps)

The overall objective of this project was the measurement and analyses of excitation coefficients for the production of metastable states of O₂, N₂ and Ne so as to provide data required for the prediction of rates of excited state and electron-ion production in gas discharge devices and systems utilizing these gases, e.g., the discharge excited oxygen-iodine laser, electron beam propagation in air, and the neon-halogen laser. This project utilizes and extends the very significant improvements in the electron drift tube technique which have recently been made in this laboratory.

The measurements and analyses of coefficients for the electron excitation of the O₂(b¹Σ) state¹⁰ were undertaken in order to provide data on the excitation of this molecule under conditions appropriate to electrical discharges. The O₂(b¹Σ) state was chosen for this initial investigation of O₂ because it emits in the photomultiplier wavelength region (762 nm) and its radiative lifetime (13 sec) is not too long compared to lifetimes against collisional quenching (~30 msec). The measured lifetimes against

quenching were much longer than the accepted values and so were verified by an auxilliary experiment¹¹ utilizing laser excitation of O₂. The measured excitation coefficients are in reasonable agreement with predicted values at low mean electron energies (<0.8 eV) but are as much as a factor of three above predictions at moderate mean electron energies (~3 eV). Attempts to determine the excited states and deexcitation processes involved in this apparent cascading from higher excited states of O₂ are continuing under another contract.

The measurements and analyses of collisional deexcitation rate coefficients¹² and electron excitation coefficients¹³ for the N₂(A^{3Σ_u⁺) metastable state and excitation coefficients for the N₂(C^{3Π_u) radiating state¹⁴ were made in order to provide data necessary for the modeling of electric discharge systems containing N₂, e.g., the well known N₂ uv laser utilizing the C^{3Π} state and proposed lasers utilizing energy transfer from the N₂(A^{3Σ}) state. Analysis of the excitation coefficient data for the N₂(A^{3Σ}) state shows that under steady-state or electron-beam-sustained electric discharge conditions the excitation coefficients for this state are virtually independent of the cross section for direct electron excitation of the N₂(A^{3Σ}) state and are determined by the very large cross sections for excitation of the vibrational levels of N₂. The analyses of the N₂(C^{3Π}) state data show that it is important to take into account the details of the excitation cross section near threshold. Finally, we find¹⁵ that using conventional solutions of the Boltzmann equation and a given set of collision cross sections for electrons in N₂ we obtain poor agreement (~30%) between calculated values of the electron excitation}}

coefficients for the $N_2(A^3\Sigma)$ state and the electron transport coefficients. As yet incomplete work under another contract suggests that this discrepancy is the result of the failure of the conventional techniques for solution of the Boltzmann equation when the inelastic cross sections are large.

The measurements of electron excitation coefficients for the lowest metastable and radiating states of neon, i.e., the $Ne(^3P_2)$ and $Ne(^3P_1)$ states, were made in order to provide data necessary for the understanding and design of electric discharge excited lasers utilizing mixtures of neon with gases such as xenon and chlorine. The more conventional electron beam techniques had been able to provide only the sum of the excitation cross sections for the lower metastable and radiating states. Because of the very long radiative lifetimes for $Ne(^3P_2)$ atoms the observation of emission is not possible and we have developed a very sensitive multipath, laser absorption technique for measuring the density of excited neon atoms. An initial analysis of the resultant excitation coefficient data¹⁶ shows that about 25% of the calculated total excitation appears as excitation of the $Ne(^3P_2)$ state. Similarly for the $Ne(^3P_1)$ state. Analyses of the experimental data and the preparation of a publication of these results are continuing.

E. Scattering, Transport and Excitation Transfer of Resonance Excitation in Gases
(Project Leaders - A. V. Phelps and A. C. Gallagher)

The experiments carried out under this project were designed to provide data essential to the understanding and prediction of the role of atoms excited to the resonance state in electrical discharges and in systems where optical excitation of atoms is used. Such data is necessary, for example, in analyses of the pulsed discharges in Na-Xe mixtures discussed in Section IB of this report.

The initial phase of this project was the completion of measurements and analyses of the transport of resonance excitation under white light excitation in pure Na and in Na-N₂ mixtures.¹⁷ These results showed that when the theory of resonance radiation transport is modified to take into account hyperfine structure of the resonance line it is able to predict the magnitude and spectral distribution of the fluorescence. Because of the broadband excitation used, these experiments are insensitive to the occurrence of the non-radiative transport of resonance excitation.

The second phase of this project was the measurement¹⁸ of rate coefficients for the collisional transfer of excitation among lower excited states of Na and Na₂. These experiments yielded rate coefficients for the transfer of excitation from the Na(3²P) state to the Na₂(a³Π_u) and Na₂(A¹Σ_u⁺) states and for the destruction of the Na₂(a³Π_u) state by dissociation to form Na(3²P) atoms and ground state atoms.

A third phase of this project was the initiation of measurements and analyses of the transport of resonance excitation using a single mode laser to excite the Na atoms rather than the white light source used in our earlier experiments. These experiments¹⁹ show that when the laser is tuned to the peak of the resonance line absorption profile the excited atoms are produced very close to the cell entrance window and are rapidly destroyed as a result of a non-radiative or diffusion type transport to the window. This type of excited atom loss is expected to be important whenever there is a large gradient in the excited atom density and to significantly reduce the efficiency of optical pumping experiments when the source is tuned to the center of the resonance line.

F. References

1. W. P. West, P. Shuker and A. Gallagher, J. Chem. Phys. 68, 3864 (1978).
2. B. Cheron, R. Scheps and A. Gallagher, Phys. Rev. A 15, 651 (1977).
3. W. P. West and A. Gallagher, Phys. Rev. A 17, 1413 (1978).
4. D. W. Wildman, L. W. Schuman and A. C. Gallagher, J. Quant. Spectrosc. Radiat. Transfer 24, 19 (1980).
5. L. Schumann, D. Wildman and A. Gallagher, J. Chem. Phys. 72, 6081 (1980).
6. A. Gallagher, in Excimer Lasers, ed. by Ch. K. Rhodes (Springer-Verlag, Berlin, 1979), Chap. 5.
7. H. L. Rothwell, D. Leep and A. Gallagher, J. Appl. Phys. 49, 4396 (1978).
8. R. Shuker, A. Gallagher and A. V. Phelps, J. Appl. Phys. 51, 1306 (1980).
9. H.-C. Chen and A. V. Phelps, Bull. Am. Phys. Soc. 22, 201 (1977).
10. S. A. Lawton and A. V. Phelps, J. Chem. Phys. 69, 1055 (1978).
11. S. A. Lawton, S. E. Novick, H. P. Broida and A. V. Phelps, J. Chem. Phys. 66, 1381 (1977).
12. D. Levron and A. V. Phelps, J. Chem. Phys. 69, 2260 (1978).
13. D. Levron and A. V. Phelps, Bull. Am. Phys. Soc. 24, 129 (1979).
14. K. Tachibana and A. V. Phelps, J. Chem. Phys. 71, 3544 (1979).
15. A. V. Phelps, D. Levron and K. Tachibana, in Electronic and Atomic Collisions, ed. by K. Takayanagi and N. Oda (Soc. for Atomic Collision Research, Japan), p. 318.
16. K. Tachibana and A. V. Phelps, Paper AA-1, 33rd Gaseous Electronics Conference, Oct. 1980. Bull. Am. Phys. Soc. 26 (in press) (1981).

17. T. Fujimoto and A. V. Phelps, Bull. Am. Phys. Soc. 21, 173 (1976).
18. L. K. Lam, T. Fujimoto, A. C. Gallagher, and M. M. Hessel, J. Chem. Phys. 68, 3553 (1978).
19. A. G. Zajonc and A. V. Phelps, Bull. Am. Phys. Soc. 23, 74 (1978) and Phys. Rev. A (submitted) (1980).

II. Reprints and Preprints of Published Papers.

Noble-gas broadening of the $6^2P_{1/2}$ - $7^2S_{1/2}$ (377.6 nm) $6^2P_{3/2}$ - $7^2S_{1/2}$ (535 nm) thallium lines*

B. Cheron,[†] R. Scheps,[‡] and A. Gallagher[†]

Joint Institute for Laboratory Astrophysics, National Bureau of Standards and University of Colorado, Boulder, Colorado 80309

(Received 7 September 1976)

The shapes of the thallium (Tl) 535- and 377.6-nm resonance lines broadened by 500–1500 Torr of noble gases have been measured at 743 K. The reported normalized emission intensities yield absorption coefficients in absolute units for all portions of the line. The shift and broadening of the Lorentzian-shaped line cores, the wavelengths of the transition to non-Lorentzian wings, wing shapes, and satellite positions, shapes, and intensities are reported. As an example, a pair of excited and ground-state interaction potentials are given for the Xe case to explain the shift, width, and intensities in all portions of the line wings.

I. INTRODUCTION

The lowest thallium (Tl) atomic levels are represented on Fig. 1. The ground state $6^2P_{1/2}$ belongs to the $6s^26p$ configuration. The other component of the doublet ($6^2P_{3/2}$) lies 7800 cm^{-1} above the ground state and is metastable. In our experiment Tl atoms are optically excited from the ground state to the $6s^27s$ ($7^2S_{1/2}$) state in the presence of noble gases and the shapes of the two subsequent fluorescence lines at 377.6 and 535 nm are studied (hereafter called the uv line and the green line, respectively). The purpose of this work is (1) to measure the shift and broadening coefficients of these two lines due to collisions with noble gases (the impact theory predicts for isolated lines a Lorentzian core of the line with a shift and width that are proportional to the density of perturbers), (2) to determine the approximate wavelength of transition between Lorentzian and non-Lorentzian broadening, and (3) to measure the line-wing intensities in the non-Lorentzian region, including the positions and intensities of the satellites. The present report emphasizes the line core and the spectral regions $|\Delta\lambda| < 10\text{ nm}$ for each line, where $\Delta\lambda = \lambda - \lambda_0$ and λ_0 is the unperturbed wavelength of the line. In the region $|\Delta\lambda| > 10\text{ nm}$ the spectrum is highly temperature dependent due to population factors, and as a consequence it can be analyzed using the quasistatic theory to yield the interatomic potentials. This is rather involved and has been reported in another paper.¹

II. EXPERIMENT AND RESULTS

The reported measurements and analysis are very similar to previously reported measurements of the Rb and Li resonance lines broadened by noble gases,^{2,3} so we give only a brief description here.

A cell containing 10^{-7} to 10^{-5} Torr of natural Tl (29.5% ^{203}Tl and 70.5% ^{205}Tl) and up to 1500 Torr

of noble gas is illuminated by light from a Tl resonance lamp filtered by an interference filter centered at 377.6 nm. The fluorescence intensity was measured with a 0.75-meter double monochromator equipped with two 2400-grooves/mm holographic gratings, and a cooled GaAs photomultiplier.

As described in Ref. 2 the line shape was obtained by combining scans of different slit width and resolution. This yields line-wing intensities unaffected by instrumental resolution but line-center shapes, typically $|\Delta\lambda| < 0.04\text{ nm}$, that are distorted by the instrumental resolution. Measurements were generally made at pressures where the broadened linewidth exceeded the instrumental width, and both greatly exceeded the Doppler width. Then the actual broadening could be accurately determined from comparisons of the measured line-center profiles with theoretical convolutions of Lorentzian lines with the instrument function. This is described in more detail below.

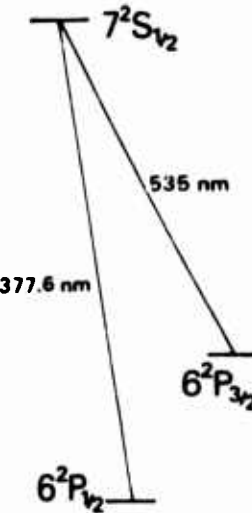


FIG. 1. Lowest three atomic levels of thallium.

The instrument function was determined with an air-cooled low-pressure isotopic mercury lamp (^{198}Hg) using the 365 and 546-nm lines. The resolution was ~ 0.005 nm at 546 nm and ~ 0.006 nm at 365 nm for the $12-\mu\text{m}$ spectrometer slit opening used to obtain the line-center data ($|\Delta\lambda| < 0.05$ nm). For the line-center data the output slit position was scanned mechanically to avoid grating-drive irregularities. The accuracy in this scanning was limited by a periodic nonlinearity, with a deviation from linearity of about 4%. The resulting $\sim 4\%$ uncertainty in apparent linewidth made a small contribution to the typical $\sim 10\%$ total uncertainty in the broadening. For $|\Delta\lambda|$ greater than about 0.05 nm, conventional grating driving was used, which did not cause irregularities on the lower resolution scale of the line-wing data.

The fluorescence intensities are reported as normalized emission coefficients $I(k)/N \int I(k) dk$ for each line, where $I(k)$ is the fluorescence intensity per wave number, $k = 1/\lambda$, $k_0 = 1/\lambda_0$, $\Delta k = k - k_0$, N is the noble gas density and the integral is over one line from $k_0 - W$ to $k_0 + W$, where $W \approx 50 \text{ cm}^{-1}$. For the pressures in our experiment this emission coefficient is independent of the Tl and noble-gas densities for wavelengths outside the Lorentzian-core region (indicating that binary interactions with the perturber rather than three-body collisions are dominant). This emission coefficient is related to the absorption coefficient by simple thermodynamic factors equivalent to the Einstein A - B relations.³

Since radiative trapping attenuates the center of a line, thereby yielding erroneous normalized wing intensities [due to inaccuracy of $\int I(k) dk$], it is necessary to measure these emission coefficients from optically thin Tl vapor, or in the limit of zero Tl density. This Tl experiment is particularly simple in this regard as the $6^2P_{3/2}$ metastable state is very slightly populated thermally and the $7^2S_{1/2}$ - $6^2P_{3/2}$ (green) line should not be radiatively trapped since, as explained later, the $6^2P_{3/2}$ state is not optically pumped. Thus the green line shape can be measured at relatively high Tl densities ($\sim 10^{-5}$ Torr), providing larger signals. Furthermore, if the ratio R of the uv to green-line total intensities is measured once in the absence of radiation trapping ($R = R_0$), this can be used to correctly normalize uv line-wing data taken in the presence of radiation trapping in the center of the uv line. In the present experiments the light intensity was low enough and the $6^2P_{3/2}$ state quenching rate due to molecular impurities (probably $\sim 10^{-1}$ Torr in 10^3 -Torr noble gas) high enough, so that insignificant optical pumping of the $6^2P_{3/2}$ state occurred. This was confirmed by the fact that the ratio R was not affected by

lowering the intensity of the excitation lamp. Then R was measured in the limit of zero Tl density to obtain R_0 , and all the line-wing data were normalized to the green line. During the line-shape measurements R was typically 10% lower than R_0 . The shape of the uv line core was measured at relatively lower Tl densities (estimated $\sim 10^{-6}$ Torr), where typically $\sim 3\%$ attenuation of the line peak occurred. This causes a few percent apparent broadening, but was deemed too small to warrant a correction.

The emission coefficients for perturber pressures between 500 and 1500 Torr are given in Fig. 2 for the uv line and in Fig. 3 for the green line. These spectra represent the actual fluorescence intensity distribution, essentially unaffected by instrument resolution, for $|\Delta\lambda| > 0.05$ nm. The solid lines in Figs. 4 and 5 represent the measured emission coefficients in the line-core region for the uv and the green lines, respectively, for various pressures. These spectra are influenced by the instrumental resolution. The experimental results are compared to theoretical convolutions of the instrument function with the Lorentzian-broadened components corresponding to the thal-

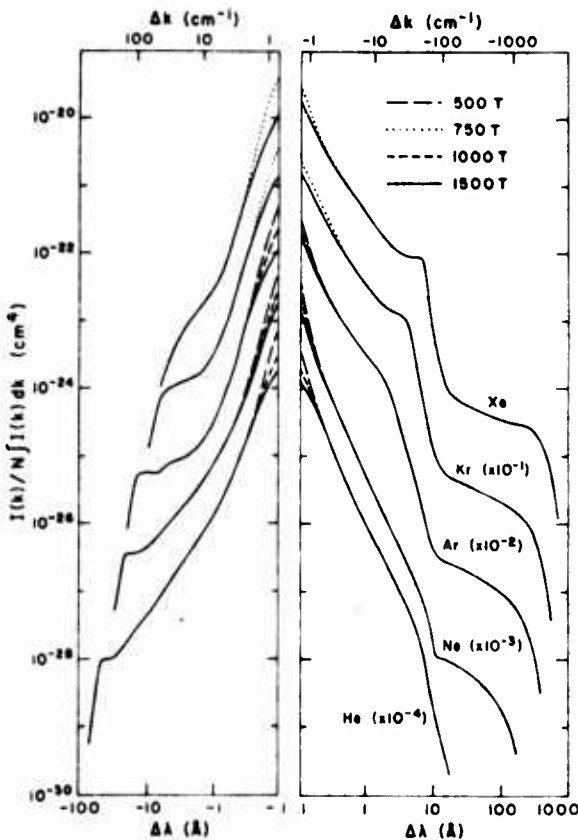


FIG. 2. Normalized emission intensities of the Tl 377.6-nm line broadened by the noble gases at the cell temperature of 743 K.

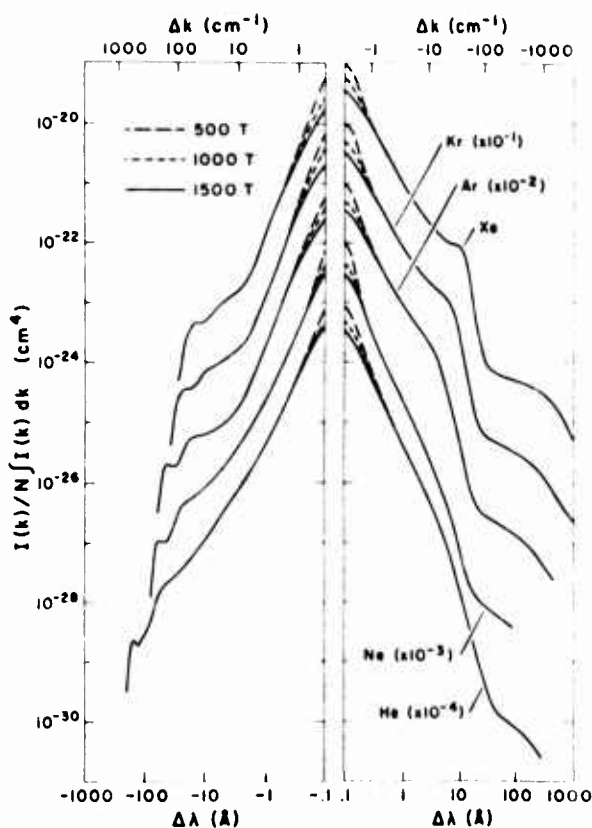


FIG. 3. Same as Fig. 2 for the Tl 535-nm line.

lum hyperfine structure.⁴ As the isotope shift is minor, only hyperfine components, shown in Figs. 4 and 5, were used. The Doppler contribution to the line shape is very minor and is partly included in the instrument function. The same Lorentzian parameters γ and Δ in $I \propto [(\frac{1}{2}\gamma)^2 + (\Delta k - \Delta)^2]^{-1}$ are used for each component. The relative intensity of the different components would be statistical for white-light excitation or complete collisional mixing, but the lamp spectrum is less at the weaker (smaller F) components and the $7^2S_{1/2}$ state is not easily depolarized by noble-gas collisions. Thus the hyperfine component intensities arising from the smaller 7^2S state F components had to be decreased about 20% from statistical to fit the experimental spectra. The convolutions are calculated with $\Delta = 0$ and then shifted to yield optimum visual fits in the line-core region. The γ parameters are chosen to optimize the fits in the line-core region where the lines appear to be nearly Lorentzian. The comparisons are shown in Figs. 4 and 5. It can be seen that except for He (uv and green lines) and Ne (uv line), a good fit to the Lorentzian convolution is obtained in the line-core region. The misfit for the He and Ne cases is not severe, and

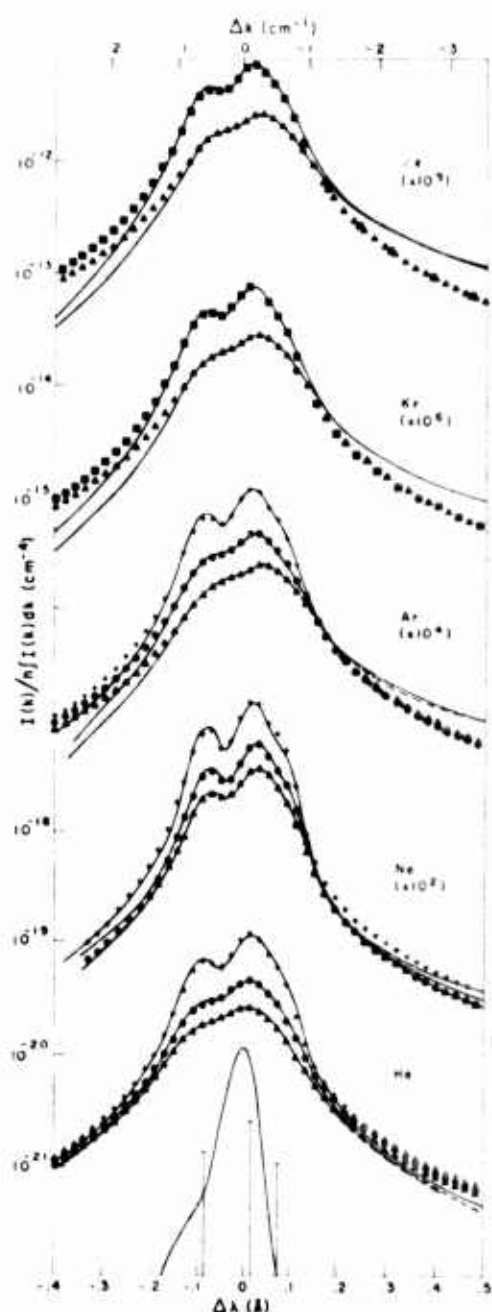


FIG. 4. Measured normalized emission intensities (full lines) in the central region of the Tl 377.6-nm line. For He, Ne, and Ar, the upper line is for 500-Torr perturber pressure, the middle for 1000 Torr and the lower for 1500 Torr. For Kr and Xe the upper line is for 750 Torr and the lower for 1500 Torr. The hyperfine structure and the instrument profile ($\sim 0.4\text{-cm}^{-1}$ resolution) are indicated at the bottom of the figure. Theoretical convolutions of the instrument function with Lorentzian-shaped line components are given as variously shaped +, Δ , and \circ points. The shift and Lorentz width parameters used in these convolutions are given in Figs. 6 and 7.

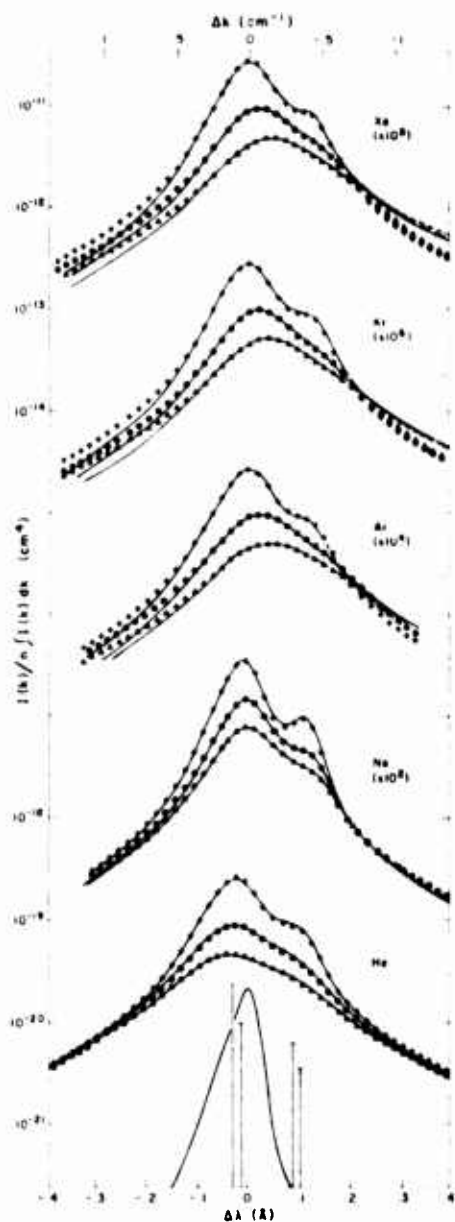


FIG. 5. Same as Fig. 4 for the Tl 535-nm line except that for each perturber case the upper line is for 500 Torr, the middle for 1000 Torr and the lower for 1500 Torr.

is attributed primarily to instrumental effects.

The shift (Δ) and full width (γ) of the Lorentzian portion of the lines are plotted versus density of perturber in Fig. 6 for the uv line and Fig. 7 for the green line. The slopes of the fitted lines in Figs. 6 and 7 are reported as shift and broadening rates in Table I. Also included in this table is the estimated value of the wavelength of the transition between Lorentzian and non-Lorentzian broadening from the convolution fitting in Figs. 4

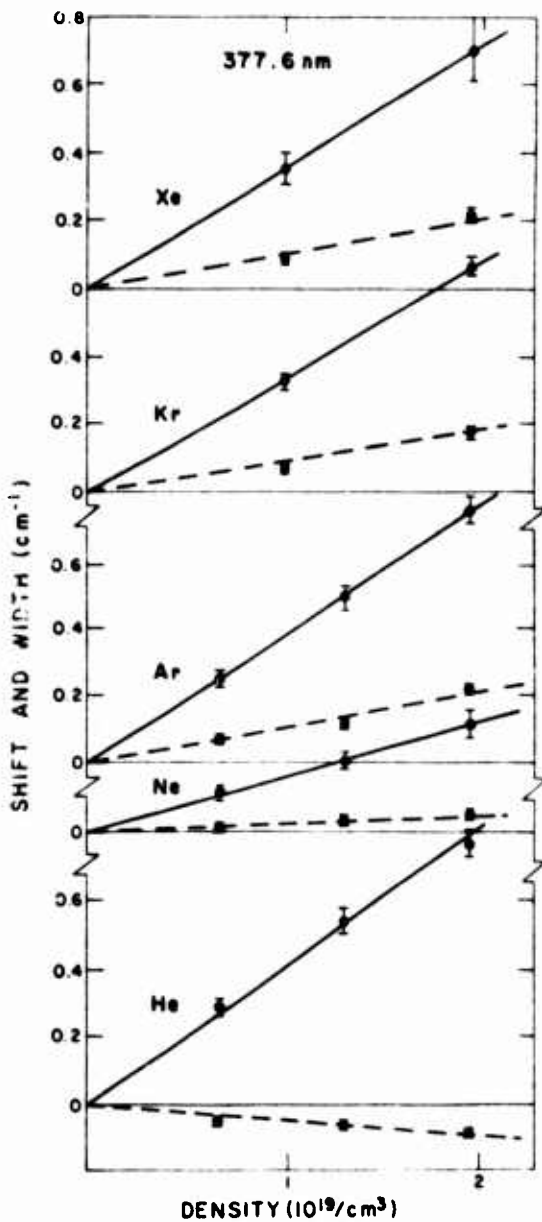


FIG. 6. Shifts Δ (dashed lines) and full Lorentz widths γ (solid lines) of the 377.6-nm line obtained from Fig. 4.

and 5. This transition point is the estimated point of departure of the actual wing slope from that predicted by the Lorentzian convolution. In Table II, we give the effective power dependence n , in $I \propto |k - k_0 - \Delta|^{-n}$, of the wing intensities in these non-Lorentzian regions adjacent to the Lorentzian core (see Figs. 2 and 3). The fitted wavelength range is also given. This is not intended to imply actual power-law intensity dependences; rather there is a region on each wing where a power law gives a good fit across 1-2 decades in intensity.

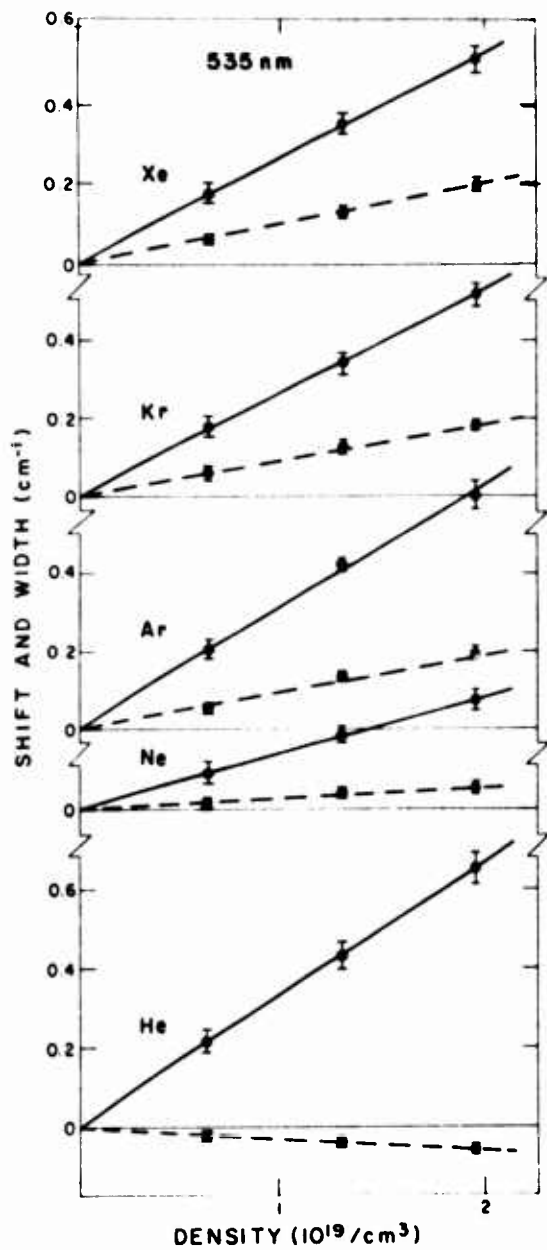


FIG. 7. Shifts Δ (dashed lines) and full Lorentz widths γ (solid lines) of the 535-nm line obtained from Fig. 5.

The fit typically determines n with about $\pm 5\%$ accuracy. Finally, we give in Table III the estimated position of the centers of the satellites in Figs. 2 and 3 and compare with other data. In many cases these satellites are so broadened that they are mere inflections whose centers are ill defined.

III. INTERATOMIC POTENTIALS FROM THE DATA

The far wings of these broadened Tl lines are due to close-range Tl-noble-gas interactions.

They can be analyzed with the use of the quasi-static theory to yield information about the interatomic potentials at internuclear separations R of typically 3–4 Å. The satellites, attributed to extrema in the difference potential $\Delta V(R) = V^*(R) - V(R)$ in the 4–8-Å regions, yield information about these portions of the potentials. The intensities in the wings adjacent to the Lorentzian core of the lines yield information on the 8–12-Å parts of the potentials. Finally, the broadening and shift are related to the potentials in the region of the Weisskopf radius, typically 12–20 Å. C_6 coefficients based on isolated atomic properties also yield potentials in these large- R regions. Thus when absolute intensity information is available in all these portions of the line it provides a very powerful tool for determining the interatomic potentials $V^*(R)$ and $V(R)$ for the upper and lower states of the transition. The inversion of the data to yield these potentials is almost unique in the small- R regions where $[V^*(R) - V^*(\infty)]/kT \geq 1$, since thermal population (Boltzmann) factors yield large temperature dependences that depend on the potentials¹. The inversion of the data in other portions of the line to yield $V^*(R)$ and $V(R)$ is much less unique. Nonetheless, we will demonstrate that this inversion can sometimes be done with surprisingly little ambiguity, and we give here an example. This analysis is much simpler if the atomic interactions produce only a single $V^*(R)$ and $V(R)$; so we choose the Tl $7^2S_{1/2}$ – $6^2P_{1/2}$ (uv) line for the example as it satisfies this criterion. [The Tl ($6^2P_{3/2}$) state splits into two $V(R)$ and must be analyzed in terms of superpositions of bands.] We will describe the Tl-Xe case in detail, since the other cases can be generalized from this with very minor changes.

The analysis of the temperature-dependent far-wing intensities ($\Delta\lambda > 15$ Å in Fig. 2) to yield $V^*(R)$ and $V(R)$ in the 3–4-Å region have already been described in Ref. 1 and will not be repeated here. These $V^*(R)$ and $V(R)$ are shown for the Tl-Xe case considered here in Fig. 8. We will now extend that analysis to the remaining, larger- R regions. We will assume a familiarity with the quasistatic theory as described in Ref. 1 and references cited therein. For the more polarizable noble-gas cases (Ar, Kr, and Xe) we expect $V^*(R)$ to be more attractive at long range than $V(R)$, since the excited-state wave function is much larger and more polarizable, i.e., $C_6^* > C_6$ in $V^*(R) - V^*(\infty) = C_6^* R^{-6}$ and $V(R) - V(\infty) = C_6 R^{-6}$. This is also required to explain the large red-wing intensities for these cases (Fig. 2). Thus $\Delta V(R) - \Delta V(\infty)$ must be negative at large R ($R > 8$ Å in Fig. 8) and approach zero with a positive slope as $R \rightarrow \infty$.

TABLE I. Shift Δ and full width γ of the Lorentzian line core.^a

Line	Perturber	Δ/N (cm ⁻¹ /r.d.)	γ/N (cm ⁻¹ /r.d.)	$k - k_0$ at non-Lorentzian ^b transition zone (cm ⁻¹)
377.6 nm	He	+0.13 ± 0.03 ^c	1.06 ± 0.1	+7
	Ne	-0.070 ± 0.02	0.44 ± 0.05	... ^d
	Ar	-0.27 ± 0.04	1.01 ± 0.06	+1.0
	Kr	-0.23 ± 0.05	0.91 ± 0.07	+1.0
	Xe	-0.27 ± 0.05	0.98 ± 0.1	+0.85
535 nm	He	+0.065 ± 0.015	0.91 ± 0.06	+9
	Ne	-0.085 ± 0.02	0.40 ± 0.04	... ^d
	Ar	-0.27 ± 0.02	0.84 ± 0.06	+0.4
	Kr	-0.25 ± 0.02	0.72 ± 0.04	+0.4
	Xe	-0.28 ± 0.02	0.72 ± 0.02	+0.4

^aThe shift and broadening coefficients are given per r.d. or relative density where 1 r.d. = 2.69×10^{19} cm⁻³ is the density of the perfect gas at standard temperature and pressure. The values are given at $T = 743 \pm 5$ K except for 377.6 nm (He, Ne, Ar) and 535 nm (Ar) where $T = 720 \pm 5$ K.

^bDue to the large hyperfine structure, the magnitude of the values indicated for Ar, Kr, Xe are upper limits.

^cThe uncertainties represent ± one standard deviation of statistical and estimated systematic effects.

^dThe transition could not be determined due to the small change in wing power dependence (see Table III).

The intense red wing in the $\Delta\lambda = 1-10$ Å portion of the Tl-Xe spectrum in Fig. 2 terminates in a red "satellite" or shoulder whose outer edge is at ~ 50 cm⁻¹. Thus $\Delta V(R)$ must reach a negative extremum of $\Delta V \approx -50$ cm⁻¹ and then reverse slope (~ 6 Å in Fig. 8). This red shoulder might also have been attributed to merely a flattening of $\Delta V(R)$ in the 6-Å region, followed by an increasingly negative ΔV ($R < 6$ Å). However, there is a severely broadened shoulder or "satellite" on the Tl-Xe blue wing in Fig. 2, which requires that $\Delta V(R)$ must have a positive maximum at some R . From the general satellite-shape theory of Sando and Wormhandt⁸ we attribute this to a maximum of

about +30 cm⁻¹ in ΔV ; a $|\Delta k|$ slightly past the shoulder where the intensity is beginning to drop more rapidly. The only R region where this positive $\Delta V(R)$ can occur is between the large R and small R regions of negative $\Delta V(R)$. This occurs very naturally at ~ 4.5 Å in Fig. 8 by a smooth extension of $\Delta V(R)$ at small R and attributing the red satellite to an actual minimum, not an inflection, at ~ 6 Å. Thus, while this result is non-unique, we believe that no other reasonable form for $\Delta V(R)$ could explain the data; it must be negative at small and large R with a positive extremum in between, as given in Fig. 8.

The R scale in Fig. 8 has been determined using

TABLE II. Wing power dependence ($I \sim |k - k_0 - \Delta|^{-n}$).

Line	Perturber	n	Blue wing		Red wing	
			$ k - k_0 $	Range (cm ⁻¹)	$ k - k_0 $	Range (cm ⁻¹)
377.6 nm	He	2.1	2.5-7		2.0	0-30
	Ne	2.3	2-5.5		2.0	0-15
	Ar	3.8	2.5-4.5		1.4	3-10
	Kr	3.2	2.5-5		1.3	3.5-9
	Xe	3.2	2.8-5		1.3	3.5-15
535 nm	He	2.0	0-7		2.0	0-12
	Ne	2.2	1-5		2.0	0-7
	Ar	2.7	1.2-7		1.5	1-10
	Kr	2.7	1.2-5		1.6	1-3.5
	Xe	2.8	1-5		1.7	1.5-7

TABLE III. Satellite positions.

Line	Perturber	Present ($T = 743$ K)	Δk (cm^{-1})	Other experiments	
		$\Delta\lambda$ (nm)		Δk (cm^{-1})	T (K)
377.6 nm	He	-4.4 ± 0.3	309 ± 21	314 ± 14 ^b	973
	Ne	-2.0 ± 0.1	140 ± 14	144 ± 10 ^b	973
	Ar	+0.2 ± 0.05 ^a	-14 ± 3.5	82 ± 7 ^b	823
		-13 ± 1	91 ± 7		
	Kr	+0.37 ± 0.03	-26 ± 2	-24.6 ± 2.0 ^b	798
		-0.55 ± 0.05	38.5 ± 3.5	35.1 ± 7 ^b	1393
	Xe	+0.68 ± 0.03	-48 ± 2	-41.5 ± 35 ^b	798
		-0.5 ± 0.1 ^a	35 ± 7		
535 nm	He	-5.0 ± 0.3 ^a	175 ± 11		
		-14.5 ± 0.2	507 ± 7	576 ^c	
	Ne	-1.5 ± 0.3 ^a	52 ± 11		
		-6.0 ± 0.5	210 ± 18	249 ^c	
	Ar	+0.37 ± 0.05 ^a	-13 ± 2		
		-1.7 ± 0.2	59.5 ± 7		
		-4.5 ± 0.2	157 ± 7	173 ^c	
	Kr	+0.6 ± 0.1 ^a	-21 ± 3.5		
		-1.0 ± 0.1 ^a	35 ± 3.5		
	Xe	+1.0 ± 0.1	84 ± 7		
		-1.5 ± 0.1	-35 ± 3.5		
			52.5 ± 3.5		

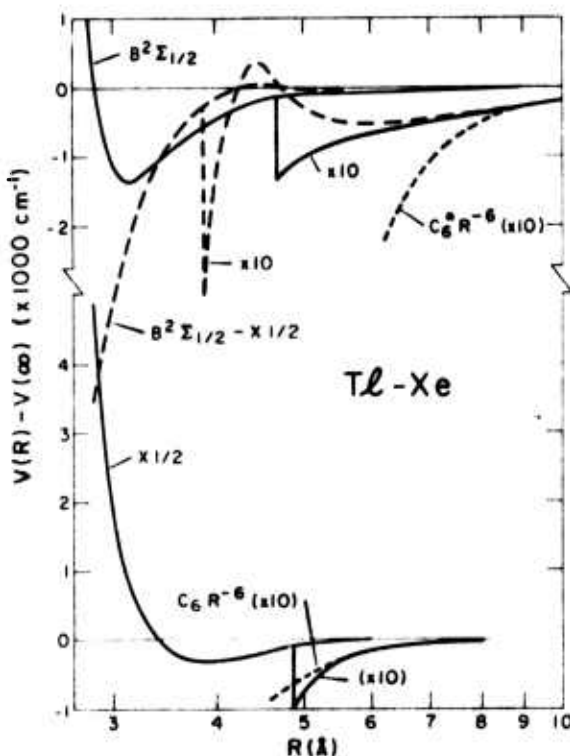
^aBroad satellites.^bReference 5.^cReference 6.

FIG. 8. Tl-Xe interatomic potentials associated with the 377.6-nm line. The $B^2\Sigma_{1/2}$ state connects to the Tl($7^2S_{1/2}$) state and the X_1^2 to the Tl($6^2P_{1/2}$) state at large R . (See Ref. 1 for the explanation of the nomenclature for the molecular states.) The region $R < 4 \text{ \AA}$ is from the analysis of Ref. 1, $C_6^* = 2800$ and $C_6 = 160 \text{ a.u.}$

the measured normalized intensities and the assumption of a transition moment independent of R in the quasistatic theory, as explained in Ref. 1 for the far wing data. Thus, for example, the differential volume $\int_R^{R_2} 4\pi R^2 dR$ in which $\Delta V(R)$ exceeds $+15 \text{ cm}^{-1}$ in Fig. 8 ($\sim 4.3\text{--}4.6 \text{ \AA}$) must equal the area $\int_{k_1}^{k_2} I_h(k) dk$ under the measured spectrum of Fig. 2 from $k_1 = +15$ to $k_2 = +40 \text{ cm}^{-1}$, which is due to the blue satellite. (Note that $\int dk$ of the normalized intensity in the cm^4 units of Fig. 2 has units of cm^3 .) As another example, the differential volume from $5.0\text{--}10.0 \text{ \AA}$ in Fig. 8, where $\Delta V(R) < -20 \text{ cm}^{-1}$, agrees with the integrated intensity from -20 to -70 cm^{-1} in Fig. 2. By thus using a large $-\Delta k$ region about the satellite the exact details of the satellite shape are not necessary to obtain the R scale. The severely smeared-out form of the blue satellite may be understood as due to the breakdown of the quasistatic approximation once the R scale is obtained in Fig. 8, because the positive $\Delta V(R)$ region is seen to be very narrow and will be traversed rapidly using a collision orbit or bound molecular vibration.

The shift and width of the line core are determined predominantly by $\Delta V(R)$ in the region of the Weisskopf radius R_w , given by the impact parameter where the phase shift $\int dt \Delta V[R(t)]/\hbar = 1$. For a $\Delta V = C_6^* R^{-6}$, $R_w = (3\pi C_6^*/8\hbar \langle v \rangle)^{1/3} \approx 19 \text{ \AA}$ in the present case. The effective $C_6^* = C_6^* - C_6$ obtained from equating the measured broadening rate to

that⁹ for $\Delta V = C_6^e R^{-6}$ is much larger than C_6 ; so it can be used to establish a C_6^* . This $C_6^* R^{-6}$ long-range form for $V^*(R)$ is shown in Fig. 8, where it can be seen to blend at large R with the $V^*(R)$ obtained from the above analysis of the wing intensities. The approximately $\Delta k^{-1.3}$ behavior at 4–15 cm⁻¹ on the Tl-Xe red wing (Table II) is consistent with a slightly more gradual change in $V^*(R)$ as compared to C_6^*/R^6 for $R > 10 \text{ \AA}$, as implied by the less attractive $V^*(R)$ shown for $R < 10 \text{ \AA}$. The red-shift to width ratio¹⁰ for a $\Delta V(R) = C_n R^{-n}$ is $|\Delta/\gamma| = 0.36$ for $n = 6$, increasing to 0.85 for $n = 4$. We observe ratios of 0.5–0.7 for the Ar, Kr, and Xe perturber cases, which also implies more gradual decreases in $V^*(R)$ at large R compared to $C_6^* R^{-6}$ interaction.

Once $\Delta V(R)$ is established, it is still desirable to obtain $V^*(R)$ and $V(R)$. As noted above, the analysis of the temperature-dependent extreme wings in Ref. 1 fixed $V^*(R)$ and $V(R)$ for $R = 2.8\text{--}0.4 \text{ \AA}$ in Fig. 8. The C_6 coefficient for the ground state can be estimated fairly reliably, as discussed in the next section, and this yields the $R > 5 \text{ \AA}$ portion of $V(R)$ in Fig. 8. The $V(R)$ shown has simply been connected smoothly between 4.0 and 5 \AA . Adding this $V(R)$ to $\Delta V(R)$ then yields the $V^*(R)$ in Fig. 8. At $R > 8 \text{ \AA}$, $\Delta V \approx V^*$ and the data yield V^* directly. It is satisfying that the $V(R)$ and $V^*(R)$ which result have typical, simple shapes with a single minimum and a single inflection. Only the relatively flat, extended portion of V^* for $R > 5 \text{ \AA}$ is at all unusual.

It is apparent from Fig. 2 that the Tl-Kr, Ar, Ne uv lines can be similarly analyzed. For the Ar and Kr cases the shape of $\Delta V(R)$ will be very similar to Tl-Xe. The $|\Delta k|$ at the minima and maxima of $\Delta V(R)$ will change to accommodate the different satellite positions, with the general trend that $\Delta V(R)$ attains a larger positive value and is positive over a larger- R range for lighter perturbers. The Δk and R range associated with the red satellites decrease with the lighter perturbers, until for He and Ne the long-range $\Delta V(R)$ probably becomes positive. The only feature in Fig. 2 which does not fit this consistent picture is the double hump at the Tl-Ar blue satellite, which might be due to a double inflection in ΔV ($R \sim 5 \text{ \AA}$) or an interference effect as observed in Ref. 7.

As noted above, the green line is due to two $V(R)$ which connect to the Tl $6^2P_{3/2}$ state. In spite of overlapping of the two $\Delta V(R)$ bands the temperature-dependent extreme red wings and blue satellites of this line could be analyzed in Ref. 1 to yield both of these $V(R)$ in the 3–5- \AA regions, starting with a $V^*(R)$ obtained from the uv line analysis. [Each of the two “satellites” on the blue wings in Fig. 3 is attributed to one of the

$V(R)$ in the 4–5- \AA region.] These $V(R)$ connect to the two ($|M| = \frac{3}{2}, \frac{1}{2}$) states arising from ${}^2P_{3/2}$, so the known $|M|$ dependence of the dipole-dipole interaction combined with the near red wing intensity and satellites allows for fairly good estimates for these $V(R)$ at $R > 5 \text{ \AA}$, at least for the Ar, Kr, and Xe cases. However, a detailed example of this does not appear appropriate at this time.

IV. DISCUSSION OF THE LINE CORE

The line-center measurements (Figs. 4 and 5) show a departure from Lorentzian shape very near the line core for Ar, Kr, and Xe perturbers. As this occurs almost within the hfs splitting, the convolution fitting analysis is somewhat uncertain. Despite this fact, the shift and Lorentzian broadening coefficients obtained from the line core fitting in Figs. 4 and 5 are linear with pressure (Figs. 6 and 7), and this uncertainty is considered to be included in the values given in Table I. The red-shift rates are approximately the same for the three heavier gases, smaller for Ne, and for He we notice a small blue shift for both lines. The broadening rates are similar for He, Ar, Kr, and Xe and smaller for Ne. This is typical behavior for many species, and can be given a similar qualitative explanation (e.g., Refs. 2 and 3). Departure from Lorentzian shape does not appear within the range of our high-resolution scans for the green line perturbed by He and Ne (Fig. 5), which is consistent with the Lorentzian power dependence observed to $|\Delta k| \geq 5 \text{ cm}^{-1}$ in the low-resolution scans (Fig. 3 and Table II). But for the uv line perturbed by He and Ne the theoretical convolutions do not fit the data in some portions of the wings (Fig. 4). The power-law dependences on these wings, as observed in the lower-resolution scans, are very nearly Lorentzian to $|\Delta k| \sim 6 \text{ cm}^{-1}$ (Fig. 2 and Table II) as roughly expected due to the higher collision velocities and close-range impacts for He and Ne. Thus the discrepancies in Fig. 4 are attributed to experimental problems. The most likely candidate is drift in the spectrometer slit width with a resultant drift in the shape of the instrument function. As the instrument function is highly asymmetric for the uv line (Fig. 4) this would most severely affect the more rapidly dropping red wings of the He and Ne broadened uv line. As the values of γ for the uv line broadened by He and Ne could be inferred from the low-intensity data out to $\sim 6 \text{ cm}^{-1}$ as well as from the $|\Delta k| < 1.5 \text{ cm}^{-1}$ portions of the high-resolution data this did not hurt the final accuracy.

The impact approximation predicts a Lorentzian line core for any form of ΔV . It is interesting to compare the wing intensity dependences just out-

side this line core with theoretical predictions for $\Delta V = -C_6^* R^{-6}$, to see if this is a reasonable approximation for the appropriate larger R range. Only Ar, Kr, and Xe have sufficient polarizability to make this comparison meaningful; so we will only consider those cases. The theory^{10,11} predicts a $\Delta k^{-1/2}$ quasistatic profile on the red wing [e.g., Eq. (8.6) of Ref. 10], and a $\Delta k^{-3/2} \exp(-K\Delta k^{5/6})$ dependence on the blue wing [e.g., Eq. (8.10) of Ref. 10, where K is a constant related to C_6^* and the average collision velocity]. This blue-wing line shape results from averaging over a kinetic velocity distribution the single-velocity result $\Delta k^{-7/3} \exp(-K'\Delta k^{5/6})$, as was obtained in Refs. 12 and 13. For noble-gas perturbers, the C_6 coefficients are proportional to

$$\alpha \sum_i f_{ij}(E_j - E_i)^{-1},$$

where α is the noble-gas polarizability, and f_{ij} and E_i are the Tl oscillator strengths and energies. Sufficient oscillator strengths are known from the 6^2P_J state to estimate these C_6 coefficients with about 30% accuracy, but the oscillator strengths which determine the dominant C_6^* for the $7^2S_{1/2}$ state are much less certain. However, Ref. 14 provides an approximation for C_6^* based on the binding energy of the $7^2S_{1/2}$ state. If we assume the measured broadening of the Lorentzian core of the line is due to a $\Delta V = -C_6^* R^{-6}$, we can also obtain a "measured" C_6^* and thereby a "measured" C_6^* from Eq. (4.19) of Ref. 10. The resulting "measured" C_6^* for Ar, Kr, and Xe perturbers are given in Table IV, where they are compared to the values calculated according to Ref. 14. The agreement in magnitude is good. However, the C_6^* obtained from the green and uv line broadenings for each gas differ considerably, and these C_6^* are not proportional to noble-gas polarizabilities as they should be. Using these "measured" C_6^* in the static wing (8.6) and antistatic wing (8.10) equations of Ref. 10, the theoretical line wings in Fig. 9 are also obtained. The experimental results can be seen to compare moderately well with these on each wing until the satellite regions are approached. Since we have fixed C_6^* to obtain $\gamma_{\text{theor}} = \gamma_{\text{expt}}$, the data converge to the Lorentzian line-core theory in the $|\Delta k| < 1 \text{ cm}^{-1}$ region not shown in Fig. 9. Most of the discrepancies in the wings can be attributed to departure of $\Delta V(R)$ from the $C_6^* R^{-6}$ form and quasistatic contributions to the blue wings from the positive $\Delta V(R)$ regions at smaller R (e.g., 4.5 Å in Fig. 8). The magnitude of this departure is reasonable since the $C_6 R^{-8}$ energy for Tl $7^2S_{1/2} + \text{Xe}$, using C_8 from Ref. 14, yields about a 10% increase in $|d/dR)\Delta V(R)|$ in the $R \sim 20 \text{ \AA}$ region responsible

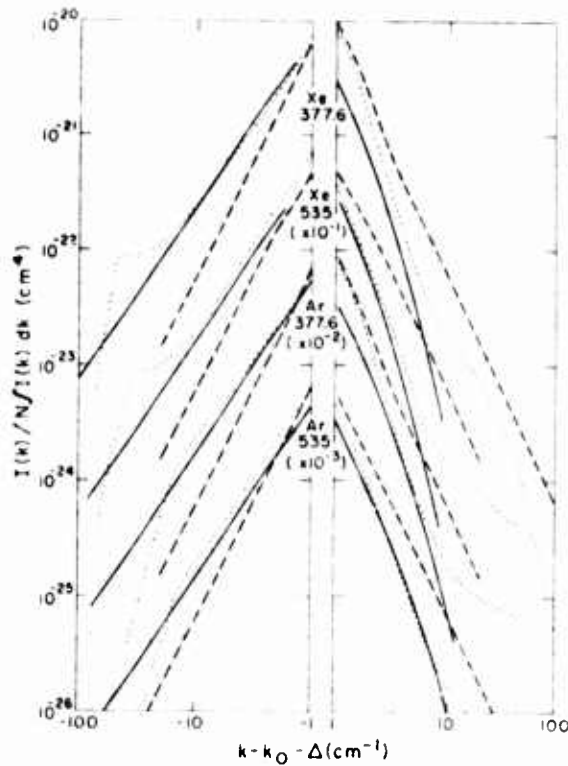


FIG. 9. Comparison of theoretical (solid line) and near-wing intensities, for $\Delta V(R) = -C_6^* R^{-6}$ with C_6^* obtained from Lorentzian linewidths, to experimental intensities (points). The Lorentzian line-core shape, convoluted with hfs and instrument function, has been extended to larger $|\Delta k|$ to show the difference between the theoretical and Lorentzian wings (dashed lines). The effect of the instrument function and hfs can be seen as minor departures of the latter from straight lines in the $|\Delta k| < 2$ regions. The static (red) wing is to the left of the figure.

TABLE IV. Tl-noble-gas C_6 coefficients.^a

Tl state	Ar	Kr	Xe
$6^2P_{1/2}$ ^b	65	100	160
$6^2P_{3/2}$ ^b	105	190	300
$7^2S_{1/2}$ (535) ^c	1050	1150	1500
$7^2S_{1/2}$ (377.6) ^c	1500	1900	2800
$7^2S_{1/2}$ ^d	650	970	1560

^a The C_6 coefficients in $V(R) - V(\infty) = -C_6 R^{-6}$, are in atomic units ($e^2 a_0^5$).

^b C_6 coefficients estimated from known oscillator strengths and sum rules. The $6^2P_{3/2}$ case is $|m|$ averaged.

^c From measured broadening rates.

^d From Ref. 14.

for the line-core data. The experimental spectra indicate a *decrease* of comparable magnitude. It is important to note that both the experimental and theoretical intensities are in the same absolute units; the only adjustable parameter in the comparisons of Fig. 9 is C_6^* , which has been chosen to yield the measured broadening. Since the theoretical broadening¹⁰ is proportional to $(C_6^*)^{0.4}$ and the red-wing intensity to $(C_6^*)^{0.5}$, the ~10% uncertainty in broadening translates into ~10% uncertainty in theoretical red-wing intensity. The discrepancies exceed this in most cases.

V. CONCLUSIONS

We have demonstrated that it is possible to invert quantitative collisional line-shape data which covers the line core to far wings to obtain the ground- and excited-state potentials at all R outside the close-range repulsive core. This is not a unique data-inversion process, particularly as it requires an assumed R dependence to the transition moment, but the results appear to be on

very firm ground. Furthermore, these $V^*(R)$ and $V(R)$ can explain all observed features of the collisional line shape using the traditional impact and quasistatic theories combined with recent satellite-shape theories; i.e., we can explain the broadening and shift of the line core, the near wing intensity dependence, the satellite positions and distinctness, and the extreme wing intensities and temperature dependences.

The comparison of the measured near-wing intensities to the theoretical intensities for $\Delta V = -C_6^* R^{-6}$ shows qualitative but not quantitative agreement (Fig. 9). Also the C_6^* obtained from the broadening rates is not well behaved at the 30% level (Table IV). This disagreement with the theory for $\Delta V \propto R^{-6}$ can be attributed primarily to the fact that the actual long-range $\Delta V(R)$ appears to vary somewhat more slowly than R^{-6} . Often a quasistatic term also contributes to the near blue wings, as in the Tl-Xe uv line case where $\Delta V(R)$ is positive in the 4.5-Å region (Fig. 8). Thus this is not altogether a definitive test of the theory for the near-wing intensities.

*This work was supported in part by the Air Force Weapons Laboratory under Contract No. AFWL-75-199 and by the Advanced Research Projects Agency under Contract No. N00014-76-C-0123.

†CNRS Fellow. Present address: Laboratoire de Spectroscopie Atomique, Université de Caen, 14032 Caen Cedex, France.

‡Present address: Westinghouse Research Laboratories, Pittsburgh, Pa.

§Staff member, Laboratory Astrophysics Division, National Bureau of Standards.

¹B. Cheron, R. Scheps, and A. Gallagher, *J. Chem. Phys.* **65**, 326 (1976).

²Ch. Ottlinger, R. Scheps, G. York, and A. Gallagher, *Phys. Rev. A* **11**, 1815 (1975).

³R. Scheps, Ch. Ottlinger, G. York, and A. Gallagher, *J. Chem. Phys.* **63**, 2581 (1975); A. Gallagher, *Phys. Rev. A* **12**, 133 (1975).

⁴C. J. Schuler, M. Ciftan, L. C. Bradley, III, and H. H. Stroke, *J. Opt. Soc. Am.* **52**, 501 (1962).

⁵S. Y. Chen, M. R. Atwood, and T. H. Warnock, *Physica*

(Utrecht) **27**, 1170 (1961).

⁶H. Krefl and R. Rompe, *Z. Phys.* **73**, 682 (1932).

⁷C. G. Carrington and A. Gallagher, *Phys. Rev. A* **10**, 1464 (1974).

⁸K. M. Sando and J. L. Wormhoudt, *Phys. Rev. A* **7**, 1889 (1973).

⁹After velocity-averaging Eq. (4.19) of Ref. 10, we obtain a width $\gamma(\text{cm}^{-1}) = 4.43 \times 10^{-21} n(\text{cm}^{-3}) [T(\text{K}) / 300\mu(\text{a.m.u.})]^{0.3} C_6(\text{a.u.})^{0.4}$ for $\Delta V(R) = C_6 R^{-6}$, where μ is the reduced mass.

¹⁰J. Szudy and W. E. Baylis, *J. Quant. Spec. Radiat. Trans.* **15**, 641 (1975).

¹¹V. V. Fomin and S. D. Tvorogov, *Appl. Opt.* **12**, 584 (1973).

¹²S. D. Tvorogov and V. V. Fomin, *Opt. Spektrosk.* **30**, 418 (1971) [Opt. Spectrosc. **30**, 228 (1971)].

¹³T. Holstein, *Phys. Rev.* **79**, 744 (1950), and unpublished work described in C. L. Chen and A. V. Phelps, *Phys. Rev. A* **7**, 470 (1973).

¹⁴T. Proctor and W. C. Stwalley, *J. Chem. Phys.* (to be published).

Quenching of optically pumped $O_2(b^1\Sigma_g^+)$ by ground state O_2 molecules*

S. A. Lawton, S. E. Novick, H. P. Broida,[†] and A. V. Phelps[‡]

Joint Institute for Laboratory Astrophysics, University of Colorado and National Bureau of Standards,
Boulder, Colorado 80309

(Received 7 October 1976)

Measurements of quenching of the $b^1\Sigma_g^+$ state of O_2 by ground state oxygen molecules have yielded rate coefficients which differ widely.¹⁻³ Very recent measurements by Martin, Cohen, and Schatz⁴ using pulsed laser excitation and photoluminescence of the atmospheric *A* band of O_2 agree with the lowest of the previously measured rate coefficients. The present experiment confirms their results at near atmospheric O_2 pressures and extends the measurements to much lower O_2 pressures. In addition, we were able to excite the O_2 using absorption at the more readily available wavelengths of the *B* band of O_2 and to observe the photoluminescence at the well-separated *A* band of O_2 . Attempts to produce photoluminescence in O_2 using other absorption bands were unsuccessful.

A flashlamp-pumped tunable pulsed dye laser operating near the head of the O_2 atmospheric *B* band⁵ at 688 nm was used to excite the $v=1$ vibrational level of the $b^1\Sigma$ state. This level relaxes⁶ to the $v=0$ level before radiating to the $X^3\Sigma$ ground state. The time dependence of the density of $b^1\Sigma$ molecules was determined by monitoring photoluminescence near 762 nm from the $(0, 0)$ $b^1\Sigma - X^3\Sigma$ transition of O_2 . The quenching rate constant was determined from the dependence of the $b^1\Sigma$ decay constant on O_2 density.

Considerable care was taken to ensure cell cleanli-

ness and O_2 purity. The cell was constructed from 3.5 cm diameter stainless steel tubing 37 cm long in the laser beam direction with 5 cm long side arms for viewing photoluminescence. Beam stops reduced scattered light at the detector. Baking the cell at 200°C overnight reduced the background pressure below 10^{-6} Pa ($\sim 10^{-8}$ torr). With the cell closed off, the pressure rise was less than 10^{-4} Pa ($\sim 10^{-6}$ torr) in 12 h. Oxygen with a purity of better than 99.99%, held in a liquid nitrogen cooled reservoir for at least one hour, was used. The O_2 pressure was measured with a Bourdon type pressure gauge accurate to ± 400 Pa ($\sim \pm 3$ torr). This gauge was isolated from the cell with a null-reading diaphragm manometer.

The laser line width of 0.3 nm spanned a number of rotational transitions. Laser pulses were 0.3 μ sec long with peak power of 3 kW at 200 msec intervals. Photoluminescence was observed with a cooled GaAs photomultiplier. The 762 nm emission was isolated by an interference filter centered at 762 nm with a 10 nm FWHM and three red-pass glass filters. When the laser was tuned to the *B* band of O_2 , the integrated 762 nm signal was comparable to the signal from scattered laser light and possible glass luminescence. Pulses from the photomultiplier were amplified and counted on a multichannel analyzer. When corrected for back-

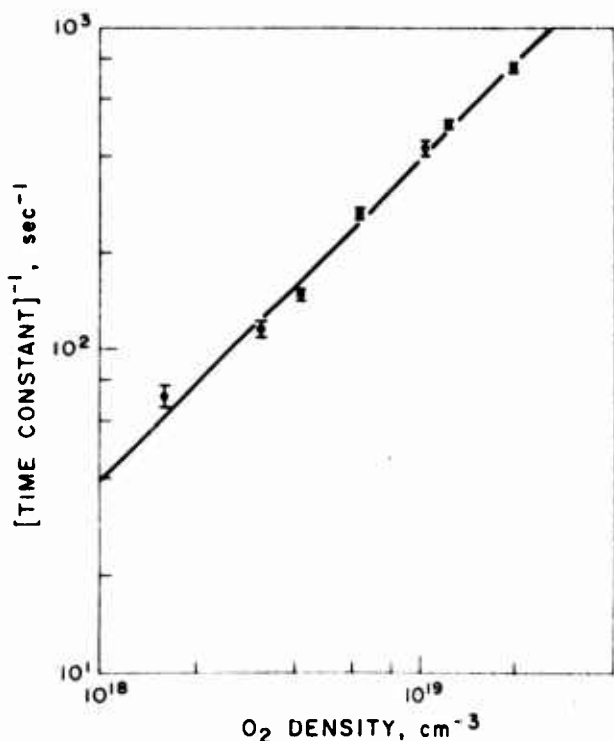


FIG. 1. Measured decay constants for $O_2(1\Sigma^+)$ radiation vs oxygen density. The error bars show the rms deviation computed from the measured decay constants.

ground signal, the observed counting rates were observed to decay exponentially for well over a decade.

Figure 1 shows measured decay constants γ as a function of oxygen density $[O_2]$ at 300 K. The radiative decay constant⁷ of about 0.08 sec^{-1} is completely negligible. The expected diffusion loss³ is less than 15% of the smallest observed decay constant. A least squares fit of the relation $\gamma = k[O_2]$ gives a measured rate coefficient k for the collisional destruction of the $b^1\Sigma$ molecules of $(3.8 \pm 0.3) \times 10^{-17} \text{ cm}^3 \text{ mol}^{-1} \text{ sec}^{-1}$. This result is in good agreement with the other recent data.³⁻⁴

We were unsuccessful with two additional O_2 photo-

luminescence experiments. First, an attempt was made to excite the $A^3\Sigma_u^+$ state of O_2 , but no emission was observed either directly from the A state or from subsequent collisional deactivation to the $b^1\Sigma_g^+$ state. The laser used was a frequency doubled nitrogen-laser-pumped tunable dye laser yielding approximately $10 \mu\text{J}$ pulses with a line width about 0.02 nm at various wavelengths near 250 nm , i.e., the $(8, 0)$ transition of the Herzberg I system⁸ of O_2 . Similarly, attempts to observe photoluminescence at 762 nm resulting from absorption⁹ in the 480 nm dimer band of $(O_2)_2$ by chopping the 476.5 nm output of a 0.6 W argon ion laser were unsuccessful at O_2 densities of $2 \times 10^{19} \text{ cm}^{-3}$.

The authors wish to acknowledge the help and loan of equipment by R. E. Druilinger, M. P. Stock, E. R. Mossburg, Jr., K. Kelly, W. C. Lineberger, and M. M. Hessel.

*This work was supported in part by the Advanced Research Projects Agency of the Department of Defense and was monitored by ONR under contract number N00014-76-C-0123 and in part by the Army Research Office-Durham under contract number DAAG29-76-G-0236.

†Visiting Scientist, National Bureau of Standards on leave from University of California at Santa Barbara.

‡Staff Member, National Bureau of Standards and Professor Adjoint, Department of Physics and Astrophysics, University of Colorado.

¹For a review of measurements prior to 1974 see: M. J. E. Gauthier and D. R. Snelling, *Photochem.* **4**, 27 (1975).

²R. G. D. Thomas and B. A. Thrush, *J. Chem. Soc., Faraday Trans. II* **71**, 664 (1975).

³S. A. Lawton and A. V. Phelps, *Bull. Am. Phys. Soc.* **21**, 160 (1976).

⁴L. R. Martin, R. B. Cohen and J. F. Schatz, *Chem. Phys. Lett.* **41**, 394 (1976).

⁵L. P. Giver, R. W. Boese, and J. H. Miller, *J. Quant. Spectrosc. Radiat. Transfer* **14**, 793 (1974).

⁶J. F. Noxon, *J. Chem. Phys.* **52**, 1852 (1970).

⁷V. D. Galkin, L. N. Zhukova, and L. A. Mitrofanova, *Opt. Spektrosk.* **33**, 837 (1972) [*Opt. Spectrosc.* **33**, 462 (1972)].

⁸G. Herzberg, *Can. J. Phys.* **30**, 185 (1952); V. Hasson, R. W. Nicholls, and V. Degen, *J. Phys. B* **3**, 1192 (1970).

⁹R. P. Blickenstorfer and G. E. Ewing, *J. Chem. Phys.* **51**, 5284 (1969).

Pressure dependence of Na resonance line broadening by Kr and Xe

W. P. West* and Alan Gallagher[†]

Joint Institute for Laboratory Astrophysics, University of Colorado and National Bureau of Standards, Boulder, Colorado 80309

(Received 3 October 1977)

The fluorescent spectrum of the Na D lines, pressure broadened by Xe and Kr, has been measured for noble-gas densities of 2×10^{19} – 3×10^{20} cm $^{-3}$; at the lower density, the lines are isolated while, at the higher, they are severely blended. The spectra are obtained in normalized intensity units allowing the nonbinary behavior of the line wing intensity to be clearly observed. At the lower density the broadening is well characterized by isolated binary interactions; at the higher density multiple-perturber interactions dominate. Nonlinearities in the pressure dependence of shifts, widths, and satellite shape are reported.

I. INTRODUCTION

The theory of collisionally broadened atomic line shapes in low-pressure gases is relatively well developed. The line shape depends on atomic interaction energies that are frequently poorly known, but methods for calculation of a line shape in terms of these interactions are well established.^{1–4} Primarily, the impact approximation is used to calculate the width and shift of the Lorentzian line core and the quasistatic approximation is used for the far wings with certain improvements^{2–6} in the neighborhood of "satellites," or intensity maxima in the line wings. The transition between "line core" and "far wing" occurs at $(\omega - \omega_0)\tau_c \approx 1$, where τ_c is the characteristic collision time, ω photon frequency, and ω_0 the unperturbed atomic frequency.

The problem of describing line shapes at high pressures, with overlapping collisions and multi-body interactions, is quite formidable. The impact approximation is not applicable in the line core and even the simple quasistatic theory requires a number of additional assumptions of questionable validity in order to be applicable in the far wings.

The quantum-mechanical improvements to the quasistatic theory in the neighborhood of satellites^{2,5,6} (see Ref. 7 for a recent review) are limited to nonoverlapping interactions (low pressures). One method that is applicable in all parts of the line at all densities is the Anderson-Talman-type semiclassical theory,⁸ which utilizes the Fourier transform of the autocorrelation function. Calculations^{3,9–11} based on this theory have utilized the approximations (i) that multiple-perturber interactions are uncorrelated and can be represented by scalarly additive identical radiator-perturber-pair interactions; (ii) that no nonadiabatic mixing of (effectively) molecular adiabatic states occurs; (iii) that the quantum-mechanical effects associated with turning points and quasibound or bound states

be neglected; and (iv) straight-line collision orbits. Other, related theories^{12,13} do not remove any of these assumptions, while treatments of nonadditive interactions are so far too formal to yield quantitative results.^{14,15} The additivity assumption for different perturbers has been tested in one case.¹⁶ In practice, only Refs. 3, 9–11, based on the Anderson-Talman-type theory, have calculated a high-pressure spectrum from interaction potentials, and they have utilized further approximations due to the severe computational difficulties. All these calculations have assumed a single-excited and ground-state binary-interaction potential, which is rarely valid (a $^2S_{1/2}$ – $^2P_{1/2}$ transition, where the $^2P_{1/2}$ – $^2P_{3/2}$ fine-structure is large, is an exception). Further, Ref. 10 utilized an unrealistic square-well potential and Ref. 9 investigated only a single interaction potential. Kielkopf³ carefully investigated the computational difficulties as well as a number of interatomic potentials, although he concentrated primarily on certain satellite shapes. This recent work represents most of our present understanding of high-pressure line shape, yet only a few qualitative conclusions of Ref. 3 are applicable to any specific transitions other than those studied therein. Furthermore, the above assumptions used so far in evaluating the Anderson-Talman theory are of questionable validity; in particular the single-potential approximation is completely inappropriate in the present case.

The inaccuracies resulting from the assumptions utilized in the theories are largely untested since, as noted in Ref. 3, available data are not sufficiently restrictive. In fact, the theories have sufficient free potential parameters to readily fit a single measured line shape,⁹ satellite shape,^{3,10} or the pressure-dependence of the line-core shift and width. Clearly, comprehensive data for systems with known interaction potentials are needed.

It is the purpose of this work to provide accurate quantitative data for the pressure dependence of

the line shape in the region of the *D* lines and a nearby red satellite. Furthermore, we have chosen a case for which the binary-pair interactions are relatively well known from theory¹⁷⁻¹⁹ and experiment.^{20,21}

At the lowest pressures studied, the line shape is predominantly due to binary interactions, and at the highest pressures the *D* lines have essentially disappeared. The line shape is analyzed to obtain the pressure dependence of the *D*-line shifts and widths, but there are no calculations available to which these results can be compared. The dependence of the satellite shape on pressure is reported, but again no calculation is presently available for comparison. We have studied the region just beyond the satellite to search for a "secondary" satellite due to NaXe₂, and made quantitative comparisons to theoretical predictions based on the additive-potential model.

For the perturber densities [Xe] of these experiments, the extreme wing intensities, at frequency shifts in excess of 100 cm⁻¹, are predominantly due to only one- and two-perturber interactions or to NaXe and NaXe₂ spectra. There are no satellites on the extreme red wing and the relatively simple, quasistatic, additive-pair interaction theory for the NaXe₂ spectra can be tested there. We have made detailed comparisons of the extreme-wing data to the predictions of this theory in a separate publication.²²

II. EXPERIMENT AND RESULTS

The fluorescence spectrum of optically excited Na(3P) in the presence of Xe and Kr was measured. The cell temperature was 450 K and the sodium density [Na] was below its equilibrium value. Details of the apparatus are given in Ref. 22. The Na vapor was optically thin ([Na] < 10¹¹ cm⁻³) and the total emission spectrum without radiation entrapment was measured. In order to obtain fluorescence signals without interference from instrumental and Rayleigh scattering, the cw dye laser (~1 W/cm² in 0.01 nm) used to excite the Na(3P) was tuned to various wavelengths 0.1–0.5 nm in the wings of the broadened resonance lines. Scattering at the laser wavelength are ignored and all portions of the emission spectrum are obtained by measuring the spectrum for different laser wavelengths. Three-photon scattering²³ was not observed, as expected for our weak laser power density. At the noble-gas densities of the experiment essentially complete spectral redistribution and ²P_{1/2} → ²P_{3/2} mixing occurs, and the fluorescence spectrum is independent of the exciting wavelength.

The results are reported as $I_N(k)$, the normal-

ized emission intensities per cm⁻¹ interval divided by noble-gas density [Xe] or [Kr],

$$I_N(k) = \frac{I(k)}{[Xe] \int I(k) (k_0/k)^4 dk} \quad (1)$$

where $I(k)$ is the measured fluorescence intensity per cm⁻¹ interval, in arbitrary units. At low [Xe] most of the integral results from the *D* lines while the line-wing intensity is predominantly due to binary Na-Xe interactions and is a constant in such a plot. In the wing of a Lorentzian line with broadened width $\gamma \propto [Xe]$, $I_N(k)$ is constant at all [Xe]. Departures from this behavior are observed in the line wings reported below. The $(k_0/k)^4$ factor in the normalization integral is a relatively minor factor that gives a physical meaning to the integral. As shown in Ref. 22, this integral equals $hck_0 \Gamma_0 [\text{Na}_7^*]$, where k_0 is the *D*-line centroid frequency, Γ_0 the spontaneous emission rate, and $[\text{Na}_7^*]$ the total concentration of excited Na(3P) in all bound and free forms.

In Fig. 1 the line-center data are given for a number of Xe densities. The rms fluctuation in individual points is ~2%, while the absolute normalization is accurate to ~5%. A number of redundant data sets were taken in the 587–593 nm region to search for any regular intensity undulations. Such undulations are known to occur in the neighborhood of some satellite structures for low²⁴ or high²⁵ perturber pressures. One calculation has indicated that such undulations might occur at high perturber pressures even though they do not occur at low pressures.¹⁰ A "satellite" structure appears in Fig. 1 as a ~591 nm red edge to the relatively constant intensity 590–591 nm region, however, no intensity undulations were discerned anywhere in the 587–593 nm wavelength for any [Xe]. The upper limit on the fractional change in any undulations is set by the experiment at ~1%. Another, much weaker satellite occurs on the blue wing at ~559 nm (Fig. 2). The lower intensity of this satellite precluded an equivalent search for undulatory structure in its wavelength region. In Fig. 2 the entire measured spectrum is plotted on a log-log scale to give an overview of the entire line wings. The $\Delta k = -100$ to -2500 cm⁻¹ region is the Na^{*}Xe *A-X* band²¹; its red edge at $\Delta k \approx -2200$ cm⁻¹ is not a satellite, rather it is due to the effect of the repulsive inner wall of the *A*-state potential on the perturber distribution.²¹ The pressure dependence of the $\Delta k = -300$ to -4500 cm⁻¹ region is the subject of Ref. 22 and is not discussed here.

The red-wing region is shown in Fig. 3 for several krypton densities. As with xenon, the pressure dependence of the $\Delta k < -100$ cm⁻¹ region is

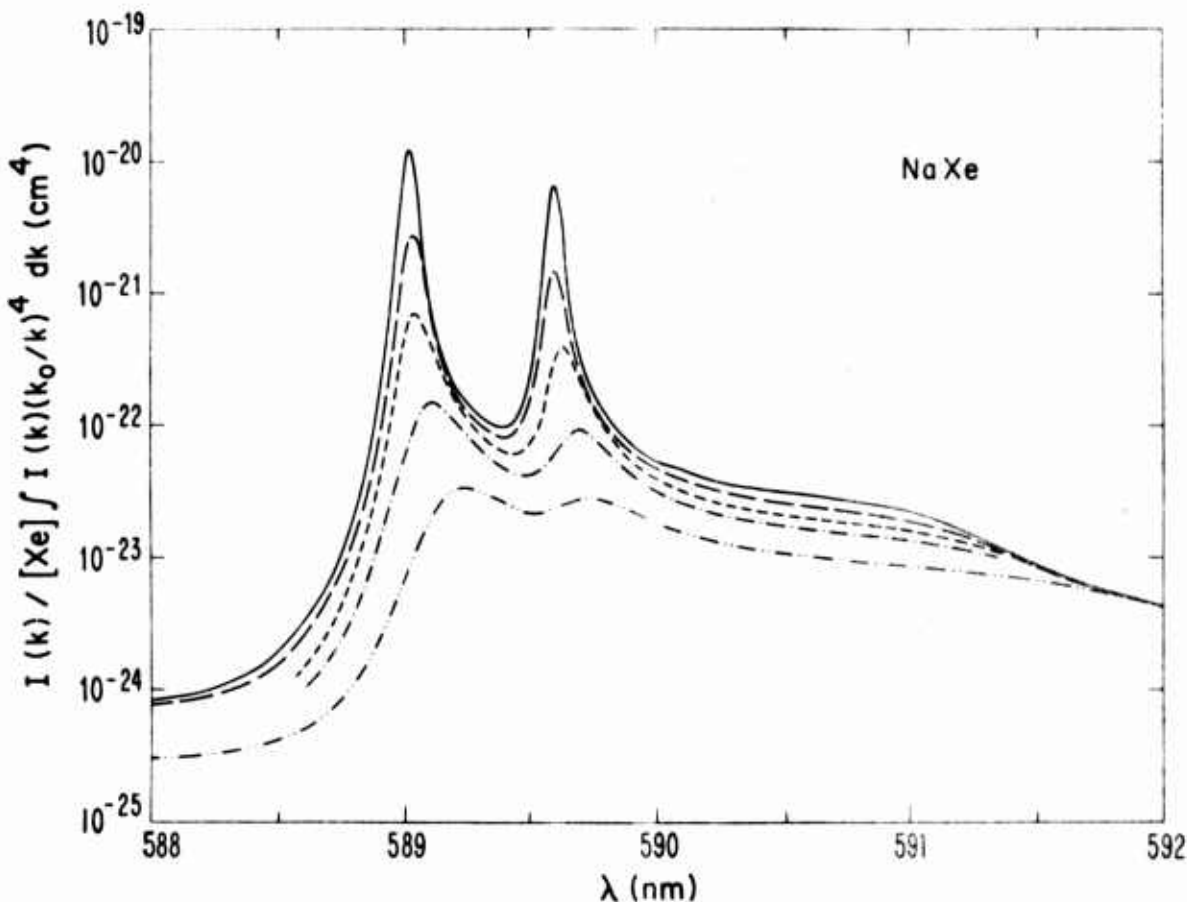


FIG. 1. Normalized fluorescence of optically thin Na at 450 K in the presence of Xe densities of $2.18 \times 10^{19} \text{ cm}^{-3}$ (solid line), $5.45 \times 10^{19} \text{ cm}^{-3}$ (long dashes), $1.06 \times 10^{20} \text{ cm}^{-3}$ (short dashes), $1.83 \times 10^{20} \text{ cm}^{-3}$ (dash-dot), and $3.20 \times 10^{20} \text{ cm}^{-3}$ (dash-double-dot). The spectrometer resolution was 0.05 nm. The lines are drawn through the average of individual data points (not indicated) at 0.02 nm intervals; individual points scatter $\sim 2\%$ rms about the averages.

covered in Ref. 22. A severely blended "satellite" occurs at $\Delta k \approx -30 \text{ cm}^{-1}$. Note that the normalized intensity between λ_0 and the satellite decreases with increasing $[Xe]$, as it did for Xe in Figs. 1 and 2. However, at $-30 \text{ cm}^{-1} < -80 \text{ cm}^{-1}$, past the satellite, the intensity increases with increasing $[Xe]$, whereas for Xe (Fig. 2) the normalized emission coefficient was essentially independent of $[Xe]$ in that region of the spectra. Again, no undulations in the spectra were apparent in the region of the satellite.

The normalized emission coefficient $I_N(k)$ at the lowest density of $2.18 \times 10^{19} \text{ cm}^{-3}$ is given in Fig. 4, where it is compared to previous absorption measurements by McCarten and Farr.²³ At the $10^{18}-10^{19} \text{ cm}^{-3}$ perturber densities of Ref. 24, the broadening of the two $\text{Na}(^2P_{1/2,3/2})$ lines is small enough that the lines can be considered independently. Their measured $P_{1/2}$ -line absorption wing shape has been converted to a spontaneous emission wing shape by multiplying by

$(k/k_0)^3 \exp[-hc(k-k_0)/k_B T]$, where k_B is the Boltzmann constant (e.g., see Ref. 21). It has been put in absolute units by connecting it at $|\Delta k| \leq 1 \text{ cm}^{-1}$, where it has a Lorentzian shape, to the $P_{1/2}$ -line Lorentzian line wing. The Lorentzian wing intensity for an isolated line of full width γ is given in $I_N(k)$ units, in terms of $\gamma/[Xe]$, by

$$\frac{I(k)}{[Xe] \int I(k) (k_0/k)^4 dk} = \frac{(k/k_0)^4 (2\pi)^{-1} (\gamma/[Xe])}{(k - k_0 - d)^2 + (\gamma/2[Xe])^2 [Xe]^2}. \quad (2)$$

The $P_{3/2}$ and $P_{1/2}$ states will be populated in the thermal ratio $2 \exp(-17 \text{ cm}^{-1}/k_B T) = 1.89$ due to Xe collisional mixing, and they radiate at the same rate. Thus, as we have normalized our data to the emission integrated across both $P_{1/2}$ and $P_{3/2}$ lines, and at this $[Xe] \approx 2 \times 10^{19} \text{ cm}^{-3}$ almost all of the emission is in the lines (Fig. 1, the $I_N(k)$ of Eq. (2), for the $P_{1/2}$ line only, must be multiplied

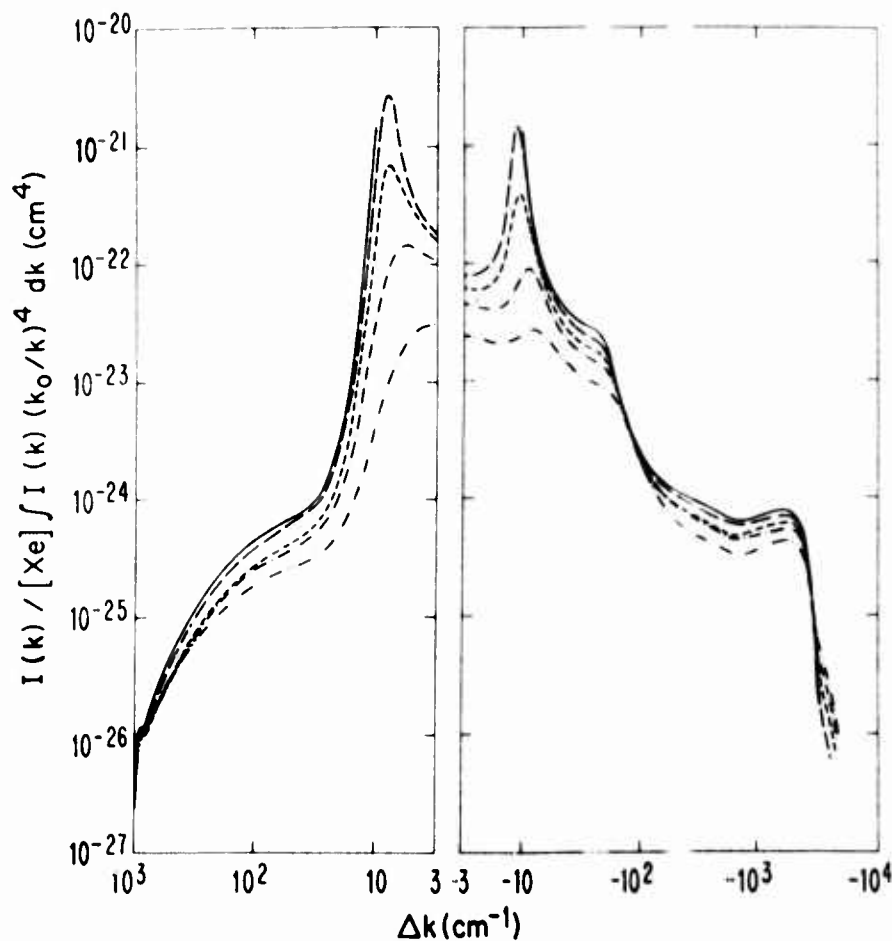


FIG. 2. Same as Fig. 1, except that the spectrometer resolution decreases to ~ 1 nm for $|\Delta k| > 300$ cm^{-1} and data points are at wider intervals at the larger $|\Delta k|$.

by 1/2.89 for the comparison to our data. As shown in Fig. 4, the resulting $I_N(k)$ calculated using the (full width) $\gamma/[Xe]$ of the $P_{1/2}$ line measured by McCarten and Farr has about the same shape as the present measurement but is lower by a factor of ~ 1.6 . A 36% larger value of $\gamma[Xe]$, and thus of $I_N(k)$, has recently been calculated by Lwin *et al.*¹⁹ As shown in Fig. 4, if the wing shape reported in Ref. 24 is normalized to the Lorentzian wing according to the procedure described above using their calculated $\gamma/[Xe]$, the agreement with the present results is much better ($\sim 20\%$). Lwin, McCarten, and Lewis¹⁹ have suggested that the $\gamma/[Xe]$ measured by McCarten and Farr²⁶ may be in error in the case of xenon and the present data support that suggestion. We are not aware of any other measurements of Xe broadening of these Na lines.

The full widths at half maximum (FWHM) of the Xe broadened $P_{1/2}$ (589.6 nm) and $P_{3/2}$ (589.0 nm) lines were measured with an instrument resolution $\Delta = 0.03$ nm at the lower [Xe] and 0.05 nm for the higher [Xe]. The observed widths (W) of ≥ 0.6 nm were corrected by (5–30)% for the instrumental

contribution using the approximation $\gamma = (W^2 - \Delta^2)^{0.5}$. The shifts (d) of the peak positions of these two lines were measured relative to a low-pressure sodium discharge lamp. Since the measurement of the shifts involves only the determination of the peak positions, the uncertainties are deemed to be significantly less than the instrumental resolution and are ± 0.003 nm at the lower [Xe] and ± 0.01 nm at the higher [Xe]. At low [Xe], γ and d are proportional to [Xe], so we have plotted $\gamma/[Xe]$ and $d/[Xe]$ vs [Xe] in Fig. 5 to indicate departures from low-pressure behavior. The low-pressure limiting values of $d/[Xe]$ shown in Fig. 5 have been measured by McCarten and Farr,²⁶ while both the calculated¹⁹ and measured²⁶ limiting values of $\gamma/[Xe]$ are shown. The uncertainty in the widths obtained in the present low-resolution measurements includes uncertainty in the above correction for instrumental broadening.

III. DISCUSSION

The general pattern of the data in Figs. 1 and 2 is a broadening and red shift of the D lines with

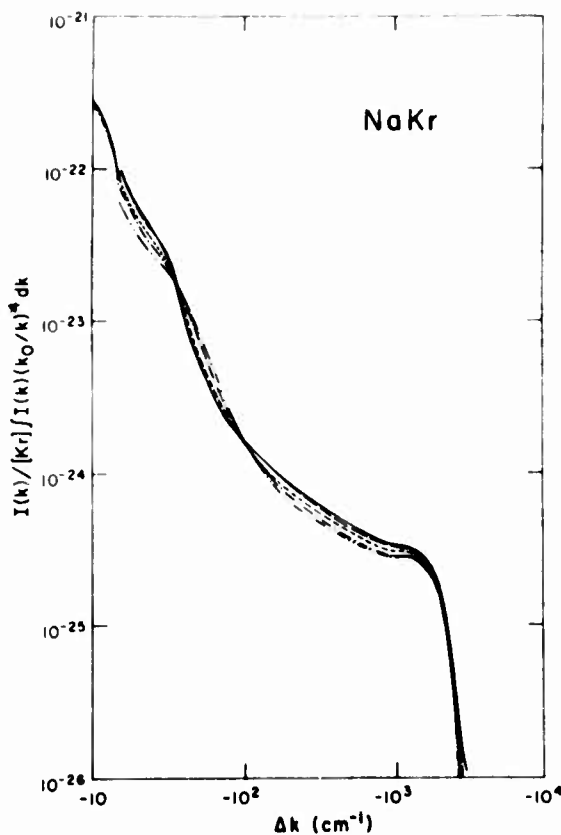


FIG. 3. Normalized fluorescence of optically thin Na at 450 K in the presence of Kr densities of $2.02 \times 10^{19} \text{ cm}^{-3}$ (solid line), $5.21 \times 10^{19} \text{ cm}^{-3}$ (long dashes), $1.04 \times 10^{20} \text{ cm}^{-3}$ (short dashes), $2.10 \times 10^{20} \text{ cm}^{-3}$ (dash-dot), and $3.16 \times 10^{20} \text{ cm}^{-3}$ (dash-double-dot).

increasing [Xe]. The intensity in the line centers decreases relative to that in the wings until they merge and the lines disappear. It is useful to recognize that a single isolated Lorentzian line would have a normalized intensity $I_N(k)$ given by Eq. (2). Thus, if $\gamma/[Xe]$ were a constant, the width of the line would be proportional to [Xe], the normalized line peak would decrease as $[Xe]^{-2}$, and the wings would appear constant (the area decreases as $[Xe]^{-1}$ by definition). Such a constant wing intensity and $\gamma/[Xe]$ is consistent with a binary (Na-Xe) interaction only. At low [Xe] the normalized wing intensities are indeed independent of [Xe], but at the high [Xe] of these experiments the normalized line-wing intensities generally decrease with increasing [Xe]. This is caused by the depletion of free Na^* atoms due to molecular formation and the fact that multibody interactions (Na^*Xe_n , $n = 2, 3, \dots$) spread the intensity into other portions of the spectrum. In essence, according to the Poisson distribution, the probability of one and only one Xe in a particular volume ΔV about a Na^* is given by $\Delta V[Xe] \exp(-\Delta V[Xe])$. Here the

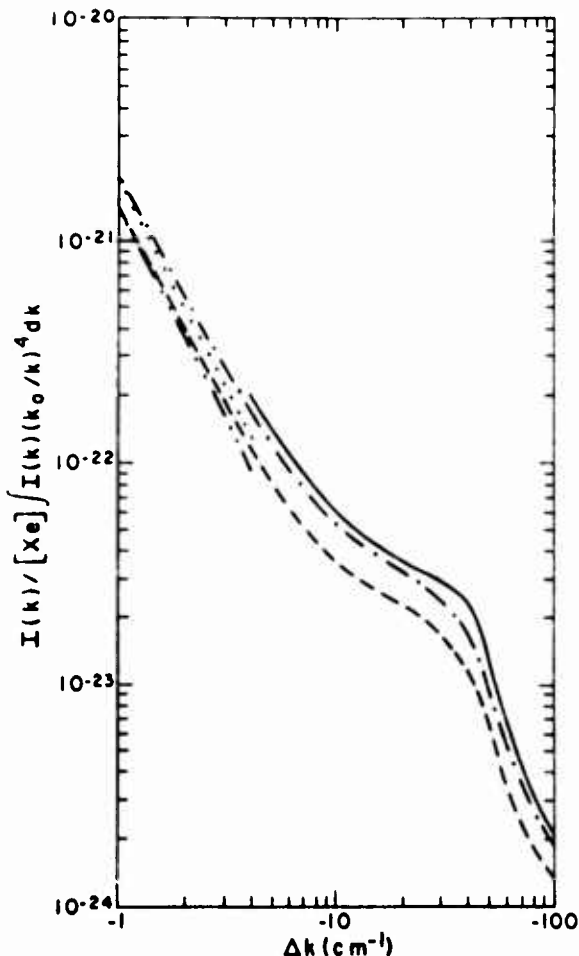


FIG. 4. Normalized fluorescence of Na at 450–460 K in the presence of Xe. Present data at $[Xe] = 2.2 \times 10^{19} \text{ cm}^{-3}$ (solid line). Data of McCarten and Farr²⁶ normalized to their measured broadening coefficient $\gamma/[Xe] = 2.79 \times 10^{-20} \text{ cm}^2$ (short dashes) and the calculated¹⁹ broadening coefficient $\gamma/[Xe] = 3.78 \times 10^{-20} \text{ cm}^2$ (dash-dot). Also shown are the pure Lorentzian shapes (dash-double-dot) and (dotted), for these two values of $\gamma/[Xe]$. Δk is measured from the center of the (unperturbed) D1 line.

probability of remaining a free Na^* with no Xe inside ΔV is $\exp(-\Delta V[Xe])$, and the remaining probability is accounted for by multiple-Xe interactions. A more complete discussion of these multibody contributions to the wing spectrum is contained in Ref. 22.

A. Shift and width

The shifts and FWHM of the D lines were plotted as $d/[Xe]$ and $\gamma/[Xe]$ vs [Xe] in Fig. 5. The low-pressure limit of the broadening rate $\gamma/[Xe]$ is uncertain by about $\pm 30\%$ due to the disagreement between the present data and Ref. 26, but within this uncertainty $\gamma/[Xe]$ does not appear to vary

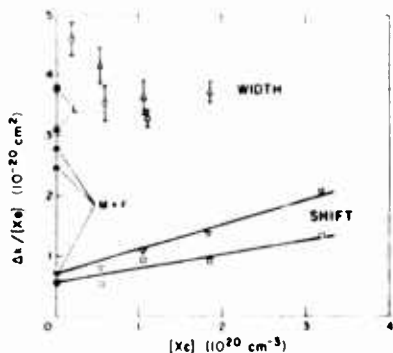


FIG. 5. Broadening rate $\gamma/[Xe]$, where γ is the full width in cm^{-1} for the 590 nm line (Δ) and 596 nm line (\circ), Shift rate $d/[Xe]$ for the 590 nm line (∇) and 596 nm line (\square). The width for $[Xe] = 2.2 \times 10^{19} \text{ cm}^{-3}$ is from the wing-intensity analysis in Fig. 4. The values on the $[Xe] = 0$ axis are by McCarten and Farr²⁴ (\blacktriangle , \bullet , \blacktriangledown , and \blacksquare for width and shift at 596 nm, and by Lwin *et al.* (\blacktriangle and \bullet for width of 590 and 596 nm). The straight lines fitted to the shift data are for comparison purposes only.

with $[Xe]$. It appears that our data for the shift rate can be fitted, within experimental accuracy, with straight lines whose intercepts are the low-pressure limits measured by McCarten and Farr.

The approximately constant $\gamma/[Xe]$ and linearly varying $d/[Xe]$ might be taken as indicative of predominantly one- and two-Xe interactions, but this may be deceptive. In the impact approximation, collisions with impact parameters greater than the Weisskopf radius R_w are ineffective at broadening, while all closer collisions contribute almost equally; the shift is predominantly due to collisions with impact parameters near R_w .¹ Here $R_w = (\gamma/[Xe]\pi v_0)^{1/2}$, with v_0 the mean interatomic-collision velocity, is the impact parameter that yields unity phase shift and "interruption" of the optical phase. To obtain a constant $\gamma/[Xe]$ and $d/[Xe]$, Na*-Xe collisions should be independent and not overlap in time. The average number N of perturbers inside R_w at one time is given approximately by $\frac{4}{3}\pi R_w^3 [Xe]$, neglecting effects due to Boltzmann factors associated with the interatomic potentials, and $N \ll 1$ is required for non-overlapping collisions. In the present case $R_w \approx 13 \text{ \AA}$ and $N \approx 2.5$ at our highest $[Xe] = 3.2 \times 10^{20} \text{ cm}^{-3}$. The Poisson distribution gives the probability $(N^n/n!) \exp(-N)$ of n -independent perturbers inside R_w , so interactions with more than one or even two Xe at a time inside R_w is highly likely. However, the large frequency shifts associated with these severely broadened lines would appear to be outside the range of validity of the impact approximation, and these large shifts may be primarily due to perturbers at $R < R_w$. Thus the reasons for the observed pressure dependences of $\gamma/[Xe]$ and $d/[Xe]$ are not clear. These highly

qualitative comments, as necessary in the absence of any directly applicable quantitative theory of nonbinary pressure broadening, are intended only to suggest the types of issues involved in interpreting data.

The parameters γ and d completely characterize a Lorentzian broadened line; however, at these high perturber densities the lines are no longer Lorentzian. At the highest density studied, $3.2 \times 10^{20} \text{ cm}^{-3}$, the D lines are broadened to such an extent that their widths are not obtainable. Therefore comparison to theory, when available, should be made using the complete line profile.

B. Secondary satellite

It has been noted that if one assumes additive-pair interactions a satellite feature at Δk_s in the binary (NaXe) spectrum will also appear in the quasistatic spectrum as a weaker satellite at $2\Delta k_s$, due to the triatomic (NaXe₂) spectrum.²⁷ These satellite features will be broadened compared to those given in Fig. 1 of Ref. 27 due to the atomic motion, but the area under each broadened satellite feature must remain nearly the same as that which the quasistatic theory predicts will occur across the same spectral region (e.g. in the present case the region of 590.3–591.7 nm in Fig. 1). The present data at $[Xe] = 3.2 \times 10^{20} \text{ cm}^{-3}$ correspond to $V_s[Xe] = 0.83$, where $V_s = (4\pi/3)R_s^3$ is the volume inside the satellite radius $R_s = 8.5 \text{ \AA}$, obtained from Ref. 18. The results of Ref. 27 are expressed in terms of $\delta = \frac{1}{32}V_s N$, where N is the perturber density, so to the extent that the 6-12 potential of Ref. 27 is applicable our data correspond to $\delta = 0.026$. From Fig. 1 of Ref. 27 it can be seen that a highly discernible secondary satellite is predicted for δ values in this range. No such feature is apparent in our measured spectrum.

In order to test more quantitatively for a satellite at $2\Delta k_s$, we have carried out an approximate calculation of the spectrum to be expected under the additive-potential assumption. We have utilized Eq. (9) of Ref. 22 to calculate the contribution of the NaXe₂ spectrum to $I_N(k)$ using knowledge of the NaXe spectrum obtained at low $[Xe]$. In essence, the low-pressure limit of $I_N(k)$, which represents the NaXe spectrum, is convoluted with itself. This approximation introduces the motional broadening into the NaXe₂ spectra as convolutions or superpositions of the observed broadening due to single-perturber motion. Royer has derived a similar expression, except utilizing the convolution of quasistatic wings with essentially the broadened line core.²⁸ The predictions of this approximation are compared to the data in Fig. 6. We have included $I_N(k)$ contributions from NaXe and NaXe₂ only, so that the calculated $I_N(\Delta k)$ is

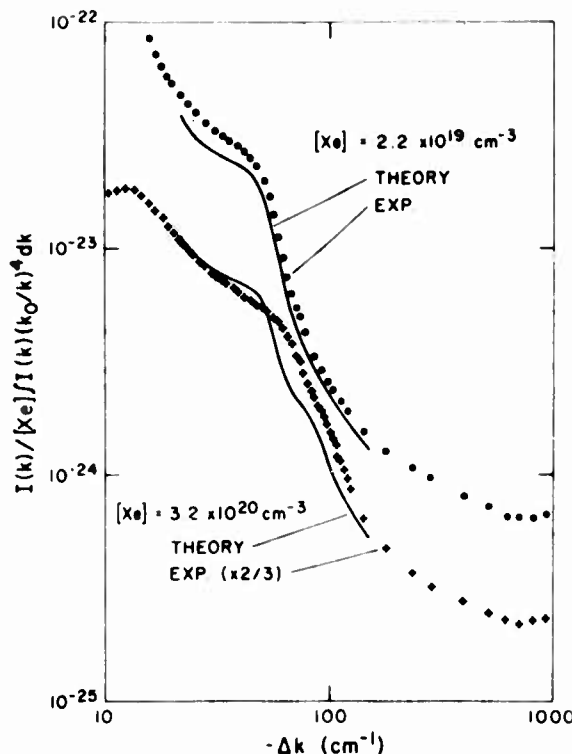


FIG. 6. Normalized Na emission in the presence of $[Xe] = 2.2 \times 10^{19} \text{ cm}^{-3}$ and $3.2 \times 10^{20} \text{ cm}^{-3}$, in the wavelength region of the red satellite. The higher-pressure data have been multiplied by 2 to avoid overlapping the low-pressure data and to facilitate comparison with the theoretical shape. Here Δk is measured from midway between the D lines.

somewhat lower than the measured $I_N(\Delta k)$. The omitted terms, representing NaXe_n ($n > 2$) spectra, are expected to be slowly varying with Δk in the satellite region under investigation, so that they should not affect this comparison of spectral shapes. In this calculation there is some ambiguity in the choice of the unperturbed atomic frequency k_0 , and a value midway between the D lines was chosen. Note the predicted NaXe_2 secondary satellite hump at $\sim 80 \text{ cm}^{-1}$ in the $[Xe] = 3.2 \times 10^{20} \text{ cm}^{-3}$ theoretical spectrum; its intensity is $\sim 10\%$ that of the primary satellite at $\sim 40 \text{ cm}^{-1}$. There is no indication of this secondary satellite in the data.

The relationship between the predicted magnitudes of the primary and secondary satellite is very useful in any search for them. This is easy to see from Eq. (9) of Ref. 22, and is consistent with the results of Ref. 27. In essence, when the area under the primary satellite $I_N(\Delta k_s)W$, where W is the observed satellite width, is a fraction ϵ of the normalized emission, Eq. (9) of Ref. 22 predicts that the area under the secondary satellite will be about $\frac{1}{2}\epsilon^2$. (This is roughly equivalent to the probability of finding two Xe inside R_s , as

given by the Poisson distribution.) Thus, for example, at $[Xe] = 2.2 \times 10^{19} \text{ cm}^{-3}$, a factor of 15 smaller $[Xe]$ than in the above comparison, the secondary satellite is 15 times weaker relative to the NaXe satellite and is no longer visible in the theoretical line in Fig. 6. McCarten and Farr²⁶ have reported a broad hump at $\sim 100 \text{ cm}^{-1}$ in the red wing of the absorption profile of Na perturber by Xe. They have attributed this feature to the (NaXe_2) secondary satellite. However, from the present normalized data it follows that at their perturber density ($3.2 \times 10^{18} \text{ cm}^{-3}$) any such secondary satellite would be about 10^3 lower in intensity than that of the primary satellite; thus it is obviously not the feature reported in Ref. 26. The beginning of the NaXe $A-X$ band absorption, the broadband at -100 to -2000 cm^{-1} in Fig. 2, is probably what was observed.

C. Intensity undulations near satellites

Another aspect of this satellite feature has already been noted in the data section; we do not observe intensity undulations at any pressure, in contradiction to the suggested^{9,10} shapes for broadening of Cs resonance lines by high-pressure Xe. This supports the suggestion in Ref. 3 that realistic potentials and considerable computational care are necessary for such calculations.

D. Conclusions

The qualitative behavior of the far-wing intensities as a function of perturber density can be understood in terms of the depletion of free Na^* due to molecular formation and the more spread out character of the NaXe_n spectra as n increases. These effects are predicted by the additive interaction model as given in Eq. (9) of Ref. 22. However, the behavior is not well understood quantitatively. In particular, we do not observe a secondary satellite or intensity undulations in the neighborhood of the red satellite, nor has the pressure dependence of $I_N(k)$ been calculated. The line-core shifts and widths appear to have a very simple $[Xe]$ dependence, for unknown reasons.

ACKNOWLEDGMENTS

We wish to thank Richard Scheps for major contributions during the construction stages of the experiment, and Jinx Cooper for valuable comments. This work was supported by the Air Force Weapons Laboratory under Grant No. AFWL 77-010, and the Advanced Research Projects Agency of the Department of Defense monitored by the Office of Naval Research under Contract No. N00014-76-C-0123.

- *Present address: Physics Dept., Univ. of California, Santa Barbara, Calif. 93106.
- †Staff member, Quantum Physics Division, National Bureau of Standards.
- ¹S. Y. Chen and M. Takeo, Rev. Mod. Phys. 29, 20 (1957).
- ²J. Szudy and W. E. Baylis, J. Quant. Spectrosc. Radiat. Transfer 15, 641 (1975).
- ³J. F. Kielkopf, J. Phys. B 9, 1601 (1976).
- ⁴J. R. Fuhr, W. L. Wiese, and L. J. Roszman, *Bibliography on Atomic Line Shapes and Shifts*, Natl. Bur. Stand. Spec. Publ. No. 366 (U.S. GPO, Washington, D.C., 1972); *ibid.*, Suppl. 1 (1974); *ibid.*, Suppl. 2 (1975).
- ⁵E. A. Andreev, Opt. Spektrosk., 34, 603 (1973) [Opt. Spectrosc. 34, 346 (1973)].
- ⁶L. M. Sando and J. C. Wormhoudt, Phys. Rev. A 7, 1889 (1974); K. Sando, *ibid.* 9, 1103 (1974).
- ⁷J. Cooper, "Comments on the Theory of Satellite Bands," Report No. 111 (1973), Joint Institute for Laboratory Astrophysics, University of Colorado, Boulder, Colorado 80309 (unpublished).
- ⁸P. W. Anderson, Phys. Rev. 86, 809 (1952); 76, 647 (1949); P. W. Anderson and J. D. Talman, Bell Tel. Syst. Tech. Publ. No. 3117 (unpublished).
- ⁹M. Takeo, Phys. Rev. A 1, 143 (1970).
- ¹⁰N. F. Allard and S. Sahal-Brechot, Phys. Lett. 48A, 135 (1974); N. F. Allard, S. Sahal-Brechot, and Y. G. Biraud, J. Phys. B 7, 2158 (1974).
- ¹¹J. Kleffer, J. Chem. Phys. 51, 1852 (1969).
- ¹²A. Royer, Phys. Rev. A 3, 2044 (1971).
- ¹³A. Jablonski, Acta Phys. Pol. 23, 493 (1963).
- ¹⁴E. Czuchajt, Acta Phys. Pol. A 5, 97 (1974), and references therein.
- ¹⁵R. W. Davies, Phys. Rev. A 12, 927 (1975).
- ¹⁶H. Jacobson, Phys. Rev. A 5, 989 (1972).
- ¹⁷W. E. Baylis, J. Chem. Phys. 51, 2665 (1969).
- ¹⁸J. Pascale and J. Vandeplanque, J. Chem. Phys. 60, 2278 (1974).
- ¹⁹N. Lwin, D. G. McCarten, and E. L. Lewis, J. Phys. B 9, L161 (1976).
- ²⁰R. B. Bernstein and J. T. Muckerman, in *Advances in Chemical Physics*, edited by J. O. Hirschfelder (Wiley, New York, 1967), Vol. 12.
- ²¹G. York, R. Scheps, and A. Gallagher, J. Chem. Phys. 63, 1052 (1975).
- ²²W. P. West, P. Shuker, and A. Gallagher, J. Chem. Phys. (to be published).
- ²³J. Carlsten and A. Szoke, Phys. Rev. Lett. 36, 667 (1978).
- ²⁴C. G. Carrington and A. Gallagher, Phys. Rev. A 10, 1464 (1974).
- ²⁵G. Moe, A. C. Tam, and W. Happer, Phys. Rev. A 14, 349 (1976).
- ²⁶D. G. McCarten and J. M. Farr, J. Phys. B 9, 985 (1976).
- ²⁷W. R. Hindmarsh and J. M. Farr, J. Phys. B 2, 1388 (1969).
- ²⁸A. Royer, Phys. Rev. A 3, 2044 (1971).

Collisional excitation transfer between Na and Na₂^{a)}

L. K. Lam,^{b)} T. Fujimoto,^{c)} and A. C. Gallagher^{d)}

Joint Institute for Laboratory Astrophysics, National Bureau of Standards and University of Colorado,
Boulder, Colorado 80309

M. M. Hessel

Laser Molecular-Physics Section, National Bureau of Standards, Washington, D.C. 20234
(Received 1 December 1977)

We have excited Na(3s) → Na(3p) with a pulsed dye laser at Na densities of 10^{14} – 10^{16} cm⁻³ with typically ~2% Na₂. From the decay time constants, intensities and spectra of the Na and Na₂ fluorescences we have identified several collisional and radiative processes in the excited sodium atom-dimer system. Comparing the solutions of coupled equations to the density dependence of the decay constants and fluorescence intensities yields a rate coefficient of $(3.4 \pm 1.6) \times 10^{-9}$ cm³sec⁻¹ for the excitation transfer process: Na*(3p) + Na₂(X¹Σ) → Na(3s) + Na₂(A¹Σ and a³Π). This indicates that some kind of long-range interaction is operative. Other rate coefficients are determined less accurately; e.g., nonradiative Na(3p) quenching rate coefficients of $10 \pm 5 \times 10^{-10}$ cm³sec⁻¹ due to dimer collisions and of $3 \pm 3 \times 10^{-12}$ cm³sec⁻¹ due to atom collisions are obtained.

I. INTRODUCTION

The energetics in the sodium atom-dimer system is interesting in connection with lasers^{1,2} and high-pressure discharge lamps.^{3–5} It is also relevant to the study of reaction kinetics between atoms and molecules⁶ and phenomena of radiation⁷ and excited state⁸ transport. Sodium vapor of density [Na] = 10^{14} – 10^{16} cm⁻³ ($T = 280$ – 430 °C) contains an equilibrium fraction of 1%–4% of Na₂. As Na₂ is bound by ~0.5 eV this fraction may be considerably reduced by superheating. At these Na densities the atomic resonance-line fluorescence is strongly trapped whereas the A-X band of Na₂ escapes the vessel. Thus Na to Na₂ excitation transfer shortens the Na(3P) decay time and converts fluorescence from the atomic lines to the Na₂ bands. Excitation transfer to the A¹Σ and a³Π states of Na₂ is energetically favored, and we observe predominantly the A-X band, presumably with a weak underlying a-X band, following optical excitation of the Na 3P state. At the lower Na density [Na] we observe quenching of the atomic fluorescence decay, at a rate proportional to the dimer density [Na₂], accompanied by a molecular fluorescence intensity also proportional to [Na₂]. We attribute these observations to the excitation transfer: Na*(3P) + Na₂(X¹Σ) → Na(3S) + Na₂(A¹Σ and a³Π), and obtain a large rate coefficient from analysis of these data. At higher [Na] the reverse process as well as other nonradiative quenching processes occur and their rate coefficients are also determined. The transfer of excitation from laser excited Na₂(B¹Π, A¹Σ) to Na(3P) has recently been reported by Kraulinja, Kopeikina, and Janson.⁹

In Sec. II we describe a model for the coupling of the excited atomic and dimer states with various radiative and collisional processes. The experiment is described in Sec. III, the analysis of data is summarized in Sec. IV, and the results are discussed in Sec. V.

II. EXCITED Na-Na₂ KINETICS

A. Na-Na₂ states

The ground and lower excited states of Na and Na₂, from Refs. 10–12, are shown in Fig. 1(a). Higher lying states in the excited molecular state manifold are neglected. Any B-X band fluorescence was much weaker than the A-X band and was not studied in the experiment. The A¹Σ_u state of Na₂ radiates to the X¹Σ_g state with a lifetime of ~12 nsec.¹³ This A-X band radiation extends from 570 to 830 nm and is responsible for the far wing of self-broadened sodium D line. The unperturbed a³Π_u state is forbidden from radiative decay to either the A¹Σ_g or x³Σ_g state due to the ΔS = 0 and $\pi \rightarrow \pi$ selection rules. The dominant depletion mode of the ³Π_u metastable state at low densities is expected to be radiative decay due to spin-orbit coupling to the A¹Σ_u state. If an amplitude b of the A¹Σ_u state is mixed into an a³Π_u vibration-rotation state, it radiates at a rate $\Gamma_A b^2$, where $\Gamma_A \approx 8 \times 10^7$ sec⁻¹ is the A¹Σ_u state radiation rate. The b for each vibration-rotation level of a³Π_u depends on the energy difference and Franck-Condon factors of the same J levels in the two electronic states. Such perturbation has been reported in the A-X band spectrum of Na₂ for v' = 0–8 in A¹Σ, and the perturbed mixing has been analyzed for the v' = 0 vibrational level.¹⁰ For these states $b^2 \sim 0.01$ on the average, and we assume that a similar value holds for higher v' states. Since we do not attempt here to differentiate the behavior of different vibration-rotation sublevels, we use a bulk average decay rate Γ_A expected to be about 0.01 Γ_A , in the data analysis. This a³Π_u state radiation is predominately in the same wavelength region as the A-X band, and is indistinguishable in this experiment.

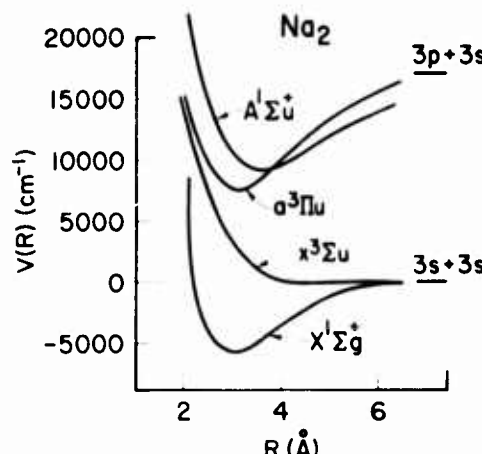
The repulsive x³Σ_g potential in Fig. 1(a), according

^{a)}Preliminary results reported in Bull. Am. Phys. Soc. **22**, 193 (1977).

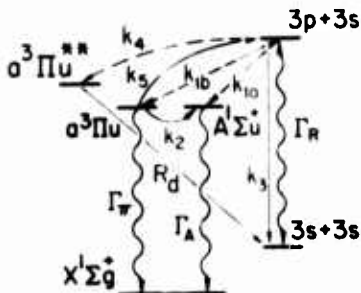
^{b)}Present address: Physics Department, University of Missouri-Rolla, Rolla, MO 65401.

^{c)}Present address: Department of Engineering Science, Kyoto University, Kyoto, Japan.

^{d)}Staff Member, Quantum Physics Division, National Bureau of Standards, Boulder, CO 80302.



(a)



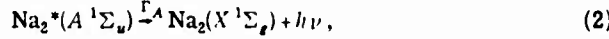
(b)

FIG. 1. (a) Potential curves of the lowest four electronic states of Na₂. The X¹Σ and A¹Σ potentials are experimental (Refs. 9, 10). The X³Σ and a³Π potentials are calculated (Ref. 11). (b) Schematic of collisional and radiative processes considered here. The solid and dashed lines are due to Na and Na₂ collisions, respectively.

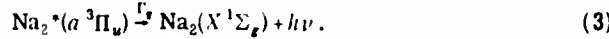
to the model-potential calculation of Bardsley *et al.*,¹² would "intersect" the a³Π_u potential, if at all, above the Na(3P) energy on the repulsive wall. "Crossing" of the curves within the a³Π_u potential well would cause rapid nonradiative quenching of excited atoms and molecules due to dissociation and predissociation. These processes are discussed further in the following section.

B. Radiative and collisional processes

The radiative and collisional processes in the Na-Na₂ system are illustrated in Fig. 1(b). Molecular states are represented by a single level since vibration-rotational levels are not differentiated. The radiative processes with their effective rate coefficients are



and



The Na(3P) has a natural lifetime of $\Gamma_0^{-1} \approx 16$ nsec but in this experiment the resonance fluorescence is heavily trapped so that the Na(3P) has an effective radiation escape lifetime $\Gamma_R^{-1} \approx 10 \mu\text{sec}$. A 5 nsec laser pulse tuned to near resonance produces 3²P_{3/2} atoms but radiation escapes in both the D₁ and D₂ lines due to collisional transfer between the 3²P_{1/2} and 3²P_{3/2} states.¹⁴ At the higher [Na] in this experiment the doublet states reach very nearly in a statistical ratio of 2:1 with an escape rate $\Gamma_R = \frac{1}{3}(2\Gamma_{3/2} + \Gamma_{1/2})$, where $\Gamma_{3/2}$ and $\Gamma_{1/2}$ are the escape rates of the D₂ and D₁ lines, respectively. At the lower [Na], Γ_R is more heavily weighted towards $\Gamma_{3/2}$. Niemax and Pichler¹⁵ have reported broadening rates of the P_{1/2} and P_{3/2} lines that are not in the statistical ratio. This would cause ~10% difference between $\Gamma_{1/2}$ and $\Gamma_{3/2}$, and the change in weighting then causes a few percent variation in Γ_R . For a self-broadened Lorentzian absorption profile $\Gamma_{1/2}$ and $\Gamma_{3/2}$ are independent of density.⁷ However, at [Na] ~ 10¹⁵-10¹⁶ cm⁻³, non-Lorentzian features in the line wings produce minor changes in $\Gamma_{1/2}$ and $\Gamma_{3/2}$. To compute this we take the absorption profile measured by Niemax

and Pichler¹⁵ and use the approximate relation⁷ that the escape factor Γ_R/Γ_0 is proportional to the transmission factor $T(l) = \int k_v \exp(-k_v l) dv / \int k_v dv$, where l is the mean escape radius of the cell. The resulting dependence of Γ_R on [Na₂] at 470 °C is shown in Fig. 2 after normalization

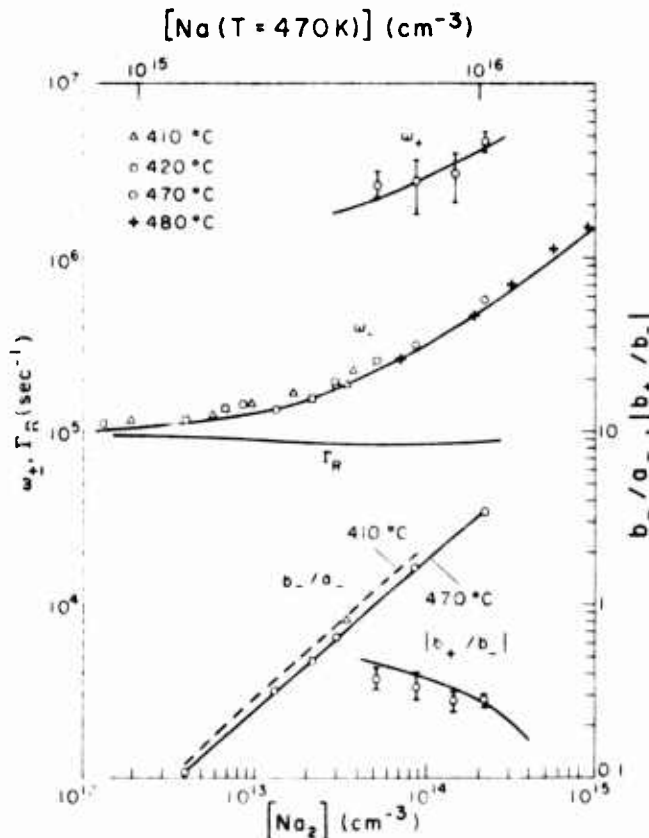
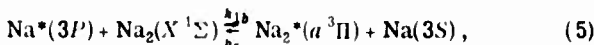
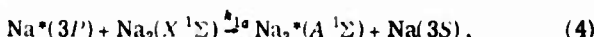


FIG. 2. Measured fast (ω_+) and slow (ω_-) exponents of the fluorescence transient, the ratio of molecular to atomic fluorescence (b_-/a_-), and the ratio of amplitude of the fast to slow components in molecular fluorescence b_+/b_- , $w_+ > b_+ < 0$ and $b_- > 0$ plotted against molecular density [Na₂]. Solid lines are calculated from the model for a cell temperature of 470 °C with parameter values given by Table I. The dotted line is the calculated b_-/a_- at a cell temperature of 410 °C.

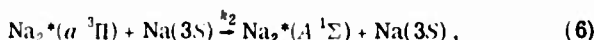
tion to a value of 10^5 sec^{-1} measured at low density. This normalization corrects for the effective cell size, which depends on cell-wall reflection coefficients and geometry. Γ_R varies by ~12% between low and high densities. Overlap of the D_1 and D_2 absorption profile decreases the escape rate by <1% and is not included.

Radiation trapping in the molecular band is negligible. However, since the $A-X$ band overlaps with the atomic D line, the initial laser pulse does excite the $A^1\Sigma$ state, producing a transient $A-X$ band fluorescence of 12 nsec which was observed. The excitation of $A^1\Sigma$ by the ~10 μsec trapped atomic resonance radiation would have an excitation rate proportional to $[\text{Na}_2]$ and it is difficult to separate its effect from collisional excitation. However, it can be shown to be negligible by the following argument. At $[\text{Na}] = 10^{14} - 10^{16} \text{ cm}^{-3}$, the absorption coefficient of the atomic line is $10^4 - 10^5 \text{ cm}^{-1}$, so that a photon travels $10^{-4} - 10^{-5} \text{ cm}$ between absorptions. The escape factor is $\sim 10^3$, so that on the average a photon travels $(10^{-4} - 10^{-5}) \times 10^3 - 10^{-1} - 10^{-2} \text{ cm}$ before it is re-emitted far into the wing and escapes after traversing the cell dimension $l \sim 1 \text{ cm}$. The broadened resonance lines are much wider than the spacing between strong Na₂ lines, so that the average absorption cross section¹⁶ of $\sim 10^{-16} \text{ cm}^2$ for the $X^1\Sigma - A^1\Sigma$ transition at ~590 nm and ~500 °C applies. The probability of a photon being absorbed by Na₂ before escaping is thus $[\text{Na}_2] \sigma l \sim 10^{-16} \text{ cm}^3 [\text{Na}]_2$, which is negligible compared to the probability of collisional excitation transfer probability given by $k_1 [\text{Na}_2] / \Gamma_R \sim 3 \times 10^{-14} \text{ cm}^3 [\text{Na}]_2$.

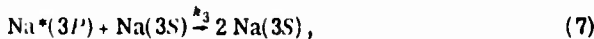
Collisional excitation transfer processes in the Na-Na₂ system, as indicated in Fig. 1b are



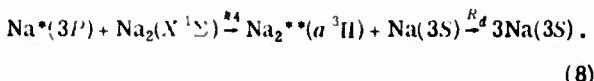
and



where $k_1 = k_{1a} + k_{1b}$ and $r = k_{1b}/k_{1a}$. Nonradiative quenching processes are:



and



Rate coefficients for the various processes are designated k_i and rates R_i . Reverse processes of (4) and (6) are neglected compared to the rapid radiative rate of the $A^1\Sigma$ state. The possibility of quenching process (7) is allowed for, as it could result from crossing of $X^1\Sigma$ and $a^3\Pi$ potentials (see Fig. 1a), but would be negligible in the absence of such crossing. The $\text{Na}^{**}(a^3\Pi)$ in Process (8) corresponds to those weakly bound $a^3\Pi$ dimers that can predissociate before radiation or vibrational stabilization to more deeply bound states which do not predissociate. Therefore only $\text{Na}_2^*(a^3\Pi)$ states that do not predissociate are included in Eqs. (5) and (6). The predissociation rate, R_4 , is faster than all other rates so that (8) proceeds effec-

tively at rate coefficient k_4 . The rate coefficient k_4 will be used to describe all forms of Na(3p) quenching by Na₂(X) which do not result in red emission. Thus, although the process in (8) is perhaps the most likely mechanism, transfer to the $B^1\Pi_u$ state followed by green $B-X$ band emission would also contribute, as would nonradiative quenching. Process (5) is expected to yield a nonthermal distribution of population in the vibration-rotation states of $a^3\Pi$. Consequently the ratio of forward to backward rates, k_{1b}/k_5 , is not expected to have a thermal value. The $A^1\Sigma$ state is not expected to predissociate, and collisions between two excited atoms are negligible due to low excited state density, $[\text{Na}^*] \sim 10^{12} \text{ cm}^{-3}$.

The rate equations corresponding to Eqs. (1)-(8), their solutions and the relation of the rate coefficients to experimentally measured quantities are given in the Appendix. This may be summarized as follows. Since the $A^1\Sigma$ state and $a^3\Pi_u^{**}$ state in Fig. 1 decay very rapidly compared to collisional rates, the equations for these level populations are taken as uncoupled. Thus only the Na₂($a^3\Pi_u$) and Na(3P) states are coupled and the solutions for their populations consist of two exponentially decaying terms [Eqs. (A4)-(A7)]. The 3P population thus decays with fast and slow exponential rates while the $a^3\Pi$ population initially grows at the fast rate and decays at the slow rate. As given in the Appendix (A7) the atomic radiation is then obtained by multiplying the Na 3P population by the radiative escape rate Γ_R and the molecular radiation is $\Gamma_A[\text{Na}_2(A^1\Sigma)] + \Gamma_B[\text{Na}_2(a^3\Pi)]$. The approximation $R_{1b} \gg R_{3P}$ is then used to obtain approximate expressions [(A11) to (A14)] that show the sensitivity of the measured parameters to the collisional rates. Finally, expressions for the nonradiative quenching are given [(A15) to (A17)]. In essence these note that the observed decay rates may be faster than can be accounted for by the radiative loss rates. The analysis of the data, using these results is given in Sec. IV.

III. EXPERIMENT

A cylindrical stainless steel cell with sapphire end windows is connected to an external Na reservoir and pumps. The Na density in the cell is controlled by the temperature of the external reservoir, and the Na₂ density is then given by the equilibrium relation at the cell temperature. A nitrogen-laser pumped dye-laser tuned near the Na resonance lines excites Na atoms to the 3P state in a ~5 nsec pulse. The laser beam is spread out to fill the cell windows and tuned off resonance in order to excite 3P atoms more or less uniformly throughout the cell. A lens past the cell focuses the transmitted laser beam into an absorber on axis and also focuses a large portion of the cell volume onto photomultipliers. The photomultipliers are filtered to detect the 590 nm region of the Na resonance lines or the 620-800 nm region of the Na₂ A-X and a-X bands, and the time dependence of these signals are recorded by a transient digitizer and/or an oscilloscope. The emission spectrum in a fixed time interval after excitation was also measured with a gated photomultiplier following a

monochromator. Details of the apparatus are given below.

A. Cell and oven

Temperatures of ~450 °C are required for [Na] of ~10¹⁶ cm⁻³. The alkali resistant cell consists of a stainless steel cell body with sapphire windows. A major problem is the brazed joint between the sapphire and the metal sleeve, which frequently cracked due to thermal strains. While more windows provide better input and output optics and reduce laser scatter, the chance of window failure increases. The final cell used is 5 cm long and 2.5 cm diameter sapphire windows at each end. The sapphire windows are also enveloped in concentric evacuated stainless steel pipes, which were welded onto the cell body with both ends protruding outside the oven and which ended in flanged quartz windows. In addition to minimizing thermal gradients, the envelope maintains vacuum and the cell remains operational as long as the sodium loss rate through minor cracks in the sapphire windows is not excessive. Covering the cell body are two closely fitted half-cylindrical brass shells which maintain a uniform temperature. With extreme care in welding the sapphire windows on the cell body and with a minimum of thermal cycling and abrupt heating or cooling during and between data taking, the windows of this cell did not leak at the end of the experiment.

The cell is connected to an external Na reservoir and then through a bakeable, stainless steel valve to the vacuum pump. The reservoir temperature fixes the Na density in the cell and the higher cell temperature fixes the molecular fraction through the temperature-dependent equilibrium constant K_{eq} in [Na₂] = $K_{\text{eq}}[\text{Na}]^2$. After initial bakeout, sodium is distilled *in situ* from an ampoule holder outside the bakeable valve into the reservoir adjacent to the cell. After distillation, impurities due to outgassing are removed periodically by opening the valve briefly while the cell and reservoir are kept hot. No impurity effects were detectable after a few days of operation.

B. Density determination

Sodium vapor density is mainly determined from thermocouple junction temperatures at the reservoir finger and at the cell body. Vapor pressure values compiled by Nesmeyanov¹⁷ are used for [Na]. Atom-dimer equilibrium constant, K_{eq} , which determines [Na₂], is calculated from the X¹Σ potential curve¹¹ according to:¹⁸

$$K_{\text{eq}} = (g_x/g_{\text{ss}}) \int_0^\infty d^3R \exp[-V_x(R)/kT] \Gamma(\frac{3}{2}, V_x/kT), \quad (9)$$

where the g 's are the multiplicity factors of the dimer and atomic states, $V_x(R)$ is the dimer X¹Σ potential, and $\Gamma(\frac{3}{2}, V_x/kT)$ is the normalized incomplete gamma function. K_{eq} as calculated in (9) has an uncertainty of 1 - exp(-ΔD_e/kT) ~ 13% given by the uncertainty in the X¹Σ well depth ΔD_e ~ 70 cm⁻¹.¹¹

The [Na] density is checked by measuring the absorp-

tion profile of the D lines with a quartz iodide lamp. From the measured absorption equivalent width and the self-broadening coefficients of sodium D lines,¹⁵ the [Na] density is determined and agrees with temperature determinations to within the measurement uncertainty of ± 10%.

C. Laser and optics

The dye laser follows the design of Hansch¹⁹ and consists of a quartz curvette dye cell in a ~20 cm long laser cavity consisting of a 5 cm diameter grating (~2000 lines/mm), a beam expander and an output mirror of transmission ~50%. The dye is pumped transversely by a nitrogen laser. Output pulse of the dye laser is ~5 nsec long, ~0.05 nm wide.

The trapped radiation escape factor depends on the excitation beam geometry as well as on cell geometry and vapor density. It is not possible to adjust the excitation beam to produce an initially excited atom profile of only the fundamental mode of the cell so that exponential decay results.⁷ A practical compromise, and a good approximation, is to excite the whole cell uniformly. For this purpose, the uniform central portion of the laser beam is expanded and passed through the cell as a parallel beam of 2.5 cm diameter. At low [Na] ~ 10¹⁴ cm⁻³, when collisional energy transfer is minor, we observed a single exponential decay of ~10 μsec lifetime for over two decades. This is presumably the fundamental radiation escape mode and higher modes are negligible. The laser beam is tuned sufficiently from line center to yield at least 70% transmission, thus providing a less than 30% variation in excitation along the cell length. The detuning was typically 0.4 nm compared to ~0.05 nm laser line width, so that the ~30% absorption is uniformly distributed over all laser wavelengths.

The energy in the 5 nsec laser pulse is kept at 10–30 μJ, since high photon density would produce stepwise excitation or, more importantly, saturation effects such as depletion of molecular ground states by excited atoms according to (4) and (5) in Sec. II. Nonexponential and long-lived tails in the transient decay were observed when we increased the laser pulse energy or used a focused beam instead of expanding it to fill the cell.

The transmitted laser beam is focused into a small light stop by a 10 cm lens placed ~10 cm beyond the cell. Multiple reflections of the laser beam would also emerge parallel and are focused onto the same stop. The small stop blocks very little of the sodium fluorescence that emerges from an extended source throughout the volume of the cell. The fluorescence is imaged by the same 10 cm lens with f/10 optics onto the detectors.

D. Signal detection and processing

The fluorescence is detected both in a wide band with optical filters and through a monochromator. For transient measurements, a ~7 nm wide interference filter is used to pass the broadened D lines, a yellow glass filter for the total fluorescence, and a glass filter passing λ ≥ 620 nm for the red portion of the A-X

band. This red portion is determined to be $73 \pm 5\%$ of the entire A-X band intensity from spectrum measurements described below. The filtered fluorescence is detected by a GaAs photomultiplier wired so that a synchronized negative voltage pulse can be applied to the first and third dynodes to switch the gain off when the laser pulse is on. Most of the time-dependent signals are then digitized by a transient recorder with ~ 10 nsec resolution, averaged in a small computer, and then stored on magnetic tape. The decay constants for the fast transients (ω_*) were measured from oscilloscope photographs.

For spectral scanning of the fluorescence, a $\frac{1}{3}$ m monochromator set at 1 nm resolution is used with an extended S-20 phototube which is also wired for gain switching. The spectral sensitivity has been measured and is used to correct measured spectrum. The signal is fed to a boxcar integrator to integrate the portion of the transient 3–7 μ sec after the laser pulse, which is free from noise due to laser firing and phototube gain switching. A multichannel analyzer then digitizes the scanned signal.

IV. DATA AND RESULTS

A. Data

Directly measurable quantities in this experiment are the relative intensities and time dependence of the atomic and molecular fluorescences. Both fluorescence signals are analyzed as two exponential components, with decay constants ω_* and $\omega_*(\omega_* > \omega_*)$, as given by Eq. (A7) in the Appendix. As expected, we observe the same ω_* exponent for the atomic and molecular fluorescence decays. The initial fast exponential component in the atomic fluorescence is masked by laser scatter, so the ω_* exponent is measured from the molecular fluorescence. Also measured from the molecular fluorescence transient is the amplitude ratio of the slow and fast components, b_*/b_* , in Eq. (A10). The ratio of molecular to atomic fluorescence I_{3P}/I_{3P} is measured in the late part of the decay, where it corresponds to b_*/a_* in Eq. (A8). Fluorescence intensities at different Na densities are not compared due to the different excitation conditions used. Thus the measurements yield the quantities ω_* , ω_* , b_*/b_* , and b_*/a_* of Eqs. (A7), (A8) and (A10) as a function of [Na] and [Na₂].

The molecular spectrum was measured at temperatures of 410–480 °C. The spectrum has been shown in Fig. 8 of Ref. 16, where it is compared to calculated thermal A-X band spectra and appears closest to that of a $T \approx 3000$ °K vibrational distribution.

The measured quantities of ω_* , ω_* , b_*/a_* and $|b_*/b_*|$ where b_* is negative, are plotted against [Na₂] in Fig. 2. A possible systematic error in the [Na₂] scale of $\pm 30\%$, due to uncertainty in [Na] and K_{eq} corresponds to a horizontal translation in the logarithmic scale and is not indicated. Most data are measured at a cell temperature of 470 °C, with $K_{\text{eq}} = 2.2 \times 10^{-16} \text{ cm}^3$. Some of the ω_* and b_*/a_* data are taken at different cell temperatures 410–480 °C as indicated in Fig. 2. An analysis of these data is given in the following sections.

B. Data analysis

The radiative decay rate ω_* was measured at [Na] = $10^{13} - 2 \times 10^{16} \text{ cm}^{-3}$, although only data for [Na] > $4 \times 10^{11} \text{ cm}^{-3}$ is shown in Fig. 2. For [Na] = $10^{13} - 2 \times 10^{14} \text{ cm}^{-3}$ we obtained $\omega_* = 1 \pm 0.1 \times 10^5/\text{s}$. Since collision processes, other than $3^2P_{1/2} \leftrightarrow 3^2P_{3/2}$ mixing, are negligible at these densities this ω_* corresponds to Γ_R , the (trapped) radiative decay rate. As noted in Sec. II B, the $3^2P_{1/2} \leftrightarrow 3^2P_{3/2}$ mixing due to Na collisions should cause only a few percent change in Γ_R , so this constant observed Γ_R confirms the prediction of Holstein's theory⁷ for resonance broadening. This constant Γ_R results because the line width as well as the number of absorbers is linear in [Na] in this density range, so that the photon escape probability is independent of [Na]. The 12% variation of Γ_R with increasing [Na], shown in Fig. 2, is obtained from the arguments in Sec. II B. At the higher densities the additional collision processes in Fig. 1(a) compete with this radiative decay rate. To obtain information regarding these additional rate coefficients we will compare the measured quantities ω_* , b_*/a_* , and b_*/b_* to the predictions of the model given in Fig. 1(a) and Eqs. (1)–(8). The resulting linear coupled equations and their solutions are given in the Appendix. These solutions, (A7)–(A10), have a relatively complicated dependence on seven unknown coefficients, so that a random search is not realistic. Three simplifications allow a relatively rapid convergence to a set of coefficients that explain the data. First, a range of reasonable values can be set for $k_1 + k_4$, Γ_n , and r ; next, upper limits can be set for the nonradiative quenching rate coefficients k_3 and k_4 , using minimal assumptions for the other coefficients; finally, approximations to (A7)–(A10) can be used to isolate the important parameters during an initial search procedure for the remaining coefficients k_2 and k_5 and improved values for k_1 , Γ_n , and r . Finally, these values are optimized and uncertainties are estimated by a least squares fitting of the exact equations to the data. These steps are described in the following paragraphs.

As [Na] increases from $5-15 \times 10^{14} \text{ cm}^{-3}$ ([Na₂] = $10^{12}-10^{13} \text{ cm}^{-3}$ in Fig. 2), ω_* varies approximately linearly with [Na₂] and is fairly independent of variations in [Na] with T (Fig. 2). This behavior corresponds to a relatively minor amount of back transfer (R_5) at these low densities, so that $\omega_* \approx R_{3P} = \Gamma_R + R_1 + R_3 + R_4$ from (A7). Assuming for the moment that the Na induced process R_3 is small, which is consistent with the relative insensitivity to T , the variations of ω_* with [Na₂] in this low-density region yields $k_1 + k_4 \sim 4 \times 10^{-9} \text{ cm}^3 \text{ sec}^{-1}$.

From analysis of $a^3\Pi_u$, $A^1\Sigma_g$ perturbation strengths¹⁰ one can infer that the majority of $a^3\Pi_u$ vibrational and rotational states will have radiative rates of $2 \times 10^5 - 10^6 \text{ sec}^{-1}$, with the rest in the $10^6-10^8 \text{ sec}^{-1}$ range. Those radiating faster than $\sim 10^7 \text{ sec}^{-1}$ are effectively grouped with the $A^1\Sigma_g$ states in this analysis, and as Γ_n represents an average rate for the remaining $a^3\Pi_u$ states we expect $2 \times 10^5 \text{ sec}^{-1} < \Gamma_n < 10^6 \text{ sec}^{-1}$.

The ratio $r = k_1/k_4$ of excitation transfer to $a^3\Pi_u$ versus that to $A^1\Sigma_g$ has a reasonable upper limit of 6,

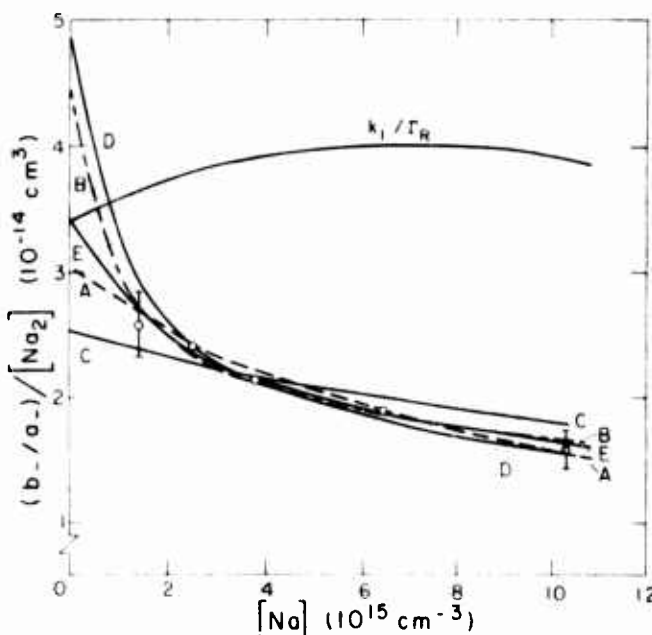


FIG. 3. Ratio of molecular to atomic fluorescence normalized by molecular density ($b_+/a_/[Na_2]$) at a cell temperature 470 °C plotted against atomic density [Na]. Lines A, B, C, D, and F correspond to model calculations with $k_1/\Gamma_R = 1.5 \times 10^{-17} \text{ cm}^3 \text{ sec}^{-1}$ and the r values of $r = k_{1b}/k_{1a}$ and k_5/Γ_R as indicated by points A, B, C, D, and E in Fig. 6.

the statistical weight ratio. In fact, since the more strongly mixed vibration-rotation $a^3\Pi_u$ states radiate rapidly, they are effectively grouped with the $A^1\Sigma_g$ states and $r < 5$ is expected. The ω_+ data in Fig. 2 do not fit $\Gamma_R + k_1[Na_2]$ and the molecular/atomic intensity ratio in Fig. 3 does not fit $k_1[Na_2]/\Gamma_R$; thus some back transfer [k_5 in Fig. 1(a)] is essential, requiring $r > 0$ and $k_5 > 0$. In fact the ratio of the actual data in Fig. 3 to k_1/Γ_R at $[Na] > 4 \times 10^{15} \text{ cm}^{-3}$ requires $r > 1.5$ for any choice of the other coefficients.

The nonradiative quenching rates, R_3 and R_4 , are given in (A17) in terms of a_+/a_- , the measured quantities ω_+ , ω_- , b_+/a_+ , and b_-/b_+ , and Γ_R which is known. The only unknown quantity on the right side of (A17) is a_+/a_- , which equals $(\omega_+ - R_{3P})/(R_{3P} - \omega_-)$ from (A9). Here $R_{3P} \equiv \Gamma_R + R_1 + R_3 + R_4$ depends on R_3 and R_4 , but is already known approximately from the above discussion of the low pressure data. Thus (A17) in the form given must be solved iteratively for $R_3 + R_4$, but this procedure converges very rapidly because the terms involving a_+/a_- are relatively minor and as soon as an initial estimate is obtained for $R_3 + R_4$, a_+/a_- is only weakly dependent on $R_3 + R_4$. In essence, $a_+/a_- \approx 0.1$, and this ratio changes by 10% or less with the addition of $R_3 + R_4$. Starting values of $k_3 = 7 \times 10^{-12} \text{ cm}^3 \text{ sec}^{-1}$ and $k_4 = 5 \times 10^{-10} \text{ cm}^3 \text{ sec}^{-1}$ can be obtained directly from the data using the (A15) approximation to (A17). Since $(R_3 + R_4)/[Na] = k_3 + k_4[Na_2]/[Na] = k_3 + k_4 K_{eq}[Na]$ we have plotted the right-hand side of (A17) divided by [Na] in Fig. 4. Thus the intercept in Fig. 4 yields k_3 and the slope $k_4 K_{eq}$ with $K_{eq} = 2.2 \times 10^{-18} \text{ cm}^3$ for the 470 °K data used. These coefficients are given in Table I. The uncertainties in Fig. 4 and in the resulting k_3 and k_4

TABLE I. Collisional and radiative rates for Na and Na₂ excited states for the processes in Eqs. (1)-(8).

k_1	$(3.4 \pm 1.1) \times 10^{-9} \text{ cm}^3 \text{ sec}^{-1} \text{ mol}^{-1}$
$r = k_{1b}/k_{1a}$	2.7 ± 0.8
k_2	$0.8 \pm 0.8 \times 10^{-11} \text{ cm}^3 \text{ sec}^{-1} \text{ atom}^{-1}$
k_3	$(3 \pm 3) \times 10^{-12} \text{ cm}^3 \text{ sec}^{-1} \text{ atom}^{-1}$
k_4	$(10 \pm 5) \times 10^{-10} \text{ cm}^3 \text{ sec}^{-1} \text{ mol}^{-1}$
k_5	$(3 \pm 1) \times 10^{-10} \text{ cm}^3 \text{ sec}^{-1} \text{ atom}^{-1}$
Γ_R	$5 \times 10^5 \text{ sec}^{-1}$

are quite large due to the subtraction of similar-sized terms on the right-side of (A17). Nonetheless, these bounds on k_3 and k_4 are very useful in establishing the validity of the assumption in paragraph two of this section, and that R_3 and R_4 play a minor role in the following determination of the remaining coefficients.

To simplify the initial search for the quantities k_1 , r , k_2 , k_5 , and Γ_R we note first that the above arguments have lead to $k_1 + k_4 \sim 4 \times 10^{-9} \text{ cm}^3 \text{ sec}^{-1}$, $1.5 < r < 5$, $3 \times 10^5 \text{ sec}^{-1} < \Gamma_R < 10^6 \text{ sec}^{-1}$. For the pressure range covered by the data it follows that $R_s \equiv \Gamma_R + R_2 + R_5 > 3R_{3P} \equiv 3(\Gamma_R + R_1 + R_3 + R_4)$. This is valid at low pressure since $\Gamma_R > 3\Gamma_R$ and at high pressure where $R_s \sim R_5$ and $R_{3P} \sim R_1$ since $R_5 \propto [Na]$ and $R_{3P} \propto [Na_2]$. (That $R_2 < R_5$ as well is necessary to explain the observed back transfer at high density.) The (A11), (A13) and (A14) approximations to (A8), (A10), and (A7) which result from assuming $R_s \gg R_{3P}$ are

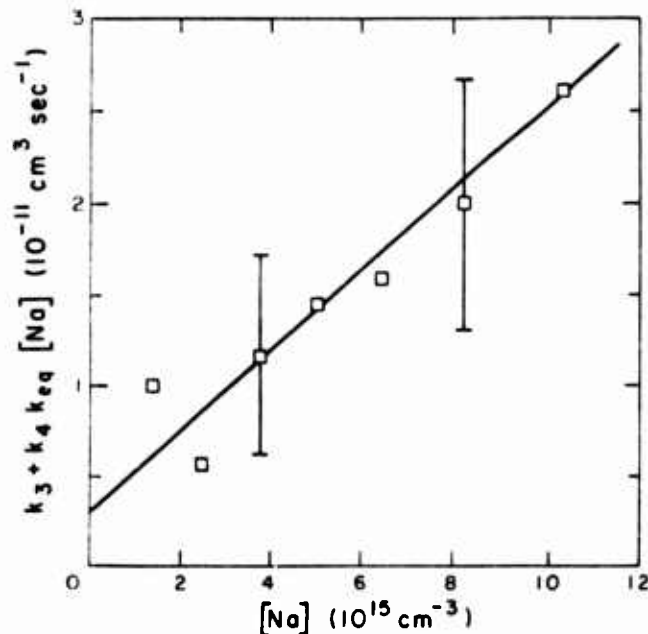


FIG. 4. Data related to the nonradiative quenching rates of Na(3P) and Na₂(a³P) normalized by sodium density [Na]. The vertical intercept gives the atomic quenching coefficient and the slope gives the dimer quenching coefficient.

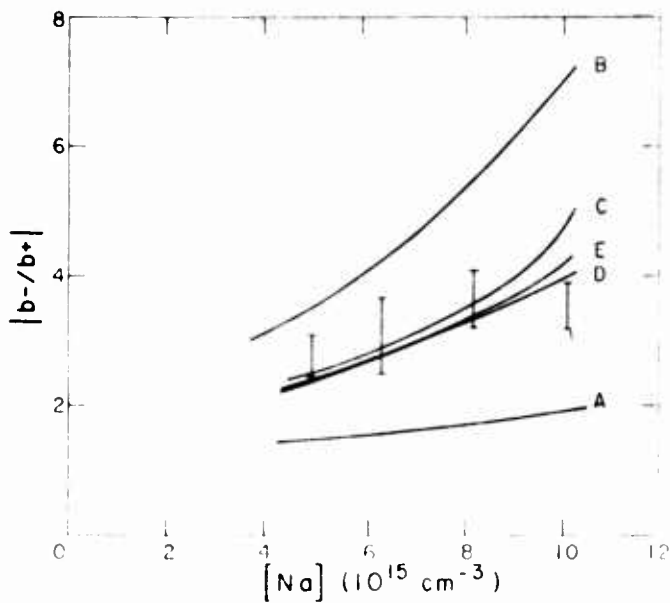


FIG. 5. Measured $|b_-/b_+|$ at a cell temperature of 470°C. See Fig. 3 caption for explanation of the lines.

$$\frac{b_-}{a_-} \frac{1}{[Na_2]} = \frac{k_1}{\Gamma_R} \left(1 - \frac{r}{r + 1} \frac{(k_5/\Gamma_{\Pi})([Na])}{1 + (k_5/\Gamma_{\Pi})([Na]) + (k_2/\Gamma_{\Pi})([Na])} \right) \quad (10)$$

$$\frac{b_-}{b_+} = 1 + \frac{1}{r} + \frac{(k_5/\Gamma_{\Pi})([Na])}{r[1 + (k_2/\Gamma_{\Pi})([Na])]}, \quad (11)$$

$$\omega_- = \Gamma_{\Pi} + (k_2 + k_5)[Na]. \quad (12)$$

Here (10) predicts a molecular/atomic intensity ratio in the late time given by Γ_R/Γ_R times the factor in parentheses, which results from the $Na(3P) \leftrightarrow Na_2(a^3\Pi_u)$ forward and backward coupling. The ratio (11) of the molecular decay coefficient b_- to the initial transient b_+ during $Na_2(a^3\Pi_u)$ population building is also influenced by the $Na(3P) \rightarrow Na_2(a^3\Pi_u)$ coupling. Since the measured ω_- (Fig. 2) are in the $2 - 4 \times 10^6 \text{ sec}^{-1}$ range and considerably exceed Γ_{Π} , (12) yields $k_2 + k_5 \sim 4 \times 10^{-10} \text{ cm}^3 \text{ sec}^{-1}$. Note that except for the multiplicative factor k_1/Γ_R in (10), the measured quantities $b_-/a_-[Na_2]$ and b_-/b_+ depend on k_5/Γ_{Π} , k_2/Γ_{Π} , and r . Thus the exact equations (A8) and (A10) will also depend primarily on these three quantities, plus the k_1/Γ_R multiplicative factor. As can be seen in (10) and (11) the $b_-/a_-[Na_2]$ and b_-/b_+ data have quite different dependences on k_5/Γ_{Π} , k_2/Γ_{Π} , and r ; as a result these parameters are well determined by fitting (A8) and (A10) to these data. To do this we have chosen sets of these three quantities and compared (A8) and (A10) to the data as a function of [Na]. As this fitting is insensitive to k_3 and k_4 , the values determined above (Table I) are of sufficient accuracy. The above arguments have also led to an approximate k_1/Γ_R , which can be improved in the present fitting. A graph of the dependences on all four parameters is too confusing, so we have fixed $k_2/\Gamma_{\Pi} = 1.5 \times 10^{-17} \text{ cm}^3$ to illustrate the dependences on k_1/Γ_R , k_5/Γ_{Π} , and r in Figs. 3, 5, and 6. In Figs. 3 and 5 the $b_-/a_-[Na_2]$ and $-b_-/b_+$ data are compared to the calculated values. The sum of the squared devia-

tions X between data and theory is plotted, as a function of k_5/Γ_{Π} and r , as contours in Fig. 6. The solid contours refer to the data in Fig. 3 and the dashed to the data in Fig. 5. For the data in Fig. 3 the smallest X occur for k_5/Γ_{Π} and r values along the dotted line AEB in Fig. 6 for the data in Fig. 5 the smallest X are along the line CED in Fig. 6. Hence fitting of both the $b_-/a_-[Na_2]$ and $-b_-/b_+$ data restricts the values of k_5/Γ_{Π} and r to the region around E in Fig. 6 for this $k_2/\Gamma_{\Pi} = 1.5 \times 10^{-17} \text{ cm}^3$ case. When k_2/Γ_{Π} is increased the set of dashed contours of Fig. 6 moves to the right while the solid contour set moves to the upper left. The AEB and CED lines then interact at much larger values of X , indicating a poorer fit to the data. When k_2/Γ_{Π} is decreased the fit to the data does not change significantly. Using a tripling of either X value at the intersection point (E in Fig. 3) as an uncertainty criterion, we thus obtain $r = 2.7 \pm 0.8$, $k_5/\Gamma_{\Pi} = (6 \pm 2) \times 10^{-16} \text{ cm}^3$ and $k_2/\Gamma_{\Pi} = (1.5 \pm 1.5) \times 10^{-17} \text{ cm}^3$. In Fig. 3 and 5 the solid curves A, B, C, D, E show how Eqs. (A8) and (A10) fit the data for values of r and k_5/Γ_{Π} at points A, B, C, D, and E in Fig. 6, e.g., at point A, $r = 5$ and $k_5/\Gamma_{\Pi} = 3 \times 10^{-16} \text{ cm}^3$. The vertical intercept in Fig. 3 gives k_1/Γ_R . For a region of good fitting around point E in Fig. 6, we obtain the value of k_1/Γ_R between 3.2×10^{-14} and $3.9 \times 10^{-14} \text{ cm}^3$. For $\Gamma_R = 10^5 \text{ sec}^{-1}$ and including (additively) an $\sim 30\%$ uncertainty in $[Na_2]$, we obtain $k_1 = (3.4^{+0.6}_{-1.1}) \times 10^{-9} \text{ cm}^3 \text{ sec}^{-1} \text{ molecule}^{-1}$. In order to emphasize the sensitivity of the data to the reverse of reaction 5, the prediction of the model for $k_5 = 0$ [$b_-/a_-[Na_2] = k_1/\Gamma_R$ from Eq. (10)] is plotted in Fig. 3 for the case $k_1 = 3.4 \times 10^{-9} \text{ cm}^3 \text{ sec}^{-1} \text{ molecule}^{-1}$. The $\sim 20\%$ variation in this k_1/Γ_R is due to the slight dependence of Γ_R on [Na] as described in Sec. VB.

Using the above $k_2/\Gamma_{\Pi} = 1.5 \times 10^{-17} \text{ cm}^3$ and $k_5/\Gamma_{\Pi} = 6 \times 10^{-16} \text{ cm}^3$, (12) reduces to $\omega_- \approx \Gamma_{\Pi}(1 + 6.15 \times 10^{-16} \text{ cm}^3 [Na])$ and yields $\Gamma_{\Pi} = 5 - 6 \times 10^5 \text{ sec}^{-1}$ from the ω_- data in Fig. 2. The resulting Γ_{Π} , k_2 and k_5 and previously determined coefficients can then be used in the

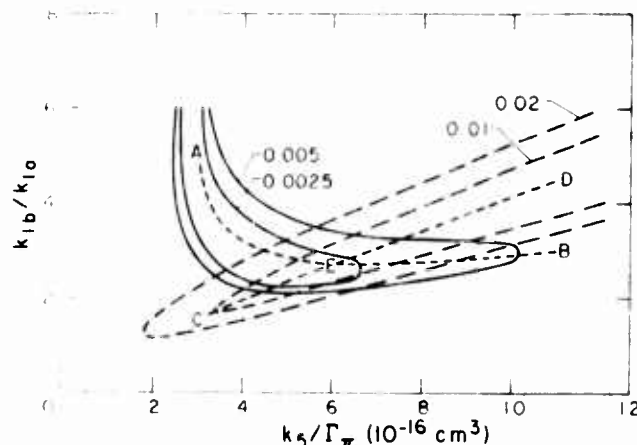


FIG. 6. Contours of sum of squares of fractional deviations, having the indicated values from fitting Eq. (10) (solid contours) and Eq. (11) (dotted contours) to data in Figs. 3 and 5, with k_2/Γ_{Π} set at $1.5 \times 10^{-17} \text{ cm}^3$. The troughs AEB and CED represent regions of good fit to data in Figs. 3 and 5 respectively, with overlapping region at E the best combined fit.

exact (A7) to obtain a more exact result $\Gamma_n = 5 \times 10^5 \text{ sec}^{-1}$. Combined with the above ratios we then have $k_2 = 8 \times 10^{-12} \text{ cm}^3 \text{ sec}^{-1}$ and $k_5 = 3 \times 10^{-10} \text{ cm}^3 \text{ sec}^{-1}$. The measured ω_* have considerable uncertainty, but these k_2 , Γ_n and k_5 values are also required to be consistent with the more accurately measured ω_* . The estimated uncertainties in all of the coefficients and Γ_n are indicated in Table I.

C. Results

The results are tabulated in Table I. With the values of Table I substituted into (A7), (A8), and (A10), we obtain the solid curves in Fig. 2 for a cell temperature of 470 °C ($K_{eq} = 2.2 \times 10^{-18} \text{ cm}^3$). At a cell temperature of 410 °C, $K_{eq} = 5.3 \times 10^{-18} \text{ cm}^3$ increases by a factor of 2.4 while b_*/a_* increases by only 20% (dotted line in Fig. 2) and ω_* does not change by more than a few percent.

V. CONCLUSIONS

We have observed a large rate coefficient, $k_1 = 3.4 \times 10^{-9} \text{ cm}^3 \text{ sec}^{-1}$, for excitation transfer between excited sodium 3P atoms and the X¹Σ sodium dimer. This is the same order as the rate coefficient, $k = 1 \times 10^{-9} \text{ cm sec}^{-1}$, for the reverse process between the B¹Π and 3P states in potassium and sodium systems reported by Krauliny *et al.*⁹ However, it is difficult to make a quantitative comparison. Krauliny *et al.*'s measurement for potassium gave a rate coefficient for the A¹Σ → 4P transfer process of $1 \times 10^{-10} \text{ cm}^3 \text{ sec}^{-1}$ compared to our $k_5 \approx 3 \times 10^{-10} \text{ cm}^3 \text{ sec}^{-1}$ for sodium a³Π → 3P transfer. As they explained, their result is small because the A¹Σ sublevels they excite (with 6328 nm light) are energetically unfavorable by ~3–4 kT for energy transfer to the 4P state. Our result $k_5 \approx 3 \times 10^{-10} \text{ cm}^3 \text{ sec}^{-1}$ is intermediate between a number of the order of $10^{-9} \text{ cm}^3 \text{ sec}^{-1}$ for the exothermic process and Krauliny's number of $1 \times 10^{-10} \text{ cm}^3 \text{ sec}^{-1}$ for the endothermic process, perhaps because it is due to populating a wide range of vibrational levels in the a³Π state in the energy transfer.

Two possible mechanisms for the large k_1 rate coefficients are (a) atom-dimer resonance interaction (the A-X bands overlaps the D lines) and (b) ion-pair intermediaries (harpooning mechanism). Both mechanisms are long-range interactions and would be expected to produce highly internally excited Na₂ A¹Σ states, qualitatively consistent with the A-X band spectrum observed.

The value of $\Gamma_n = 5 \times 10^5 \text{ sec}^{-1}$ is consistent with a³Π-A¹Σ perturbation analysis⁹ and the value of $k_2 \approx 1 \times 10^{-11} \text{ cm}^3 \text{ sec}^{-1}$ is of the order of gas kinetic rates, as expected. The small quenching coefficient $k_3 \approx 3 \pm 3 \times 10^{-12} \text{ cm}^3 \text{ sec}^{-1}$ indicates that the a³Π and A¹Σ states are not strongly quenched due to curve crossing with the X¹Σ state. This agrees with the qualitative feature of the calculated a³Σ and a³Π curves¹² which shows any crossing would occur only high on the repulsive wall. The nonzero value of k_4 , on the other hand, indicates that nonradiative molecular quenching of Na(3P) occurs. It, as just suggested, the X¹Σ and a³Π

potentials did not cross below the 3P energy, this should not occur by the predissociation process in (8).

ACKNOWLEDGMENT

We wish to thank A. V. Phelps for invaluable assistance and guidance during all phases of this work. This work was supported in part by ERDA Contract No. (49-1)-3800, and by the Advanced Research Projects Agency through the Office of Naval Research under Contract No. N00014-76-C-0123.

APPENDIX

Considering (1)–(8) Sec. II, the rate equations are ($R_i = k_i [\text{Na}_2(X^1\Sigma)]$ for $i = 1a, 1b, 4$; $R_j = k_j [\text{Na}(3s)]$ for $j = 2, 5$):

$$d[\text{Na}^*(3p)]/dt = -R_{3p}[\text{Na}^*(3p)] + R_5[\text{Na}_2^*(a^3\Pi)] + P(t), \quad (\text{A1})$$

$$\begin{aligned} d[\text{Na}_2^*(A^1\Sigma)]/dt = & -\Gamma_A[\text{Na}_2^*(A^1\Sigma)] \\ & + R_2[\text{Na}_2^*(a^3\Pi)] + R_{1a}[\text{Na}^*(3p)] + P'(t), \end{aligned} \quad (\text{A2})$$

and

$$d[\text{Na}_2^*(a^3\Pi)]/dt = -R_r[\text{Na}_2^*(a^3\Pi)] - R_{1b}[\text{Na}^*(3p)], \quad (\text{A3})$$

where $R_{3p} \equiv \Gamma_R + R_1 + R_3 + R_4$, $R_r \equiv \Gamma_r + R_2 + R_5$, $R_1 \equiv R_{1a} + R_{1b}$, Γ_R is the radiative rate of Na^{*}(3p) with trapping and $P(t)$ and $P'(t)$ are the laser pumping rate of the 3p and A¹Σ states respectively in the first ~5 nsec. The 3p and a³Π states are coupled by (A1) and (A2). Neglecting transients within $t \sim 5$ nsec or Γ_A^{-1} , which includes $P'(t)$, we have the initial conditions:

$$\begin{aligned} [\text{Na}(3p)] &= 1, d[\text{Na}^*(3p)]/dt = -R_{3p}, \\ [\text{Na}_2^*(a^3\Pi)] &= 0, d[\text{Na}_2^*(a^3\Pi)]/dt = R_{1b}, \end{aligned}$$

with solutions:

$$\begin{aligned} [\text{Na}^*(3p)] &= (\omega_* - \omega_*)^{-1} [(R_{3p} - \omega_*) \exp(-\omega_* t) \\ & + (\omega_* - R_{3p}) \exp(-\omega_* t)], \end{aligned} \quad (\text{A4})$$

$$[\text{Na}_2^*(a^3\Pi)] = (\omega_* - \omega_*)^{-1} R_{1b} [-\exp(-\omega_* t) + \exp(-\omega_* t)], \quad (\text{A5})$$

and

$$\begin{aligned} [\text{Na}_2^*(A^1\Sigma)] &= (\omega_* - \omega_*)^{-1} \left[\frac{(R_{1a}(R_{3p} - \omega_*) - R_2 R_{1b})}{\Gamma_A - \omega_*} \right] \exp(-\omega_* t) \\ & + \left[\frac{(R_{1a}(\omega_* - R_{3p}) + R_2 R_{1b})}{\Gamma_A - \omega_*} \right] \exp(-\omega_* t), \end{aligned} \quad (\text{A6})$$

where

$$\omega_* = \frac{1}{2} (R_r + R_{3p}) \pm \left[\frac{1}{4} (R_r - R_{3p})^2 + R_5 R_{1b} \right]^{1/2}, \quad (\text{A7})$$

The photon intensity in the atomic fluorescence is

$$I_{3p} = \Gamma_R[\text{Na}^*(3p)] = a_* \exp(-\omega_* t) + b_* \exp(-\omega_* t),$$

and that in the molecular band is

$$\begin{aligned} I_{\Sigma} &= \Gamma_A[\text{Na}_2^*(A^1\Sigma)] + \Gamma_r[\text{Na}_2^*(a^3\Pi)] \\ &= b_* \exp(-\omega_* t) + b_* \exp(-\omega_* t). \end{aligned}$$

For $t \gg \omega_z^{-1}$ and the excellent approximation $\Gamma_A/(\Gamma_A - \omega_z) \approx 1$, the molecular to atomic fluorescence ratio is

$$I_{\text{DP}}/I_{3p} = b_z/a_z = \Gamma_R^{-1} [R_{1a} + R_{1b}(R_2 + \Gamma_r)(\omega_z - R_{3p})^{-1}] \quad (\text{A8})$$

The amplitude ratio of the slow to fast component is

$$a_z/a_s = (\omega_z - R_{3p})/(R_{3p} - \omega_z) \text{ for atomic fluorescence} \quad (\text{A9})$$

and

$$\begin{aligned} b_z/b_s &= [R_{1a}(\omega_z - R_{3p}) + (R_2 + \Gamma_r)R_{1b}]/[R_{1a}(R_{3p} - \omega_z) \\ &\quad - (R_2 + \Gamma_r)R_{1b}] \text{ for molecular fluorescence.} \end{aligned} \quad (\text{A10})$$

Equations (A7)–(A10) can be simplified by use of the approximation $R_r \ll R_{3p}$, to obtain ($r = k_{1b}/k_{1a}$):

$$\begin{aligned} \omega_z &\approx R_r + R_5 R_{1b}(R_r - R_{3p})^{-1} \approx R_r \\ &\quad + \Gamma_r + R_2 + R_5, \end{aligned} \quad (\text{A11})$$

$$\begin{aligned} \omega_z &\approx R_{3p} - R_5 R_{1b}(R_r - R_{3p})^{-1} \approx R_{3p} - R_5 R_{1b} R_r^{-1} \\ &\approx \Gamma_R + R_3 + R_4 + R_1 [1 - r(r+1)^{-1} R_5(\Gamma_r + R_2 + R_5)^{-1}], \end{aligned} \quad (\text{A12})$$

$$b_z/a_z = \Gamma_R^{-1} R_1 [1 - r(r+1)^{-1} R_5(\Gamma_r + R_2 + R_5)^{-1}], \quad (\text{A13})$$

and

$$-b_z/b_s \approx 1 + r^{-1} + r^{-1} R_5(\Gamma_r + R_2)^{-1}. \quad (\text{A14})$$

From (A12) and (A13), R_5 can be seen at increasing [Na] as a competing process with Γ_r in transferring the excitation energy from the $a^3\Pi$ state back to the $3P$ state, thereby reducing the effective forward excitation transfer rate R_1 . Eliminating this feedback factor in square brackets in (A12) and (A13), the quenching rates can be expressed as

$$R_3 + R_4 \approx \omega_z - \Gamma_R(b_z/a_z + 1). \quad (\text{A15})$$

A way to obtain the neglected terms in this approximate expression is to balance the initial number of excited $3P$ atoms with the sum of time-integrated collisional and radiative decays:

$$\begin{aligned} 1 &= \int (\Gamma_R + R_3 + R_4)[\text{Na}^*(3p)]dt + \int \Gamma_A[\text{Na}_2^*(A^1\Sigma)]dt \\ &\quad + \int \Gamma_r[\text{Na}_2^*(a^3\Pi)]dt \\ &= \{a_z[1 + (R_3 + R_4)\Gamma_R^{-1}] + b_z\}\omega_z^{-1} \\ &\quad + \{a_z[1 + (R_3 + R_4)\Gamma_R^{-1}] + b_z\}\omega_z^{-1}. \end{aligned} \quad (\text{A16})$$

The exact expression for $R_3 + R_4$ is thus

$$\begin{aligned} R_3 + R_4 &= \left(1 + \frac{\omega_z a_z}{\omega_z a_s}\right)^{-1} \left\{ \omega_z \left(1 + \frac{a_z}{a_s}\right) \right. \\ &\quad \left. - \Gamma_R \left[1 + \frac{b_z}{a_s} \left(1 + \frac{\omega_z b_z}{\omega_z b_s}\right) + \frac{\omega_z a_z}{\omega_z a_s}\right] \right\}. \end{aligned} \quad (\text{A17})$$

For $[\text{Na}] \sim 10^{15} - 10^{16} \text{ cm}^{-3}$, we have $\omega_z/\omega_s \approx 0.1$, $a_z/a_s \approx 10^{-2}$, $(\Gamma_R/a_s) - 1 \leq 10^{-2}$, and $b_z/b_s \leq 0.4$. Hence (A17) reduces to (A15) with minor correction terms.

¹G. York and A. Gallagher, "High Power Gas Lasers Based on Alkali-Dimer A-X Band Radiation," JILA Report No. 114, Univ. of Colorado (1974).

²M. A. Henesian, R. L. Herbst, and R. L. Byer, *J. Appl. Phys.*, **47**, 1515 (1976).

³J. F. Waymouth, *Electric Discharge Lamps* (MIT, Cambridge, 1971).

⁴J. J. DeGroot and J. van Rooten, "The Photon Absorption Cross-Section of Na₂ Molecules and the Influence of These Molecules on the Spectrum of the High Pressure Sodium Arc," Proc. of 12th International Conference on Ionization Phenomena in Gases, p. 135 (1975); J. J. De Groot and J. A. J. M. van Vliet, *J. Phys. D* **8**, 651 (1975).

⁵E. T. Wyner and J. Maya, *Bull. Am. Phys. Soc.* **22**, 198 (1977).

⁶D. R. Herschbach, *Adv. Chem. Phys.* **10**, 319 (1966); J. J. Moseley, R. E. Olson and J. R. Peterson, *Case Studies in Atomic Physics*, edited by M. R. C. McDowell and E. W. McDaniel (North Holland, Amsterdam, 1975), Vol. 5, p. 1.

⁷T. Holstein, *Phys. Rev.* **72**, 1212 (1947); *Phys. Rev.* **83**, 1159 (1951); L. M. Biberman, *JETP* **17**, 416 (1947).

⁸A. V. Phelps and C. L. Chen, *Bull. Am. Phys. Soc.* **15**, 428 (1970); D. G. Hummer and P. B. Kunasz, *J. Quant. Spectrosc. Radiat. Transfer* **16**, 77 (1976).

⁹E. K. Kraulinja, E. K. Kopiekina and M. L. Janson, *Chem. Phys. Lett.* **39**, 565 (1976); E. K. Kopiekina and M. L. Janson, *Opt. Spektrosk.* **41**, 378 (1976) [*Opt. Spectrosc.* **41**, 217 (1976)].

¹⁰P. Kusch and M. M. Hessel, *J. Chem. Phys.* **63**, 4087 (1975).

¹¹W. Demtroder, M. McClintock, and R. N. Zare, *J. Chem. Phys.* **53**, 3094 (1970).

¹²J. N. Bardsley, B. R. Junker, and D. W. Norcross, *Chem. Phys. Lett.* **27**, 502 (1976).

¹³T. W. Ducas, M. G. Littman, M. L. Zimmerman, and D. Kleppner, *J. Chem. Phys.* **65**, 942 (1976).

¹⁴J. Pitre and L. Krause, *Can. J. Phys.* **46**, 125 (1968).

¹⁵K. Niemax and G. Pichler, *J. Phys. B* **8**, 179 (1975).

¹⁶L. K. Lam, A. C. Gallagher, and M. M. Hessel, *J. Chem. Phys.* **66**, 3550 (1977).

¹⁷A. N. Nesmeyanov, *Vapor Pressure of Chemical Elements* (Elsevier, Amsterdam and New York, 1963).

¹⁸R. E. Hedges, D. L. Drummond and A. C. Gallagher, *Phys. Rev. A* **6**, 1519 (1972). The function $\Gamma(\frac{1}{2}, m)$ is $P(m | \nu = 3)$ in Table 26.7 of M. Abramowitz and A. Stegun, *Handbook of Mathematical Functions* (U. S. Government Printing Office, Washington, D.C., 1964).

¹⁹W. Hansch, *Appl. Opt.* **11**, 895 (1972).

The effects of multiperturber interactions on the sodium-rare gas excimer bands^{a)}

W. P. West,^{b)} P. Shuker, and Alan Gallagher^{c)}

Joint Institute for Laboratory Astrophysics, University of Colorado and National Bureau of Standards,
Boulder, Colorado 80309
(Received 6 October 1977)

The extreme wing ($600 < \lambda < 820$ nm) of the sodium D lines perturbed by xenon and krypton has been measured in fluorescence at perturber densities between 2×10^{19} and $3 \times 10^{20} \text{ cm}^{-3}$. At these perturber densities the observed fluorescence results mostly from the $\text{NaXe}^*(\text{NaKr}^*)$ molecule in the wavelength range of $600 < \lambda < 720$ nm ($600 < \lambda < 680$ nm) and from the $\text{NaXe}_2^*(\text{NaKr}_2^*)$ molecule in the range $740 < \lambda < 820$ nm ($700 < \lambda < 820$ nm). The fluorescence emission coefficient is obtained in normalized units, allowing quantitative comparison to theory. The quasistatic line-broadening theory, including multiple-perturber interactions, is used to calculate the density dependence of the spectra which would result from trimer potential surfaces given by scalarly additive pair interactions. This approximation explains some of the observations; discrepancies between this model and the experimental results are discussed.

I. INTRODUCTION

The spectra of alkali metal atoms perturbed by rare gases (RG) has been the subject of many studies. Such effects as the broadening, shift, and satellite features of allowed lines^{1,2}; collisionally induced absorption and emission^{3,4}; and absorption from the ground state van der Waals molecule⁵ have been investigated. Among the work reported from this laboratory are several studies of the extreme wing spectra of the alkali resonance lines perturbed by noble gases.⁶⁻¹⁰ These earlier studies of the excited state fluorescence were carried out at perturber densities $\lesssim 10^{19} \text{ cm}^{-3}$ and were interpreted in terms of diatomic excimer radiation. Here we report an extension of this work for the $\text{Na}(3P-3S)$ resonance lines perturbed by Xe and Kr at densities up to $3 \times 10^{20} \text{ cm}^{-3}$, where the effects of multiple-perturber interactions or polyatomic molecules are observed. These experimental results are compared to calculated spectra which are obtained by incorporating multibody effects into the quasistatic line broadening theory.

As shown in Fig. 1, the NaXe molecule⁹ is an excimer, i.e., the $\text{NaXe} X^2\Sigma$ ground-state molecule is repulsive, with only a weak van der Waals minimum at large internuclear separation. The first excited state, $A^2\Pi$, which results from a combination of an excited $\text{Na}(3P)$ atom and a $\text{Xe}(^1S_0)$ ground state atom, is bound by $\sim 1200 \text{ cm}^{-1}$, while at the temperatures of these experiments $kT \approx 300 \text{ cm}^{-1}$. The observed fluorescence spectrum from the $A^2\Pi$ state is a continuum resulting predominantly from bound-free and free-free $A^2\Pi - Y^2\Sigma$ transitions and is shifted to the red side of the $\text{Na}(3P)-\text{Na}(3S)$ resonance lines. In addition to the $A^2\Pi$ state, the combination of a $\text{Na}(3P)$ atom and a $\text{Xe}(^1S_0)$ atom can result in a repulsive $B^2\Sigma$ excited state (not shown in Fig. 1)

which has a fluorescence continuum to the blue side of the resonance lines. York *et al.*⁹ have investigated the behavior of the sodium-rare gas fluorescence spectra at several rare gas densities [RG] in the range $10^{16} \text{ cm}^{-3} \leq [\text{RG}] \leq 10^{19} \text{ cm}^{-3}$ and have derived the interatomic potentials shown in Fig. 1. That study, as well as the present one, is concerned with the excimer A-X band at large frequency shifts (100 cm^{-1} or more) from the atomic transition frequency, where it is essentially a molecular spectrum. The data closer to the atomic lines are discussed in a separate publication.¹¹

Since the $A^2\Pi$ potential well is relatively shallow, at $[\text{RG}] = 10^{19} \text{ cm}^{-3}$ an excited $\text{Na}(3P)$ atom (Na^*) has less than a 5% probability of radiating when a rare gas atom is sufficiently close (within $\sim 6 \text{ \AA}$) to cause a $\gtrsim 50 \text{ cm}^{-1}$ shift in the frequency of the resonance transition. Thus if one assumes approximately equal interactions between Na^* and each RG atom the probability that a Na^* atom will have two or more rare gas atoms within this range when it radiates is quite small ($\sim 2.5\%$ of 5%). This was utilized in Refs. 9 and 10 to study the NaXe excimer

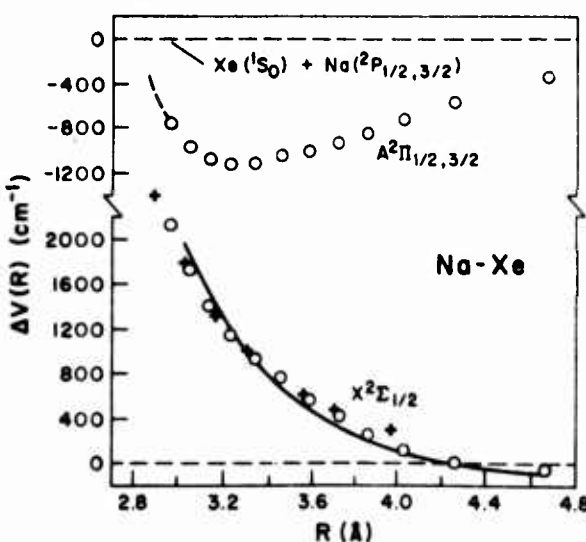


FIG. 1. The potential curves of the $\text{NaXe} X^2\Sigma$ and $A^2\Pi$ molecular states obtained from Ref. 9.

^{a)}Work supported in part by the Air Force Weapons Laboratory and in part by the Advanced Research Projects Agency of the Department of Defense, monitored by ONR under contract N00014-76-C-0123.

^{b)}Present address: Physics Department, University of California, Santa Barbara, CA 93106.

^{c)}Staff Member, Quantum Physics Division, National Bureau of Standards.

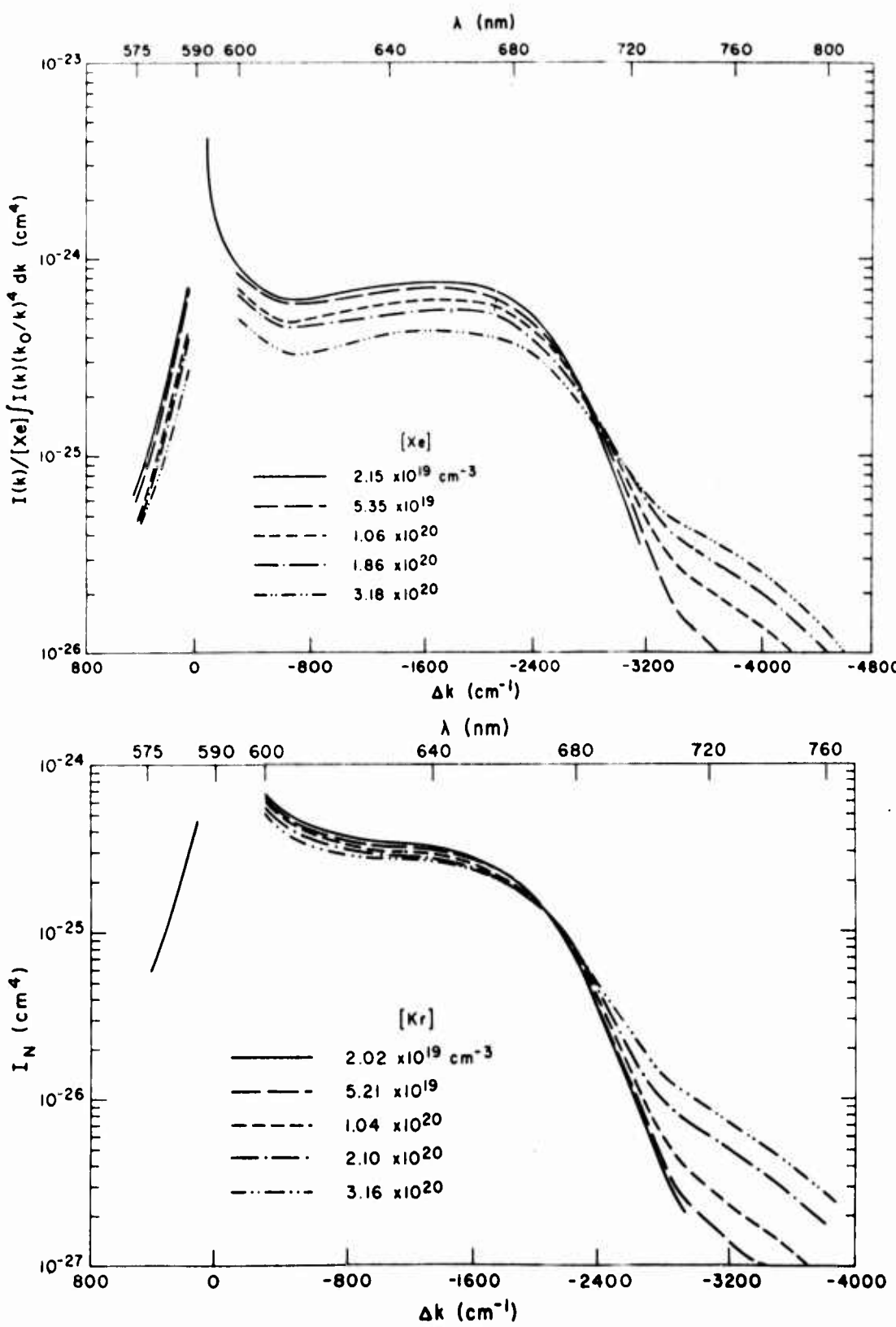


FIG. 2. The measured normalized emission coefficient as a function of Δk at several rare gas densities for (a) Na-Xe and (b) Na-Kr.

molecule without significant interference from multiple Xe interactions. However, in the present experiment the spectra are observed at $2 \times 10^{19} \text{ cm}^{-3} \leq [\text{RG}] \leq 3 \times 10^{20} \text{ cm}^{-3}$ and the effects of polyatomic (NaXe_2) molecules become quite apparent. The normalized spectra in the 600–720 nm region shown in Fig. 2(a) which results

predominately from the $\text{NaXe } A^2\Pi$ fluorescence, is weakened by the presence of additional Xe atoms close proximity to Na^* , while NaXe_2 fluorescence in the 740–820 nm region of the spectrum increases with increasing [Xe]. These intensity variations can be expressed in terms of [Xe] and $[\text{Xe}]^2$, but at $[\text{Xe}] \geq 10^{20}$

cm^{-3} evidence of still higher order $[\text{Xe}]^n$ terms has been observed in the long wavelength region. Figure 2(b) shows similar behavior for the sodium-krypton case.

As is well known, the classical Franck-Condon principle (CFCP) or the equivalent quasistatic line broadening theory describe the average intensity distribution in the far wings of perturbed resonance lines. This theory combines the statistical distribution of perturber atoms around the radiating (or absorbing) atoms with the approximation $h\nu = V^*(R) - V(R)$ to predict the spectrum.^{1,6-8,12-14} [Here $V^*(R)$ is the upper and $V(R)$ the lower molecular adiabatic state potential.] In the present work the statistical distribution will include a significant probability of one, two, and more perturber atoms being near the emitter (Na), and therefore the potential surfaces of the NaXe_n ground and excited states with $n > 2$ must be known in order to predict the spectrum. As noted above, previous intensity measurements⁹ have obtained the NaXe potential curves in the range of 3 to 5 Å. Smalley *et al.*⁵ have verified the accuracy of these potentials in the Na-Ar case using much more accurate bound-bound spectroscopy. However, the present data do not provide sufficient information to determine the three-body potential surfaces, so we compare the measured pressure dependent spectra to the prediction of the CFCP using assumed potentials. We have tested the data against the simplest of polyatomic potentials, the additive pair interaction potential. As discussed previously by Margenau,¹⁵ Jabłoński,¹⁶ and others,¹⁷⁻²⁰ the effect of $\text{Na}(\text{RG})_n$ on the far wing spectra can be approximately evaluated using the CFCP if the NaRG_n potentials are assumed to be the sum of independent, scalarly additive multiple Na-RG and Na^*-RG pair interactions. These theories are directed primarily toward the line shape in the quasistatic region but close to the atomic transition frequency, which is due to weak, long-range interactions. Theories directed to the line core shape are discussed in Ref. 11, which reports our data in this spectral region. In order to correct for far wing effects, to relate to the normalized fluorescence intensity units of these experiments and to more traditional molecular-spectra models, and in preparation for introducing the interactions between RG atoms, we derive equivalent expressions below. We first obtain simple relations, equivalent to those in Ref. 17, between the measured low-pressure (diatomic) spectra and the polyatomic spectra predicted by this simple model. These theories ignore the RG-RG interactions, so we next calculate the changes to be expected in the present problem due to this interaction. As the various NaXe_n bands overlap and are observed as continua, there is no way to distinguish them experimentally. We therefore re-express the theoretical results for intensity at each wavelength as a power series in $[\text{RG}]$ for comparison to experiments. Quantitative comparisons to the experimental results are made, discrepancies are discussed in the light of the additive potential assumption, and corrections to this assumption are suggested.

II. THE EXPERIMENT

A schematic of the apparatus is shown in Fig. 3. The experimental methods have been described in Refs. 6-

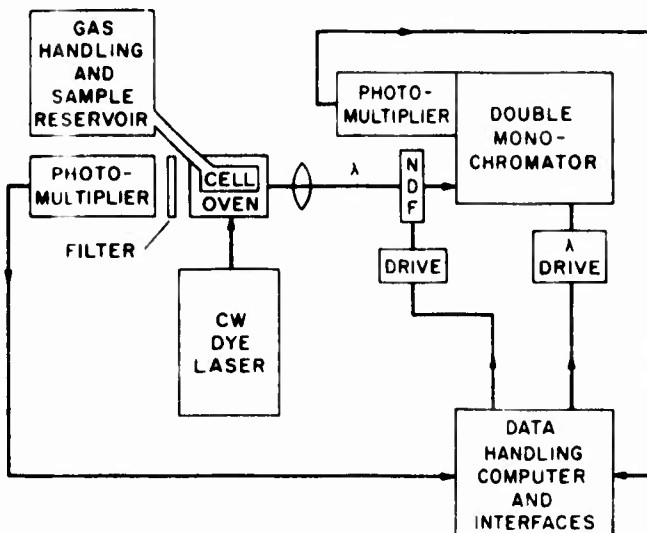


FIG. 3. Schematic of the apparatus.

10, so only a brief summary with emphasis on changes will be given.

The experimental cell, which was machined from a solid stainless steel block and had four sapphire windows, contained a droplet of sodium metal and was connected to an external gas handling system. For the data presented the temperature of the cell was maintained at $453 \pm 10^\circ\text{K}$. The sodium vapor density (typically $\sim 10^{11} \text{ cm}^{-3}$) was low enough to avoid reabsorption of the fluorescence near the resonance energy, k_0 (radiation trapping). Initially, the windows were sealed to the cell body with thin teflon gaskets; however, it was found that the sodium vapor reacted with the teflon, releasing gases that reacted with the Na vapor and thereby reduced the fluorescence signal. The teflon gaskets were therefore replaced by commercially available silver-plated hollow-metal O rings, improving the performance. At the high rare gas densities used in the present experiment, even the small percentage of impurities introduced in the cell when noble gas was added was sufficient to temporarily decrease the sodium vapor density. The hollow metal O rings allowed the cell to be heated to $\sim 300^\circ\text{C}$, which was sufficient to overcome the impurity quenching of Na density. The cell could then be cooled to the experimental temperature of 180°C and sufficient vapor remained in the cell.

In previously reported experiments with sodium,^{9,10} a commercial Na lamp providing typically $100 \mu\text{W}/\text{cm}^2$ of resonance light was used to excite the vapor in the cell. However, at the noble gas pressures used in the present work, the absorption profile of the sodium vapor was shifted and broadened significantly compared to the unperturbed resonance energy. This resulted in an insufficient population of excited sodium atoms in the cell, especially when coupled with the problem of obtaining a reasonable Na vapor pressure. Therefore in order to obtain greater signals, the resonance lamp was replaced with a cw dye laser. Using rhodamine 6G dye solution, the laser was operated at an output power of $\sim 10 \text{ mW}$ with a beam diameter of $\sim 1 \text{ mm}$ at the cell and a spec-

tral width of $\sim 0.1 \text{ \AA}$, which was less than that of the pressure broadened absorption line. In addition to increasing the pump power and resulting signal levels, tuning the laser a few \AA into the wings of the absorption lines allowed the observation of the $\text{Na}(3^2P_{1/2,3/2})$ line center region without interference from instrumentally scattered laser radiation. (Complete radiative redistribution occurs at our [RG] since the collisionally broadened linewidths greatly exceed the natural width.) The fluorescence spectra were measured with a double grating monochromator, which allowed measurement of wing intensities as low as 10^{-8} of the resonance line intensity without leakage of the much stronger line fluorescence. The line wing intensities were measured with an instrumental resolution of $\sim 1.5 \text{ nm}$. In order to correct for any drift in the sodium vapor density or in dye laser frequency and power, the fluorescence in the far red wing of the resonance lines was monitored with a photomultiplier that viewed the cell through a $\lambda \sim 600 \text{ nm}$ transmitting filter (Fig. 3). The relative response of the apparatus as a function of wavelength was measured using light from a calibrated tungsten filament lamp reflected from a BaSO_4 surface in place of the cell. A weak fluorescence from the sapphire windows was present, but was $\sim 5\%$ of the fluorescence signal for all reported data.

The experiment measured a signal which, when corrected for the spectral sensitivity of the detection optics, we define as $S(k)$. This $S(k)$ is proportional to the intensity $I(k)$ of fluorescence per unit frequency interval (cm^{-1}). We use the notation $k = 1/\lambda$, $k_0 = 1/\lambda_0$, $\lambda_0 = 589.3 \text{ nm}$ is the wavelength midway between the D lines, and $\Delta k = k - k_0$. The results, both experimental and theoretical, are presented as a normalized intensity $I_N(k)$

$$I_N(k) = I(k)/[\text{RG}] \int_{-\infty}^{\infty} I(k)(k_0/k)^4 dk, \quad (1)$$

which as shown in Sec. III and the Appendix is the spontaneous emission intensity $I(k)$ per $[\text{Na}_\ddagger]$ and per $[\text{RG}]$, where $[\text{Na}_\ddagger]$ is the total density of $\text{Na}(3^2P_{1/2} + 3^2P_{3/2})$ in all bound and free forms. $I(k)$ appears in the numerator and denominator of (1), so we replace it with $S(k)$ to obtain $I_N(k)$ from the data. Since bound and free forms of NaXe_n for all n radiate in the same wavelength region it is not possible to normalize to any particular portion of the Na_\ddagger radiation (e.g., to free Na^*). Thus a normalization to the integrated emission, as in Eq. (1), is the only practical form. The minor $(k_0/k)^4$ factor is included to give the physical meaning noted above to $I_N(k)$.

Figures 2(a) and 2(b) show the measured $I_N(k)$ for sodium-xenon and sodium-krypton mixtures at several xenon and krypton densities. The 600–700 nm (600–680 nm) region is dominated by the $\text{NaXe}(\text{NaKr})A^2\Pi-X^2\Sigma$ emission bands, while the 720–800 nm (690–720 nm) region is predominately due to $\text{NaXe}_2(\text{NaKr}_2)$. The blue wing of the resonance lines (570–590 nm) is due to the $\text{NaXe}(\text{NaKr})B^2\Sigma-X^2\Sigma$ band. As noted above, the B -state potential was not determined by the measurements of Ref. 9, but from those measurements and from theoretical calculations,²¹ it is expected to be repulsive and produce the observed blue wing. The $I_N(k)$ measured for $[\text{RG}] = 2 \times 10^{19} \text{ cm}^{-3}$ is very similar in shape to that

previously reported from this laboratory,⁷ but it is about 20% (15%) weaker for sodium-xenon (sodium-krypton) for $\lambda \geq 620 \text{ nm}$. This discrepancy exceeds the combined uncertainties in the experiments by $\sim 5\%$; its cause has not yet been determined.

III. THEORY

A. Qualitative discussion

Before discussing the full theory and quantitative comparisons to the data, we will note some simple physical arguments which qualitatively explain the observations. Previous experimental work has shown that at a [RG] of 10^{19} cm^{-3} , the $A^2\Pi$ diatomic vibrational and rotational state distribution is very nearly in thermal equilibrium with the gas prior to emission.^{9,10} It is therefore appropriate to consider the equilibrium condition between the various NaRG_n^* excited state molecules when analyzing the spectra. The 600–800 nm regions in Figs. 2(a) and 2(b) are dominated by the diatomic $A-X$ bands and are relatively flat and featureless. As [RG] is increased the normalized intensity $I_N(k)$ in the diatomic bands decreases primarily due to depletion of free Na^* , where "free" means without an RG closer than $\sim 6 \text{ \AA}$. More specifically, if we consider only the dominant effect of binary Na-RG interactions, $[\text{Na}_\ddagger] \approx [\text{Na}^*] + [\text{NaRG}^*]$ with $[\text{NaRG}^*] = K_1[\text{Na}^*][\text{RG}]$ and K_1 is the equilibrium constant. Thus in the spectral region dominated by the diatomic $A-X$ band

$$\begin{aligned} I_N(k) &\propto \frac{I(k)}{[\text{RG}][\text{Na}_\ddagger]} \approx \frac{K_1[\text{Na}^*][\text{RG}]P_1(k)}{[\text{RG}][\text{Na}^*] + K_1[\text{Na}^*][\text{RG}]} \\ &= \frac{K_1 P_1(k)}{1 + K_1[\text{RG}]} . \end{aligned} \quad (2)$$

Here $P_1(k)$, with $\int P_1(k)dk = 1$, represents the normalized $\text{NaRG}^* \rightarrow \text{NaRG}$ intensity distribution due to free and bound NaRG^* molecules, K_1 refers to all Na^* -RG at separations less than a separation $R_0 \sim 6 \text{ \AA}$, and $[\text{Na}^*]$ refers to all $\text{Na}(3P)$ without any RG closer than R_0 . (As discussed in the Appendix, General Model section, this somewhat unusual definition of an equilibrium constant is necessary due to the indistinguishability of bound-and-free-state emission.) At small [RG], $K_1[\text{RG}] \ll 1$ and $I_N(k)$ is approximately independent of [RG]. At the largest [Xe] of these experiments $K_1[\text{Xe}] \sim 1$ so that $I_N(k)$ decreases by about a factor of 2. For the Kr case, $K_1[\text{Kr}] \sim 0.5$ at the highest [Kr]. This decrease in $I_N(k)$ is partly compensated for by $\text{Na}(\text{RG})_n^*$ radiation in the same spectral region.

Considering next the $\lambda > 720 \text{ nm}$ regions of Fig. 2, these are dominated by the $\text{Na}(\text{RG})_2$ excimer bands. Thus

$$\begin{aligned} I_N(k) &\propto \frac{I(k)}{[\text{RG}][\text{Na}_\ddagger]} \approx \frac{K_2[\text{Na}^*][\text{RG}]^2 P_2(k)}{[\text{RG}][\text{Na}^*] + K_1[\text{Na}^*][\text{RG}]} \\ &= \frac{K_2[\text{RG}]P_2(k)}{1 + K_1[\text{RG}]} , \end{aligned} \quad (3)$$

where K_2 and $P_2(k)$ refer to excited NaRG_2 with both RG at $R \leq 6 \text{ \AA}$. At small [RG] where $K_1[\text{RG}] \ll 1$ this $I_N(k)$ rises linearly with [RG]. At the higher [RG] this $\text{NaRG}_2^* \rightarrow \text{NaRG}_2$ intensity rises less rapidly than linearly, again

due to the decreasing number of free Na* (those without an RG atom within $\sim 6 \text{ \AA}$). The theory which follows explains these terms in more detail, gives more exact expressions, and allows quantitative comparisons to the data.

B. Theory for additive Na-RG pair interactions

As noted in Sec. III, A, we assume an equilibrated distribution of vibrational and rotational states within each NaXe_n^{*}, and equilibrium relations between the densities of different molecules. We will summarize here the results of the theory given in the Appendix. The normalized spectrum $I_N(k)$ is expressed as a sum of NaXe_n^{*} → NaXe_n band intensities in (A4), which we repeat here (with RG = Xe):

$$I_N(k) = \frac{(k/k_0)^4}{[\text{Xe}][\text{Na}^*]} \sum_{n=0}^{\infty} [\text{NaXe}_n^*] P_n(k), \quad (4)$$

where $P_n(k)$ is the normalized probability of NaXe_n^{*} emission at $k + dk$ and Na^{*}, defined by (A1), is the total concentration of excited Na^{*} in all bound and free forms. For additive Na^{*}-Xe and Na-Xe interactions and independent Xe atoms (no Xe-Xe interactions), Eq. (A11) yields

$$[\text{NaXe}_n^*] = [\text{Na}^*] e^{-K_1[\text{Xe}]} K_1^n [\text{Xe}]^n / n!, \quad (5)$$

where K_1 is the probability that any particular Xe atom may be inside a cutoff separation $R_0 \sim 6 \text{ \AA}$ (i.e., it is the NaXe^{*} equilibrium constant of the previous section). From the CFCP and the additive-pair-interaction assumption, the probability of NaXe_n^{*} → NaXe_n radiation at k is determined by the various Na^{*}-Xe pair separations R_i according to [see (A13) and (A17)]:

$$\Delta k \equiv \Delta k(R_1, \dots, R_n) = \sum_{i=1}^n \Delta k(R_i), \quad (6)$$

where $\Delta k(R_i) = k(R_i) - k_0$ is the frequency shift due to the i th pair interaction only, given by

$$\hbar c k(R_i) = V_j^*(R_i) - V(R_i), \quad (7)$$

with $V_j^*(R)$ the NaXe^{*} ($j = A^2\Pi$ or $B^2\Sigma$) potential and $V(R_i)$ the NaXe($X^2\Sigma$) potential (the form of the polyatomic potentials and the assumed scalar additivity will be discussed later). As in (A19) the probability of Δk in (6) is thus the product of single-perturber probabilities $P_1(\Delta k_i)$, or $P_1(R_i)$ with $R_i = R(\Delta k_i)$, integrated over all combinations of Δk_i that satisfy (6). Thus (A19) and (5) in (4) yield $I_N(k)$ predicted by this model:

$$I_N(\Delta k) = \left(\frac{k}{k_0} \right)^4 \frac{e^{-K_1[\text{Xe}]}}{[\text{Xe}]} \sum_{n=0}^{\infty} \frac{(K_1)^n [\text{Xe}]^n}{n!} \\ \times \int' dk_1 \cdots \int' dk_{n-1} P_1(\Delta k_1) \cdots P_1 \left(\Delta k - \sum_{i=1}^{n-1} \Delta k_i \right). \quad (8)$$

Since only perturbers at $R < R_0$ are included in (8), only Δk_i corresponding to $R < R_0$ are included in the integrals. This is indicated by the symbol $'$. Thus $\int' dk_i$ is from $k_i = -\infty$ to k_* and k_* to ∞ , where k_* and k_- are on either side of the resonance line and correspond to $k(R_0)$.

The equivalence of this molecular picture to the Poisson distribution is noted in the Appendix. Equation (8)

is a prescription for calculating $I_N(k)$ from known Na^{*}-Xe and Na-Xe interaction potentials, as these are used in (A8) and (A15) to calculate K_1 and $P_1(\Delta k_i)$. Some of these potentials are known in some R regions from Refs. 5 and 9; this information could be combined with calculated potentials²¹ to estimate the potentials at all R and then to evaluate (8). However, slight inaccuracies in these potentials would prevent the resulting $I_N(k)$ from agreeing with the measurements even at low [RG]. It is much more direct to express $P_1(\Delta k)$ and K_1 directly in terms of $I_N^0(k)$, the $I_N(k)$ measured at low [Xe], as is done in (A20) and (A22). Then $I_N(k)$ at all [Xe] is given in (A21) as:

$$I_N(k) = \frac{e^{-K_1[\text{Xe}]}}{[\text{Xe}]} \left\{ \delta(k - k_0) + [\text{Xe}] I_N^0(k) + \sum_{n=2}^{\infty} \frac{[\text{Xe}]^n}{n!} \right. \\ \left. \int' dk_1 \cdots \int' dk_{n-1} I_N^0(\Delta k_1) \cdots I_N^0 \left(\Delta k - \sum_{i=1}^{n-1} \Delta k_i \right) \right\}. \quad (9)$$

Here the first term is due to free Na^{*}, which in the model radiates at k_0 . The second, NaXe^{*} term $\exp(-K_1[\text{Xe}]) I_N^0(k)$ is the probability of finding one Xe atom at an $R < R_0$ that yields k , with all other Xe at $R > R_0$. Similarly the n th term is the probability of n Xe atoms at $R < R_0$ positions that yield a net shift Δk , with all other Xe at $R > R_0$. Note that the contribution of each NaXe_n^{*} spectrum is attenuated by the $\exp(-K_1[\text{Xe}])$ factor, which represents the depletion of free Na^{*}. The term $1 + K_1[\text{RG}]$ in the denominator of (2) and (3) is an approximation to this which corresponds to including only the depletion of [Na^{*}] due to [NaXe^{*}] and ignoring the depletion due to Na^{*}Xe_n, $n \geq 2$.

For comparison to the data and conceptual purposes it is convenient to re-express (8) as a power series in [Xe] by expanding $\exp(-K_1[\text{Xe}])$:

$$I_N(\Delta k) = \left(\frac{k}{k_0} \right)^4 \left\{ \frac{P_0(\Delta k)}{[\text{Xe}]} + K_1 P_1(\Delta k) + K_1^2 [\text{Xe}] [P_2(\Delta k)/2! \right. \\ \left. - P_1(\Delta k)] + K_1^3 [\text{Xe}]^2 [P_3(\Delta k)/3! - P_2(\Delta k)/2! \right. \\ \left. + P_1(\Delta k)/2!] + \dots \right\}. \quad (8')$$

The equivalent expansion of (9) is obtained by taking in (8) $P_0(\Delta k) = \delta(k - k_0)$, $P_1(\Delta k) = I_N^0(\Delta k)$, and $P_n(\Delta k)$ from (A19').

The size of the equilibrium constant K_1 , which is determined by R_0 or the integration cutoffs k_* , determines the relative magnitude of the terms in (8), (8'), and (9). As k_* and k_- are moved closer to k_0 , R_0 encompasses perturbers at larger internuclear separation and the relative magnitude of the higher order [Xe]ⁿ terms is increased. If all terms are included in the sum over n in (8) or (9), the resulting far wing intensities are almost independent of K_1 , but in the present work the $n \geq 2$ terms have not been calculated and are not included in our $I_N(k)$, i.e., only the NaXe and NaXe₂ spectra are included. The effect of changing K_1 or k_* and k_- in our calculation is shown in Figs. 4 and 5. It can be seen that changing K_1 does not significantly affect the calculated spectra in the diatomic emission band region. This results from the fact that the coefficient of the [Xe]

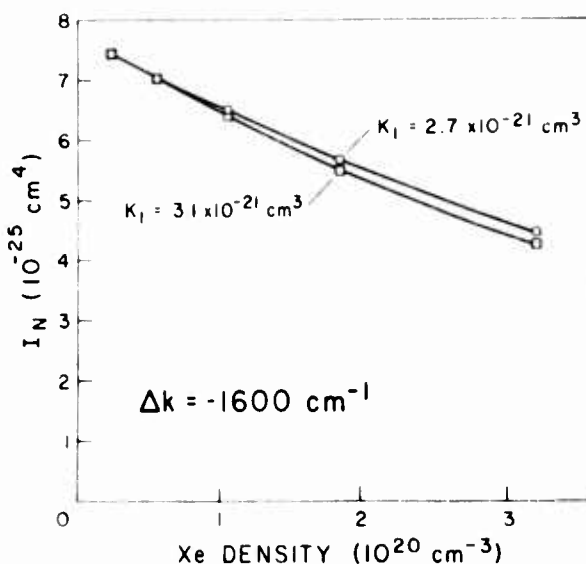


FIG. 4. The calculated normalized emission coefficient as a function of [Xe] at two values of K_1 in the spectral region where the diatomic emission dominates. The open circles are for $K_1 = 2.7 \times 10^{-21} \text{ cm}^3$, $k_+ = 72 \text{ cm}^{-1}$, and $k_- = 47 \text{ cm}^{-1}$; the open squares are for $K_1 = 3.1 \times 10^{-21} \text{ cm}^3$, $k_+ = 69 \text{ cm}^{-1}$, and $k_- = 34 \text{ cm}^{-1}$.

term in (8'), which is the most important term in this region of the spectra, is the difference of two terms which both increase as K_1 is increased. In the triatomic (NaXe_2) band region of large, negative Δk , the $P_1(\Delta k)$ terms in (8') are zero. Thus, as we have not included $P_3(\Delta k)$, our calculation reduces to

$$I_N(k) \approx \left(\frac{k}{k_0} \right)^4 \frac{K_1^3}{2!} \{ [\text{Xe}] P_2(\Delta k) - [\text{Xe}]^2 K_1 P_2(\Delta k) \}, \\ (\Delta k \ll 0). \quad (10)$$

Here $P_2(\Delta k)$ is independent of k_+ and k_- since these large

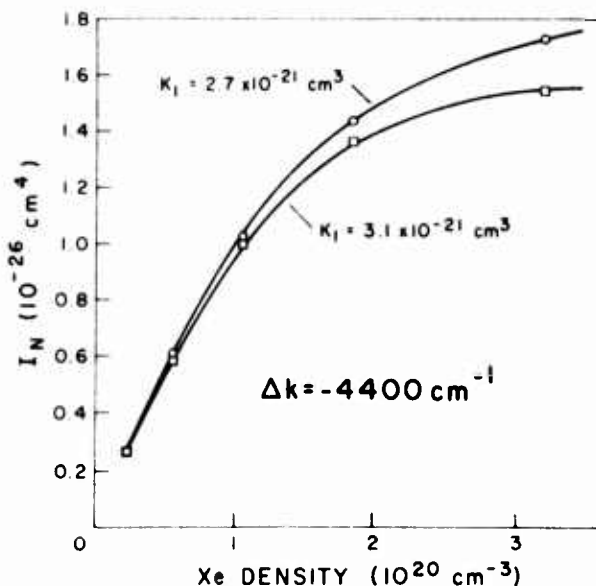


FIG. 5. The calculated normalized emission coefficient as a function of [Xe] at two values of K_1 (open circles and open squares same as Fig. 4) in the spectral region where the triatomic emission dominates.

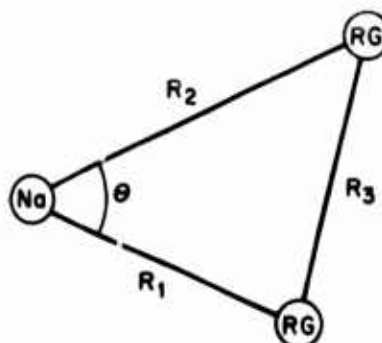


FIG. 6. Diagram of the NaRG_2 molecule useful in describing the additive potential.

$|\Delta k|$ only come from large $|\Delta k_1|$ and large $|\Delta k_2|$ = $|\Delta k - \Delta k_1|$ contributions to the integral in (9) or (A18'). In a more complete calculation the $1 - K_1[\text{Xe}]$ dependence on k_+ and k_- in (10) would be partly compensated by the inclusion of $P_3(\Delta k)$ and higher n terms, as these radiate partly in the region of the NaXe_2 band. Thus there is some ambiguity to the theoretical intensity in this Δk region. It should be noted that unusually large choices for $|k_+ - k_0|$ or $|k_- - k_0|$ (small K_1 and R_0) would minimize the effect of these $n \geq 3$ terms, but it also can distort the predicted spectra, since perturbers at internuclear separations larger than R_0 would then cause a significant Δk_i , although in the model these contributions to the total Δk are ignored.

C. Interactions between perturbers

In the above derivation of $P_2(\Delta k)$, the interaction $V_3(R)$ between perturbers was ignored. However, the Na-RG separation at the minimum of the $A^2\Pi$ potential well, where the diatomic radiation is strong, is $\sim 3.3 \text{ \AA}$, while the RG-RG interaction becomes strongly repulsive at $\sim 3 \text{ \AA}$. Thus we expect considerable effects due to the RG-RG interactions. This effect could be included as an additional $\exp(-V_3/kT)$ Boltzmann factor in the integrand of the $n=2$ term of (8), where the Na^* -RG Boltzmann factors are already included in the $P_1(\Delta k_1)$ and $P_1(\Delta k_2)$. However, as kT considerably exceeds the RG-RG van der Waals binding energy, we will approximate the RG-RG interaction as a hard-sphere repulsion. This is then included in the calculation of $P_2(k)$ by requiring that the noble gas-noble gas separation (R_3) in Fig. 6 must be greater than the hard sphere radius R_h which has been estimated from noble gas dimer ground state potential curves previously derived from experimental data.^{22,23} Since the Na-RG separations $R_1(\Delta k_1)$ and $R_2(\Delta k_2)$ (see Fig. 6) can be determined using the potential curves of York *et al.*,⁹ the minimum angle $\theta_m(R_1, R_2)$ or $\theta_m(\Delta k_1, \Delta k_2)$ which yields $R_3 \geq R_h$ for $\theta \geq \theta_m$ can be calculated from the law of cosines

$$\cos \theta_m = \frac{R_1^2 + R_2^2 - R_h^2}{2R_1R_2}. \quad (11)$$

If the expression on the right is ≥ 1 , then $|R_1 - R_2| > R_h$ and θ_m is zero; if the expression is ≤ -1 , then $|R_1 + R_2| < R_h$ and θ_m is 180° .

The ratio F of the available volume to the volume for

$R_h = 0$, for the R_1 , R_2 combination, can be shown to be given by

$$F = \frac{1}{2}(1 + \cos\theta_m) , \quad (12)$$

and the integrand of the $n=2$ term in (8) or (9) can be multiplied by this fraction. This correction is significant only for large negative Δk , where both R_1 and R_2 are near or less than the $A^2\Pi$ potential minimum (~ 3 Å). This correction also changes $K_n(n \geq 2)$ in (A7), but this is a minor correction and has been ignored.

The appropriate value for R_h can be reasonably bracketed between two extremes, assuming the Xe-Xe interaction potentials of Refs. 14 and 15 are correct. An upper limit of $R_h = 3.7$ Å can be obtained from the condition $V(R_h) = 2kT$, since the Boltzmann density factor $\exp[-V(R)/kT]$ is very small at smaller separations. A lower limit of 2.8 Å is obtained if one attempts to roughly include the effect of the van der Waals attraction in the 4–6 Å region of separation, which increases the number of Xe pairs in this range of separation. This value of R_h comes from equating the excluded area under the hard-sphere Boltzmann density factor to that under the actual $V(R)$.

$$\int_{R_h}^{R_L} d^3R = \int_0^{R_L} e^{-V(R)/kT} d^3R , \quad (13)$$

where R_L is some large value of R such that $V(R_L) \approx 0$.

D. Statistical weights of the triatomic molecules

The triatomic molecular "states" resulting from the additive potential model may be thought of as the sum of two Na^*-RG diatomic states; each of these diatomic states may be a Σ or Π state. Since the Σ state emits only in the blue wing of the $I_N^0(k)$ spectrum and the Π state emits only in the red wing, the $n=2$ integral in (9) can be divided into four different contributions: (1) when both Δk_1 and $\Delta k - \Delta k_1$ are in the red wing, both $V_j(R_1)$ and $V_j(R_2)$ are $j=A^2\Pi$ potentials; (2) when Δk_1 is in the red wing and $\Delta k - k_1$ is in the blue wing, $V_j(k_1)$ is an $A^2\Pi$ potential and $V_j(R_2)$ is a $B^2\Sigma$ potential; (3) $V_j(R_2)$ is an $A^2\Pi$ potential and $V_j(R_1)$ is a $B^2\Sigma$ potential; and (4) $V_j(R_1)$ and $V_j(R_2)$ are $B^2\Sigma$ potentials. These combinations may be interpreted as four "states" of the triatomic molecule. The $I_N^0(k)$ obtained from the low-pressure spectrum contain intrinsically a statistical weight ratio g_i/g_f [see (A9)] where g_i is the statistical weight of excited molecular states and g_f is the statistical weight of the adiabatically connected atomic states. In the present case $g_i = 6$; $g_i = 4$ for the $A^2\Pi_{1/2}$ and $A^2\Pi_{3/2}$ diatomic states responsible for the diatomic red wing, while $g_i = 2$ for the $B^2\Sigma$ diatomic state. The four possible combinations of diatomic states listed above yield effective statistical weight ratios g'_i/g_f for the triatomic states, from $P_2(k)$, given by the product of the g_i/g_f values for each pair of diatomic states: (1) for the $\Pi + \Pi$ state $g'_i/g_f = (2/3)(2/3) = 4/9$; (2) for the $\Pi + \Sigma$ state $g'_i/g_f = (2/3)(1/3) = 2/9$; (3) for the $\Sigma + \Pi$ state $g'_i/g_f = 2/9$; and (4) for the $\Sigma + \Sigma$ state $g'_i/g_f = 1/9$. It is clear that these statistical weight ratios are unrealistic, since the statistical weight of the separated atoms, g_f , is 6 and the statistical weights g_i of the triatomic molecular states must be given by an integer.

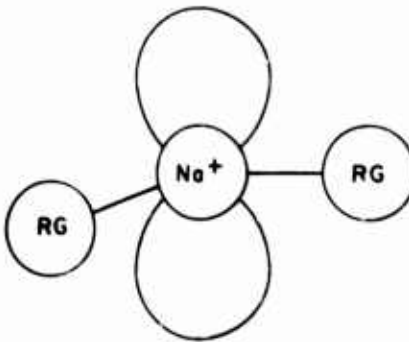


FIG. 7. Electron density distribution of the 2B_1 state of NaRG_2 for an arbitrary angle between RG atoms (using t^+ convention as in Ref. 24).

Building up the triatomic molecule from the separated atomic states, neglecting the $\text{Na}(3P)$ fine structure, yields only three states, ${}^{24}{}^2A_1$, 2B_1 , and 2B_2 , which have statistical weights of 2; thus for each of the three triatomic states, $g'_i/g_f = 1/3$.

The electron configuration of the $\Pi - \Pi$ additive potential state is shown in Fig. 7. Since the alkali electron is perpendicular to the plane of $\text{Xe}-\text{Na}^*-\text{Xe}$, it has simultaneous Π character for both Na^*-Xe interactions. This configuration has the same symmetry as the 2B_1 state and the resulting $V^*(R_1, R_2, R_3)$ should be similar to that of the 2B_1 state. Thus the statistical factor 4/9 from the additive-potential model should more appropriately be 1/3. The other two additive-potential model combinations ($\Pi - \Sigma$ and $\Sigma - \Sigma$) have no corresponding symmetry relations to the correct 2A_1 and 2B_2 states; and doubtless give poor representations of $V^*(R_1, R_2, R_3)$. As they only contribute NaXe_2 intensity in the spectral region dominated by NaXe radiation, the inaccuracy of the resulting predictions for $I_N(k)$ are not noticeable. It is not known if the actual 2A_1 or 2B_2 states contribute significantly to $I_N(k)$ in the triatomic ($\lambda > 720$ nm) region, but it appears unlikely based on electron-orbital pictures.

IV. COMPARISONS

Equation (9), up to and including $n=2$ terms, has been evaluated for a number of Kr and Xe densities, using $I_N^0(k) = I_N(k)$ for $[\text{RG}] = 2 \times 10^{19} \text{ cm}^{-3}$. For Xe values of $k_s = k_0 + 70 \text{ cm}^{-1}$, $k_a = k_0 - 50 \text{ cm}^{-1}$ were used, from which $K_1 = 2.7 \times 10^{-21} \text{ cm}^3$ and for Kr $k_s = k_0 + 60 \text{ cm}^{-1}$, $k_a = k_0 - 30 \text{ cm}^{-1}$ and $K_1 = 1.7 \times 10^{-21} \text{ cm}^3$. The choice of k_s and k_a is somewhat arbitrary, however as discussed above values too far from k_0 can distort the polyatomic molecular spectra leading to erroneous values for $I_N(k)$, and values too near k_0 lead to a slow convergence of Eq. (9). These calculated $I_N(k)$ are given in Figs. 8(a) and 8(b); it can be seen that they are quite similar to the measured $I_N(k)$ in Fig. 2. In Figs. 9 and 10 the measured and calculated $I_N(k)$ are plotted against noble gas density at a single k . In Fig. 9, the k values are near the center of the diatomic band region. The good agreement is characteristic of all k values in this region. As discussed in the theory section, the major pressure dependence here is the decrease in the normalized inten-

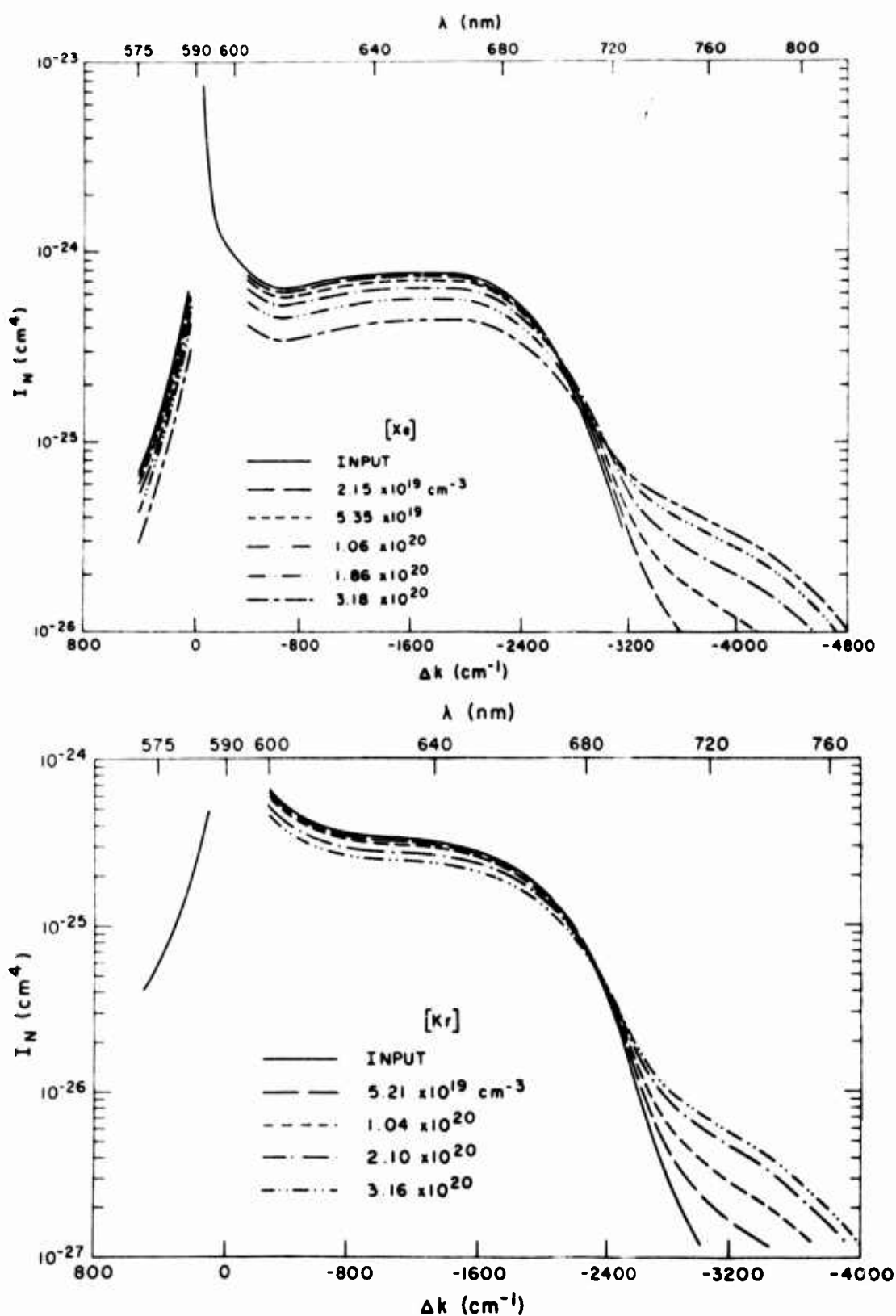


FIG. 8. The calculated normalized emission as a function of Δk at several rare gas densities for (a) sodium-xenon, $K_1 = 2.7 \times 10^{-21} \text{ cm}^3$, $R_h = 2.8 \text{ \AA}$, and (b) sodium-krypton, $K_1 = 1.7 \times 10^{-21} \text{ cm}^3$, $R_h = 3.0 \text{ \AA}$. The curves labeled "Input" are the binary spectrum, $I_N^0(k)$ of Eq. (9).

sity due to the decreasing $[\text{Na}^+]$. In this region of the spectrum, the calculation is not strongly dependent on the assumptions made concerning: (1) the transition probability $A(k)$, and (2) the potential surfaces $V^*(R_1,$

$R_2, R_3)$ and $V_2(R_1, R_2, R_3)$. In addition the three-body term, which represent about 20% of the total $I_N(k)$ in this wavelength region at $[\text{Xe}] = 2 \times 10^{20} \text{ cm}^{-3}$, results mostly from one xenon atom near the potential minimum

of the $A^2\Pi$ state and the other xenon atom at a much larger distance from the excited sodium atom. In such a configuration, the additive potential might be expected to be a good approximation for the triatomic molecule.

At $\lambda \sim 680$ nm for Kr and 700 nm for Xe, the diatomic spectrum drops quickly, and at perturber densities of $\sim 10^{20} \text{ cm}^{-3}$, the triatomic emission bands dominate. Figure 10 shows the results (labeled initial calculation) for both Na-Xe and Na-Kr in this k region. The emission in this $\lambda \sim 700$ nm region is due, for the most part, to the excited triatomic molecules in a configuration such that both perturber atoms are relatively close to the excited sodium atom, and the additive potential is not expected to be reliable under these conditions. Thus the discrepancies between the calculated and observed intensities are not surprising.

As noted in Sec. III.D, a possible correction to the calculated intensity in the triatomic emission band region results from the fact that the additive potential model leads to a $^2\Pi - ^2\Pi$ or 2B_1 -state contribution of incorrect statistical weight. The dashed line in Fig. 10 is the original calculation multiplied by 3/4 to allow for such a change in statistical weight. This improves the fit to the Na-Xe data, although the calculation is still somewhat higher than the data. In the case of Na-Kr, the statistical-weight corrected results in Fig. 10 are in better agreement with the experimental I_N at the lower densities studied; however the data increase linearly with density, whereas the calculated density dependence shows negative curvature. This curvature, also observable in the Na-Xe calculated curves in Fig. 10, is due to the $\exp(-K_1[Xe])$ factor in Eq. (16). Inclusion of higher order terms (NaXe_n with $n > 2$), which have been left out of the calculation, may be important in this region of

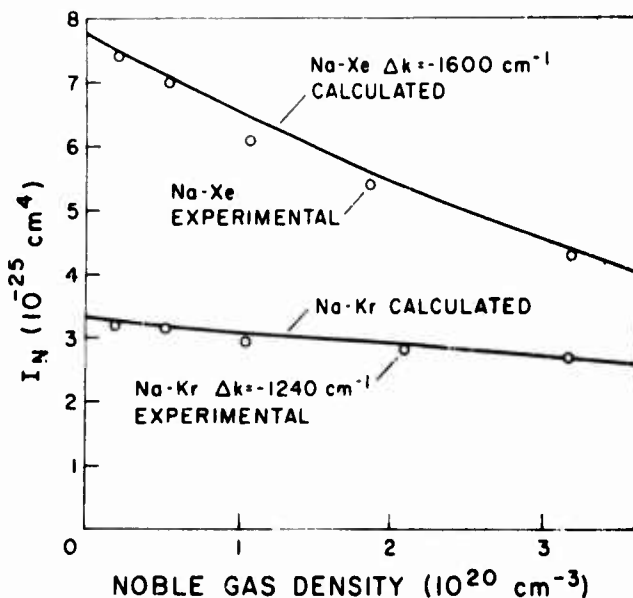


FIG. 9. The calculated and measured normalized emission as a function of rare gas density in a spectral region where the diatomic emission dominates. The upper curve and experimental points are for sodium-xenon at $\Delta k = -1600 \text{ cm}^{-1}$ and the lower curve and points are for sodium-krypton at $\Delta k = -1240 \text{ cm}^{-1}$. K_1 and R_h have the same value as in Fig. 8.

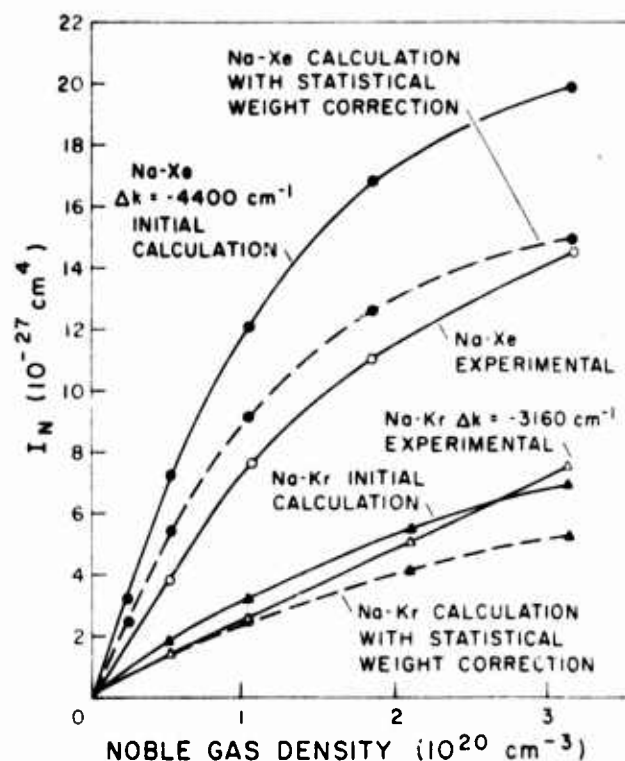


FIG. 10. The calculated and measured normalized emission as a function of rare gas density in a spectral region where the triatomic emission dominates. The upper curves and points are for sodium-xenon at $\Delta k = -4400 \text{ cm}^{-1}$ and the lower curves and points are for sodium-krypton at $\Delta k = -3160 \text{ cm}^{-1}$. The solid curves are as initially calculated and the dashed curves included the statistical weight correction (i.e., $\pm 3/4$). K_1 and R_h have the same values as in Fig. 8.

the spectra at densities above 10^{20} cm^{-3} . These terms would increase the calculated $I_N(k)$ at densities $\gtrsim 10^{20} \text{ cm}^{-3}$, and therefore decrease the negative curvature of the lines in Fig. 10.

The effects of the rare gas-rare gas interaction on the calculated spectra are shown in Figs. 11 and 12. In

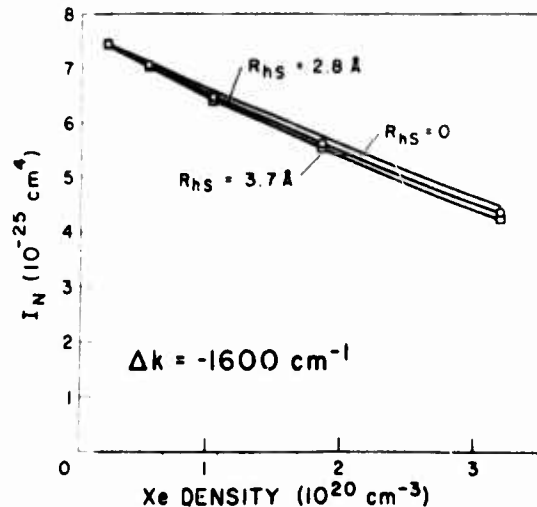
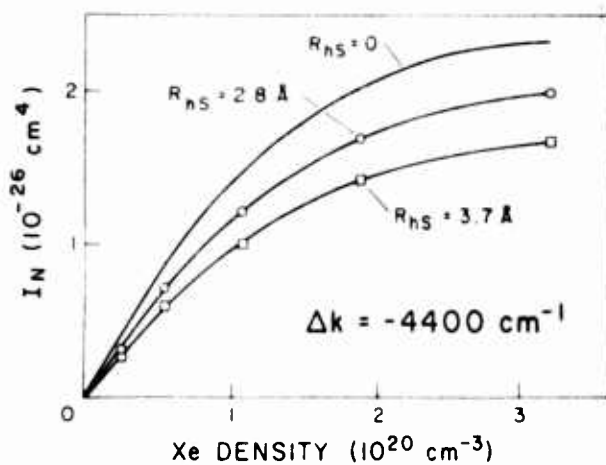
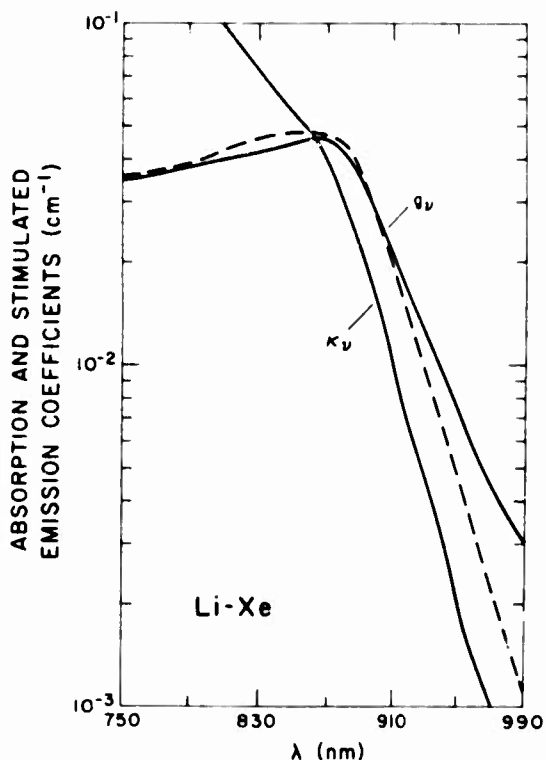
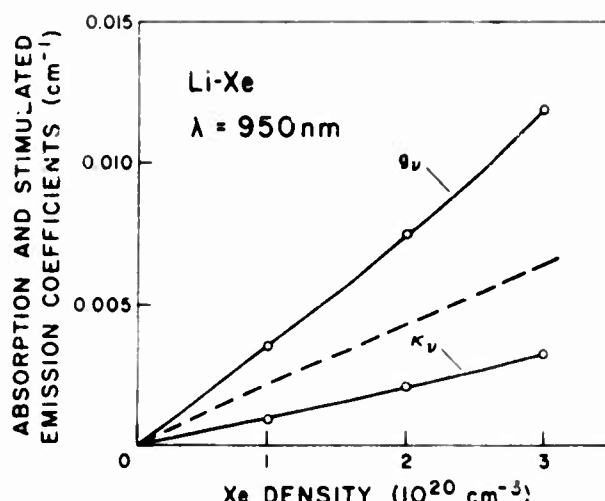


FIG. 11. The calculated normalized emission as a function of xenon density at two xenon-xenon hard sphere radii, $R_h = 2.8$ and 3.7 \AA , at $\Delta k = -1600 \text{ cm}^{-1}$. $K_1 = 2.7 \times 10^{-21} \text{ cm}^3$.

FIG. 12. Same as Fig. 11 at $\Delta k = -4400 \text{ cm}^{-1}$.

each figure, the normalized intensity I_N is plotted for $R_h = 0$ and for the two hard-sphere radii from Sec. III.C: $R_h = 2.8 \text{ \AA}$, which is the value that attempts to include the effect of the van der Waals attractions between Xe atoms, and $R_h = 3.7 \text{ \AA}$, which is simply a separation inside of which the two Xe atoms rarely penetrate. In the wavelength region around $\lambda = 1600 \text{ cm}^{-1}$ the NaXe* spectra dominate, so that the calculated spectra are not strongly dependent on the $P_2(k)$ terms in (8') that depend on R_h ; thus the R_h term has only a small effect in Fig. 11. However, at $\Delta k = -4400 \text{ cm}^{-1}$ the NaXe₂ terms dominate, as given by (10). Therefore, as seen in Fig. 12, these calculated spectra are more sensitive to the rare gas-rare gas interaction.

FIG. 13. The calculated absorption K_ν and stimulated emission g_ν coefficients for lithium-xenon as a function of wavelength at $[\text{Li}] = 10^{17} \text{ cm}^{-3}$, $[\text{Xe}] = 2 \times 10^{20} \text{ cm}^{-3}$, and $[\text{Li}^+]/[\text{Li}] = 0.05$. The dashed line is obtained for g_ν if multiple-perturber interactions are ignored.FIG. 14. The calculated absorption K_ν and stimulated emission g_ν coefficients for lithium-xenon as a function of [Xe] at $\lambda = 950 \text{ nm}$. The dashed line is obtained for g_ν if multiple perturber interactions are ignored.

V. ABSORPTION AND STIMULATED EMISSION COEFFICIENTS

The additive potential model yields results of sufficient accuracy to be useful in predicting absorption and stimulated emission coefficients for other gases, for which only low [RG] spectra are available. For example, conditions proposed for high power operation of the lithium-xenon excimer laser system^{25,26} are a lithium density [Li] of 10^{17} cm^{-3} at a temperature of 1180 K, a lithium excitation fraction of $[\text{Li}^+] = 0.05[\text{Li}]$ and a xenon density of $2 \times 10^{20} \text{ cm}^{-3}$. The normalized emission coefficient $I_N(k)$ has not been measured at such high pressure conditions, but an estimate, including polyatomic interactions, would be of interest. Previous data by Scheps *et al.*⁸ taken at a lower temperature of 670 K may be used to determine $I_N^0(k)$ at 1180 K at xenon densities of $\sim 10^{19} \text{ cm}^3$. From Eqs. (A15) and (A20) it can be shown that

$$I_N^0(k)_T = I_N^0(k)_{T_e} \exp[(\beta_e - \beta) \Delta V^*(k)], \quad (14)$$

where $I_N^0(k)_{T_e}$ denotes the measured $I_N^0(k)$, defined in (9), at the experimental temperature T_e , $\beta^{-1} = kT$, and $\Delta V^*(k)$ is the LiXe excited state potential at internuclear separation $R(k)$. Using (9) this LiXe $I_N^0(k)_T$ may then be used to calculate the complete $I_N(k)$ including multi-body interactions at the larger Xe densities of interest for high-power excimer lasers. As shown in Refs. 8 and 25 the absorption coefficient K_ν and the stimulated emission coefficient g_ν are given in terms of $I_N(k)$ by

$$K_\nu = I_N(k) [\text{Xe}] [\text{Li}] [8\pi k^2 c]^{-1} \frac{A_0 k_0}{k} \frac{g_0}{g} \exp[+\beta h c \Delta k], \quad (15)$$

and

$$g_\nu = I_N(k) [\text{Xe}] [\text{Li}^*] [8\pi k^2 c]^{-1} \frac{A_0 k_0}{k}, \quad (16)$$

where c is the speed of light and A_0 is the unperturbed atomic transition rate. Calculations of K_ν and g_ν as a function of wavelength for the given conditions are shown in Fig. 13, while Fig. 14 shows these coefficients

as functions of Xe density at $\lambda = 950$ nm. More detailed discussions of the potential behavior of this medium can be found in Refs. 25 and 26. Equations (15) and (16) can also be directly applied to the $I_N(k)$ measured at high densities; however, the temperature correction given by Eq. (14) applies only to equilibrated diatomic spectra, typically that measured at densities near 10^{19} cm $^{-3}$; the high density data cannot easily be corrected for changes in temperature.

VI. CONCLUSIONS

The additive potential model for multiple-perturber interactions or polyatomic molecules, which is used in many situations involving a high density of weakly-bound particles, has been shown to give a simple and useful picture of the extreme wing of the press re-broadened sodium D lines at rare gas densities in the range of 10^{20} cm $^{-3}$. When this model of the molecular interactions is used with the quasistatic line broadening theory, as discussed previously in the literature,¹⁵⁻²⁰ the measured pressure dependence of the normalized fluorescence intensity can be given a simple interpretation. Overall, a respectable quantitative agreement is obtained between the predictions of this simple model and the measurements, particularly when RG-RG interactions are included.

This model has been extended here by the addition of two corrections. (This level of detail appears justified here since this is the first quantitative intensity data for a range of perturber densities that include both low and high density.) The interaction between the rare gas perturber atoms has been approximated as a hard-sphere potential and included in the model. Possible scaling corrections due to the statistical weights of the triatomic molecular states have been included in the wavelength region dominated by triatomic emission.

Discrepancies between the calculated and measured $I_N(k)$ do however indicate the inadequacy of the simple model in predicting accurate quantitative results. The inadequacy is twofold: (1) the scalarly additive potential is an inadequate representation of these polyatomic molecules; it not only leads to states of unrealistic statistical weights, but the additivity is severely questionable when more than one perturber is close to the excited sodium atom; and (2) as the perturber density is increased beyond 10^{20} cm $^{-3}$, the effects of NaXe $_n$ molecules with $n \geq 3$ become significant. These effects are not included in the present calculations as they are more difficult to calculate; even when the additive potential is assumed for the molecules the integrals become somewhat cumbersome.

ACKNOWLEDGMENTS

We wish to thank Richard Scheps for assistance with the design and construction of the apparatus, Chela Kunasz for assistance with the computations, and W. E. Baylis and J. Cooper for helpful discussions.

APPENDIX: THEORY OF $I_N(k)$ PRESSURE DEPENDENCE

General model

The total density of excited-state species [Na $_{\gamma}^*$] (associated with the Na*(3P) configuration) is given by

$$[\text{Na}_{\gamma}^*] = [\text{Na}^*] + [\text{NaXe}^*] + [\text{NaXe}_2^*] + \dots \\ = \sum_{n=0}^{\infty} [\text{NaXe}_n^*]. \quad (\text{A1})$$

where [Na *] is the density of free excited sodium atoms, [NaXe *] the density of excited diatomic molecules, etc. If each excited molecular species NaXe $_n^*$, with a thermal population distribution, emits an intensity $s_n(k)$ in $k - k + dk$ then from (A1) the total intensity emitted per unit volume [$I(k)$] is

$$[I(k)] = \sum_{n=0}^{\infty} [\text{NaXe}_n^*] s_n(k). \quad (\text{A2})$$

The intensity $s_n(k)$ of NaXe $_n^*$ emission at k is the product of hck time the spontaneous emission rate $\Gamma_n(k)$ times the probability $P_n(k)$ of being in a configuration that emits at k . [$P_n(k)$ includes branching ratios from a single state and $\int P_n(k) dk = 1$.] Then if the transition moment is constant, $\Gamma_n(k) = \Gamma_0(k/k_0)^3$,

$$s_n(k) = hck_0 \Gamma_0(k/k_0)^3 P_n(k). \quad (\text{A3})$$

From (1), (A1), (A2), and (A3)

$$I_N(k) = \frac{\sum_{n=0}^{\infty} [\text{NaXe}_n^*] s_n(k)}{[\text{Xe}] \sum_{n=0}^{\infty} [\text{NaXe}_n^*] / s_n(k) (k_0/k)^4 dk} \\ = \frac{(k/k_0)^4}{[\text{Xe}] [\text{Na}_{\gamma}^*]} \sum_{n=0}^{\infty} [\text{NaXe}_n^*] P_n(k), \quad (\text{A4})$$

and

$$[\text{Na}_{\gamma}^*] = \int I(k) (k_0/k)^4 dk. \quad (\text{A4}')$$

Equation (A4') results from the assumed constant dipole transition moment, and applies to all bound-bound, bound-free, and free-free radiation, i.e., its validity is not limited by that of the classical Franck-Condon principle used here to obtain it.

The traditional meaning of NaXe $_n^*$ is a bound molecule, that of Na * is a free atom, and the equilibrium constant K_n normally refers to equilibrium for the reaction NaXe $_{n-1}^*$ + 2Xe \rightleftharpoons NaXe $_n^*$ + Xe between bound molecules. In the present problem the bound NaXe $_n^*$ radiate a continuum plus a large number of closely-spaced lines that are observed as part of the total continuum, i.e., the bound-molecule emission is not distinguishable. Furthermore, according to the CFCF the frequency radiated by the Na * - Na transition only depends on the distances R_i between the Na * atom and all Xe atoms; it does not matter if any or all of these Xe are bound to the Na * atom. Consequently, we define a "molecule" in terms of the distances R between the Na * and the individual Xe atoms: All Xe at $R < R_0$ from a Na * are considered part of a NaXe $_n^*$ "molecule" and all at $R > R_0$ are free atoms. Thus a NaXe $_n^*$ "molecule" has n Xe atoms inside R_0 , any number of which may be bound or free. The NaXe $_n^*$ spontaneous emission spectrum then refers to the Na *

— Na transition in the presence of n Xe atoms at $R < R_0$. Since the spectrum will be described in terms of the sum of these NaXe_n^* — NaXe_{n-1}^* spectra and Xe atoms at $R > R_0$ are not included in the "molecule," this model ignores the energy shift due to all Xe at $R > R_0$. That this ignored energy shift is bounded and small results from the fact that for large R the perturbation energy due to a single Xe atom varies as R^{-6} while the number of Xe at $R = R + 1/R$ is proportional to R^2 and their interactions are roughly additive.

The separation R_0 is chosen to be a distance which produces a significant shift in the $\text{Na}^* - \text{Na}$ transition frequency. In the present problem we are concerned with total frequency shifts of $100 - 3200 \text{ cm}^{-1}$, due primarily to one or two RG atoms near the Na^* . Thus R_0 is typically chosen to correspond to a frequency shift $\sim 50 \text{ cm}^{-1}$. (This choice very well satisfies the condition given by Royer,¹⁷ that R_0 must be less than the Weisskopf radius.) Note that once the free states are included in the "molecule," for any $[\text{Xe}]$ the density of molecules of each NaXe_n^* form depends on the choice of R_0 . In order to minimize the computational effort we would like to use a small R_0 so that the NaXe_n^* with small n values predominate and only their spectra need be considered. If R_0 is too small, however, significant perturbations by other Xe atoms are incorrectly ignored. A second criteria for validity of this model is the validity of the CFCP. At large R , or small frequency shifts, the CFCP breaks down due to: (1) non-adiabatic mixing of nearly-degenerate adiabatic states by the finite interatomic velocity; and (2) impact broadening effects. This is not considered a serious problem at the R_0 chosen for analysis of the present very large frequency shifts.

Royer¹⁷ has shown that the effects of the long-range interactions can be included by convoluting the calculated wing shape with the line core intensity distribution, $I_c(k)$, where $I_c(k)$ is normalized such that $\int I_c(k) dk = 1$. This additional convolution has the effect of broadening and shifting any sharp features in the wing just as the line core is broadened and shifted from the unperturbed resonance line. However, there are no such features in the present spectra; this additional broadening has a negligible effect and is neglected here.

Additive pair-potential model with independent perturbers

In this model we assume that the adiabatic molecular potential energy $V(R_1, \dots, R_N)$ is the sum of Na^* -Xe or Na-Xe pair interaction energies $\Delta V(R_i) = V(R_i) - V(\infty)$. For the triatomic case in Fig. 6 this becomes:

$$\begin{aligned} V(R_1, R_2, R_3) &= \Delta V(R_1) + \Delta V(R_2) + \Delta V(R_3) + V^{*(\alpha, \alpha, \alpha)}, \\ V^{*(R_1, R_2, R_3)}_{j_1 j_2} &= \Delta V^{*(R_1)}_{j_1} + \Delta V^{*(R_2)}_{j_2} \\ &\quad + \Delta V^{*(R_3)} + V^{*(\alpha, \alpha, \alpha)}, \end{aligned} \quad (\text{A5})$$

where the subscripts $j_i = 1$ or 2 on $V^*(R)$ indicate that each Na^* -RG pair may interact on one of two different potentials ($A^2\Pi$ or $B^2\Sigma$). For later use, we have included the RG-RG interaction $\Delta V(R_3)$ in (A5). However, as in the normal applications of this model,⁹⁻¹⁶ we as-

sume in this section that the RG atoms act independently; this is equivalent to taking $\Delta V(R_3) = 0$ in (A5).

As noted in the text, we have assumed an equilibrium distribution of vibrational and rotation states, and that $[\text{NaXe}_{n+1}^*]$ and $[\text{NaXe}_n^*]$ are in equilibrium, so that

$$\frac{[\text{NaXe}_n^*]}{[\text{NaXe}_{n-1}^*]} = K_n [\text{Xe}], \quad (\text{A6})$$

where

$$K_n = \frac{Z_n}{Z_{n-1}} = \frac{(1/n!) Z_1(R_1) Z_1(R_2) \cdots Z_1(R_n)}{[1/(n-1)!] Z_1(R_1) Z_1(R_2) \cdots Z_1(R_{n-1})} = \frac{K_1}{n}. \quad (\text{A7})$$

Here Z_n is the total partition function for NaXe_n^* , $Z_1(R_i)$ is that for the i th Na^* -Xe pair, and $Z_1(R_i) = K_1$, the diatomic NaXe^* equilibrium constant. Equation (A7) follows from the assumption that each Na^* -Xe interaction is independent and equal to that for diatomic NaXe^* . In a normal bound-molecule picture

$$K_1 = \sum_{J, v', J'} (g_J/g_a) g_{J'} \exp\{-\beta E(v', J', j)\}$$

refers to a sum over the bound states v' , J' , and adiabatic states j , with $\beta = 1/kT$, and g_J and g_a are the statistical weights of the molecular adiabatic states and the adiabatically connected atomic states, respectively. In the present case where a NaXe_n^* "molecule" has n Xe atoms at $R > R_0$ from the Na^* , we can use the classical phase-space integral⁶:

$$K_1 = \sum_j \frac{g_J}{g_a} \int_0^{R_0} d^3 R \exp\{-\beta \Delta V_j^*(R)\}. \quad (\text{A8})$$

This particularly simple form holds since the $d^3 P$ portion of the phase-space integral extends over nuclear momentum $P = 0$ to ∞ to include all bound and free states at each $R < R_0$. This yields⁶ the normalized probability $P_1(R)$ of separation R :

$$\begin{aligned} P_1(R) d^3 R &= \sum_j P_1(R_j) d^3 R \\ &= \sum_j \frac{g_J}{g_a} \frac{d^3 R}{K_1} \exp\{-\beta \Delta V_j^*(R)\}, \end{aligned} \quad (\text{A9})$$

which has been integrated in (A8) to yield K_1 . From (A1), (A6), and (A7):

$$[\text{Na}_n^*] = [\text{Na}^*] \left\{ 1 + \sum_{n=1}^{\infty} \frac{1}{n!} K_1^n [\text{Xe}]^n \right\} = [\text{Na}^*] e^{K_1 [\text{Xe}]}. \quad (\text{A10})$$

Comparing (A1) and (A10):

$$[\text{NaXe}_n^*] = [\text{Na}^*] \frac{K_1^n [\text{Xe}]^n}{n!} = [\text{Na}_n^*] e^{-K_1 [\text{Xe}]} \frac{K_1^n [\text{Xe}]^n}{n!}. \quad (\text{A11})$$

To summarize, from (A4) and (A11) the normalized emission spectrum becomes

$$I_N(k) = \left(\frac{k}{k_0} \right)^4 \frac{e^{-K_1 [\text{Xe}]}}{[\text{Xe}]} \sum_{n=0}^{\infty} \frac{(K_1)^n [\text{Xe}]^n}{n!} P_n(k). \quad (\text{A12})$$

Note that $K_1 [\text{Xe}]$ is the average number of Xe atoms inside R_0 and according to the Poisson distribution $\exp(-K_1 [\text{Xe}]) K_1^n [\text{Xe}]^n / n!$ is the probability of n and only n Xe atoms inside R_0 . The normalized spectrum

$(k/k_0)^4 P_n(k)$ due to these n Xe atoms will be given below in terms of the product $P_1(R_1)P_1(R_2)\dots P_1(R_n)/n!$ of single particle probabilities $P_1(R_i)$ of finding each i th atom at separation R_i . Thus the entire result, which we have derived in terms of molecular densities, is identical to the Poisson distribution of independent-particle probabilities (see also Ref. 17).

We now utilize the CFCP to evaluate the $s_n(k)$ or $P_n(k)$ corresponding to this model. $s_0(k)$ or $P_0(k)$ refers to the "free" Na radiation, so that $P_0(k) = \delta(k - k_0)$ may be considered a δ function. As the model will only be applied at $k \neq k_0$, this term in (A17) will normally be zero. To evaluate $P_1(k)$, note that the CFCP predicts the internuclear kinetic energy and separation do not change during an electronic transition; thus the photon energy radiated by a diatomic molecule at separation R in state j is given by

$$\hbar c k = V_j^*(R) - V(R) . \quad (\text{A13})$$

This defines the relation $k(R)$, or $R(k)_j$, and the probability of emitting $k - k + \Delta k$ is then given by the probability $P_1(R)_j$ of being in adiabatic state j with separation $R + \Delta R$. In order to express $P_1(R)_j$ in (A9) as $P_1(k)_j$, (A13) yields $R(k)$, and $d^3 R(k)_j = [d^3 R(k)_j/dk] dk$. Thus

$$P_1(k) = \sum_j P_1[R(k)_j] [d^3 R(k)_j/dk] , \quad (\text{A14})$$

and combining (A14) and (A9)

$$P_1(k) = \sum_j \frac{g_j}{g_n K_1} \frac{d^3 R(k)_j}{dk} \exp\{-\beta \Delta V_j[R(k)_j]\} . \quad (\text{A15})$$

Here $d^3 R/dk$ is normally written as $4\pi R^2 / |dk/dR|$ due to the occasional double-value character of $R(k)_j$.

For the NaXe_2^* case the CFCP yields

$$\hbar c k = V_{j_1 j_2}^*(R_1, R_2, R_3) - V(R_1, R_2, R_3) . \quad (\text{A16})$$

Combining (A5) and (A16):

$$\begin{aligned} \hbar c (k - k_0) &= \{\Delta V_{j_1}^*(R_1) - \Delta V(R_1)\} \\ &\quad + \{\Delta V_{j_2}(R_2) - \Delta V(R_2)\} , \\ &\equiv \hbar c (k_1 - k_0) + \hbar c (k_2 - k_0) , \end{aligned} \quad (\text{A17})$$

where we have defined the frequency shift due to the i th Na⁺-Xe interaction at R_i as $k_i - k_0 \equiv \Delta k_i$. Thus with $\Delta k \equiv k - k_0$, (A17) simply states $\Delta k = \Delta k_1 + \Delta k_2$, or that the total frequency shift is the sum of the two independent binary-interaction shifts. The probability that a single independent perturber causes a Δk_i shift is $P_1(\Delta k_i)$ given in (A15), so the probability of Δk_1 and Δk_2 is $P_1(\Delta k_1)P_1(\Delta k_2)$. All configurations which yield $\Delta k_1 + \Delta k_2 = \Delta k$ must be integrated over, so that

$$P_2(\Delta k) = \int_{-\infty}^{\infty} dk_1 P_1(\Delta k_1) P_1(\Delta k - \Delta k_1) . \quad (\text{A18})$$

Equations (A17) and (A18) can be generalized to the NaXe_n case for which $\Delta k = \sum_{i=1}^n \Delta k_i$:

$$P_n(\Delta k) = \int dk_1 \dots \int dk_{n-1} P_1(\Delta k_1) P_1(\Delta k_2) \dots P_1\left(\Delta k - \sum_{i=1}^{n-1} \Delta k_i\right) . \quad (\text{A19})$$

Equations (A18) and (A19) with $P_1(k)$ given by (A15) can be substituted into (A12) to obtain $I_N(k)$ corresponding to additive Na-RG interactions and the CFCP. Note, however, that $P_1(k)$ is given by (A15) only for $R \leq R_0$, and is zero for those k corresponding to $R > R_0$. From the CFCP, if $k(R) = V_j^*(R) - V(R)$; and for $j = B^2 \Pi_{1/2,3/2}$ this yields a $k(R_0)$ on the blue wing which we label k_+ . For the $j = A^2 \Pi_{1/2,3/2}$ case it yields $k(R_0) = k_-$, a value on the red wing. Thus $P_1(k)$ is given by (A15) for $k < k_+$ and $k > k_-$, and $P_1(k) = 0$ for $k_- < k < k_+$. (See Fig. 4.) Royer¹⁷ has indicated that the Weisskopf frequency represents a good choice for k_+ . However, in the present problem, larger $|k_+ - k_0|$ allow an adequate description of the spectrum to be obtained using only two- and three-body spectra, whereas many more terms would otherwise be required.

From (A12), in the $k < k_-$ and $k > k_+$ regions where $P_0(k) = 0$,

$$I_N^0(k) = \lim_{\text{Xe} \rightarrow 0} I_N(k) = \left(\frac{k}{k_0}\right)^4 K_1 P_1(k) , \quad (k < k_-, k > k_+) . \quad (\text{A20})$$

From (A18) and (A20) and $P_1(k) = 0$ for $k_- < k < k_+$,

$$K_1^2 P_2(\Delta k) = \int' dk_1 \left(\frac{k_0}{k_0 + \Delta k_1}\right)^4 I_N^0(\Delta k_1) \left(\frac{k_0}{k_0 + \Delta k - \Delta k_1}\right)^4 I_N^0(\Delta k - \Delta k_1) \approx \left(\frac{k_0}{k}\right)^4 \int' dk_1 I_N^0(\Delta k_1) I_N^0(\Delta k - \Delta k_1) , \quad (\text{A18}')$$

where the primed integration extends from $k = -\infty$ to k_- and from k_+ to $+\infty$. For the general case, (A19) and (A20) yield

$$K_1^2 P_n(\Delta k) \sim \left(\frac{k_0}{k}\right)^4 \int' dk_1 \dots \int' dk_{n-1} I_N^0(\Delta k_1) \dots I_N^0\left(\Delta k - \sum_{i=1}^{n-1} \Delta k_i\right) , \quad (\text{A19}')$$

where the inaccuracy in the approximation is on the order of $(\Delta k/k_0)^2$, or less than 4% for the present data. Finally, combining Eqs. (A18') and (A19') with (A12):

$$I_N(k) \approx e^{-\kappa_1 \text{Xe}} \left\{ \frac{\delta(k - k_0)}{[\text{Xe}]} + I_N^0(k) + \sum_{n=2}^r \frac{[\text{Xe}]^{n-1}}{n!} \int' dk_1 \dots \int' dk_{n-1} I_N^0(\Delta k_1) \dots I_N^0\left(\Delta k - \sum_{i=1}^{n-1} \Delta k_i\right) \right\} . \quad (\text{A21})$$

Here

$$K_1 = \int dk_i (k_0/k_i)^4 I_N^0(k_i) , \quad (\text{A22})$$

so that taking $\int dk(k_0/k)^4$ on the right side of (A21) yields $\exp(-K_1[\text{Xe}] \sum_{n=0}^{\infty} K_n^n [\text{Xe}]^n / n'[\text{Xe}] \cdot [\text{Xe}]^{-1})$ as required. Equation (A21) is equivalent to Eq. (3.5) of Ref. 17, except for an additional broadening factor $I_c(\omega)$ in the latter expression. That broadening factor is negligible in the far wings considered here.

Since all k_i in Eq. (23) are at $k_i = k_*$ or $k_i < k_*$, one should choose small enough R_0 , or k_* and k_* far enough from k_0 , that the CFCP is valid. This implies the traditional validity criteria for the "quasistatic" wing, that $|\omega - \omega_0| \ll 1/\tau_c$ at $\omega/2\pi c = k_*$ or k_* , and this yields $k_* \sim k_0 \pm 10 \text{ cm}^{-1}$. However, as there is a diffuse red satellite at $\Delta k \sim 20-50 \text{ cm}^{-1}$ the simple CFCP is not very accurate in this region. We have taken k_* at $\sim k_0 - 50 \text{ cm}^{-1}$ and the results of variations in k_* and k_* have been discussed in the text.

- ¹S. Chen and M. Takeo, Rev. Mod. Phys. **29**, 20 (1957).
- ²W. L. Wiese, L. J. Roszman, and J. R. Fuhr, *Bibliography on Atomic Line Shapes and Shifts (1889 through March 1972)*, National Bureau of Standards Special Publication 366 (U. S. GPO, Washington, DC 1972).
- ³(a) W. Happer, G. Moe, and A. C. Tam, Phys. Lett. A **54**, 405 (1975); (b) A. Tam, G. Moe, W. Park, and W. Happer, Phys. Rev. Lett. **35**, 85 (1975).
- ⁴J. G. Eden, B. E. Cherrington, and J. T. Verheyen, IEEE J. Quantum Electron. **QE-12**, 698 (1976).
- ⁵R. E. Smalley, D. A. Auerbach, P. S. H. Fitch, D. H. Levy, and L. Wharton, J. Chem. Phys. **66**, 3778 (1977).

- ⁶R. E. M. Hedges, D. L. Drummond, and A. Gallagher, Phys. Rev. A **6**, 1519 (1972).
- ⁷D. L. Drummond and A. Gallagher, J. Chem. Phys. **60**, 3426 (1974).
- ⁸R. Scheps, Ch. Ottlinger, G. York, and A. Gallagher, J. Chem. Phys. **63**, 2581 (1975).
- ⁹G. York, R. Scheps, and A. Gallagher, J. Chem. Phys. **63**, 1052 (1975).
- ¹⁰R. Scheps and A. Gallagher, J. Chem. Phys. **65**, 859 (1976).
- ¹¹W. P. West and A. Gallagher (submitted for publication).
- ¹²H. Kuhn, Phys. Rev. **52**, 133 (1937).
- ¹³A. Jabłonński, Phys. Rev. **68**, 78 (1945).
- ¹⁴T. Holstein, Phys. Rev. **79**, 744 (1950).
- ¹⁵H. Margenau, Phys. Rev. **48**, 755 (1935).
- ¹⁶(a) A. Jabłonński, Acta Phys. Polonica **23**, 493 (1963); (b) A. Jabłonński, Phys. Rev. **68**, 78 (1944).
- ¹⁷A. Royer, Phys. Rev. A **3**, 2044 (1971).
- ¹⁸A. Royer, J. Chem. Phys. **50**, 1906 (1969).
- ¹⁹J. Kieffer, J. Chem. Phys. **51**, 1852 (1969).
- ²⁰M. Takeo, Phys. Rev. A **1**, 1143 (1970).
- ²¹J. Puscale and J. Vandeplanque, J. Chem. Phys. **60**, 2278 (1974).
- ²²J. M. H. LeVelt Sengers, M. Klein, and J. S. Gallagher, AIP Handbook, edited by D. E. Gray, (McGraw-Hill, New York, 1972), 4-204.
- ²³J. M. Farrar, T. P. Schafer, and Y. T. Lee, *Transport Phenomena*, AIP Conf. Proc. **11**, 279 (1973).
- ²⁴G. Herzberg, *Molecular Spectra and Molecular Structure: III. Electronic Spectra and Electronic Structure of Polyatomic Molecules* (Van Nostrand, Princeton, New Jersey, 1967).
- ²⁵A. V. Phelps, "Tunable Gas Lasers Utilizing Ground State Dissociation," JILA Rept. 110 (1972) Joint Institute for Laboratory Astrophysics, University of Colorado, Boulder, Colorado 80309..
- ²⁶G. York and A. Gallagher, "High Power Gas Lasers Based on Alkali-Dimer A-X Band Radiation," JILA Rept. 114 (1974) Joint Institute for Laboratory Astrophysics, University of Colorado, Boulder, Colorado 80309.

Excitation of the $b^1\Sigma_g^+$ state of O₂ by low energy electrons

S. A. Lawton^{a)} and A. V. Phelps^{b)}

Joint Institute for Laboratory Astrophysics, National Bureau of Standards and University of Colorado,
Boulder, Colorado 80309
(Received 20 February 1978)

Rate coefficients for excitation of the $b^1\Sigma_g^+$ state of O₂ by low energy electrons have been measured using a drift tube technique. The time dependence of the absolute intensity of the 762 nm band emission was measured for O₂ densities between 10^{16} and 2×10^{18} molecules/cm³. When corrected for electron attachment, ionization, and metastable diffusion, the number of $b^1\Sigma_g^+$ molecules produced per centimeter of electron drift and per O₂ molecule calculated from the 762 nm emission varied from 1.3×10^{-18} cm² at $E/N = 5 \times 10^{-17}$ V cm² to 2.1×10^{-16} cm² at $E/N = 2 \times 10^{-15}$ V cm². These values of electric field to oxygen density ratio E/N correspond to mean electron energies of 0.75 and 6 eV, respectively. Measured decay constants for the 762 nm radiation yield a value for the product of the diffusion coefficient and the O₂ density of $(5.0 \pm 0.3) \times 10^{18}$ cm⁻¹ sec⁻¹ and a quenching coefficient for the $b^1\Sigma_g^+$ state of $(3.9 \pm 0.2) \times 10^{-17}$ cm³ sec⁻¹. Comparison of measured excitation coefficients with values calculated using a recommended set of electron collision cross sections for O₂ show that the cross sections for direct excitation of the $b^1\Sigma_g^+$ state are accurate near threshold and suggest that essentially all of the O₂ molecules excited to levels at and above 1.63 eV result in the formation of molecules in the $b^1\Sigma_g^+$ state.

I. INTRODUCTION

The metastable states of O₂ play an important role in the earth's atmosphere through their ability to radiate measurable amounts of energy as well as to enhance rates of atmospheric reactions by virtue of their stored energy. Thus, measurements of the radiation from the $a^1\Delta_g$ and $b^1\Sigma_g^+$ states of O₂ during certain auroras suggested a serious deficiency in the models of energy input and conversion to radiation.¹⁻³ It has been proposed that the needed excitation is the result of electron heating by electric fields produced by the aurora,³ while other authors suggest that the secondary electrons present in auroras are a sufficient source of excitation.² In either case there is a need for accurate cross sections and rate coefficients for electron excitation of the oxygen metastable states. The experiment described in this paper supplies the total rate coefficient for electron excitation of the $b^1\Sigma_g^+$ state of O₂ including electron excitation via cascading from higher molecular states. This is in contrast to the electron beam scattering experiments⁴⁻⁶ which yield only the direct excitation of the molecular states. Furthermore, the experiments to be described yield rate coefficient data for the collisional destruction of the $b^1\Sigma_g^+$ metastable for comparison with other laboratory measurements,⁷⁻¹⁰ air glow models,¹¹ and simulation experiments.¹²

The experimental technique described in this paper is that of measurement of the absolute intensity of the 762 nm radiation emitted by the O₂($b^1\Sigma_g^+$) molecules excited by electrons drifting through the O₂ under the influence of a uniform electric field. The technique is an extension of that used previously¹³ for the 4.3 μm bands

of CO₂. The relevant theory of the experiment is outlined in Sec. II, while the apparatus and calibration procedures are described in Sec. III. The rate coefficients for quenching of the $b^1\Sigma_g^+$ state by O₂ are discussed in Sec. IV and the excitation coefficient measurements are presented in Sec. V.

II. THEORY OF THE EXPERIMENT

The potential energy curves¹⁴ for those states of O₂ which are germane to $b^1\Sigma_g^+$ excitation are shown in Fig. 1. The $b^1\Sigma_g^+$ state has an excitation threshold of 1.63 eV. Direct electron excitation to the $v=0$ vibrational level exceeds excitation to $v=1$ by about an order of magnitude,^{4,5} and excitation of levels with $v \geq 2$ has not been observed in electron beam experiments. The $v=0$ level radiates to the ground state in a band around 762 nm with a radiative lifetime of about 12 sec.^{14,15} A radiative transition to the $a^1\Delta_g$ state has also been observed and the transition probability^{15,16} is about 0.006 sec⁻¹. The $c^1\Sigma_g^+$, $C^3\Delta_u$, and $A^3\Sigma_g^+$ states are also metastable,¹⁴ so that radiative transitions from these states to the $b^1\Sigma_g^+$ state are not expected to lead to significant $b^1\Sigma_g^+$ production. Only the $c^1\Sigma_g^+$ state is shown from among the states with vertical excitation energies in range from 4.5 to 6 eV above the ground state. Dissociation of O₂ to form excited oxygen atoms can also lead to $b^1\Sigma_g^+$ excitation as discussed in Sec. V.

A. Excitation of O₂($b^1\Sigma_g^+$)

Electrons drift through the oxygen gas under the influence of a square wave modulated electric field in what can be approximated by an infinite, parallel-plane geometry. During the half-period when voltage is applied the electrons emitted from the cathode gain energy from the electric field until they reach a steady-state distribution of energies in which the energy gain is balanced by energy losses in collisions with the O₂ molecules. As the electrons drift toward the anode they can (a) excite the O₂ molecules to any one of a

^{a)}Present address: University of Illinois, Urbana, Illinois 61801.

^{b)}Staff Member, Quantum Physics Division, National Bureau of Standards, and Lecturer, Department of Physics and Astrophysics, University of Colorado.

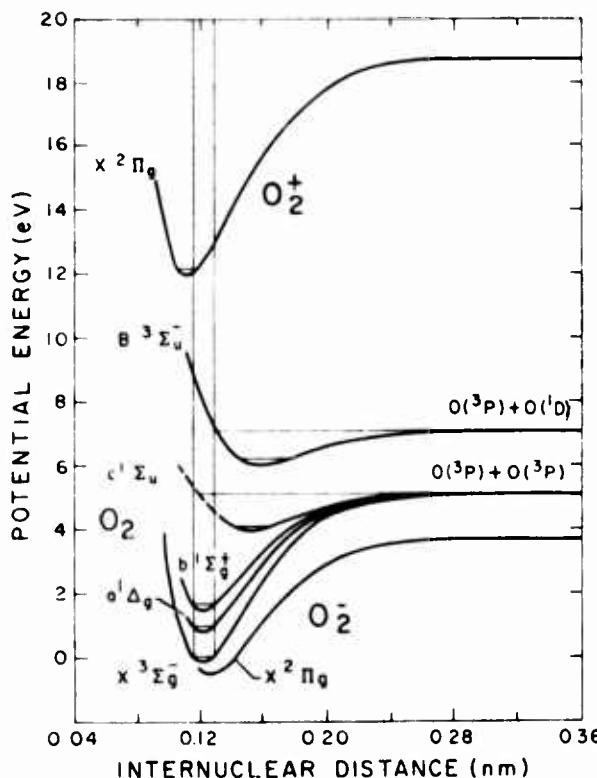


FIG. 1. Potential energy curves for O₂. The vertical lines show the Franck-Condon region for excitation from the $X^2\Sigma_g^-$ ground state.

number of vibrational or electronic states, (b) attach to the O₂ in two-body or three-body collisions, or (c) ionize the O₂. During the half-period of zero electric field the electrons rapidly cool to the gas temperature and can no longer excite or ionize the O₂. Excited molecules in the $b^1\Sigma^+$ state can (a) radiate to lower states as in the 762 nm band, (b) be collisionally de-excited to lower states, or (c) diffuse to the electrodes or wall of the collision chamber. The experimental technique used in this paper makes use of absolute intensity measurements to determine the density of $b^1\Sigma$ molecules and, together with decay constant measurements, the rate of loss of $b^1\Sigma$ molecules. The product of the steady-state density and the decay constant is proportional to the production rate. In the remainder of this section we derive the equations which relate these densities and decay constants to the measured, time-varying 762 nm signal and drift tube current. Because of the importance of electron attachment and ionization and metastable diffusion, we cannot use much of the theory derived¹³ for the experiments in CO₂.

The time and spatial dependence of the electron density $n_e(z, t)$ is given by the solution of the equation

$$\frac{\partial n_e}{\partial t} + w_e \frac{\partial n_e}{\partial z} = -k_2 N n_e - k_3 N^2 n_e + k_i N n_e, \quad (1)$$

where N is the ground state density, k_2 and k_3 are, respectively, the two- and three-body attachment rate constants, k_i is the ionization rate constant, and w_e is the electron drift velocity. After the accelerating voltage is turned on, the electron density distribution will

reach a steady-state spatial distribution in a time of $L/w_e \sim 10^{-6}$ sec, where L is the separation of the electrodes. Since the period of the accelerating voltage square wave is at least 50 msec, the electron density distribution can be found from the steady-state solution of Eq. (1), i.e.,

$$n_e(z, r) = n(0, r)e^{-\alpha z},$$

where

$$\alpha = \alpha_s - \alpha_i, \quad \alpha_s = (k_3 N^2 + k_2 N)/w_e, \quad \alpha_i = k_i N/w_e,$$

and $n(0, r)$ is the electron density produced at the cathode by the external uv source. Here we have assumed that secondary electron production at the cathode can be neglected. In the remainder of this paper we will assume that the cathode emission is independent of radius, i.e., $n(0, r) = n(0)$ for r less than the cathode radius R .

The time dependence of the density of $b^1\Sigma$ molecules n_b is given by

$$\frac{\partial n_b}{\partial t} = -(A + k_d N)n_b + D \frac{\partial^2 n_b}{\partial z^2} + k_{eb} N n_e, \quad (3)$$

where A is the radiative transition probability, k_d is the rate coefficient for de-excitation of the $b^1\Sigma$ state in collisions with ground state molecules, k_{eb} is the effective rate coefficient for electron excitation of the $b^1\Sigma$ state, and D is the $b^1\Sigma$ state diffusion coefficient. De-excitation of the $b^1\Sigma$ state by electrons has been neglected due to the low electron density ($< 10^4$ cm⁻³). There is negligible reabsorption of the 762 nm band by the O₂ due to the low oscillator strength for this transition.^{11,15} The "energy pooling" reaction O₂($a^1\Delta$) + O₂($a^1\Delta$) → O₂ + O₂($b^1\Sigma$) has been ignored because of the low $a^1\Delta$ densities in our experiment and the low rate coefficient (2×10^{-17} cm³ sec⁻¹).¹⁷ Indirect excitation through higher energy states has been assumed to occur on a time scale very short compared to the effective lifetime of the $b^1\Sigma$ state and will be discussed later. Quenching of the $b^1\Sigma$ state by any added gases or impurities can be included in Eq. (3) by the addition of a term equal to the product of the impurity density, the quenching rate constant, and n_b . Radial diffusion out of the field of view has been neglected (see Appendix A).

The solution of Eq. (3) using the electron density distribution of Eq. (2) and assuming $n_b = 0$ at $t = 0$ and $n_b = 0$ at $z = 0$ and $z = L$ for all t is

$$n_b = k_{eb} N n(0) \sum_m (b_m / \gamma_m) \sin(m\pi z/L)(1 - e^{-\gamma_m t}), \quad (4)$$

where

$$\gamma_m = A + k_d N + D(m\pi/L)^2,$$

$$b_m = 2\pi m (1 - e^{-\alpha}) \cos(m\pi) [a^2 + (m\pi)^2]^{-1},$$

$m \geq 1$, and $a = \alpha L$. If the half-period of the square wave of voltage applied to the drift tube is long enough, i.e., at least $5/\gamma_1$, then the decay of the $b^1\Sigma$ density during the voltage-off half-period is obtained by replacing the final parenthesis in Eq. (4) by $e^{-\gamma_m t}$. In the limit of no diffusion, the sum in Eq. (4) or the direct solution of Eq. (3) for $n_b = 0$ at $t = 0$ is

$$\begin{aligned} n_b &= [k_{eb} N n(0) / \gamma_0] e^{-\alpha_s} (1 - e^{-r_0 t}) \\ &= n_{b0}(z) (1 - e^{-r_0 t}), \end{aligned} \quad (5)$$

where $\gamma_0 = A + k_d N$.

B. 762 nm signal

The 762 nm signal developed by the photomultiplier and subsequent amplifiers is given by

$$S(t) = f_w A D(\nu_i) \langle f_i \rangle (\Delta\Omega_c / 4\pi) \int_V \eta n_b dV, \quad (6)$$

where

$$\langle f_i \rangle = \int_0^\infty f_i(\nu) R(\nu) d\nu / \int_0^\infty R(\nu) d\nu.$$

Here f_w is the fractional transmission of the windows between the excited molecules and the detector, $D(\nu_i)$ is the responsivity per photon of the photomultiplier and amplifier system at the frequency of peak transmission of the interference filter, $f_i(\nu)$ is the fractional transmission of the interference filter, $R(\nu)$ is the relative intensity of radiation emitted¹⁸ by $b^1\Sigma$ molecules in the frequency interval $d\nu$, $\Delta\Omega_c$ is the solid angle subtended by the photomultiplier cathode from the volume element dV at the center of the drift tube, and η is the efficiency of photon detection at various parts of the drift tube relative to that at the center. In Eq. (5) we have taken advantage of the fact that the response of the detector per photon is essentially independent of photon energy over the range of significant transmission of the interference filter.¹⁹ The distribution of emitted energy $R(\nu)$ is taken from Noxon¹⁸ and from Bastien and Lecuiller.²⁰ In contrast to the situation for the measurement¹³ of 4.3 μm excitation in CO₂, the formulation of Eq. (6) is simplified by the fact that absorption of the 762 nm band by O₂ between the drift region and the detector is negligible.¹¹ Note that η is determined experimentally and includes such factors as the variations in solid angle, changes in photomultiplier sensitivity with angle, and the scattering of light by electrodes.

It is convenient to normalize the spatial integral indicated in Eq. (6) to the value obtained with a constant detection efficiency and with the spatial distribution of excited atoms calculated in the absence of diffusion as in Eq. (5). Thus, we define a geometrical factor G such that

$$G = (\gamma_1 / \gamma_0) \int_V \eta n_b dV / \int_V n_{b0} dV = \sum G_m, \quad (7)$$

where n_b^* is given by Eq. (4) in the limit of $\gamma_m t \rightarrow \infty$ and

$$G_m = \frac{\alpha b_m \gamma_1}{(1 - e^{-\alpha}) \gamma_m} \int_0^L \eta(z) \sin(m\pi z/L) dz.$$

Note that since we have assumed the electron current at the cathode to be independent of r and have neglected radial diffusion of the metastables so that n_b is independent of r , we use the radially averaged value of n in G_m . In the case of uniform detection efficiency, i.e., $\eta_A(z) = 1$, only odd values of m contribute and the summation indicated in Eq. (7) can be carried out to yield a geometrical factor G_A such that

$$G_A = \frac{(a^2 + d^2)}{(a^2 - d^2)} \left[\frac{a \tanh(d/2)}{d \tanh(a/2)} - 1 \right], \quad (8)$$

where $d^2 = k_d N L^2 / D$. In the low density limit, i.e., $a \rightarrow 0$ and $d^2 \rightarrow 0$, Eq. (8) yields $G_A \sim \pi^2/12$. For negligible diffusion and attachment, $G_A \sim 1$. The results of analytical evaluations of G for other simple forms of $\eta(z)$ and for our experiment are discussed in Appendix A.

C. Electron and total current relations

It is now necessary to relate the electron density at the cathode $n(0)$ to the measured current through the drift tube. We begin with the differential equations describing the time dependence of the negative ion and positive ion densities while the electric field is applied, i.e.,

$$\frac{\partial n_-}{\partial t} + w_- \frac{\partial n_-(z, t)}{\partial z} = k_1 N n_e, \quad (9)$$

and

$$\frac{\partial n_+}{\partial t} + w_+ \frac{\partial n_+(z, t)}{\partial z} = (k_3 N^2 + k_2 N) n_e, \quad (10)$$

where w_- and w_+ are the positive and negative ion drift velocities, respectively. The recombination of electrons and negative ions with positive ions is neglected because of the low charge densities present in this experiment. Radial and longitudinal diffusion of electrons²¹ and ions and detachment of the negative ions have been neglected. Since the electron, negative ion, and positive ion densities reach their steady-state values in a time short compared to the half period of the square wave, the time derivatives in Eqs. (9) and (10) can be neglected. This means that the densities of the ions can be obtained by integration of Eqs. (9) and (10) subject to the boundary conditions that $n_- = 0$ at $z = 0$ and $n_+ = 0$ at $z = L$.

The contribution of the various charged particles n_b to the currents in the external circuit i_b are then obtained from the relation

$$i_b = \frac{\pi R^2 e w_b}{L} \int_0^L n_b(z) dz. \quad (11)$$

If the electron current leaving the cathode is $i_e = \pi R^2 c w_p n(0)$, the measured magnitudes of the electron component of the current i_e and the total current i are given by

$$i_e = i_c (1 - e^{-a}) / a \quad (12)$$

and

$$i = i_c (\alpha_e - \alpha_i e^{-a}) / a. \quad (13)$$

Therefore,

$$\frac{i_e}{i} = \frac{(1 - e^{-a})}{(\alpha_e L - \alpha_i L e^{-a})} = \frac{1}{q}. \quad (14)$$

The experimental determination of q , α_e/N , and α_i/N using these relations is discussed in Appendix B.

The magnitude of the quasi-steady-state signal at the detector S_0 may now be written in terms of the excitation rate coefficient, various geometrical and frequency averages, and the observed current. Thus, substitution

of Eq. (4) into (6) and the use of Eqs. (7) and (14) yields

$$S_0 = f_w f_i \langle D(\nu_i) \rangle \frac{\Delta\Omega_c}{4\pi} \frac{A}{\gamma_1} \frac{i \alpha_b L}{eq}, \quad (15)$$

where $\alpha_b = k_{eb} N/n_e$ is the number of excitation events per unit distance in the field direction.

D. Comparison with radiance standard

As in the CO₂ experiments, the detector was calibrated against a radiance standard. Thus, the signal reaching the detector, when illuminated by the incandescent source, was

$$S_r = f_w f_r a_r \Delta\Omega_r D(\nu_i) \int_0^\infty f_i(\nu) \epsilon(\nu) B(\nu) d\nu, \quad (16)$$

where f_r is the fractional transmission of the windows and neutral density filters between the radiance standard and the drift region, a_r is the area of the aperture between the standard and the collision chamber, $\Delta\Omega_r$ is the solid angle of the detector as seen from the limiting aperture, $\epsilon(\nu)$ is the emissivity of the tungsten ribbon, and $B(\nu) d\nu$ is the number of photons per second emitted by a black body in the frequency interval $d\nu$ per square centimeter of surface per unit solid angle at the operating temperature of the standard.

The final expression for the excitation rate coefficient is obtained by combining Eqs. (15) and (16) to obtain

$$\frac{\alpha_b}{N} = \frac{C q \gamma_1 S_0}{G i A N S_r}, \quad (17)$$

where

$$C = \frac{4\pi f_r a_r \Delta\Omega_r \epsilon}{\Delta\Omega_c L (f_i)} \int_0^\infty f_i(\nu) \epsilon(\nu) B(\nu) d\nu.$$

Note that in C the area of the cathode of the photomultiplier used in the calculation of the solid angles as well as the magnitude of the transmission of the interference filter cancel out. In Eq. (17) the responsivity of the detection system for measuring S_0 and S_r cancels out provided that the system is linear over the range of signals used.

III. EXPERIMENTAL APPARATUS AND PROCEDURE

The apparatus is shown schematically in Fig. 2. Electrons from the photocathode drift through the O₂ target gas under the influence of a uniform electric field. Excitation of the $b^1\Sigma$ state was determined by measuring the intensity of 762 nm radiation with a photomultiplier calibrated against a standard of spectral radiance.²²

The photocathode consisted of a 0.64 cm thick uv transmitting quartz disk 6 cm in diameter which was coated on the inner surface with a 70% transparent film²³ of a 60% gold, 40% palladium alloy. This alloy is resistant to oxidation and has a high photoelectron yield. The photocathode was illuminated through the quartz disk by the radiation from a high pressure mercury lamp.²⁴ In order to reduce the amount of stray 762 nm radiation reaching the detector, the light from the mercury lamp was passed through two ultraviolet filters centered at 200 nm with full widths at half-max-

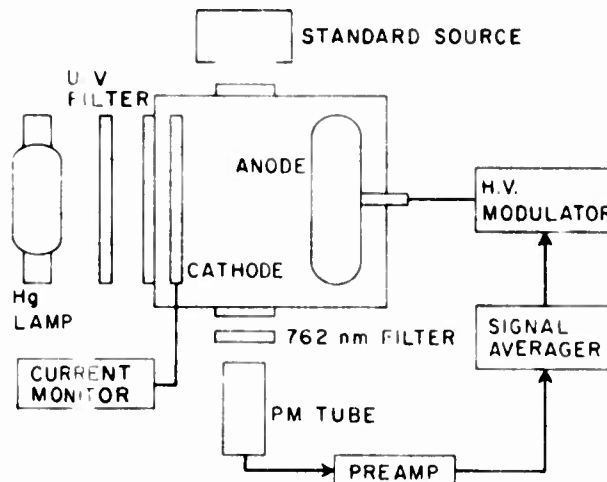


FIG. 2. Schematic of the apparatus in the excitation coefficient measuring mode. The electrodes and surrounding chamber are not drawn to scale.

imum of about 50 nm. Attempts to reduce scattered light by coating the exposed metal surfaces with carbon black lead to erratic results, apparently because of high vapor pressure impurities which were not removed by the relatively low temperature ($\sim 150^\circ\text{C}$) bakeout. Photocurrents of about 5×10^{-7} A were observed with the interaction region evacuated. For the experimental range of E/N , photocurrents of about 5×10^{-8} A were obtained. The total drift tube current was passed through a low pass RC filter and was monitored by observing the voltage across the $10^6 \Omega$ input impedance of a digital voltmeter which integrated the voltage for the duration of the measurement. The estimated accuracy of the current monitoring system was $\pm 5\%$.

A uniform electric field in the electron drift region was created by applying a positive potential between the shaped anode and the 25 cm diameter cathode plane. The anode was 16 cm in diameter with a $\psi = 2\pi/3$ Rogowski profile²⁵ over the central 14 cm and with broadly rounded corners. The cathode-anode spacing at the point of minimum separation was 3.84 cm and the diameter of the semitransparent cathode was 6 cm. This design also reduced the problems with breakdown at the higher E/N . A zero-based, square wave accelerating voltage was applied to the anode. The period of the voltage modulation was determined by the time constant of the 762 nm signal and varied from 50 to 500 msec. In order to minimize the effects of contact potential differences, a minimum accelerating voltage of 12 V was used. The maximum accelerating voltage was 900 V. The voltages were measured to $\pm 1\%$. The maximum space charge distortion of the electric field is caused by negative ions and positive ions and is estimated to be 5% and occurs at the lowest E/N .

The gas used was specified to be 99.99% pure O₂. The gas was held in a reservoir at liquid nitrogen temperature for approximately 1 h and then was slowly bled into the experimental chamber so as to avoid boiling of the liquid oxygen. Pressures were measured using a calibrated capacitance manometer with a stated accuracy

of better than $\pm 1\%$. The system was baked with heating tapes and lamps for 48 h so that typical outgassing rates at room temperature were 10^{-3} Pa (7×10^{-6} torr) per min. The O₂ gas was changed at sufficiently short intervals to assure that contamination caused by outgassing was negligible.

The 762 nm signal was measured with a GaAs photomultiplier cooled to dry ice temperature. The signal processing was the same as for the CO₂ experiments.¹³ If absolute measurements of α/N were to be made, the anode current from the photomultiplier tube was amplified, digitized, and stored on a 256 channel multichannel scaler, which also controlled the timing of the accelerating voltage. Integration times of 200 sec were satisfactory at the larger values of E/N , while integration times of 40 min were necessary for the lowest E/N points. The period of one sweep was adjusted to be equal to about $10/\gamma$. If only relative values of α/N as a function E/N and at fixed O₂ density were desired, the photomultiplier current was amplified and measured with a lock-in amplifier. The reference output of the amplifier was used to synchronize the drift-tube accelerating voltage. The output of the lock-in amplifier was integrated on the multichannel scaler for about 15 min.

The 762 nm band was isolated from the background radiation at the photomultiplier by an interference filter with 64% peak transmission at 762 nm and a 10 nm FWHM. This filter is not sufficiently narrow to reject any radiation from the (1, 1) $b^1\Sigma_g^+ - X^3\Sigma_u^-$ transition¹⁴ at 771 nm which could have made a small contribution to the signal. The transmission of the 762 nm interference filter was measured from 750 to 780 nm on a double pass 3/4 m monochromator with 0.1 nm resolution. The calculated fraction of 762 nm band radiation transmitted through the filter (f_i) is the same to within 1% for the measured band intensity distributions.^{16,20} The filter transmission was used with the manufacturer's specifications for the standard lamp and the relative photomultiplier sensitivity to obtain the integral in Eq. (17).

The calibration of the detection system was checked before and after each series of measurements. The photomultiplier observed the radiation from a standard of spectral radiance²² with a stated calibration accuracy of $\pm 6\%$. This radiance was an average value over an area 0.6 by 6 mm at the center of the tungsten strip filament. The 10 \times 4 mm photomultiplier cathode viewed an area 0.6 by 1.5 mm through an aperture of (27.6 \pm 1.0 μm diameter) placed in front of the lamp. The maximum error introduced by observing this smaller area of the filament was determined by moving the aperture horizontally and vertically and was less than 4%. In order to reduce the intensity of the lamp to a value comparable to that observed for $b^1\Sigma$ emission, a neutral density filter was inserted in front of the lamp. The transmission of this filter at 762 nm was measured to be $(1.03 \pm 0.05)\%$ using a monochromator and white light source. A chopper between the standard lamp and the photomultiplier modulated the signal at

65 Hz. The calibration signal was amplified and time averaged in a manner identical to that for the data so as to calibrate the total signal processing system.

The spatial variation of the detection efficiency η was determined by mapping the drift region with a light-emitting-diode covered with a 6 mm diameter diffuser. The measurements were corrected for the measured angular emissivity of this source. The inclination of the photomultiplier cathode resulted in a loss of sensitivity near the anode. The center of the drift tube was chosen as the reference point because it is aligned with the radiance standard and results in illumination of the photomultiplier cathode from the same angle as from the radiance standard. Although the use of a broad-band source does not provide a measure of the loss of detector sensitivity caused by the shift of about 1 nm in wavelength of maximum transmission of the interference filter at angles corresponding to the positions of the electrodes, this effect is estimated to be less than 5%. The estimated uncertainty in the geometrical factor G caused by uncertainties in η is $\pm 5\%$ for the data reported, i.e., for $-1.3 \leq \alpha L \leq 3.5$.

Although not expected to be important because of the low electron ($< 10^4 \text{ cm}^{-3}$) and metastable state ($< 10^{10} \text{ cm}^{-3}$) densities, a test was made for 762 nm production as the result of successive excitation events. Fine screens were inserted between the mercury lamp and the photocathode so as to reduce the photocurrent by factors of 3 and 10 at $E/N = 6 \times 10^{-16} \text{ V cm}^2$. The resultant α_b/N values varied by less than 5%. This test also rules out any sequence of electron excitation and of photodissociation or photon excitation by light from the mercury lamp unless the photon induced step is fast on the time scale of this experiment, i.e., unless the photon induced reaction time is short compared to 1 msec with the total photon flux of about $3 \times 10^{16} \text{ photons cm}^{-2} \text{ sec}^{-1}$ or the photon cross section is greater than about 10^{-14} cm^2 .

The principal sources of uncertainty in the determination of E/N are in the measurement of the electrode spacing ($\pm 2\%$), the voltage applied to the gap ($\pm 1\%$), and the gas density ($\pm 1\%$) and in estimation of the effects of space charge distortion ($\pm 5\%$), contact potential ($\pm 4\%$), and electric field nonuniformity (+ 5 to - 15%) for a total estimated uncertainty in E/N of + 6 to - 17%. The principal sources of uncertainty in the determination of α_b/N are in the manufacturer's calibration of the lamp ($\pm 6\%$); our measurement of the neutral density filter attenuation ($\pm 5\%$), the aperture area ($\pm 8\%$), variations in detection sensitivity ($\pm 5\%$), the contribution of reflection from the walls of the chamber ($\pm 5\%$), fitting the observed wave form ($\pm 5\%$), the current through the drift tube ($\pm 5\%$), and the fraction of the current caused by electrons ($\pm 10\%$); our calculations of the detector solid angles ($\pm 5\%$) and the diffusion correction ($\pm 5\%$); and the literature value of the transition probability ($\pm 10\%$) for total estimated uncertainty in α_b/N of $\pm 25\%$. The principal sources of uncertainty in the determination of the decay constants γ are in the fitting of the exponentials to the experimental data ($\pm 5\%$).

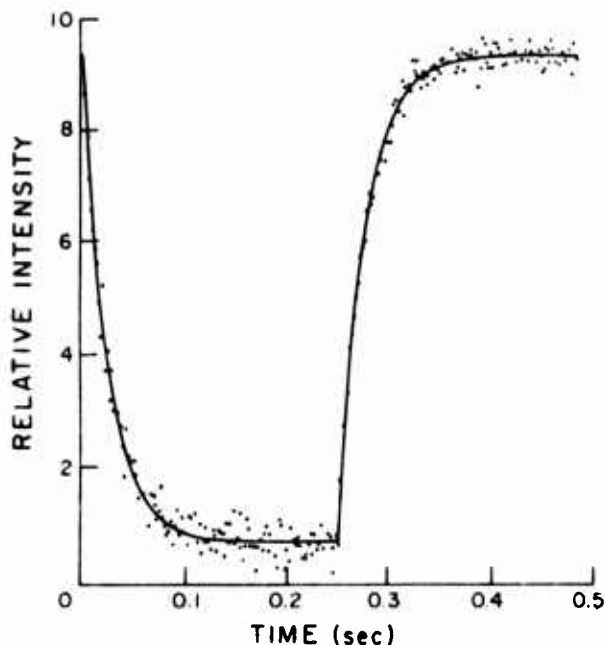


FIG. 3. Relative 762 nm intensity as a function of time. The accelerating voltage was turned off at $t = 0$ and on at $t = 0.256$ sec. The experimental parameters were $[O_2] = 1.6 \times 10^{17} \text{ cm}^{-3}$, $E/N = 9 \times 10^{-17} \text{ V cm}^2$, $i = 5.6 \times 10^{-6} \text{ A}$, and $L = 3.26 \text{ cm}$. The signal amplitude corresponds to about $5 \times 10^{-14} \text{ W/cm}^2$ incident on the photomultiplier cathode at 25 cm from the collision chamber. The decay constant is 38 sec^{-1} .

IV. QUENCHING RATE COEFFICIENTS

Figure 3 shows a representative curve of 762 nm intensity as a function of time. The solid curve shows the least-squares fits to the data of functions of the form $s \exp(-\gamma_a t)$ and $s[1 - \exp(-\gamma_b t)]$. As discussed in Appendix A, the decay constant $\gamma = (\gamma_a + \gamma_b)/2$ is expected to be equal to the decay constant for the fundamental diffusion mode to within 2%. The decay constant γ is plotted versus O₂ density in Fig. 4. For a 12 sec radiative lifetime, $A \ll \gamma$, so that $\gamma = D/\Lambda^2 + k_d N$. Here Λ is the diffusion length for the cylindrical collision chamber of height L and radius R , i.e., $1/\Lambda^2 = \pi^2/L^2 + (2.405)^2/R^2$. For densities less than 10^{17} cm^{-3} , γ is determined by the rate of diffusion of the metastables to the electrodes where they are quenched. The solid line of Fig. 4 indicates the best fit value of $DN = (5.0 \pm 0.3) \times 10^{-16} \text{ cm}^{-1} \text{ sec}^{-1}$. This diffusion coefficient is in good agreement with previous values.^{1,8} The deviation of the data points from the solid line at low densities may indicate reflection of the metastables at the walls,¹⁷ although a rather high reflection coefficient⁸ from the metal electrodes (~ 0.9) would be required.

At densities above about 10^{18} cm^{-3} the time constant is determined by the rate of quenching of the $b^1\Sigma$ in collision with ground state molecules. Until recently, measurements of the rate constant for quenching of the $b^1\Sigma$ by the O₂ molecules have yielded values which differed by an order of magnitude.⁷⁻⁹ The present data indicate a quenching rate constant of $(3.9 \pm 0.2) \times 10^{-17} \text{ cm}^3 \text{ sec}^{-1}$. This value is in agreement with the rate constants obtained by Thomas and Thrush⁸ in known

mixtures of O₂ and water vapor and by Martin *et al.*⁹ and Lawton *et al.*,¹⁰ who observed laser excited photoluminescence from the $b^1\Sigma$ state.

V. EXCITATION COEFFICIENTS

A. Pure O₂

Figure 5 shows experimentally determined excitation coefficients α_b/N as a function of N for $E/N = 8 \times 10^{-17}$ and $8 \times 10^{-16} \text{ V cm}^2$. The solid points were calculated using Eq. (17) with $\gamma_i S_0$ replaced by $s(\gamma_a + \gamma_b)/2$ and with $q = 1$ and $G = \langle n \rangle = 0.78$. A radiative transition probability^{14,15} of $A = 0.085 \text{ sec}^{-1}$ was used in calculating these and other α_b/N values. The open points show the results of correction for the effects of attachment, ionization, and diffusion calculated using Eq. (14) for q and the evaluation of $G = G_s$ as discussed in Appendix A. According to our model for this experiment, the α_b/N values represented by the open points should be independent of [O₂]. Less than one-half of the decrease in the apparent α_b/N values at low [O₂] is caused by radial diffusion as discussed in Appendix A. The major cause may be the finite distance required for the photoelectrons to reach a steady-state energy distribution.²⁶ The averages of the high N data from a series of plots such as Fig. 5 provide the absolute values of α_b/N shown by the solid circles in Fig. 6. The open circles in Fig. 6 were obtained from relative values of s/i versus E/N obtained at constant N . These values were corrected for attachment and ionization and then normalized to the absolute value of α_b/N at $E/N = 4 \times 10^{-16} \text{ V cm}^2$. Empirically, the experimental values of α_b/N are $(1.5 \pm 0.4) \times 10^{-16} \exp(-4.67 \times 10^{14} N/E) \text{ cm}^3$ for $E/N \leq 5 \times 10^{-16} \text{ V cm}^2$ and $(4.7 \pm 1.2) \times 10^{-3} (E/N)^{0.60} \text{ cm}^3$ for $E/N \geq 1.5 \times 10^{-16} \text{ V cm}^2$. Measurements were made for E/N between 2×10^{-15} and $8 \times 10^{-15} \text{ V cm}^2$ but are not shown because of the large and uncertain corrections for diffusion and for low detector sensitivity near the

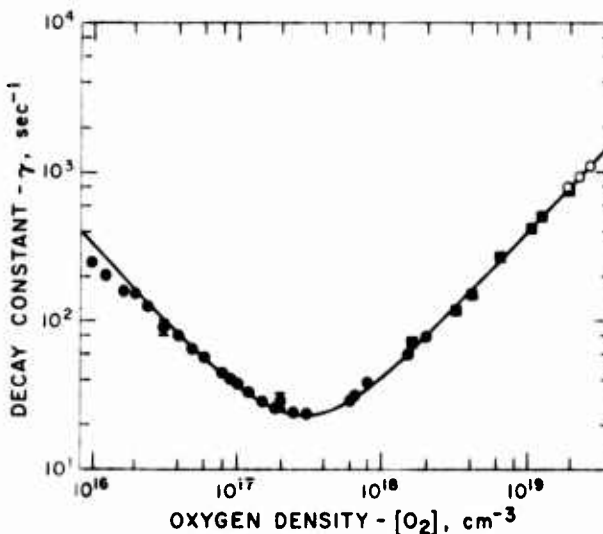


FIG. 4. Decay constant of 762 nm radiation versus O₂ density. The solid line indicates the fit of the sum of the diffusion and two-body quenching terms. The solid circles are the present results while the solid squares (Ref. 10) and open circles (Ref. 9) are measurements using laser induced fluorescence.

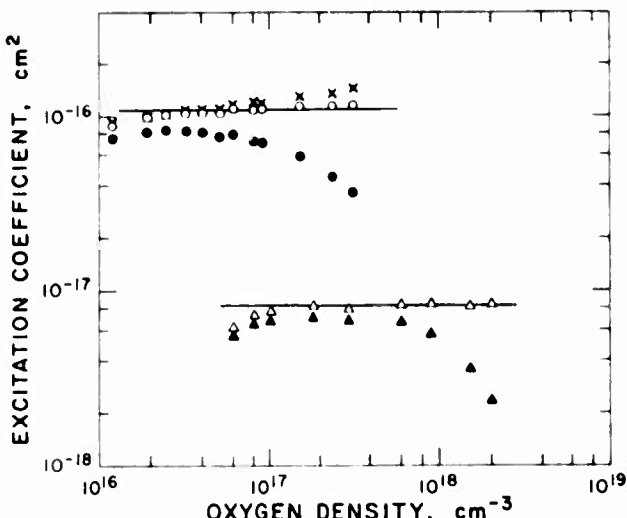


FIG. 5. Density dependence of excitation coefficients for 762 nm radiation in O₂. The solid points are calculated from the observed 762 nm signals using the average value for the detection efficiency but without correction for attachment, ionization, or diffusion. The open points are calculated using α_e/N values which maximize the O₂ density range for which the α_e/N values are independent of density. The crosses are for values of α_a/N which are too large. The upper set of points is for $E/N = 8 \times 10^{-16} \text{ V cm}^2$, $\alpha_e/N = 2.8 \times 10^{-19} \text{ cm}^2$, and α_a/N values of (●) 0, (○) 2×10^{-18} , and (×) $2.5 \times 10^{-18} \text{ cm}^2$. The lower set of points is for $E/N = 8 \times 10^{-17} \text{ V cm}^2$, $\alpha_e/N = 0$ and α_a/N values of (▲) 0, and (△) $(2.1 \times 10^{-17} [\text{O}_2] + 2 \times 10^{-20})$.

anode when $(-\alpha L)$ is large and because of the possible failure of the electrons to reach a steady-state energy distribution in a distance small compared to L .

The solid curve of Fig. 6 shows the rate coefficients calculated from the cross sections for direct excitation

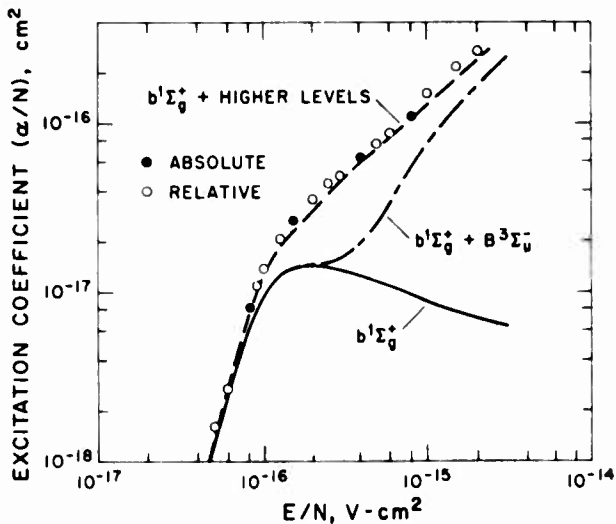


FIG. 6. O₂($b^1\Sigma_g^+$) excitation coefficient versus E/N . The solid circles are obtained from plots such as that of Fig. 5. The open circles are corrected for attachment and ionization and then normalized to the absolute values. The solid curve is the direct excitation coefficient while the long-short dashed curve is that obtained by summing the contributions of excitation to the $b^1\Sigma$ and $B^3\Sigma$ states. The dashed line is the calculated total excitation coefficient for the $b^1\Sigma_g^+$ and all higher energy O₂ electronic states.

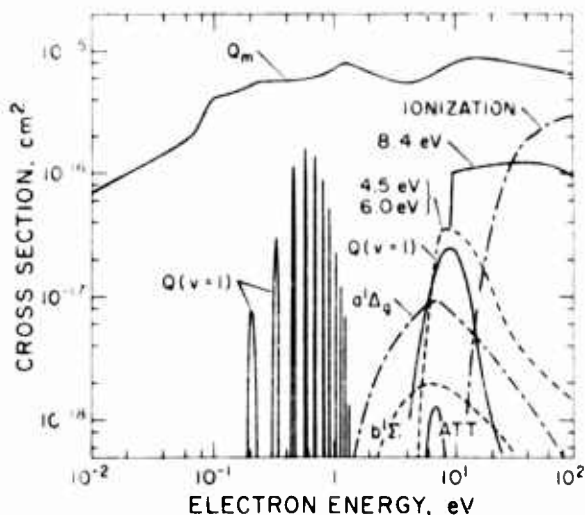
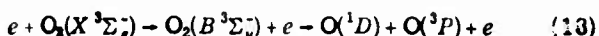
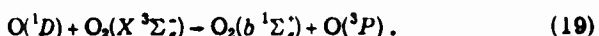


FIG. 7. Cross sections for electron excitation of O₂ used in the calculation of the rate coefficients for excitation of the O₂($b^1\Sigma$) state. The basis for the choice of the set of cross sections is discussed in Appendix C. The dissociative attachment cross section used for the calculated α_e/N curve of Fig. 10 is 1.2 times that labeled ATT in this figure.

of the $b^1\Sigma$ state measured by Linder and Schmidt⁴ and by Trajmar *et al.*⁵ Use of the cross sections measured by Konishi *et al.*⁶ leads to rate coefficients which are a maximum of 5% larger than those shown by the solid curve. The cross section set for electron collisions in O₂ used in this calculation is shown in Fig. 7. The basis for this set is discussed in Appendix C. An additional known process for the production of $b^1\Sigma$ molecules is via dissociative excitation of O₂ to produce O(¹D) atoms and their subsequent excitation transfer to the $b^1\Sigma$ state, i.e., the reactions



and



Determinations²⁷ of the efficiency of Reaction (19) in pure O₂ range from <1% to 100%. If we assume that processes (18) and (19) are 100% efficient and add the calculated rate coefficient for excitation of the $B^3\Sigma$ state to that for direct excitation of the $b^1\Sigma$ state, we obtain the long-short dashed curve of Fig. 6. Note that since the measured²⁸ rate coefficient for Reaction (19) is $4 \times 10^{-11} \text{ cm}^3 \text{ sec}^{-1}$, typical O(¹D) lifetimes in our experiment are $\sim 1 \mu\text{sec}$ and are not observable in the buildup of the 762 nm signal. We see that the agreement between these calculations and experiment is good only for $E/N < 8 \times 10^{-17} \text{ V cm}^2$, i.e., for mean electron energies less than 1.3 eV.

We have been unable to find a completely satisfactory explanation of the discrepancy between experiment and the sum of the excitation coefficients for processes which are known to lead to the $b^1\Sigma$ state. At present the most likely explanation for the excess in the observed excitation rate coefficient is that the excitation to states which we have labeled by the 4.5 and 6 eV energy losses (see Appendix C) result in the production

of bound levels of, for example, the $c^1\Sigma_u^+$ state⁵ which are collisionally de-excited to the $b^1\Sigma$ state. If we include the calculated excitation coefficients for these states in the summation, we obtain the short dashed curve of Fig. 6 which agrees reasonably well with the experimental data. A difficulty with this explanation is that the application of the Frank-Condon principle to potential energy curves¹⁴ for O₂ leads to the prediction that excitation of the molecular states characterized by energy losses of 5.1 to 7 eV results in dissociation to form two O(³P) atoms. The reassociation of these atoms appears very unlikely. The association of atoms from different molecules is slower²⁹ than loss by diffusion and their contribution to the 762 nm signal would vary as the square of the electron current in contrast to experiment. Similarly, the formation²⁹ of O₃ and its subsequent photodissociation is slow compared to diffusion and so would be inefficient and time varying.

The possibility of excitation transfer from vibrationally excited ground state molecules to the $b^1\Sigma$ state is ruled out by the wrong dependence on E/N and by the small amount of energy transferred from the electrons to the vibrational manifold. The energy pooling process¹⁷ involving two O₂($a^1\Delta_g$) molecules is ruled out by the observed linear variation of 762 nm signal with photoelectric current, by the relatively fast and current independent decay of the $b^1\Sigma$ population, and by the wrong E/N dependence of the unexplained excitation. We have been unable to think of any $b^1\Sigma$ excitation process involving $a^1\Delta$ molecules which is not ruled out by considerations such as these.

If we are willing to assume that the electron beam experiments are significantly in error, a reasonable fit to the α_b/N data can be obtained by adding the cross sections given in Fig. 7 for the 4.5 and 6.1 eV energy losses to the cross section for $b^1\Sigma$ excitation and by reducing the cross sections for the excitation of the 4.5 and 6 eV processes by factors of 1.63/4.5 and 1.63/6, respectively. This proposal increases the cross section for direct $b^1\Sigma$ excitation by about a factor of 10. It seems very unlikely that the electron beam experiments could be in error by this much.

B. O₂-N₂ mixtures

A few determinations of α_b/N were made in mixtures of N₂ and O₂ and are shown for [N₂]/[O₂] = 1/9 in Fig. 8. As for pure O₂, the experimental rate coefficients are much larger than the calculated values for direct excitation of the $b^1\Sigma$ state (solid line) or for direct excitation plus excitation transfer from O(¹D) (long-short dashed line), but agree reasonably well with the sum of the excitation rate coefficients for the $b^1\Sigma$ state³⁰ and all higher energy electronic states of O₂ (short dashed line). The measured O₂($b^1\Sigma$) lifetimes were consistent with previous measurements⁹ of $b^1\Sigma$ destruction by N₂. Note that in measurements at the higher N₂ fractional concentrations the interfering radiation from the (3-1) band of the $B^3\Pi_g - A^3\Sigma_u^+$ (first positive) transition of N₂ can be easily separated from the 762 nm signal because of the very rapid buildup of the N₂ radiation to a quasi-

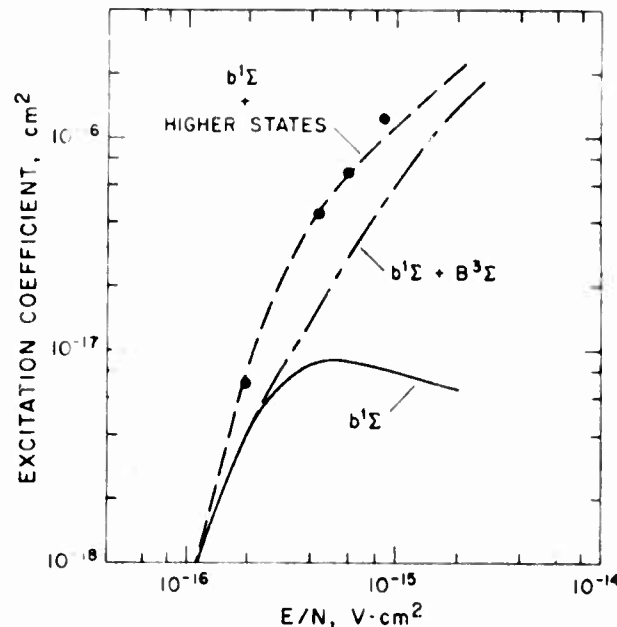


FIG. 8. Excitation coefficient α_b/N versus E/N for $[N_2]/[O_2] = 1/9$. As in Fig. 6, the smooth curves show the predicted rate coefficients for excitation of the $b^1\Sigma$ state.

steady-state value. No information regarding excitation transfer from excited N₂ to O₂($b^1\Sigma$) was obtained because of the large rate of electron excitation of O₂ at the relatively large ratios of [O₂]/[N₂].

VI. DISCUSSION

The measurements of excitation rate coefficients for the O₂($b^1\Sigma^+$) state obtained in these experiments agree well with predictions only for mean electron energies below 1.3 eV. These predictions are based on electron-beam measured cross sections for direct excitation of the $b^1\Sigma$ state, known collisional cascading processes, and current understanding of the dissociation of O₂ molecules. It appears that a significant revision of this model is required in order to explain the large excitation rate coefficients obtained in the present experiment. The simplest revision would be to find a way to understand nondissociative excitation of the O₂ levels responsible for the observed electron energy losses in the 4.5 to 7 eV range.

Measurements which would provide data useful in the explanation of this discrepancy are (a) the time lag in the growth of $b^1\Sigma$ population caused by the finite reaction rates in the cascading processes; (b) the rate coefficient for the dissociative excitation of O₂; (c) the rate coefficients for excitation of the O₂($a^1\Delta_g$) state³¹; and (d) rate coefficients for the vibrational excitation of O₂ using, for example, excitation transfer to CS₂ and its subsequent emission at 6.7 μ m to monitor the density of vibrationally excited O₂.¹³

In connection with potential applications of electron excitation of O₂, we note that the efficiency of energy transfer from electrons to O₂($b^1\Sigma$) molecules reaches a maximum of about 30% at $E/N = 2 \times 10^{-16}$ V cm² and decreases to about 20% at $E/N = 2 \times 10^{-15}$ V cm². If our hypothesis of large rate coefficients for excitation of

the 4.5–6 eV levels is correct, then about 60% of the input energy goes into these levels at E/N near 3×10^{-16} V cm².

ACKNOWLEDGMENTS

The authors wish to acknowledge helpful discussions with J. F. Noxon, G. M. Lawrence, and A. Gallagher. We also wish to thank M. Fellinger, C. E. Pelander, R. T. Weppner, and C. H. Muller III for help in the design, construction, and operation of the experimental apparatus. This work was supported in part by the Defense Nuclear Agency through the Air Force Cambridge Research Laboratories Project Order Nos. Y74-885 and Y75-933 and in part by Advanced Research Projects Agency and monitored by the Office of Naval Research under Contract N00014-76-C-0123.

APPENDIX A. DETECTION EFFICIENCY AND DIFFUSION CORRECTIONS

In this Appendix we first evaluate the geometrical factor G for various assumed spatial variations of the relative detection efficiency and for an analytic approximation to the experimentally measured variation of η . We next estimate the small corrections to G caused by radial diffusion. Finally, we evaluate the difference between the decay constant γ obtained by fitting to the measured transient and that of the fundamental diffusion mode.

I. Variable detection efficiency

The evaluation of the geometrical factor G discussed in Sec II, B for our experiment is most easily carried out by considering two additional simple forms of the detection efficiency. Thus, for $\eta_B(z) = \sin(\pi z/L)$, we find

$$G_B = \frac{\pi a(1 + e^{-a})}{(\pi^2 + a^2)(1 - e^{-a})} \quad (A1)$$

and in the limit of $a \rightarrow 0$, $G_B = 2/\pi$. Note that if the experiment were designed such that $\eta = \eta_B$, the evaluation of G and of α_b/N would not require a knowledge of the diffusion loss. Finally, for $\eta_C = (1 - 2z/L)$, only even values of m contribute to \sum_m and

$$G_C = \frac{a(\pi^2 + d^2)}{(a^2 - d^2)} \left[\frac{\coth(d/2)}{d} - \frac{2}{d^2} - \frac{\coth(a/2)}{a} + \frac{2}{a^2} \right]. \quad (A2)$$

Since the metastable molecule density has been assumed to be independent of radius, the experimental values of relative detection efficiency are first averaged over radius and angle to obtain $\eta_E(z)$. We find that to an accuracy of $\pm 5\%$ the efficiency $\eta_E(z)$ is given by

$$\eta_E = 0.45 + 0.55 \sin(\pi z/L) + 0.18(1 - 2z/L), \quad (A3)$$

so that

$$G_E = 0.45G_A + 0.55G_B + 0.18G_C. \quad (A4)$$

The estimated uncertainty in G_E is less than $\pm 5\%$ for the conditions of the data reported. Thus, in the limit of $d^2 \rightarrow \infty$ the values of G_E calculated using Eq. (A4) agree with numerically calculated values to within $\pm 3\%$ for values of a encountered in these experiments. The

variations in the magnitude of the correction for the spatial dependence of the detection sensitivity and for the effects of diffusion are most readily summarized by evaluating the ratio of the average detection efficiency to the values adjusted for the effects of diffusion and attachment, i.e., the ratio

$$\frac{\eta}{G_E(a, d)} = \frac{G_E(a = 0, d = \infty)}{G_E(a, d)}. \quad (A5)$$

For the data reported in this paper, the ratio in Eq. (A5) is 1.11 at low [O₂]. At the highest [O₂] values shown in Fig. 5 the ratio varies from 1.07 at $E/N = 8 \times 10^{-17}$ V cm² to 1.24 at $E/N = 8 \times 10^{-16}$ V cm². Note that at the higher [O₂] values these corrections are much smaller than the corrections for attachment included in the current ratio q .

II. Radial diffusion

The effects of radial diffusion can be estimated by replacing the circular cross section of the drift-tube chamber by a square cross section. In this approximation the emitting portion of the cathode is assumed to have an edge dimension of $2R$ and the square cross section of the chamber to have an edge dimension of $2T$ equal to the diameter of the drift-tube chamber. The volume seen from the photomultiplier is approximated by a rectangular box of dimensions L , by $2T$ along the line-of-sight or y direction, and by $2B$ along the x direction at right angles to the line-of-sight and to the drift-tube axis. Changes in effective solid angle intercepted by the photomultiplier cathode with distance from the photomultiplier are assumed to be compensated by departures from the assumed rectangular volume so that over the active volume the detection efficiency η is independent of the x and y positions for $|x| < B$ and $|y| < T$. With these assumptions a Fourier series expansion in the x , y , and z directions followed by the application of Eq. (7) yields

$$G_{3D} = \frac{a}{(1 - e^{-a})} \sum_{m=1}^{\infty} \sum_{j=1}^{\infty} \sum_{k=1}^{\infty} \frac{\gamma(111)}{\gamma(mjk)} \frac{2b_m}{m\pi} \theta(j, B)\theta(k, T), \quad (A6)$$

where

$$\theta(l, \tau) = \frac{8T \sin(l\pi R/2T) \sin(l\pi \tau/2T)}{l^2 \pi^2 R}$$

and

$$\gamma(mjk) = D(\pi/2T)^2(j^2 + k^2) + \gamma_m.$$

In these equations j , k , and m are odd integers and are associated with the x , y , and z directions, respectively. Note that for the purposes of this and the next subsection we have generalized the definition of G and Eq. (17) by replacing γ_1 by $\gamma(111)$, the decay constant for the fundamental diffusion mode in rectangular geometry.

The summations over j and k are carried out using the relation

$$p^2 \sum_l \frac{\theta[(2l-1), \tau]}{[(2l-1)^2 \pi^2 + p^2]} = 1 - \frac{2T}{pR} \frac{\sinh(pR/2T) \cosh(p/2 - p\tau/2T)}{\cosh(p/2)}, \quad (A7)$$

where $R < \tau < T$. Equation (A7) is first applied to the k summation with $\tau = T$ and $p^2 = j^2\pi^2 + (2T/L)^2(m^2\pi^2 + d^2)$. For the conditions of Fig. 5 the second term on the right-hand side of Eq. (A7) is 2% for $m = j = 1$ and the lowest gas density and decreases with increasing m , j , and [O₂]. This correction will be neglected and Eq. (A7) applied to the j summation with $\tau = B = 4, 5$ cm and $p^2 = (2T/L)(m^2\pi^2 + d^2)$. In this case, and for the data of Fig. 5, the correction term for $m = 1$ reduces the expected signal by 6% to 0.02% as the oxygen density increases. This correction applies directly to G_B , for which $m = 1$. Since the correction given by Eq. (A7) for higher values of m is less than 1%, the reductions in G_A , G_C , and the expected signal are less than for G_B .

III. Decay constant from fitting procedure

The systematic "error" resulting from the least-squares fitting of a single exponential to the data is estimated as follows: First, the theoretical "true" signal $S(t)$ including the effects of diffusion is calculated by replacing Eq. (7) by (A6). The signal during the production half-period can then be written as

$$S(t) = \beta \sum_m \sum_j \sum_k G(mjk) \{1 - \exp[-\gamma(mjk)]\}, \quad (A8)$$

where $\beta = S_0/G$ from Eq. (15) and the $G(mjk)$ are the terms in the summations in Eq. (A6). Next, the function

$$I = \int_0^\infty [S(t) - s(1 - e^{-\eta t})]^2 dt \quad (A9)$$

is evaluated for $\eta = \eta_A = 1$. Note that here we have assumed that the half-periods used for recording data are long enough so that the upper limit may be taken as $t = \infty$. Because of this long half period and because our fitting routine requires that the amplitude s be the same for the production and decay half periods, the amplitude is that given by the amplitude in Eq. (A8) at large times, i.e., by βG_{3D} . The value of γ obtained by minimizing the function I is very close to $\gamma(111)$ for both half periods, i.e.,

$$\frac{\gamma}{\gamma(111)} = 1 - \sum_{mjk} \frac{\rho(mjk)[3\gamma(111) + \gamma(mjk)][\gamma(mjk) - \gamma(111)]}{\rho(111)[\gamma(111) + \gamma(mjk)]^2}, \quad (A10)$$

where the ratios of amplitudes of time varying components of the signal are given by

$$\frac{\rho(mjk)}{\rho(111)} = \frac{\gamma(111)\theta(j, B)\theta(k, T)(\pi^2 + a^2)}{\gamma(mjk)\theta(1, B)\theta(1, T)(m^2\pi^2 + a^2)}.$$

The correction to γ given by Eq. (A10) is largest at the lowest density in Fig. 5. In our experiments only the $m = 1$, $j = 1$ or 3, and $k = 1$ or 3 terms contribute significantly to the summation and there is considerable cancellation among the terms. As a result, the value of γ expected from the fitting procedure is smaller than $\gamma(111)$ by less than 2%. This reduction is well within the uncertainty assigned to the diffusion coefficient obtained in Sec. IV.

The estimated reduction in the excitation rate coefficients obtained in Sec. V as the result of the neglect

of radial diffusion is approximately the sum of the calculated reductions in G and γ , i.e., about 10% at the lowest [O₂] of Fig. 5 and less than 0.1% at the highest densities. The estimated uncertainty in the final values of α_b/N by the neglect of radial diffusion is less than 3% and is negligible compared to other uncertainties.

APPENDIX B. DETERMINATION OF ELECTRON CURRENT AND ATTENUATION COEFFICIENT

In order to determine the electron contribution to the measured drift tube current and the electron attenuation coefficient α , the apparatus was modified as follows: The dc mercury lamp was replaced with a deuterium discharge lamp³² with rise and fall times of less than a microsecond. Pulse durations of 4–30 μ sec were used. The anode voltage was held constant and the current in the anode circuit was amplified and recorded with a transient digitizer with an overall time resolution of 0.1 μ sec. Peak currents of about 10^{-7} A were observed. Figure 9 illustrates a current profile obtained for $E/N = 3 \times 10^{-16}$ V cm² and [O₂] = 2.5×10^{17} cm⁻³ and a D₂ lamp pulse duration of 4 μ sec. The initial spike is caused primarily by electrons which drift across the gap in about 0.5 μ sec. The long tail is caused entirely by the relatively slow ions. At this value of E/N the ions are formed almost exclusively by two-body attachment³³ and no detachment should occur.³⁴ The O⁺ ions formed by dissociative attachment are rapidly converted into O₃⁺ ions with an expected transit time of about 160 μ sec.

Derivations of theoretical expressions for the current waveforms appropriate to the present experiments have been given by a number of authors.³⁵ We are concerned primarily with the determination of the ratio of the

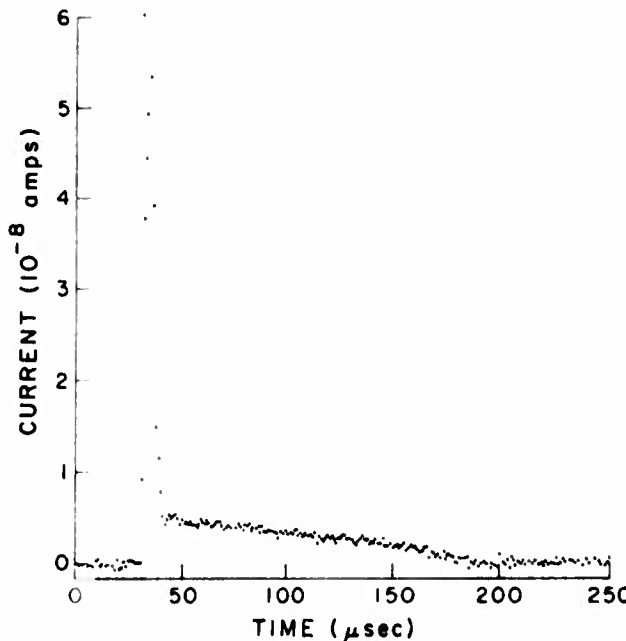


FIG. 9. Current waveform in the anode circuit resulting from illumination of drift tube cathode with a 4 μ sec pulse from a D₂ lamp. The O₂ density was 2.5×10^{17} cm⁻³ and $E/N = 3 \times 10^{-16}$ V cm². The charge in the electron pulse is 30% of the total charge.

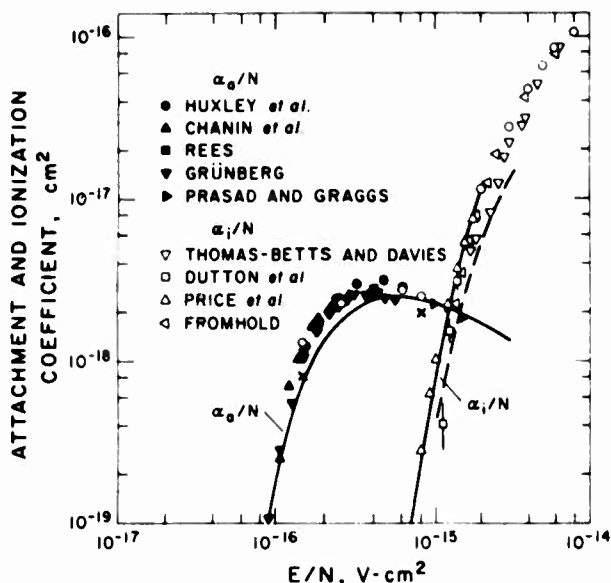


FIG. 10. Attachment and ionization coefficients in O₂. The open circles are the data obtained as discussed in Appendix B. The crosses show the attachment coefficients used to obtain the solid circles in Fig. 6. The dashed curve shows the average values of α_1/N obtained by Corbin and Fromhold (Ref. 57). The solid curves are calculated using the cross section set of Fig. 7.

electron current to the total current and make use of the equality of this ratio to the ratio of the charge in the electron current pulse to the total charge crossing the gap.³⁶ The experimental value for q is readily obtained by integrating waveforms such as shown in Fig. 9 on the multichannel analyzer. Thus, $1/q$ is the ratio of change in counts between the breaks in the waveform at the beginning and end of the electron pulse to the total change in counts from the beginning of the electron pulse to the end of the ion current pulse. A small correction is made for ion current flowing during the electron pulse.

In order to carry out the spatial averaging indicated in Eq. (7) one needs to know α_0 and α_1 rather than q . We have therefore used the measured values of q and Eq. (14) to obtain α_0/N at $E/N \geq 10^{-16}$ V cm² and α_1/N at $E/N \geq 2 \times 10^{-15}$ V cm². At the lower E/N these calculations made use of α_1/N values calculated using the cross sections of Fig. 7 and shown in Fig. 10. The two- and three-body attachment processes were then separated by taking the k_3/w_e values of Grünberg³⁶ as known. The values of k_2/w_e determined in this manner are shown by the open circles in Fig. 10, along with results of other experimental determinations³³ of k_2/w_e and a calculation using the cross section set of Fig. 7. The present experimental results are in good agreement with the earlier data. At the higher E/N the present determinations of α_1/N used α_0/N values calculated using the cross section set of Fig. 7. The resultant α_1/N values are in agreement with the larger of the earlier experimental values³³ and with the present calculations at $E/N = 2 \times 10^{-15}$ V cm².

The cross (\times) shown for $E/N = 8 \times 10^{-16}$ V cm² in Fig. 10 is the value²¹ of α_0/N which gave the values of α_1/N

shown by open circles in Fig. 5, while the set of crosses in Fig. 5 are the values of α_0/N calculated using our measured value of α_0/N and our calculated value of α_1/N . The crosses shown for $E/N = 1.5 \times 10^{-16}$ and 4×10^{-16} V cm² are the values of α_0/N used to obtain the corresponding values of α_1/N shown in Fig. 6. The reason for the differences between some of the α_0/N values obtained from the measurements of q and from the α_0/N versus N plots is unknown. Fortunately, the derived values of α_1/N are not very sensitive to the values of α_0/N used in the data analysis. For $E/N = 8 \times 10^{-17}$ V cm² and $[O_2] > 10^{17}$ cm⁻³ three-body attachment process dominates and the attachment coefficient used to obtain the open triangles of Fig. 5 is consistent with previous measurements.³⁴

APPENDIX C. ELECTRON COLLISION CROSS SECTION SET

This appendix gives the basis for our recommended set of cross sections shown in Fig. 7. This set is a modernization of that of Hake and Phelps³⁷ and differs from that of Watson *et al.*³⁸ partly because of its emphasis on low energy electrons. One requirement for the final data set is that it leads to calculated electron transport coefficients which are reasonably consistent with experiment.^{33,39} A second requirement is that the energy dependence of the cross sections be consistent with electron beam experiments. We believe that the cross section set of Fig. 7 comes much closer to meeting these conditions than previously available sets. The bases for the choices of the various cross sections are as follows:

(1) The momentum transfer cross section used is that of Hake and Phelps³⁷ except at energies below 1 eV, where $Q_m(\epsilon)$ has been reduced in order to improve agreement with recent drift velocity data by Nelson and Davis.⁴⁰ Note that the differential elastic scattering cross sections given by Trajmar, Cartwright, and Williams⁵ (hereafter referred to as TCW) give a much smaller elastic momentum transfer cross section at energies above about 7 eV than the total momentum transfer cross section of Hake and Phelps.³⁷ On the basis of the beam data⁵ it seems unlikely that the inelastic contribution will be sufficient to account for the difference.

(2) Rotational excitation (not shown in Fig. 7) is included by means of (a) a set of resonances at the energies of the O₂ states, each with the energy integrated cross section as given by Parlant and Fiquet-Fayard⁴¹ for elastic scattering, and (b) an effective quadrupole moment³⁷ of $0.3 ea_0^2$. This rotational cross section is intended to give the maximum possible energy loss which could occur via resonance rotational excitation.⁴² The set of resonances is entered using a single level approximation³⁷ to the large number of rotational levels. In the calculations of the electron energy distributions and the rate coefficients, the widths of the peaks are chosen consistent with the energy grid used in the calculations. Note that for high mean energies it is necessary to replace the peaked cross sections with smoothed (averaged) cross sections. Because of the small resonance widths in O₂, the contribution of this

process to the average electron energy loss is small, i.e., less than 5%. The effective quadrupole moment is determined by fitting drift velocity data⁴⁰ at electron energies below the first resonance, i.e., below about 0.09 eV.

If one uses the rotational excitation cross sections of Geltman and Takayanagi⁴³ in the single level approximation,³⁷ one obtains very large energy losses to rotational excitation and very poor agreement with measured transport data. Since we do not know how to modify their cross section to predict rotational excitation at energies well above threshold, we will absorb any such excitation in the cross sections for higher energy processes.

(3) Three-body electron attachment is represented by an equivalent cross section (not shown) for an oxygen density of one molecule per cm³ based on the integrated magnitudes of the electron energy dependent three-body coefficients of Spence and Schulz.⁴⁴ The attachment resonances above the first are located at the same energy as for vibrational excitation and the peak shapes are the same. The lowest attachment resonance has been split into peaks shaped as calculated by Fiquet-Fayard.⁴⁵ In order to fit the three-body attachment coefficient data at thermal energies⁴⁶ and at^{36,47} 2×10^{-18} eV/cm^2 , the lowest energy pair of peaks was centered at 0.10 eV and the integrated magnitude lowered to 70% of Spence and Schulz' value. Note that for our purposes there is little point in splitting the higher energy resonances. As pointed out by Spence and Schulz,⁴⁴ the magnitude of the lowest attachment resonance changes with gas temperature so that the "activation energy" found by Truby⁴⁸ cannot be used directly to calculate the location of the first attachment resonance.

One reason for including the three-body attachment in the analysis is an attempt to obtain more information about the near-thermal behavior of the electrons. Such data would help make up for the lack of D_T/μ data usually used to establish the energy scale. The available D_L/μ data from Nelson and Davis⁴⁰ do not extend to sufficiently low E/N and do not differ much from the thermal value. A second reason, of course, is to make comparisons with the three-body attachment measurements by Chanin, Phelps, and Biondi,⁴⁷ by Rees,⁴⁷ and by Grünberg.³⁶

(4) Vibrational excitation at electron energies below 4 eV is assumed to occur entirely by way of the O₂ resonances, such as shown in Fig. 7 for excitation of the $v=1$ level. The cross sections were obtained by choosing numerically convenient peak widths and, except for the first resonance, by raising the energy integrated values given by Linder and Schmidt⁴ by a factor of 2. Relative magnitudes not available from experiment were scaled from theory.⁴¹ These values are larger than those of Spence and Schulz⁴⁸ by about a factor of 20. The energy integrated magnitude of the first peak was increased to about 250 times the theoretical value of Parlant and Fiquet-Fayard.⁴¹ These increases were necessary in order to fit experimental values of the transport coefficients, i.e., to fit plots of v_u/N versus ϵ , such as shown in Ref. 37. The apparent need

to increase the Linder and Schmidt resonant cross section could be caused by our neglect of "direct" vibrational excitation or by our use of rotational excitation cross sections which are much too small. The former seems unlikely since Linder and Schmidt saw no evidence for significant direct excitation. Additional experiments are necessary in order to determine the relative importance of rotational and vibrational excitation.

At electron energies above 4 eV we have normalized the differential excitation cross sections of Wong, Boness, and Schulz⁴⁹ to the integrated values given at a few energies by TCW.

(5) Cross sections for electron excitation of the $a^1\Delta_g$ and $b^1\Sigma^+$ states of O₂ are taken directly from the published cross sections of TCW and of Linder and Schmidt.⁴ As indicated in Sec. V. A, our experiment is not sensitive to the differences between the cross sections given by TCW and by Konishi *et al.*⁶ With the addition of the $a^1\Delta_g$ and $b^1\Sigma^+$ cross sections, the resonance type cross section between 4.5 and 5.0 eV introduced by Hake and Phelps³⁷ was dropped.

(6) With regard to two-body attachment, we first note that several authors¹³ have revised their experimental two-body attachment coefficients upward because of the recognition of the need for correction due to anisotropic diffusion. We have multiplied the dissociative attachment cross section of Schulz⁵⁰ by a factor of 1.2 in order to improve the fit of calculated two-body attachment coefficients to the measured values at $E/N > 3 \times 10^{-16} \text{ V cm}^2$. This procedure results in calculated values which are about 70% of experiment at mean electron energies near 2 eV, i.e., $E/N \sim 2 \times 10^{-16} \text{ V cm}^2$. As in Hake and Phelps,³⁷ a number of different cross section sets were tried in an unsuccessful attempt to obtain good agreement with experiment attachment coefficients for $10^{-16} < E/N < 10^{-15} \text{ V cm}^2$ while retaining agreement with measured drift velocities and characteristic energies.

(7) The cross sections for energy losses of 4.5, 6, and 8.4 eV involve a lot of guess work. The available data include determinations of total inelastic cross sections by TCW and by Chantry⁵¹; trapped electron spectra by Schulz and Dowell⁵²; differential and integral cross section data by Trajmar, Williams, and Kupperman⁵; cross sections for the production of uv radiation, such as Mumma and Zipf⁵³; evidence for relative electronic excitation cross sections, such as Chantry⁵⁴; and theoretical papers, such as Cartwright *et al.*⁵⁵ and Watson *et al.*⁵⁶

There seems to be general agreement^{5,38,51,54} that for electron energies above 15 eV, the 8.4 eV energy loss, presumably $B^3\Sigma^+$ excitation, exceeds the other nonionizing energy loss processes by about an order of magnitude. Accordingly, we have simplified our calculations by neglecting all processes with more than 8.4 eV energy loss except ionization. The $B^3\Sigma^+$ cross section shown is equal to the total electronic cross sections of TCW and of Chantry⁵¹ for energies below 45 eV and the energy dependence at high energies is from

Watson *et al.*⁵⁶ Trajmar, Williams, and Kupperman⁵⁷ suggest that the dominant excitation process leading to the broad energy loss peak in the 4.5–7.5 energy range is excitation of the $c^1\Sigma_u$ state and that this cross section falls rapidly with increasing electron energy. The onset of significant energy loss at 4.5 eV is based on the trapped electron data of Schulz and Dowell.⁵² We have chosen to represent the energy losses between 4.5 and 8.4 eV by two cross sections, i.e., cross sections with 4.5 and 6.0 eV losses. The former was an attempt to represent the formation of excited O₂ in bound vibrational levels of the $c^1\Sigma_u$ state while the latter was intended to represent excitation of continuum states leading to the production of O(³P) atoms. The results presented in Sec. V seem to require that both excitation processes result in bound excited states of O₂. The relative magnitudes of these two cross sections is completely unknown and only their sum is shown in Fig. 7.

(8) We have used the ionization cross sections measured by Tate and Smith.⁵⁸ The calculated ionization rate coefficients are in satisfactory agreement with measurements except for the very recent results of Corbin and Fromhold.⁵⁷

Tabulations of the cross section set shown in Fig. 7 are given in JILA Data Center Memo No. 3 (unpublished). This memo also contains a data set in which the 8.4 ($B^3\Sigma$) cross section has been lowered at energies below 20 eV in order to bring the $B^3\Sigma$ excitation rate coefficient into approximate agreement with the rate coefficient for dissociation of O₂ as determined by Smith and Austin.⁵⁸ The cross section for the 6.0 eV loss process has been increased to a peak value of $1.5 \times 10^{-16} \text{ cm}^2$ at 12 eV so as to keep the total rate of electron energy loss in agreement with experiment. In this analysis the excitation of the 4.5 and 6.0 eV loss processes does not lead to dissociation of O₂ so that the resultant excited states of O₂ are available for collisional quenching to the $b^1\Sigma$ state. Thus, the low rate coefficients for dissociation of O₂ obtained by Smith and Austin are consistent with our rate coefficients for excitation of the $b^1\Sigma$ state.

⁵⁶J. F. Noxon, *J. Geophys. Res. Space Phys.* **75**, 1875 (1970); H. I. Schiff, J. C. Haslett, and L. R. Megill, *J. Geophys. Res. Space Phys.* **75**, 4363 (1970).

⁵⁷For a recent discussion and references to earlier papers see A. J. Deans, G. G. Shepherd, and W. F. J. Evans, *J. Geophys. Res. Space Phys.* **81**, 6227 (1976).

⁵⁸J. C. G. Walker, *Planet. Space Sci.* **18**, 1043 (1970); L. R. Megill, A. M. Despain, D. J. Baker, and K. D. Baker, *J. Geophys. Res. Space Phys.* **75**, 4775 (1970).

⁵⁹F. Linder and H. Schmidt, *Z. Naturforsch. Teil A* **26**, 1617 (1971).

⁶⁰S. Trajmar, W. Williams, and W. Kupperman, *J. Chem. Phys.* **56**, 3759 (1972); S. Trajmar, D. C. Cartwright, and W. Williams, *Phys. Rev. A* **4**, 1482 (1971); R. L. Hall and S. Trajmar, *J. Phys. B* **8**, L293 (1975).

⁶¹A. Konishi, K. Wakuya, M. Yamamoto, and H. Susuki, *J. Phys. Soc. Jpn.* **29**, 526 (1970).

⁶²See, for example, M. J. E. Gauthier and D. R. Snelling, *J. Photochem.* **4**, 27 (1975).

⁶³R. G. O. Thomas and B. A. Thrush, *J. Chem. Soc. Faraday Trans.* **271**, 664 (1975).

- ⁹L. R. Martin, R. B. Cohen, and J. F. Schatz, *Chem. Phys. Lett.* **41**, 394 (1976).
- ¹⁰S. A. Lawton, S. E. Novick, H. P. Broida, and A. V. Phelps, *J. Chem. Phys.* **66**, 1381 (1977).
- ¹¹L. Wallace and D. M. Hunten, *J. Geophys. Res.* **73**, 4813 (1968).
- ¹²R. B. O'Neill and A. M. Hart, in *Electronic and Atomic Collisions*, Abstracts of Papers of the IXth International Conference on the Physics of Electronic and Atomic Collisions, edited by J. S. Risley and R. Geballe (University of Washington, Seattle, 1975), p. 125.
- ¹³B. I. Bulos and A. V. Phelps, *Phys. Rev. A* **14**, 615 (1976).
- ¹⁴P. H. Krupenie, *J. Phys. Chem. Ref. Data* **1**, 423 (1972).
- ¹⁵D. I. Burch and D. A. Gryvnak, *Appl. Opt.* **8**, 1493 (1969). See also V. D. Galkin, L. N. Zhukova, and L. A. Mitrofanova, *Opt. Spektrosk.* **33**, 837 (1972) [Opt. Spectrosc. **33**, 462 (1972)].
- ¹⁶J. F. Noxon, *Can. J. Phys.* **39**, 1110 (1961).
- ¹⁷R. G. Derwent and B. A. Thrush, *Trans. Faraday Soc.* **67**, 2036 (1971).
- ¹⁸S. S. Penner, *Quantitative Molecular Spectroscopy and Gas Emissivities* (Addison-Wesley, Reading, Mass., 1959), Chap. 5.
- ¹⁹According to manufacturer's specifications the quantum efficiency varied by less than 2% over the 10 nm FWHM of the interference filter.
- ²⁰F. Bastien and M. Lecuiller, *J. Phys. B* **8**, 1981 (1975).
- ²¹The diffusion of electrons causes a small reduction (< 5%) in α from the values given by definitions following Eq. (2) and discussed in Appendix B. See, for example, R. W. Crompton, *J. Appl. Phys.* **38**, 4093 (1967).
- ²²This tungsten-strip-lamp radiance standard was traceable to NBS through a calibration provided by the manufacturer. For a description of similar lamps see R. Stair, R. G. Johnston, and E. W. Halbach, *J. Res. Natl. Bur. Stand. Sect. A* **64**, 291 (1960).
- ²³J. L. Moruzzi, *Rev. Sci. Instrum.* **38**, 1284 (1967); K. Martin and P. E. Secker, *J. Phys. E* **7**, 432 (1974).
- ²⁴The ~100 W commercial mercury lamp was removed from its glass envelope and mounted in a water-cooled metal housing.
- ²⁵See J. D. Cobine, *Gaseous Conductors* (McGraw-Hill, New York, 1941), p. 177.
- ²⁶The energy relaxation distance for electrons approaching a steady-state energy distribution is given by D_e/w_e , where D_e is the electron diffusion coefficient. See J. J. Lowke, J. H. Parker, Jr., and C. A. Hall, *Phys. Rev. A* **15**, 1237 (1977). For the conditions of Fig. 5 this calculated distance is 10% of the electrode separation for $[O_2] = 1 \times 10^{16} \text{ cm}^{-3}$ at $E/N = 8 \times 10^{-16} \text{ V cm}^2$. This prediction is consistent with the experimental data of Fig. 5, which shows that the excitation coefficients for this E/N reach about 90% of their final value at $[O] \approx 1.5 \times 10^{16} \text{ cm}^{-3}$. For $E/N = 8 \times 10^{-17} \text{ V cm}^2$, one predicts that the equilibrium distance is 10% of the electrode separation for $[O_2] \approx 3 \times 10^{16} \text{ cm}^{-3}$.
- ²⁷R. P. Wayne, in *Physics and Chemistry of Upper Atmospheres*, edited by B. M. McCormac (Reidel, Dordrecht, 1973), p. 128; and K. F. Langley and W. D. McGrath, *Planet. Space Sci.* **19**, 416 (1971).
- ²⁸G. F. Striet, C. J. Howard, A. L. Schmeltekopf, J. A. Davidson, and H. I. Schiff, *J. Chem. Phys.* **65**, 4761 (1976).
- ²⁹See, for example, R. F. Hampson and D. Garvin, "Chemical Kinetic and Photochemical Data for Modeling Atmospheric Chemistry," *Natl. Bur. Stand. (U.S.) Tech. Note 866* (1975).
- ³⁰The fraction of the O(¹D) atoms escaping destruction by N₂ so as to transfer excitation to the O₂($b^1\Sigma$) states was calculated to be 92% for the $[N_2]/[O_2] = 1/9$ mixture.
- ³¹This measurement was the original motivation for the present work, but could not be carried out because of failure of the high-sensitivity detector of 1.27 μm radiation.

- ³²R. F. Weeks, J. Opt. Soc. Am. **49**, 429 (1959).
- ³³J. Dutton, J. Phys. Chem. Ref. Data **4**, 577 (1975). For a recent revision of some of the data, see L. G. H. Huxley and R. W. Compton, *The Diffusion and Drift of Electrons in Gases* (Wiley, New York, 1974), Chap. 14.
- ³⁴For a review of detachment and other reactions of negative ions in oxygen, see D. A. Parkes, Vacuum **24**, 561 (1974).
- ³⁵See, for example, D. Edelson and K. B. McAfee, Jr., Rev. Sci. Instrum. **35**, 187 (1964); L. Fromhold, Forschr. Phys. **12**, 597 (1964); and H. Raether, *Electron Avalanches and Breakdown in Gases* (Butterworths, London, 1964), Chap. 2.
- ³⁶R. Grünberg, Z. Naturforsch. Teil A **24**, 1039 (1969). The quantity q is given in the final equation in the appendix.
- ³⁷R. D. Hake, Jr. and A. V. Phelps, Phys. Rev. **158**, 70 (1967); see also, H. Meyers, J. Phys. B **2**, 393 (1969); A. T. Bell and K. Kwong, Ind. Eng. Chem. Fundam. **12**, 90 (1973); J. Lucas, D. A. Price, and J. L. Moruzzi, J. Phys. D **6**, 1503 (1973); K. Mašek, T. Růžička, and L. Láska, Czech. J. Phys. B **27**, 888 (1977); K. Mašek, L. Láska, and T. Růžička, J. Phys. D **10**, L25 (1977).
- ³⁸C. E. Watson, V. A. Dulock, Jr., R. S. Stolarski, and A. E. S. Green, J. Geophys. Res. **72**, 3961 (1967).
- ³⁹The cooling rates and cross sections recommended by S. S. Prasad and D. R. Furman, J. Geophys. Res. **78**, 6701 (1973) lead to serious disagreement between calculated and measured electron transport coefficients.
- ⁴⁰D. R. Nelson and F. J. Davis, J. Chem. Phys. **57**, 4079 (1972).
- ⁴¹G. Parlant and F. Fiquet-Fayard, J. Phys. B **9**, 1617 (1976); see also F. Kotke, J. Phys. Soc. Jpn. **35**, 1166 (1973).
- ⁴²See, for example, N. Chandra and P. G. Burke, J. Phys. B **6**, 2355 (1973).
- ⁴³S. Geltman and K. Takayanagi, Phys. Rev. **143**, 25 (1966).
- ⁴⁴D. Spence and G. J. Schulz, Phys. Rev. A **5**, 724 (1972).
- ⁴⁵F. Fiquet-Fayard, J. Phys. B **8**, 2880 (1975); see also J. E. Land and W. Raith, Phys. Rev. A **9**, 1592 (1974).
- ⁴⁶F. K. Truby, Phys. Rev. A **6**, 671 (1972).
- ⁴⁷L. M. Chanin, A. V. Phelps, and M. A. Biondi, Phys. Rev. **128**, 219 (1962); J. A. Rees, Austr. J. Phys. **18**, 41 (1965).
- ⁴⁸D. Spence and G. J. Schulz, Phys. Rev. A **2**, 1802 (1970).
- ⁴⁹S. F. Wong, M. J. W. Boness, and G. J. Schulz, Phys. Rev. Lett. **31**, 969 (1973).
- ⁵⁰G. J. Schulz, Phys. Rev. **128**, 178 (1962).
- ⁵¹P. J. Chantry, Final Report, Contract DAHC04-69-C-0094, Westinghouse Research Laboratories, August 1970 (unpublished).
- ⁵²G. J. Schulz and J. T. Dowell, Phys. Rev. **128**, 174 (1962).
- ⁵³M. J. Mumma and E. C. Zipf, J. Chem. Phys. **55**, 1661 (1971).
- ⁵⁴P. J. Chantry, J. Chem. Phys. **55**, 1851 (1971).
- ⁵⁵D. C. Cartwright, W. J. Hunt, W. Williams, S. Trajmar, and W. A. Goddard III, Phys. Rev. A **8**, 2436 (1973).
- ⁵⁶J. T. Tate and P. T. Smith, Phys. Rev. **39**, 270 (1932).
- ⁵⁷R. J. Corbin and L. Fromhold, Phys. Rev. A **10**, 2273 (1974).
- ⁵⁸A. I. S. Smith and J. M. Austin, Dyn. Mass Spectrom. **4**, 211 (1976).

Quenching of $N_2(A^3\Sigma_u^+; \nu=0,1)$ by N_2 , Ar, and H_2

D. Levron and A. V. Phelps^{a)}

Joint Institute for Laboratory Astrophysics, National Bureau of Standards and University of Colorado,
Boulder, Colorado 80309

(Received 24 April 1978)

This note presents improved measurements of rate coefficients for the quenching of the $\nu=0$ and $\nu=1$ levels of the $A(^3\Sigma_u^+)$ metastable state of N_2 by N_2 , Ar, and H_2 , using very low levels of excitation and high gas purity. Designating the $\nu=1$ and $\nu=0$ vibrational levels of the $A^3\Sigma_u^+$ state by A^1 and A^0 , respectively, our rate coefficients or their upper limits vary from agreement with published values^{1,2} for $N_2(A^0)$ quenching by H_2 to 100 times smaller than published values¹⁻³ for $N_2(A^0)$ and $N_2(A^1)$ quenching by Ar.

Nitrogen molecules were excited by low energy electrons in the drift tube described in Ref. 4. Following a pulse of applied voltage and resultant photocurrent the decays of the $N_2(A^0)$ and $N_2(A^1)$ densities were determined from the intensities of the 0-6 and 1-9 bands of the $A-X$ system⁵ near 276 and 320 nm, respectively.

No emission was observed from $N_2(A^3\Sigma_u^+, \nu > 1)$ or from NO, e.g., the 259.6 nm band. The radiation was observed with a cooled bi-alkali quartz-window photomultiplier using an $f/6.3$ monochromator with 2.5 nm (FWHM) resolution. Photomultiplier pulses were accumulated for about 10 min. After several days bakeout at 150–200°C the pressure was below 10^{-5} Pa. The gas was changed frequently so that the outgassing of less than 3×10^{-4} Pa h⁻¹ could be neglected. High purity gases (> 99.999%) were held at liquid nitrogen (for N_2 and H_2) or dry ice (for Ar) temperatures for at least two hours before use. Pressures were measured to $\pm 0.25\%$. The electric field to gas density E/N values used were $8-12 \times 10^{16}$ V cm² for N_2 and N_2-H_2 and $1-1.5 \times 10^{16}$ V cm² for N_2-Ar . Quenching by N atoms or excited N₂ was avoided by use of a short excitation pulse, e.g., a pulse length about equal to the lifetime of the $N_2(A^1)$ metasta-

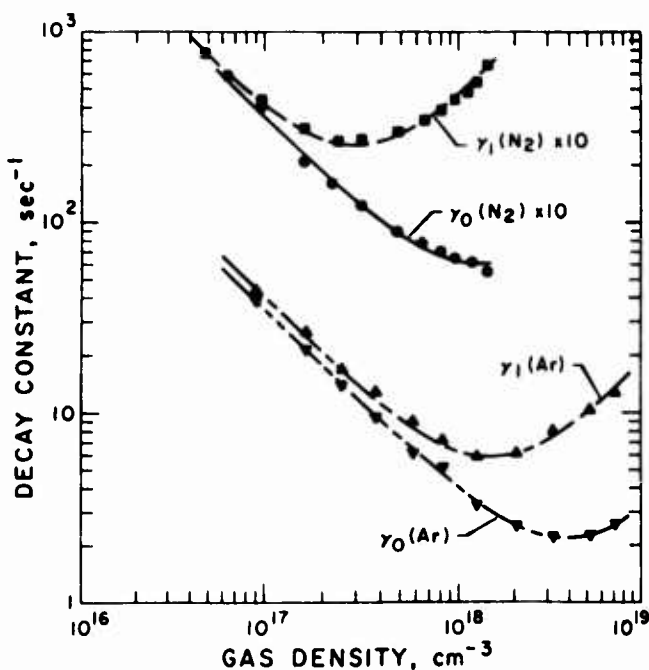


FIG. 1. Decay constants for the $\nu=0$ and $\nu=1$ levels of the $N_2(A^3\Sigma^+_u)$ state. The \bullet and \blacksquare are decay constants for the A^0 and A^1 levels in N_2 , while the \blacktriangledown and \blacktriangle show data for the A^0 and A^1 levels in Ar. Note that the data shown for Ar have been corrected for the small ($<30\%$) effect of quenching by N_2 on the decay constant. The curves are least-square fits to the data.

ble, and by keeping the peak photocurrent and excited molecule densities less than $1.5 \times 10^{-9} \text{ A/cm}^2$ and 10^9 cm^{-3} for pure N_2 and about a factor of 3 smaller for $\text{Ar}-N_2$. Argon and hydrogen metastables decayed rapidly compared to $N_2(A^3\Sigma^+)$ metastables.

The molecular metastable density at late times decreases exponentially with a decay constant by $\gamma = A + kN + D/\Lambda^2$. Here A is the radiative transition probability, k is the quenching rate constant, N is the quenching gas density, D is the diffusion coefficient, and Λ (1.18 cm) is the lowest mode diffusion length⁴ of the drift tube. The counting rate minus background decayed exponentially over almost two decades.

The upper sets of points in Fig. 1 show decay con-

stants γ_0 and γ_1 measured for the $N_2(A^0)$ and $N_2(A^1)$ levels versus nitrogen density. The smooth lines are least-squares fits of the formula for γ . The lower sets of points show values of γ_0 and γ_1 for N_2 -Ar mixtures after subtraction of the kN term due to the 1%-15% N_2 present in the mixture. The A value of $0.5 \pm 0.2 \text{ sec}^{-1}$ obtained from $N_2(A^0)$ measurements in $\text{Ar}-N_2$ agrees with Shemansky's value⁶ and was used to analyze other data. The diffusion coefficients at unit density were $(5.0 \pm 0.3) \times 10^{18} \text{ cm}^{-1} \text{ sec}^{-1}$ for $N_2(A^0)$ in N_2 and Ar and $N_2(A^1)$ in N_2 and $(5.5 \pm 0.2) \times 10^{18} \text{ cm}^{-1} \text{ sec}^{-1}$ for $N_2(A^1)$ in Ar. The N_2 value agrees with previous measurements.^{7,8} The rate coefficients for $N_2(A^0)$ and $N_2(A^1)$ de-excitation by H_2 were obtained by fitting $\gamma = k_{H_2}[H_2] + C$ to the decay constant data when H_2 was added to N_2 .

Quenching rate coefficients from Fig. 1, the H_2-N_2 data, and recent publications are summarized in Table I. Our coefficients for $N_2(A^0)$ quenching by N_2 and Ar are believed to be upper limits due to impurities admitted with the gases. Our upper limit for $N_2(A^0)$ quenching by N_2 is about four times faster than obtained by reanalysis of data by Brömer and Spieweck.⁸ Since quenching of $N_2(A^0)$ and $N_2(A^1)$ by oxygen greatly exceeds that by H_2O , etc.,^{1,2,9} the rate coefficients in Table I listed under "final k " for $N_2(A^1)$ in N_2 and Ar are obtained by assuming that $N_2(A^0)$ quenching in N_2 and Ar is caused by O_2 and by using measured relative quenching coefficients to correct for quenching of $N_2(A^1)$ by O_2 . The corrected rate coefficients shown have large uncertainties because of disagreements among the published O_2 data.^{1,2,9}

In Table I quenching rate coefficients obtained by excitation transfer^{1,2} or photoionization¹⁰ techniques are assigned to the more slowly decaying $N_2(A^0)$ level. This assignment leads to agreement between our value and published data^{1,2} for $N_2(A^0)$ quenching by H_2 . On the other hand, the agreement between our value for $N_2(A^1)$ quenching by N_2 and the quenching coefficient obtained for $N_2(A^0, A^1)$ by Vidaud *et al.*¹⁰ suggests that their photoionization technique is level selective.

Experiments to be reported later show that the $N_2(A^1)$ molecules are deexcited to $N_2(A^0)$ by H_2 and N_2 as proposed by Noxon¹¹ for N_2 . The available measurements

TABLE I. Quenching rate coefficients at 300°K in $\text{cm}^3 \text{ molecule}^{-1} \text{ sec}^{-1}$.

Excited State/Quencher	Measured k	Final k^*	Previous k
$N_2(A^0)/N_2$	$(2.0 \pm 0.6)(-18)^b$	$< 2.6(-18)$	$< 1(-17),^1 < 4.7(-16)^3$ $< 6(-19),^8 (4.5 \pm 1.2)(-17)^{10}$
$N_2(A^1)/N_2$	$(4.3 \pm 0.2)(-17)$	$(3.8 \pm 0.4)(-17)$	$< 4.4(-16),^3 \sim 4(-19)^{11}$
$N_2(A^0)/\text{Ar}$	$(1.8 \pm 0.2)(-19)$	$< 2.0(-19)$	$< 1(-17),^1 < 7(-15)^2$
$N_2(A^1)/\text{Ar}$	$(1.8 \pm 0.2)(-18)$	$(1.3 \pm 0.3)(-18)$	$(2.1 \pm 0.8)(-16)^3$
$N_2(A^0)/H_2$	$(2.4 \pm 0.3)(-15)$	$(2.4 \pm 0.3)(-15)$	$3(-15),^1,^2 1.9(-15)^2$
$N_2(A^1)/H_2$	$(4.4 \pm 0.4)(-14)$	$(4.4 \pm 0.4)(-14)$	----

*These values for $N_2(A^1)$ quenching by N_2 and Ar are corrected for estimated quenching by O_2 while the values for $N_2(A^0)$ quenching by N_2 and Ar are the upper limits of the measured values.

^b $(2.0 \pm 0.6)(-18)$ means $(2.0 \pm 0.6) \times 10^{-18}$.

Letters to the Editor

in Ar-N₂ mixtures do not allow us to determine the state of the product of quenching collisions.

This work was supported in part by the Advanced Research Projects Agency and was monitored by the Office of Naval Research under Contract N00014-76-C-0123.

^aStaff Member, Quantum Physics Division, National Bureau of Standards and Lecturer, Department of Physics and Astrophysics, University of Colorado.

¹A. B. Callear and P. M. Wood, *Faraday Soc. Trans.* 67, 272, 598 (1971).

²R. A. Young, G. Black and T. G. Slanger, *J. Chem. Phys.* 50, 303 (1969); G. Black, T. G. Slanger, G. A. St. John, and R. A. Young, *J. Chem. Phys.* 51, 116 (1969); T. G. Slanger, B. J. Wood, and G. Black, *J. Photochem.* 2, 63 (1973/74).

³J. W. Dreyer and D. Perner, *J. Chem. Phys.* 58, 1195 (1973);

C. R. Roy, J. W. Dreyer and D. Perner, *Ibid.* 63, 2131 (1975).

⁴S. A. Lawton and A. V. Phelps, *J. Chem. Phys.* 69, 1055 (1978). See also R. R. Bulos and A. V. Phelps, *Phys. Rev.* 14, 615 (1976).

⁵A. Lofthus and P. H. Krupenie, *J. Phys. Chem. Ref. Data* 6, 113 (1977).

⁶D. E. Shemansky, *J. Chem. Phys.* 51, 689 (1969).

⁷E. C. Zipf, Jr., *J. Chem. Phys.* 38, 2034 (1963); G. N. Hays, C. J. Tracy, A. R. Demonchy, and H. J. Oskam, *Chem. Phys. Lett.* 14, 352 (1972).

⁸H. H. Brömer and F. Spieweck, *Planet. Space Sci.* 15, 689 (1967).

⁹J. A. Meyer, D. W. Setser, and D. H. Stedman, *J. Phys. Chem.* 74, 2238 (1970); O. J. Dunn and R. A. Young, *Int. J. Chem. Kinet.* 8, 161 (1972); J. W. Dreyer, D. Perner, and C. R. Roy, *J. Chem. Phys.* 61, 3164 (1974).

¹⁰P. H. Vidaud, R. P. Wayne, M. Yaron, and A. von Engel, *J. Chem. Soc., Faraday Trans. II* 72, 1185 (1976).

¹¹J. F. Noxon, *J. Chem. Phys.* 36, 926 (1962).

High-power discharge in Na-Xe vapor

H. L. Rothwell,^{a)} D. Leep,^{b)} and A. Gallagher^{c)}

Joint Institute for Laboratory Astrophysics, University of Colorado and National Bureau of Standards, Boulder, Colorado 80309

(Received 2 March 1978; accepted for publication 5 April 1978)

High-power (10–100 MW/liter) pulsed discharges in Na-doped Xe vapor have been studied at Na densities of 10^{15} – 10^{16} cm⁻³ and Xe densities of 10^{19} – 10^{20} cm⁻³, as appropriate for excimer-laser use. Stable steady-state discharges are obtained for a number of microseconds in a small-volume cell, without use of preionization or sustainers. This stability is attributed to the observed positive V - I characteristic. Measured spectra are interpreted to yield Na excited-state densities, and the implications for a potential excimer laser are discussed.

PACS numbers: 52.25.Ps, 52.80.-s, 42.55.Hq

I. INTRODUCTION

Continuous discharges in alkali vapors, often mixed with a noble gas or Hg, have been studied for many years because of their importance in lighting.¹ These discharges, or arcs in some cases, are characterized by nearly identical gas, excitation, and electron temperatures in any local region. High-power visible tunable excimer lasers² and metal-dimer lasers³ based on these same gas mixtures have been proposed, with the possibility of efficient transfer of energy to the lasing states an attractive feature. In these proposed laser systems, the excitation temperature must greatly exceed the gas temperature to achieve net gain, and required discharge power densities are typically 10^2 MW/liter, more than 10^4 times that encountered in lighting. To maintain approximately the initial gas temperature at these power densities for even a few microseconds, a high-density ($> 10^{19}$ cm⁻³) buffer gas is required as a heat sink. In the proposed metal-noble-gas excimer lasers, the buffer gas also forms the excimer molecules, with the high densities also being necessary to yield useful gain coefficients for these weakly bound excimers. The high power, high density, and relatively high excitation temperatures (≥ 0.5 eV) necessary for lasing action increase the possibility of arcing or discharge instabilities. To establish the viability of these potentially valuable lasers, the electrical and optical properties of high-power pulsed discharges must be determined. We report here our measurements of these properties in a small-volume prototype system. Modeling of the plasma processes is also underway for comparison to these measurements.⁴

We report here studies of a Na and Xe mixture. This is an interesting laser candidate, the NaXe (excimer) and Na₂ (dimer) bands are well understood, and the important gas and electron collisional properties are better known for Na than for the other alkalis. Studies of other mixtures are also under way, with results for

a TLXe discharge system in preparation. Additional details of the apparatus measurements and results can be found in Ref. 5.

II. APPARATUS

A sketch of the gas cell and discharge region is shown in Fig. 1. Temperatures ranging from 350 to 500°C are used to maintain Na in the desired saturated vapor density of 10^{15} to 10^{16} cm⁻³. The temperature is monitored by a thermocouple affixed to the base of the anode. Measurements of the absorption-line profiles of the Na resonance lines were carried out to determine the number density of Na atoms. Our results agreed to within the experimental uncertainty of $\pm 50\%$ with the published vapor pressure,⁶ and the latter were used throughout the experiment to convert cell temperature to sodium concentration.

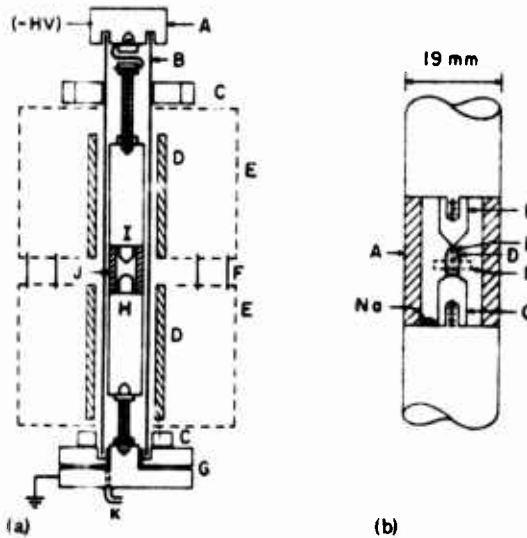


FIG. 1. (a) Discharge cell: A, stainless cap; B, quartz jacket, indium soldered to the top cap and bottom flange; C, water cooling; D, heater coils; E, firebrick enclosure; F, quartz windows; G, bottom flange and anode base with indium gasket seal; H, anode support (Kovar); I, cathode support (Kovar); J, Sapphir tube; K, pump out and gas inlet. (b) Cross section of discharge region, drawn to scale for a 5.3-mm gap. A, sapphire tube; B, cathode (molybdenum); C, anode (molybdenum); D, discharge positive column; E, cathode bright spot; F, viewed region for diagnostics of positive column.

^{a)}Present address: Physics Dept., Denver University, Denver, Colo. 80210.

^{b)}Present address: Physics Dept., University of Washington, Seattle, Wash. 98195.

^{c)}Staff Member, Quantum Physics Division, National Bureau of Standards.

Since Na vapor reacts with Pyrex and quartz, a sapphire sleeve is used to help confine the vapor to the discharge region. The ground ends of the sapphire are in mechanical contact with the Kovar electrode supports and do not make a vacuum seal.

An initial quartz-metal sealing configuration employing rubber O-rings was unreliable, and air impurities in this cell, estimated as $\sim 10^{16} \text{ cm}^{-3}$, were observed to cause $\sim 50\%$ reduction in the excimer-band light output during the discharge. An indium solder quartz-metal seal is used in the present cell and impurities are deemed insignificant in the data presented below. A distillation procedure for the Na was also used as a precaution, but identical discharge operation was obtained using a chip of freshly cut Na placed on the anode just prior to final assembly. In addition the research-grade xenon was passed through a baked-out titanium sponge before entering the gas cell.

The discharge region is viewed through four windows in the oven wall. The physical appearance of the discharge can be photographed with a camera which is not used for quantitative measurements. The time dependence of light emitted from region F in Fig. 1(b) is monitored by photomultiplier tubes, each detecting a wavelength region defined by an interference filter. The filters are chosen to include a wavelength region in the NaXe excimer band (670 nm) and one at the Na resonance lines. The rise time of the associated electronics is 20 nsec. The spatial-intensity distribution in region F in Fig. 1(b) is measured with an SIT vidicon tube, which records the total light emitted in the 630–640-nm wavelength region during a discharge pulse. The discharge spectrum is measured with a scanning 0.5-m spectrometer with $\sim 3\text{-}\AA$ resolution. The associated photomultiplier output is sampled in a specific time interval, typically centered at 2 μsec after onset of the discharge. Repetitive discharges are necessary for accumulation of a spectrum; the discharge repetition rate is limited to 10 Hz to avoid possible gas heating. The spectral sensitivity of the spectrometer and the photomultiplier sensitivities, as filtered, are measured using a diffuse reflector, illuminated by a calibrated tungsten iodide lamp, in place of the discharge.

The interelectrode current and voltage are monitored by a commercial current transformer and high-voltage probe. These and the photomultiplier outputs are displayed on an oscilloscope; the time resolution is ~ 20 nsec.

III. DISCHARGE STABILITY

In order to allow comparison to steady-state models, we have maintained the discharge in a current-regulated constant-current mode for several microseconds following initial preionization. Preionization by a uv flashlamp and by multiphoton ionization with a dye laser was investigated but found to be unnecessary to maintain discharge stability. For the data presented, the discharge was initiated by applying a voltage of ~ 4 kV across a 0.5-cm gap, using a current-regulated pentode tube circuit. After 0.2–1 μsec , depending on densities, the current increased rapidly and discharged the electrode capacitances. Following ~ 1 μsec of

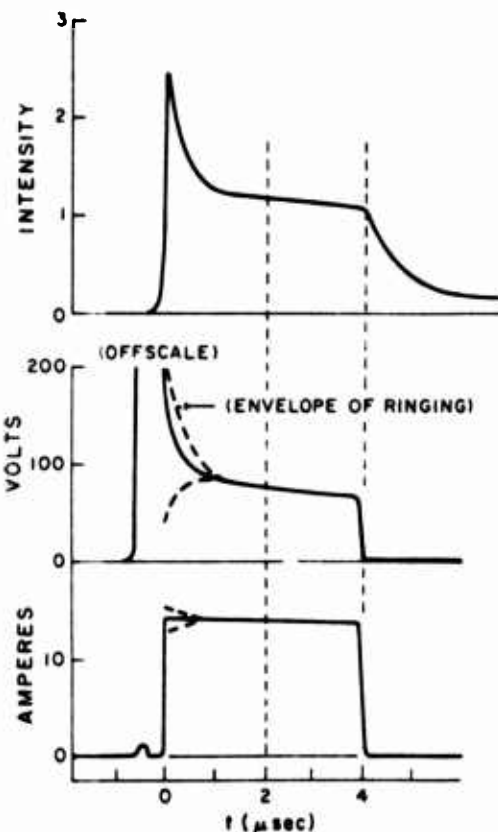


FIG. 2. Time dependences for a 4- μsec discharge. Light intensity from zone F in Fig. 1(a) at 562 nm (through a 0.5-nm half-width filter), total interelectrode voltage, and total discharge current are shown for $[\text{Na}] = 6.3 \times 10^{15} \text{ cm}^{-3}$ and $[\text{Xe}] = 4.4 \times 10^{19} \text{ cm}^{-3}$.

ringing, the voltage settled in the neighborhood of 100 V with the discharge current regulated at 1–20 A. The current, voltage, and light output for a representative set of conditions are reproduced in Fig. 2.

As can be seen in Fig. 2, the discharge voltage slowly sagged during the (constant current) discharge pulse. The gas heating during this 4- μsec 130-A/cm² pulse is $\sim 70^\circ\text{C}$ in region F of Fig. 1(b). As an example of a longer discharge, a 7-A/cm² pulse was held on for ~ 100 μsec , representing a gas heating of $\sim 200^\circ\text{C}$ in region A. These pulses were terminated to protect the current-regulating tetrode, so these values represent lower limits to the feasible energy deposition.

Initially, molybdenum button electrodes were used. Using only Xe vapor at 10^{19} – 10^{20} cm^{-3} density, a single filamentary arc would discharge between the electrodes, as is normally observed in pure noble gases. But at $[\text{Na}] > 10^{14} \text{ cm}^{-3}$, the discharge homogeneously filled the volume between electrodes at a current $I \leq 0.5$ A. At $I \geq 1$ A, the discharge would spread out from bright cathode spots, with the number of spots increasing with I . With the onset of cathode spots, the cathode fall voltage dropped from ~ 150 to ~ 20 V. In order to control the positions and number of cathode spots, a conical molybdenum cathode of 90° full angle and buffed to a rounded point was then used. This cathode, combined with a 5-mm-diam flat anode was used for the results reported here. The electrode gap was nor-

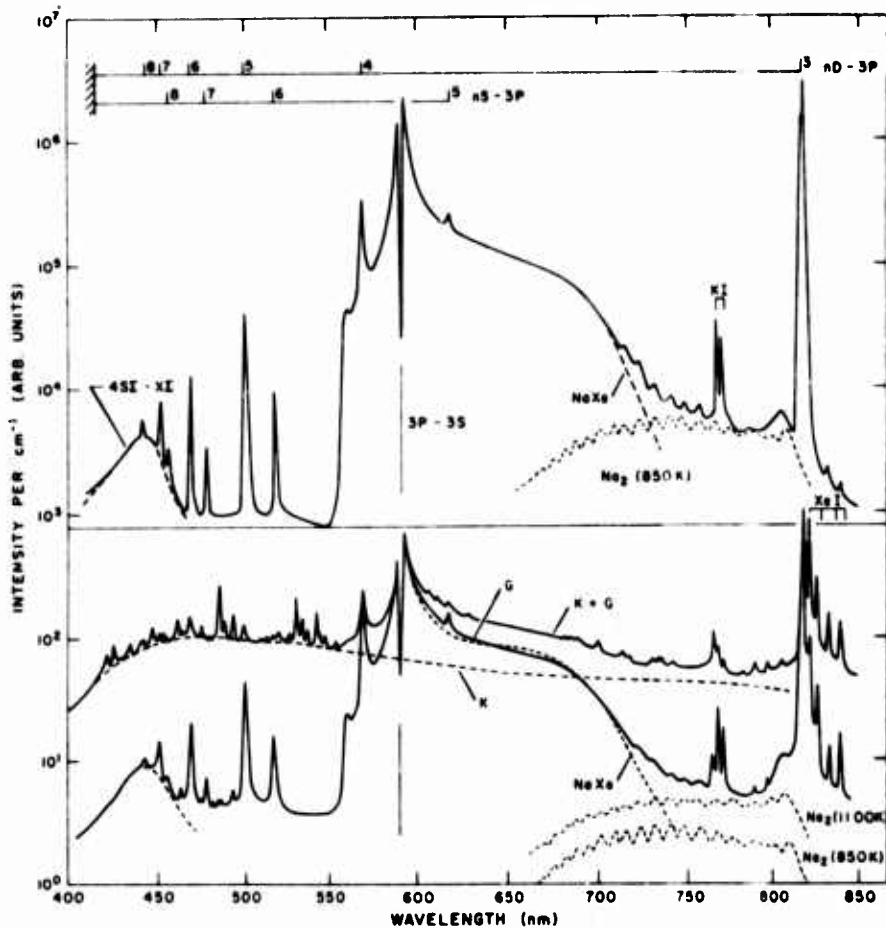


FIG. 3. Discharge intensity per unit frequency interval for two discharge conditions. Top spectrum: $[Na] = 6.8 \times 10^{15}$; $[Xe] = 2.8 \times 10^{19} \text{ cm}^{-3}$; current density $\approx 7 \text{ A/cm}^2$; interelectrode voltage $\approx 100 \text{ V}$. Bottom spectrum: $K + G$, from an 8-mm-wide 2-mm-high zone that includes the cathode bright spot; G , from region F in Fig. 1(b), in the positive column; K , difference between $K + G$ and G spectrum, attributed to cathode bright spot, $[Na] = 6.3 \times 10^{16} \text{ cm}^{-3}$; $[Xe] = 4.4 \times 10^{19} \text{ cm}^{-3}$, current density $\approx 130 \text{ A/cm}^2$, $E/N \approx 3 \times 10^{-18} \text{ V cm}^2$. The $Na_2(A-X)$ bands, from a thermalized A state, at the indicated temperatures, are from Ref. 9.

mally 5.3 mm, except for a respacing to 10.0 mm to establish the fraction of the total voltage attributable to the cathode fall. At all $[Na]$, $[Xe]$, and currents ($1-20 \text{ A}$) studied, the discharge spread out from a small bright spot at this cathode point into a homogeneous volume discharge, as indicated in Fig. 1(b). The width of the discharge in the glow region (region F in Fig. 1(b)] was measured and found to increase with increasing I and decreasing N , with the anode size clearly limiting the discharge area in some cases. The size of the bright cathode spot and the widths of the glow-discharge region were essentially constant during the several microseconds of discharge.

IV. RESULTS

The emission spectrum is shown in Fig. 3 for two discharge conditions. The contribution of the $NaXe$ $A-X$ band,⁷ the $4S\Sigma-X\Sigma$ band,⁸ and the $Na_2 A-X$ band⁹ are identified in Fig. 3 along with lines from higher-lying Na levels. The top spectrum is from the $I < 0.5 \text{ A}$ homogeneous glow mode (current density $\sim 7 \text{ A/cm}^2$). With the exception of a few Xe I lines beyond 800 nm and a trace amount of potassium, all emission from this discharge is attributed to excited Na. In the lower half of Fig. 3 spectra from two different spatial regions are compared. The solid-line curves G are representative of a high-current-density ($\sim 130 \text{ A/cm}^2$) discharge spectrum for light emitted from the positive column region, region F in Fig. 1(b). The curve labeled $K + G$ is typical of light originating from a $\sim 2\text{-mm-high}$

4-mm-wide zone that includes the cathode. Since light from outside the cathode spot is included in this, we have estimated the spectrum of the cathode spot by subtracting the spectrum of zone A, normalized to remove the Na lines in the $K + G$ spectrum. This yields the line labeled K , which is assumed to characterize the cathode spot. This spectrum looks like a thermal continuum and is similar to a high-pressure Xe flash-lamp spectrum.

The dotted line labeled $NaXe$ is the shape of the $A-X$ band, as measured in Ref. 7 and adjusted to our operating temperature. The minor difference in the shape of the dotted curve could be due to an elevated vibrational temperature of the $NaXe^*$ A state. This could be due to electron collisions with $NaXe^*$ plus gas heating.

The regular intensity undulations in the 720–780-nm region in Fig. 3 are attributed to the $Na_2 A-X$ band, as they match the expected positions of the $A-X$ band peaks.⁹ The emission spectrum from the $Na_2 A$ state with an 850-K thermal-population distribution is shown in the top and bottom of Fig. 3, with an intensity sufficient to explain the observed intensity undulations in each case. In order to explain the total intensity in the 720–800-nm region for the 130-A/cm^2 case, we then need to postulate an additional broad continuum, with intensity ~ 4 in units of Fig. 3; this appears consistent with the observed intensity in the 470–550-nm region. However, the 720–800-nm intensity could also be attributed entirely to a $Na_2 A-X$ band from a thermal

A-state population distribution at ~1100 K, as shown in the bottom of Fig. 3. Such an elevated-temperature distribution could easily result from *A*-state collisional destruction before complete vibrational relaxation. The broad feature observed at 810 nm in both spectra may also be the Na₂ *A-X* band satellite,⁹ but as can be inferred from the two Na₂ bands shown in Fig. 3, it is necessary to invoke a nonthermal *A*-state population distribution to explain both the satellite intensity and the magnitude of the intensity undulations in either spectrum. The actual Na₂ *A-X* band intensity thus remains somewhat uncertain, and one cannot tell if Na₂ *A*-state atoms are being depleted relative to NaXe *A*-state atoms at the higher current densities. Such depletion of Na₂ *X*- and *A*-state molecules is expected to occur at high current densities, due to electron-collisional dissociation of the *X* and *A* states.

The discharge is cylindrically symmetric, and for most conditions the observed spatial distribution of the light from the positive column is close to that given in Fig. 4. Minor asymmetries are attributed to reflections from the sapphire and quartz cylinders, and for a given set of conditions this distribution was reproducible to $\pm 10\%$ from shot to shot. This observed distribution is compared in Fig. 4 to that which would result from an emission intensity per unit area given by a uniform cylinder and by a Gaussian distribution in r , the off-axis dimension. As can be seen in Fig. 4, the measured distribution is between the two approximations. We have converted total intensities to intensities per unit area and total current to current density j by dividing by $\frac{1}{3}\pi W^2$, corresponding to the cylindrical approximation. When the half-widths W and total intensities in the two idealized distributions are matched, as in Fig. 4, the intensity per unit area on axis is 8% lower for the Gaussian distribution. Thus, the uncertainty in using this approximation to obtain the axial intensity and current density is less than 10%, quite negligible compared to other uncertainties.

Absolute-intensity measurements of the NaXe *A-X* band, from region F in Fig. 1(b), are reduced to a

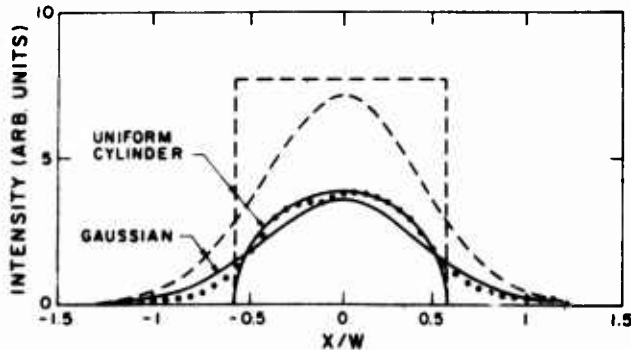


FIG. 4. Transverse intensity distribution (solid lines) that would be observed for a cylindrically symmetric source with brightness per unit volume given by the dashed lines, i.e., distributed either as a uniform intensity cylinder or a Gaussian distribution. The off-axis dimension is x , W is the observed width at half-height, and the total current is the same for both distributions. The measured intensity distribution at 670 nm for $[Na] = 4 \times 10^{15} \text{ cm}^{-3}$, $[Xe] = 5 \times 10^{19} \text{ cm}^{-3}$, and $j = 95 \text{ A/cm}^2$ is indicated as dots.

Na 3P density [Na(3P)] using the normalized emission data of Ref. 5 and the effective area described in the previous paragraph. From this density, calculated transition probabilities,¹⁰ and the discharge cross-sectional area we can establish that, except for the 4S-3P and 3D-3P transitions, the nS-3P and nD-3P lines in Fig. 3 are optically thin. The total intensity from these line shapes thus equals $[Na(nS)]\Gamma_{nS-3P}$ and $[Na(nD)]\Gamma_{nD-3P}$, where Γ is the spontaneous-emission rate. The resulting axial densities of various excited Na states, divided by their statistical weights, are plotted in Fig. 5 for two current densities. A lower limit to the residual (un-ionized) [Na(3S)] in the discharge can be obtained by subtracting the electron density n_e , obtained from the measured current density and calculated mobilities,^{4,11} from the initial Na density $[Na]_0$. Some of the electrons may result from Xe ionization, but as $n_e/[Na]_0 < 0.35$, this is not a major uncertainty. The resulting residual Na densities as well as $[Na]_0$ are plotted in Fig. 5. It is noteworthy that for each j the measured populations fall nearly on a straight line corresponding to a single excitation temperature.

By varying the electrode gap the voltage drop attributed to the cathode fall has been determined to be ~15 V, out of a typical total voltage drop of 50 to 100 V. Thus, the electric field E in the positive column is

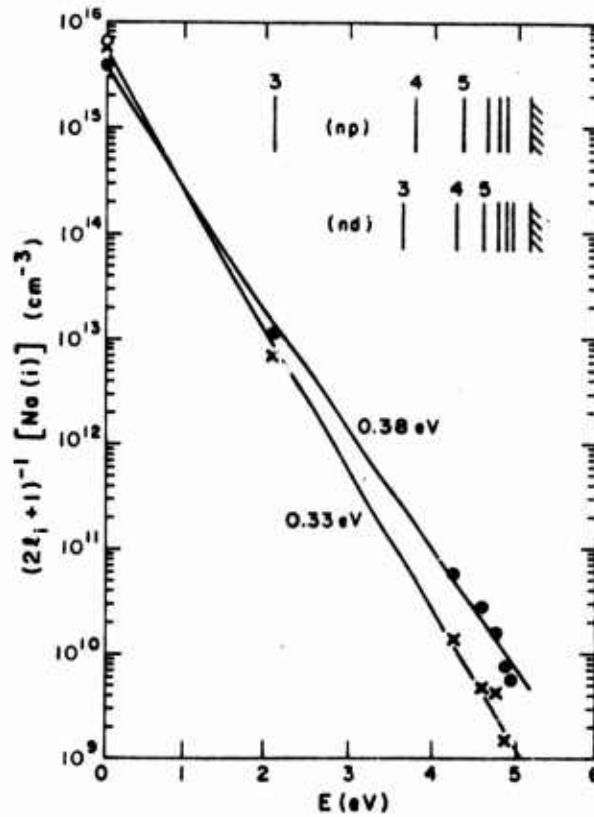


FIG. 5. Ratio of excited-state population to statistical weight as a function of energy above the ground state, for $[Xe] = 4.5 \times 10^{19} \text{ cm}^{-3}$, an initial $[Na] = 6.3 \times 10^{15} \text{ cm}^{-3}$ (○), and current density $\approx 130 \text{ A/cm}^2$ (●); 13 A/cm^2 (x). The density of [Na(3S)] during the discharge is indicated as (●) or (x); the 3S, 3P, and 3D, $n=4-8$ state population are given. The straight lines correspond to 0.38- and 0.33-eV excitation temperatures in the 130- and 13-A/cm² cases.

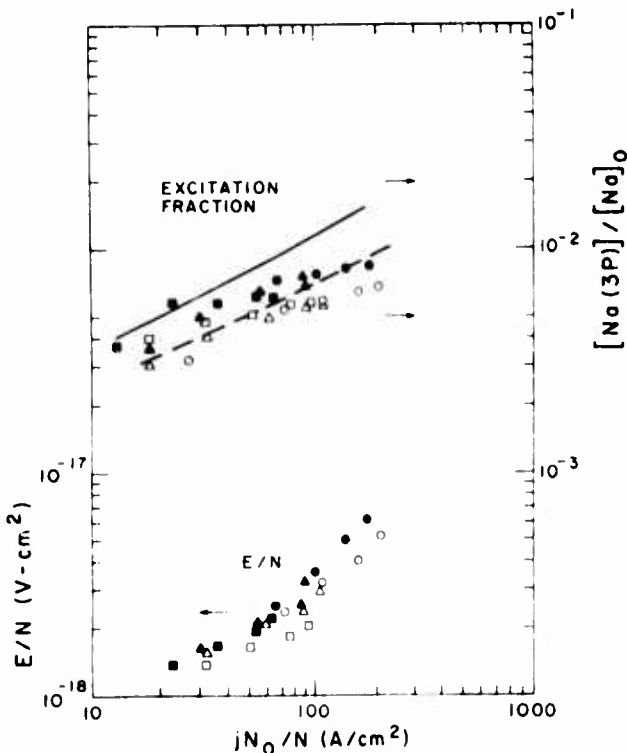


FIG. 6. E/N and $[Na(3P)]/[Na]_0$ in the positive column versus $j(N_0/N)$, where $N = [Xe]$, $N_0 = 2.7 \times 10^{19} \text{ cm}^{-3}$ and $N/N_0 = 2.04$ (\square and \blacksquare), 1.07 (Δ and \blacktriangle), 0.50 (\wedge and \bullet). The ratio $[Xe]/[Na] = 3600$ for the open symbols and dashed line and 8000 for the solid symbols and solid line. The lines are averages of $[Na(3P)]/[Na(3S)]$ for the same data, where $[Na(3S)] = [Na]_0 - n_e$.

known from the electrode voltages. In Fig. 6 E/N and $[Na(3P)]/[Na(3S)]$ are plotted as a function of j/N for the range of conditions covered in the experiment ($N = [Xe]$). Since the discharge area increases with cell current (J), j does not cover as large a range as I . An extremely valuable result displayed by Fig. 6 is the positive-resistance characteristic of the discharge, a condition that seems to be closely connected to the absence of discharge instabilities and the spreading of the discharge with increasing I .

V. CONCLUSIONS

The ratio $[Na^*(3P)]/[Na(3S)]_0 \sim 0.01$ achieved in the discharge (see Fig. 6) is insufficient for net optical gain on the $A-X$ band at $\lambda \sim 700$ nm where the gain coefficient is relatively large {i.e., $[Na^*][Na]^{-1}(g/g^*) \exp[-h(\nu - \nu_0)/kT]$ must exceed 1}.^{2,3} There is net gain on this band in the 800–900-nm region, but the gain coefficient is quite small.¹² When $Na(3S)$ depletion is allowed for, as in the lines in Fig. 6, it appears that $[Na^*(3P)]/[Na(3S)]$ might reach the desired 0.03 to 0.05 values at $jN_0/N > 10^3 \text{ A cm}^{-2}$, but the gain coefficient would be small due to neutral Na depletion, and efficiency would probably be very low.

We have not measured the $Na^*(4S)$ density, but if it is assumed to fit on the line in Fig. 5, then using the same criteria based on $h(\nu - \nu_0)/kT$, where $h\nu_0$ is the $3s-4s$ transition energy, $[Na^*(4S)]/[Na(3S)]$ is also insufficient for net gain on the $4S\bar{\Sigma}-X\Sigma$ band. If Na could be introduced at similar densities but lower gas temperatures (e.g., using volatile Na-containing molecules or gas flow), net gain and a larger gain co-

efficient could be achieved on the $A-X$ and $4S\bar{\Sigma}-X\Sigma$ bands. However, this is an added level of complexity and possible accompanying problems with the discharge behavior might occur as well.

The single effective excitation temperature observed for all Na excited states is quite surprising in view of the competing processes of collisions with energetic electrons, having a high effective temperature, and cold-gas collisions. Detailed models for the electron-energy distribution and excited-state rate equations are being used in an attempt to understand these results, and publication of these is planned.⁴

Na_2 A -state and X -state depletion at the higher current densities was expected on the basis of estimates of the Na_2 and Na_2^* electron-collisional dissociation rates.¹ Due to uncertainty in the Na_2 A -state population distribution the observations are not definitive on this issue. For the higher j case in Fig. 3, the Na_2 A state may be more depleted, relative to the $NaXe$ A state, than in the lower j case. However, the data could also be explained by a hotter A -state vibrational-population distribution. In the absence of this depletion, absorption by Na_2 in the 700-nm region would be very serious, even if net gain were achieved on the excimer band. This depletion of a minor but relatively strongly bound molecular constituent can often be a problem for excimer lasers, so such depletion has broad implications. Minor molecular constituents only reassociate slowly following electron-collisional dissociation, due to the small density of the appropriate atomic species. (That the molecular form is favored at equilibrium requires that they are dissociated very slowly by gas collisions.) Electron-collisional dissociation can be expected to severely deplete many strongly bound but minor constituents in high-power discharges.

ACKNOWLEDGMENTS

We are indebted to A. V. Phelps for encouragement and valuable discussions throughout this work. Support was provided by the Advanced Research Projects Agency of the Department of Defense, under contract No. N00014-76-C-0123.

¹J. F. Waymouth, *Electric Discharge Lamps* (MIT, Cambridge, Mass., 1971).

²A. V. Phelps, JILA Report 110, 1972 (unpublished).

³G. York and A. Gallagher, JILA Report 114, 1974 (unpublished).

⁴R. Shuker, L. Morgan, A. Gallagher, and A. V. Phelps (unpublished); Bull. Am. Phys. Soc. **23**, 142 (1977).

⁵D. Leep, Ph.D. thesis (University of Colorado, 1977) (unpublished).

⁶R. E. Honig and D. A. Kramer, RCA Rev. **30**, 285 (1969).

⁷G. York, R. Scheps, and A. Gallagher, J. Chem. Phys. **63**, 1052 (1975). The conditions for Fig. 11 are $[Xe] = 2 \times 10^{19} \text{ cm}^{-3}$, $[Na] = 10^{11} \text{ cm}^{-3}$, $[Na^*]/[Na] = 0.05$, and $T = 810 \text{ K}$.

⁸A. Tam, G. Moe, B. Bulos, and W. Happer, Opt. Commun. **18**, 376 (1976).

⁹L. Lam, A. Gallagher, and M. Hessel, J. Chem. Phys. **66**, 3550 (1976).

¹⁰W. L. Wiese, M. W. Smith, and B. M. Miles, *Atomic Transition Probabilities*, NSRDS-NBS 22 (U.S. GPO, Washington, D.C., 1969).

¹¹L. A. Schlie, Bull. Am. Phys. Soc. **21**, 172 (1976); J. Appl. Phys. **47**, 1397 (1976).

¹²W. P. West, P. Shuker, and A. Gallagher, J. Chem. Phys. **68**, 3864 (1978).

Excitation of the $C^3\Pi_u$ state of N_2 by low energy electrons^{a)}

K. Tachibana^{b)} and A. V. Phelps^{c)}

Joint Institute for Laboratory Astrophysics, University of Colorado, Boulder, Colorado and National Bureau of Standards, Boulder, Colorado 80309
(Received 25 June 1979; accepted 9 July 1979)

Electron excitation rate coefficients for N_2 are important to the development of models of N_2 lasers,¹ gas discharges² and ionospheric phenomena³ and in determining electron collision cross sections.⁴⁻⁷ Although cross sections for the excitation of the $N_2(C^3\Pi_u)$ state have been measured by a number of authors,⁷ there are only a few measurements of excitation rate coefficients.^{8,9} This Note presents measurements of this excitation rate coefficient obtained using the drift tube technique used for $O_2(b^1\Sigma_g^+)$ molecules¹⁰ and $N_2(A^3\Sigma_u^-)$ molecules.¹¹ We also recommend a set of electron- N_2 collision cross sections.

Excitation rate coefficients for the $C^3\Pi_u$ state were obtained from measurements of the absolute intensity of 2nd positive system¹² emitted when electrons drift through N_2 in the presence of an electric field E . The drift tube, detector calibration and data analysis procedures, and corrections for nonuniform detection sensitivity, ionization,¹³ etc. are described in Ref. 10. The interference filter was replaced by an $f/6.3$ monochromator with a resolution (FWHM) of 2.5 nm in order to resolve the 2nd positive and Vegard-Kaplan bands.¹² Most of the measurements were made with 5% H_2 and 95% N_2 in order to maintain electron emission by the gold-palladium photocathode.¹¹

The observed band emission is analyzed by first writing a rate equation, e.g., Eq. (3) of Ref. 10, for the density n_i of each vibrational level of the C state. When these equations are added, vibrational relaxation terms cancel. The radiative transition probabilities are nearly independent of the vibrational level,^{12,14} i.e., $A_i = \sum A_{ij} = 2.7 \times 10^7 \text{ sec}^{-1}$, and diffusion effects¹⁰ are negligible. The assumption that collisional quenching coefficients are independent of the vibrational level leads to a simple relation for the total C -state density, i.e.,

$$\Sigma n_i = \Sigma \frac{S_{ij}}{g_{ij} A_{ij}} = \frac{(\alpha/N_T)_C J_e N_T}{e(A_i + k_e N_T)} . \quad (1)$$

Here the S_{ij} , g_{ij} and A_{ij} are the signal generated by the detector per unit volume of the source, the detection efficiency, and Einstein coefficient for the transition between the i th vibrational levels of the C state and j th level of the $B^3\Pi_g$ state, $(\alpha/N_T)_C$ is the excitation coefficient per unit distance of electron drift¹⁰; e and J_e are the electron charge and the average current density; $k_e N_T = k_{eN} N + k_{eH} [H_2]$ is the reciprocal lifetime against quenching by nitrogen k_{eN} and by hydrogen k_{eH} ; and N_T , N and $[H_2]$ are the total, nitrogen and hydrogen densities. See Ref. 10 for details of the spatial averaging, etc. The measured S_{ij} were for bands near 337.1(0-0),

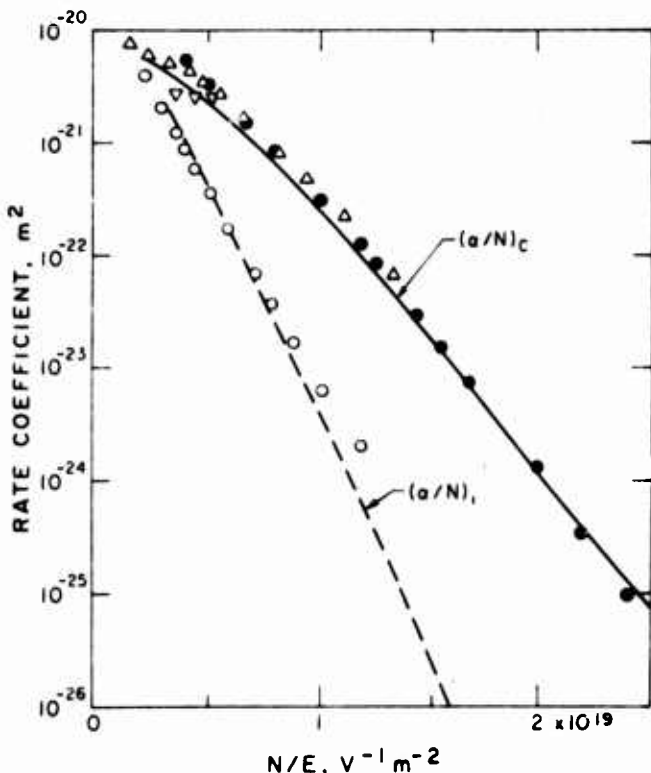


FIG. 1. $C^3\Pi_u$ excitation $(\alpha/N_T)_C$ and ionization $(\alpha/N)_I$ coefficients for electrons in N_2 . The experimental points and authors are: ● this work, △—Legler, ▽—Urosević *et al.*, ○—Haydon and Williams. The solid and dashed lines are from calculations using the recommended set of cross sections (see text).

315.9(1-0), 297.7(2-0) and 389.5(3-6) nm. Their relative intensities at low N_2 densities agreed well with previous measurements,^{9,12} which were used to estimate the small contribution of higher levels. A plot of $J_e N_T (\Sigma n_i)^{-1}$ vs N_T at $E/N_T = 1 \times 10^{-19} V \cdot m^2$ yields k_e . Values of $(\alpha/N_T)_C$ were then calculated using Eq. (1). The $(\alpha/N_T)_C$ values were independent of electron current for $1.6 \times 10^{-5} < J_e < 10^{-4} A/m^2$. The nitrogen density was varied from 3×10^{22} to $6 \times 10^{23} m^{-3}$. A measurement in pure N_2 at $E/N = 1 \times 10^{-19} V \cdot m^2$ yields an $(\alpha/N)_C$ value which is indistinguishable from the corresponding $(\alpha/N_T)_C$ value in the H_2-N_2 mixture. We have therefore dropped the subscript T from the $(\alpha/N_T)_C$ vs N_T/E data shown in Fig. 1. Empirically, the measured $(\alpha/N)_C$ are fitted by $(6.5 \pm 0.5) \times 10^{-20} \exp[-5.5 \times 10^{-19}/(E/N)] m^2$ for $E/N < 2 \times 10^{-19} V \cdot m^2$.

Our k_e value of $2.1 \times 10^{-17} m^3/sec$ for 5% H_2 -95% N_2 , is larger than, but consistent with, $k_{eN} = 1.3 \times 10^{-17} m^3/sec$ calculated from pure N_2 data of Legler.⁸ It is not consistent with the values for $v=0$ levels from Urosević *et al.*⁹ or Becker *et al.*¹⁴ Collision cascading from the E state¹⁵ does not affect our k_e value.

Figure 1 shows that our values of $(\alpha/N)_C$ agree with those measured by Legler.⁸ Agreement with the measurements by Urosević *et al.*⁹ is good only at their lowest E/N . The solid curve of Fig. 1 shows our application of the techniques of Ref. 4 to the calculation of $(\alpha/N)_C$ values. The final cross section set included:

(a) momentum transfer cross sections from Ref. 4 for electron energies ϵ below 10 eV and the sum of the elastic and inelastic momentum transfer cross sections of Cartwright⁷ for $\epsilon > 10$ eV; (b) rotational and near-threshold ($\epsilon \sim 1.5$ eV) vibrational excitation cross sections from Ref. 4; (c) these vibrational excitation cross sections for $1.7 < \epsilon < 5$ eV increased by the factor of 1.9 previously found necessary to fit measured excitation rate coefficients for the $A^3\Sigma_u^+$ state¹¹; (d) cross sections for the C and E states from Cartwright *et al.*⁷ plus a sharp peak near the E -state threshold¹⁶; (e) the other electronic excitation cross sections of Cartwright *et al.* multiplied by 0.8; and (f) ionization cross sections totaling to that of Rapp and Englander-Golden.¹⁷ Calculated curves of $(\alpha/N_T)_C$ vs E/N_T for 5% H_2 -95% H_2 and of $(\alpha/N)_C$ vs E/N for pure N_2 differ by less than the experimental scatter. Agreement between calculated and experimental $(\alpha/N)_C$ is good at low E/N . The higher E/N data suggest a need for additional excitation of the C state. Cascading from the E state contributes $\sim 10\%$ to the $(\alpha/N)_C$ values.

The calculated ionization coefficients of Fig. 1 were brought into agreement in magnitude with experiment¹³ by applying the 0.8 factor to most of the excitation cross sections. The more rapid variation of calculated $(\alpha/N)_I$ than experimental $(\alpha/N)_I$ with N/E appears to result from adjusting the vibrational excitation cross section to obtain a fit of calculated and measured A -state excitation coefficients, i.e., earlier calculations^{1,4,5} agree with experimental $(\alpha/N)_I$ data but greatly overestimate α/N values for the A state.¹¹ Efforts to improve the fit between calculation and experiments for N_2 are continuing.¹⁸ In the meantime the present cross section set gives reasonable agreement with five different electron swarm coefficients, i.e., drift velocity,⁴ characteristic energy,⁴ A -state excitation,¹¹ C -state excitation and ionization.¹³

^aThis work was supported in part by the Defense Advanced Research Projects Agency through the Office of Naval Research under Contract No. N00014-76-C-0123.

^bOn leave from Kyoto Technical University, Kyoto, Japan.

^cStaff Member, Quantum Physics Division, National Bureau of Standards, and Lecturer, Department of Physics and Astrophysics, University of Colorado.

¹O. Judt, IEEE J. Quantum Electron. QE-12, 78 (1976); L. A. Newman and T. A. DeTemple, J. Appl. Phys. 47, 1912 (1976); W. A. Fitzsimmons, L. W. Anderson, C. E. Riedhauser and J. M. Vrtilek, IEEE J. Quantum Electron. QE-12, 624 (1976).

²Yu. A. Ivanov, I. N. Karabashev, A. A. Ovsyannikov, L. S. Polak and D. I. Slovenskii, Teplofiz. Vys. Temp. 13, 465 (1975); S. Gudermann and R. Winkler, Beitr. Plasmaphys. 15, 251 (1975); O. V. Ravodina, T. N. Popova and N. A. Prilezhaeva, Opt. Spektrosk. 40, 730 (1976).

³See, for example, D. C. Cartwright, J. Geophys. Res. 83, 517 (1978) and references therein.

⁴A. G. Englehardt, A. V. Phelps, and C. G. Risk, Phys. Rev. A 135, 1566 (1964).

⁵R. Winkler and S. Pfau, Beitr. Plasmaphys. 13, 243 (1973); 14, 169 (1974); S. Pfau and R. Winkler, *ibid.* 18, 113 (1978); T. Taniguchi, H. Tagashira and Y. Sakai, J. Phys. D 11,

- 1757 (1978).
- ⁶K. Takayanagi and T. Takanashi, Rept. Ionos. Space Res. Jpn. **20**, 357 (1966); C. H. Jackman, R. H. Garvey, and A. E. S. Green, J. Geophys. Res. **82**, 5081 (1977).
- ⁷D. C. Cartwright, S. Trajmar, A. Chutjian, and W. Williams, Phys. Rev. A **16**, 1041 (1977); A. Chutjian, D. C. Cartwright, and S. Trajmar, *ibid.* **16**, 1052 (1977); D. C. Cartwright, J. Appl. Phys. **49**, 3855 (1978). These papers contain references to earlier electron beam measurements.
- ⁸W. Legler, Z. Physik **173**, 169 (1963).
- ⁹V. V. Urošević, Lj. D. Žeković, S. R. Stojković, and J. V. Božin, Contributed Papers 11th International Conference on Ionization Phenomena in Gases, edited by I. Stoll *et al.* (Czechoslovakian Academy of Science, Prague, 1973), p. 4.
- ¹⁰S. A. Lawton and A. V. Phelps, J. Chem. Phys. **69**, 1055 (1978).
- ¹¹D. Levron and A. V. Phelps, Bull. Am. Phys. Soc. **24**, 129 (1979).
- ¹²A. Loithus and P. H. Krupenie, J. Phys. Chem. Ref. Data **6**, 113 (1977).
- ¹³S. C. Haydon and O. M. Williams, J. Phys. D **9**, 523 (1976).
- ¹⁴See Table in K. H. Becker, H. Engels and T. Tatarczyk, Chem. Phys. Lett. **61**, 111 (1977).
- ¹⁵D. J. Burns, D. E. Golden and D. W. Galliardt, J. Chem. Phys. **65**, 2616 (1976).
- ¹⁶W. L. Borst, Phys. Rev. A **5**, 648 (1972); W. L. Borst, W. C. Wells, and E. C. Zipf, Phys. Rev. A **5**, 1744 (1972).
- ¹⁷D. Rapp and P. Englander-Golden, J. Chem. Phys. **43**, 1464 (1965).
- ¹⁸L. C. Pitchford (private communication).

5. Metal Vapor Excimers

A. Gallagher

With 17 Figures

Reprint from
Topics in Applied Physics
Volume 30: Excimer Lasers
Editor: Ch. K. Rhodes

© Springer-Verlag Berlin Heidelberg 1979
Printed in Germany. Not for Sale.

In this chapter we consider diatomic excimer molecules (AB) in which a Group I, II, or III metal atom is the radiative species (A). Group II metal atoms can play the role of a noble gas (B), since they have 1S_0 ground states and have predominantly repulsive interactions with ground-state atoms. Thus Group II and VIII atoms will be included in the class of "B" atoms and we have divided the discussions of specific systems into the six cases of Group I, II, or III atoms paired with Group II or VIII atoms.

These metal-based excimer molecules share several important characteristics. First, their excimer bands are on the wings of the metal-vapor lines; hence the important bands from the ground to first excited states are generally in the visible or near uv and ir wavelength regions. Next, many of the excited states AB^* associated with these bands are weakly bound (i.e., by less than $10 kT$). With the partial exception of Hg, elevated temperatures are necessary to obtain adequate metal vapor pressures for reasonable gain coefficients and high powers. An associated engineering problem is a frequent reactivity with window and gasket materials. Finally, the lowest excited states of the metal atoms generally have excitation energies of less than half their ionization energies. This has important consequences for the electron collisional cross sections which determine the efficiencies of potential e-beam or discharge-excited high-power lasers. In particular, as noted in Sect. 5.3 below this may allow the possibility of efficient, high power, direct electric discharge lasers.

The weakly bound character of many metal-based excimers has a profound effect on their optical properties as a laser medium. It results in a low-gain coefficient per excited metal atom, homogeneous broadening across the excimer band, rapid transitions between excited atoms A^* and the associated excimer molecules AB^* , the necessity of a high "noble gas" density, and relatively stringent requirements on the fractional excitation of the metal atoms necessary for net gain. The optical properties of such weakly bound excimers can be characterized by some very simple and relatively universal relations, which are discussed in Sect. 2.12. These are also described in Sect. 5.1, which discusses the excimer vibrational-rotational population distributions, relations between stimulated and spontaneous emission and absorption, and the consequences of the classical Franck-Condon principle and homogeneous broadening. These discussions, in fact, apply with very minor modifications to many strongly bound excimers as well, and this generalization is discussed therein. The results of Sect. 5.1 are applied in Sect. 5.2, which discusses those

metal-based excimers for which we have information. The last section discusses potential excitation methods and their potential efficiencies, with emphasis on a prototype example of discharge-excited Na-Xe.

The weakly bound character of many metal based excimers leads to the possibility of high power levels, resulting from the low gain coefficient and homogeneous broadening, and high pulse energies due to the high-pressure noble-gas heat sink. (Some of the more strongly bound cases such as Hg₂ also have small gain coefficients in the bands associated with the lowest excited states.) However, the low gain coefficients combined with the possibility of spatial variations in the index of refraction associated with the high pressure gas make these systems difficult to develop into successful lasers. Some promising candidates are now under study, particularly Tl-Hg, but laser action has yet to be demonstrated.

5.1 Optical Properties

5.1.1 Vibrational-Rotational Population Distribution in High-Pressure Gases

We consider one or more relatively low density molecular species in the presence of a high pressure atomic gas, with energy deposition by an electron current, a high-energy electron beam, an external light source, or some combination thereof. A major fraction of the deposited energy is presumed to go into electronic excitation, ionization, and gas heating.

Vibrational and rotational excitation also result from electron collisions and molecular fluorescence. Collisions of the excited molecules with the high-pressure gas drive excited vibrational and rotational populations toward equilibrium with the gas-kinetic temperature, so these forms of energy deposition also go ultimately into gas heating.

For light, strongly bound molecules, the vibrational separations are so large that slow atomic collisions are inefficient at relaxing bound-state vibrational populations. The present discussions will be primarily aimed at heavy, large and/or weakly bound diatomic molecules in which the vibration spacings are small and the *vibrational relaxation* probability is high. Factors which often contribute to this rapid vibrational relaxation are attractive long-range interactions with the atomic buffer gas, combined vibration-rotation transitions, and a high probability of many vibrational steps in a single heavy-particle collision once the single step probability is high [5.1]. Typical vibrational relaxation times thus correspond to only a few gas-kinetic collisions, and at the typical inert gas densities [B] of 10^{20} cm^{-3} proposed for laser, this corresponds to a $10^{-9}\text{--}10^{-10} \text{ s}$ relaxation time. By comparison radiative rates for visible atomic transitions and their associated excimer bands are generally 10^{-8} s or longer, while radiative trapping further decreases the effective radiation decay rate for resonance transitions. If excimer vibrational

excitation rate coefficients by electron impact, of which we have no direct information, were similar to those of the stable molecular gases then they would typically be ~ 10 times smaller than for electronic superelastic collisions and the latter will limit the time available for gas vibrational relaxation rates for $n_e/[B] \sim 10^{-3}$. The proposed discharge excited laser systems (Sect. 5.3) typically utilize electron densities a factor of 1–100 smaller than this. Thus, in the models considered below, vibrational and rotational relaxation rates will generally be assumed to be faster than the electron collision and radiative rates with which they compete. The distribution of population within the vibrational and rotational states will be characterized by a temperature. The gas kinetic temperature will normally be used, although a somewhat higher effective temperature could be used if relaxation is not complete. This applies to the strongly bound as well as the weakly bound excimers as long as they do not involve light atoms such as H or He and the buffer gas densities are in the typical 10^{20} cm^{-3} range. On the other hand, the total bound-state population may not be in equilibrium with the associated atomic-state concentrations for strongly bound excimers, and the total populations of different electronic states will definitely not be in equilibrium at the gas temperature if net laser gain is to be achieved.

The total populations of each molecular electronic state will result from competition between gas collisional processes, radiative processes, and electron collisions in electrically excited systems. If the gas collisional dissociation rate R_d is the dominant destruction mechanism and the three-body association rate R_i (via complexes or any mechanism) the dominant formation rate for a particular state, then the populations will approximately satisfy the equilibrium relation at the gas temperature T . That is $[AB_{ij}]/[A_i][B_j] = R_i/R_d = K_{eq}(T)$, where the state AB_{ij} dissociates into $A_i + B_j$, K_{eq} is the equilibrium constant for state AB_{ij} and the brackets refer to densities. Collisional dissociation rates vary approximately exponentially with binding energy divided by kT , so this will generally be the dominant destruction mechanism only for shallow potentials, typically up to 5 or $10 kT$ deep depending on the size of competing rates and buffer gas density. Three-body association will often be the dominant production mechanism for such weakly bound states since most of the constituents A_i and B_j are then in the atomic form ($[AB_{ij}]/[A_i] \ll 1$ and $[AB_{ij}]/[B_j] \ll 1$). Thus, the total molecular population of such weakly bound electronic states will frequently be in equilibrium with the parent atomic components, particularly in cases where the atomic form predominates at equilibrium. In this case it is conceptually most useful to relate the absorption and stimulated emission coefficients to $[A_i][B_j]$ rather than $[AB_{ij}]$. One other advantage of the description in terms of $[A_i][B_j]$ for weakly bound states is that the radiation from free and quasi-bound collision states of AB_{ij} is naturally included, as it should be since they also contribute to the excimer spectrum. On the other hand, a formulation in terms of the molecular concentration and its equilibrium constant refers only to bound states; these adequately describe the optical properties only for strongly bound electronic states. The Hg_2 case described

below is an example of the strong-binding limit and is discussed directly in terms of $[AB_{ij}]$.

For repulsive interatomic potentials, the free nuclear states of the collision complex replace the bound vibrational states in the above "molecular" picture. In this case the continuum distribution of vibrational states is always in equilibrium with the atomic concentrations at the gas kinetic temperature. In the discussions below we treat free and bound vibrational states in the same manner; thus the derived relations can be applied uniformly to bound-bound, bound free and free-free transitions. In addition they are applicable from the wings of atomic lines on through the associated molecular bands.

5.1.2 Thermodynamic Relations Between Absorption and Emission

Many of the results of this section have been given previously by *Phelps* [5.2] and *York and Gallagher* [5.3]. We first note a generalization of the Einstein relation for atomic or molecular lines (2 is the upper and 1 the lower level)

$$N_2 B_{2 \rightarrow 1} = \frac{\lambda^2}{8\pi} N_2 A_{2 \rightarrow 1} \quad (5.1)$$

to cover continuum radiation or portions of lines. We replace $N_2 A_{2 \rightarrow 1}$ with a spectral distribution $S(v)$ and $N_2 B_{2 \rightarrow 1}$ with G_v

$$G_v = \frac{\lambda^2}{8\pi} S(v). \quad (5.2)$$

Here G_v is the stimulated emission coefficient and $S(v)dv$ the spontaneous emission rate per unit volume for $v \rightarrow v + dv$ photons. $N_2 B_{2 \rightarrow 1} = \int_{\text{line}} G_v dv$ and $N_2 A_{2 \rightarrow 1} = \int_{\text{line}} S(v)dv$. The traditional definition of the absorption coefficient k_v is the difference between pure absorption, which we label K_v , and G_v ($k_v = K_v - G_v$). Next we recall that for a vapor contained in a vessel of temperature T and in equilibrium with the walls, the net absorption of the black-body radiation must at every v be balanced by spontaneous emission at the same v

$$(K_v - G_v) \frac{8\pi}{\lambda^2(e^{h\nu/kT} - 1)} = S(v). \quad (5.3)$$

Combined with (5.2) this yields

$$\frac{G_v}{K_v} = e^{-h\nu/kT} \quad (5.4)$$

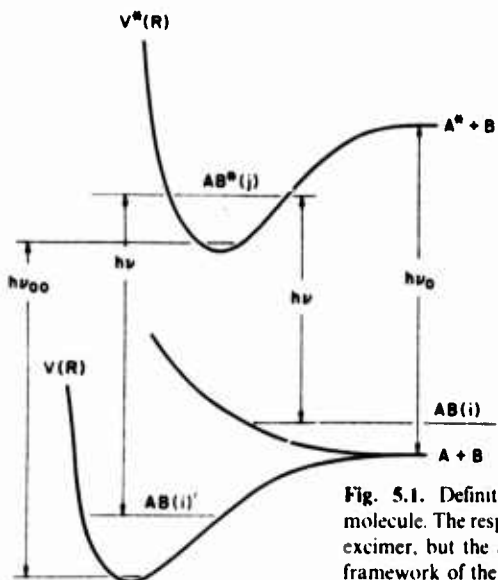


Fig. 5.1. Definition of terms for an idealized diatomic molecule. The repulsive ground-state case corresponds to an excimer, but the attractive case is also included within the framework of the theory in Sect. 5.1.

for an equilibrium vapor. Also, for an equilibrium vapor, the atomic state densities are given by

$$\frac{[A^*]}{[A]} = \frac{g^*}{g} e^{-h\nu_0/kT}, \quad (5.5)$$

where we have replaced A_1 and A_2 with A and A^* for a ground and electronically excited state, and $h\nu_0$ is the excitation energy of A^* (see Fig. 5.1). Combining (5.4) and (5.5) yields

$$\frac{G_v}{K_v} = \frac{[A^*]}{[A]} \frac{g}{g^*} e^{-h(v-v_0)/kT} \quad (\text{equilibrium vapor}). \quad (5.6)$$

We now consider a situation in which $[A^*]/[A]$ exceeds the equilibrium ratio for the gas temperature T , but the population ratios $[AB^*(j)]/[A^*][B]$ and $[AB(i)]/[A][B]$ are still in equilibrium at temperature T . Here $AB(i)$ refers to a bound or free vibrational and rotational state i in the ground electronic state, and $AB^*(j)$ to a state j in the excited electronic state (Fig. 5.1). Equation (5.6) then still applies, but with $[A^*]/[A]$ independently determined (e.g., by electron collisional or optical excitation). If one represents the ratio $[A^*]/[A]$ in terms of an effective excitation T_e

$$[A^*]/[A] = (g^*/g) \exp(-h\nu_0/kT_e). \quad (5.7)$$

Combining this with (5.6), one obtains

$$\frac{G_v}{K_v} = \exp \left[-\frac{h}{k} \left(\frac{v_0}{T_e} - \frac{v - v_0}{T} \right) \right]. \quad (5.8)$$

The condition for net gain ($G_v/K_v > 1$) and laser action is thus

$$\frac{v_0 - v}{v_0} > \frac{T}{T_e}. \quad (5.9)$$

This condition was given by *Carbone* and *Litvak* [5.4] for Hg_2 excimer lasers, and was generalized in *Phelps* [5.2]. Here we note that (5.9) applies to all molecular electronic transitions if $[AB^*]/[A^*][B]$ and $[AB]/[A][B]$ attain their equilibrium values $K_{eq}^*(T)$ and $K_{eq}(T)$ at the gas temperature T . This requirement effectively limits (5.9) to weakly bound or repulsive lower and upper state potentials. These equations are most useful in the case where the majority of A and A^* are in the atomic form, as generally occurs for weakly bound excimers. In the next paragraph we consider the opposite case.

As noted in Sect. 5.1.1, the atomic versus molecular population ratios $[AB^*(j)/[A^*][B]$ are only expected to be in equilibrium at the gas temperature T for weakly bound or repulsive $V^*(R)$. But we expect the ratios of bound-state populations $[AB^*(j)]/[AB^*(j')]$ to be characterized by equilibrium ratios at temperature T or a somewhat elevated temperature. In the strong-binding case it is better to refer the G_v/K_v ratios to a ratio of bound-state populations, since most of the excited and ground-state species will be in the form of bound molecules. Here we will refer to the population ratio $[AB^*(0)]/[AB(0)]$, where the 0's refer to the $V=0, J=0$ states (Fig. 5.1). Then (5.5) is replaced by

$$\frac{[AB^*(0)]}{[AB(0)]} = \frac{g_m^*}{g_m} e^{-hv_{00}/kT}, \quad (5.5a)$$

where hv_{00} is the energy separation of $AB^*(0)$ and $AB(0)$, and g_m^* and g_m refer to the molecular electronic states (Fig. 5.1). Then (5.6) is replaced by

$$\frac{G_v}{K_v} = \frac{[AB^*(0)]}{[AB(0)]} e^{-hv - hv_{00}/kT} \quad (\text{equilibrium vapor}). \quad (5.6a)$$

Defining an effective excitation temperature similarly to (5.7)

$$\frac{[AB^*(0)]}{[AB(0)]} = \frac{g_m^*}{g_m} \exp(-hv_{00}/kT'_e), \quad (5.7a)$$

we obtain

$$\frac{G_v}{K_v} = \exp \left[-\frac{h}{k} \left(\frac{v_{00}}{T'_e} - \frac{v - v_{00}}{T} \right) \right]. \quad (5.8a)$$

The net gain condition becomes

$$\frac{v_{00} - v}{v_{00}} > \frac{T}{T_e} \quad (5.9a)$$

In both cases, (5.6) or (5.6a), the ratio G_v/K_v increases as $\exp(-hv/kT)$ with increasing wavelength, which is a key point of this discussion. The excited state fraction necessary for net gain thus decreases exponentially as the photon energy decreases. It should be apparent that this result refers to all portions of a band, including discrete lines, portions thereof, and continua. Extending the range of states i and j to include quasi-bound resonance states and free-continuum states also causes no changes in (5.6-9) and (5.6a-9a) as long as a single temperature T is used to characterize the entire population distribution.

In some cases it is more useful to refer the $[AB^*(i)]$ to total bound-state populations, $[AB^*] = \sum_i [AB^*(i)]$, rather than $[AB^*(0)]$ as in (5.6a) and similarly for the ground-state. Using $[AB^*] = [AB^*(0)]Z^*(T)$ and $[AB] = [AB(0)]Z(T)$, where $Z(T)$ is the partition function, (5.6a) can be reduced to this form, as was done by York and Gallagher [5.3]. Equations (5.6) and (5.6a) are equivalent conditions, but (5.7) and (5.7a) are not equivalent for $T_e = T_e'$. Equations (5.6) and (5.6a) are universal equations for vapors with vibrational and rotational populations in an equilibrium distribution at temperature T , but the population ratios $[A^*]/[A]$ or $[AB^*(0)]/[AB(0)]$ in electronically excited vapors will be a consequence of the competition between various collisional and radiative processes. Estimating these population ratios required rather detailed modeling. Examples and references are given below.

5.1.3 Applications of the Classical Franck-Condon Principle

The classical Franck-Condon principle (CFCP), which is the basis of the quasistatic theory of line broadening [5.5], predicts that the internuclear separation R and nuclear kinetic energy do not change during an electronic radiative transition. Consequently, the photon energy hv equals $V_i^*(R) - V_j(R)$ for a transition that occurs at R , regardless of the initial motion. (In the interest of simplicity, we will discuss only one R coordinate, equivalent to a diatomic molecule, but generalization to polyatomic is implied.) Here $V_i^*(R)$ is the electronic energy of the i th adiabatic state which dissociates to $A^* + B$, while $V_j(R)$ dissociates to $A + B$. For excimer molecules B is in a 1S_0 state with statistical weight $g_B = 1$. Thus $A^* + B$ forms g_A adiabatic states and $A + B$ forms g_A states, half of which are effectively degenerate if A or A^* is not a 1S_0 state. The total rate $[S(v)dv]$ is, therefore, given by the total density of excited molecules with separations $R + R + dR$, where $hv = V_i^*(R) - V_j(R)$, times the transition rate $A(R)_{ij}$, i.e., if we define $[AB^*(R)_{ij}]$ as the density of molecules in

adiabatic state i with internuclear separations less than or equal to R ,

$$[S(v)] = \sum_{ij} A(R)_{ij} \frac{d[AB^*(R)_i]}{dv}. \quad (5.10)$$

The stimulated emission coefficient is related to this by (5.2), and the absorption coefficient is given by g_j/g_i^* times equivalent expressions for ground-state molecules

$$G_v = \frac{\lambda^2}{8\pi} \sum_{ij} A(R)_{ij} \frac{d[AB^*(R)_i]}{dv} \quad (5.11a)$$

and

$$K_v = \sum_{ij} \frac{g_i^*}{g_j} \frac{\lambda^2}{8\pi} A(R)_{ij} \frac{d[AB(R)_j]}{dv}. \quad (5.11b)$$

Note that if the ij continuum band has a width Δv_{Band} and a mean radiative rate \bar{A}_{ij} , the stimulated emission coefficient can be approximated by the familiar expression

$$\frac{G_v}{[AB_i^*]} = \frac{\lambda^2}{8\pi} \frac{\bar{A}_{ij}}{\Delta v_{\text{Band}}} \quad (5.12)$$

Molecular bands associated with dipole-allowed transitions of excimer molecules frequently have $\bar{A}_{ij} \sim A_0$, the rate for the separated atom, since the wave functions are not severely perturbed by the relatively weak interaction energies.

Since the CFCP is a classical principle, it is also appropriate to use a classical canonical phase-space distribution to describe the equilibrium distribution of states of nuclear motion [5.6]. The distribution vs R is obtained by integrating over nuclear momentum coordinates

$$\begin{aligned} d[AB(R)_j] &= Z_j^{-1} h^{-3} dR^3 \int dP^3 e^{-[P^2/2 + V_j(R)]/kT} \\ &= \frac{g_j}{g_A} [A][B] d^3 R \exp[-(V_j(R) - V_j(\infty))/kT], \end{aligned} \quad (5.12a)$$

where Z_j is the partition function. An identical expression with $[A^*]$, g_A , g_i and V_i^* in place of $[A]$, g_A , g_i and V applies for $d[AB^*(R)_i]$. Also, for diatomic molecules $d^3 R = 4\pi R^2 dR$. Combining (5.11) and (5.12a) we obtain, as in *Phelps* [5.2] and *Hedges* [5.6]

$$G_v = \frac{\lambda^2}{8\pi} \sum_{ij} A(R)_{ij} \left(\frac{d^3 R}{dv} \right)_{ij} \frac{g_i^*}{g_A} [A^*][B] \exp\{-[V_i^*(R) - V_i^*(\infty)]/kT\}, \quad (5.13a)$$

and

$$K_s = \frac{\lambda^2}{8\pi} \sum_{ij} \frac{g_i^*}{g_4} A(R)_{ij} \left(\frac{d^3 R}{dv} \right)_{ij} [A][B] \exp \{-[V_f(R) - V_f(\infty)]/kT\}, \quad (5.13b)$$

where $d^3 R / dv$ is often written as $4\pi R^2 / |dv/dR|$. In the case $A=B$, as for Hg_2 , $[A][B] \rightarrow [A]^2/2$ in (5.13a).

Thus, application of the CFCP to a classical equilibrium distribution of bound and free vibrational and rotational states leads to the absorption and stimulated emission coefficients in (5.13). The resulting ratio G_s/K_s agrees with the previous (5.6), as it must. These relations apply to both attractive and repulsive states; in cases where the equilibrium constants for $[AB]/[A][B]$ or $[AB^*]/[A^*][B]$ are less than one, most of A or A^* is in the atomic form and (5.13) are most useful. If either equilibrium constant greatly exceeds one, it may be more appropriate to refer to molecular populations, by substituting $[A][B]=[AB] K_{eq}$ or $[A^*][B]=[AB^*] K_{eq}^*$ in (5.13). In this form (5.13) will be correct even if $[A^*]/[AB^*]$ is not in the equilibrium ratio. These relations will be applied to the examples below.

5.1.4 Homogeneous Broadening

A characteristic of considerable importance in the generation of subnanosecond pulses is the homogeneous broadening, or proportion of the $[AB^*]$ capable of radiating at a given wavelength at one time. Three distinctly different cases occur for molecular electronic transitions, bound-bound, bound-free, and free-bound, or free.

In the case of a bound-bound molecule transition, each excited vibrational-rotational state radiates typically ~ 20 strong lines distributed across $\sim 2000 \text{ cm}^{-1}$. If each line is collisionally broadened by the buffer gas to a few cm^{-1} , then each excited state typically radiates into a few percent of the band. The lines from different excited states are interleaved to yield a virtual continuum, particularly for heavy molecules, but at any one time only a few percent of the excited states interact with a single laser wavelength. For heavy molecules vibrational and rotational relaxation occurs with roughly gas-kinetic cross sections, or about once per 0.05 ns for 10^{20} cm^{-3} buffer gas density. But each collision has only a statistical probability of a few percent for transferring population into the states that interact with the laser wavelength, so typically ~ 30 collisions or 1.5 ns are required to stimulate most of the $[AB^*]$ to radiate. Thus, bound-bound transitions are unfavorable for efficient, subnanosecond pulse laser gain tubes.

If the ground state is repulsive, as for excimers, each bound excited state (V', J') radiates a continuum that undulates through $V' + 1$ maxima generally spread across a large portion of the band. Consequently, each excited state interacts strongly with more than half of the wavelengths in its portion of the band and a single laser wavelength in the strong portion of the band stimulates

the majority of bound states to emit. Thus, only a few vibrational relaxation collisions are needed to stimulate almost the entire AB^* population to emit, a process that typically occurs in ~ 0.1 ns for 10^{20} cm^{-3} density of buffer gas.

If the excited state is repulsive, as in the Li-He case in Sect. 3.1, each free collisional vibrational state radiates an undulating continuum that fills more than half of the "band," or collisionally broadened "far-wing" of the atomic line" in the language of pressure broadening. Furthermore, each excited atom in 10^{20} cm^{-3} density of buffer gas impacts a different perturber with a new collision energy about every 3 ps. Thus, it fills a new 50% portion of the continuum every 3 ps, and the resultant "homogeneous broadening time" is less than 10 ps. This result is independent of the repulsive or attractive character of the lower state.

5.2 Excimer Systems

5.2.1 Group I-VIII Excimers

The most thoroughly studied metal-noble gas excimers are the alkali-noble gases. The A state potentials have been measured, and found to be weakly attractive; the X states are repulsive except for a weak, long range van der Waals minimum [5.7–9]. The $A-X$ bands appear as extended continua on the red-wings of the alkali resonance lines with the strongest bands generally for Xe. These $A-X$ bands have been suggested as potential excimer laser systems by *Phelps* [5.2] and *York* et al. [5.7] and as discharged excited excimer lasers by *Palmer* et al. [5.10], *Schlie* [5.11], and *Shuker* et al. [5.12]. In addition to these $A-X$ bands, which are in the 600–1100 nm region for the various alkalis, excimer bands associated with the first excited 2S and 2D states of the alkalis occur in 400–700 nm regions. The absorption coefficients, and effectively the emission coefficients using relations in Sect. 5.1, have been measured for these shorter-wavelength excimer bands [5.13]. The bands associated with the 2S state have been suggested as potential excimer laser systems [5.13], but have not been modeled quantitatively. Some of the potentials associated with these higher 2S and 2D parentage excimers have been estimated from a combination of fitting experimental band shapes and inferences drawn from approximate potential calculations [5.14]. We will discuss first the more thoroughly studied $A-X$ bands, and then discuss the potential behavior of the shorter wavelength bands as excimer lasers.

$A-X$ Bands

Since the A states are weakly attractive, very large noble-gas densities ($\sim 10^{21} \text{ cm}^{-3}$) are required to shift a majority of resonance-line spontaneous emission to the $A-X$ band [5.15]. With the exception of Li-He, and partial

exception of NaHe, Xe produces the strongest, widest $A-X$ bands and thereby optimizes the gain and inversion for a given fraction of excited alkali. For this reason modeling efforts have concentrated on alkali-Xe excimers which are described below. To obtain sufficiently large gain coefficients, noble gas densities of $\sim 10^{20} \text{ cm}^{-3}$ and alkali densities of $10^{16}-10^{17} \text{ cm}^{-3}$ are normally considered. If pure metal vapors are utilized, temperatures of 200–900°C are required to obtain these alkali densities. Under such conditions the A states are less than $3kT$ deep and the molecular populations rapidly equilibrate with the atomic populations. For molecular A -state populations in equilibrium with the A^* concentrations, the collisional dissociation rate should exceed the sum of the radiative rate (typically $\sim 20 \text{ ns}$) and the somewhat faster stimulated emission rate. These A -state dissociation rate constants are $\sim 3 \times 10^{-11} \text{ cm}^3 \text{ s}^{-1}$ at temperatures corresponding to $[A] \geq 10^{11} \text{ cm}^{-3}$ [5.16], and can be expected to be $\sim 10^{-10} \text{ cm}^3 \text{ s}^{-1}$ at the higher temperatures appropriate for excimer lasers. Thus, the equilibrium condition is well satisfied for $[B] \sim 10^{20} \text{ cm}^{-3}$, i.e., the $A^* + 2B \rightarrow AB^* + B$ process is not a "bottle neck" unless the excimer stimulated emission rate exceeds $\sim 10^{10} \text{ s}^{-1}$. Under these circumstances (5.13a) is a good approximation and (5.6–9) are directly applicable.

The feasibility of various metal-noble gas combinations for excimer laser action can be investigated in three steps. First, from knowledge of the $A-X$ band intensity and shape we can determine the excitation fraction $[A^*]/[A]$ necessary for net gain and the alkali and noble gas densities necessary for a given gain coefficient. Next we can estimate, or calculate in some cases, the effect of other overlapping absorption bands. Finally, we consider the feasibility of obtaining the required $[A^*]/[A]$ by various methods of excitation. The latter issue is discussed in Sect. 5.3, in which the potential efficiency is also considered.

For weakly bound excimers, (5.6) or (5.13a)/(5.13b) require that $([A^*]g/[A]g^*)\exp[h(v_0 - v)/kT]$ must exceed one for net gain. This condition is most easily satisfied at the longest wavelength region of the $A-X$ bands, recalling, of course, that the gain drops rapidly in this region. Consequently, a key feature of a good excimer laser candidate is a large red-shift. Since $hv = V^*(R) - V(R)$ this net gain criterion depends only on the difference potential, but the size of the gain coefficient depends on the size of $s(v)$. Thus, a larger stimulated emission and gain coefficient occurs if V^* is attractive at wavelengths where net gain is achievable. A strongly attractive A state and highly repulsive X state are valuable (e.g., such as found in the rare gas halogens) but by no means necessary. Conversely, lower gain coefficients allow greater energy storage before superfluorescence, and they allow higher power gain cell or laser operation if net cavity gain can be achieved. We will discuss some examples before considering other absorptions.

As an example case the potentials and excimer band of NaXe are shown in Figs. 5.2 and 5.3a [5.7]. The A state has $\sim 2kT$ of binding at $T = 750 \text{ K}$ and optimum gain occurs at $\sim 700 \text{ nm}$, compared to $\lambda_0 = 590 \text{ nm}$. For $\lambda = 700 \text{ nm}$ and $T = 750 \text{ K}$ one obtains $(g/g^*)\exp[h(v_0 - v)/kT] = 55$ so that an excited

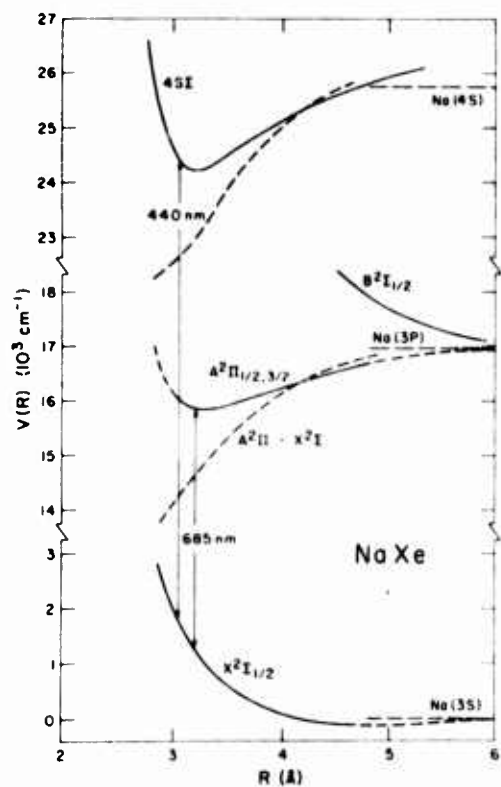


Fig. 5.2. Potential energies (—), $V^*(R) - I(R)$ differences (---), and some excimer band wavelengths for the NaXe molecule. The B and X states are theoretical [5.14], with the X state closely matched by atomic beam scattering results [5.9]. The A state is from $A-X$ band analysis [5.8], which also agrees with the theoretical X state. The $4S \Sigma$ state, which is not known experimentally, is from a minor adjustment of the theoretical potential [5.9] to match some features of the spectroscopic data [5.13]

fraction $[Na^*(3P)]/[Na] > 0.018$ is required for net gain at this wavelength. Preliminary discharge modeling [5.12] yields an excited fraction 0.01–0.10, depending on various assumptions. For the purpose of showing the entire curve, the gain shown in Fig. 5.3b corresponds to the 0.10 case, corresponding to the upper limit of the estimated range. This Na excitation fraction of 0.10 corresponds to $kT_e = 0.62\text{ eV}$ in (5.7). The Na_2 coefficients in Fig. 5.3b are discussed below.

The Li-He case is an example of a repulsive or very weakly attractive A state (present data cannot distinguish between these possibilities, but require that any attraction must be less than $0.2 kT$ [5.7]). For similar densities as the Na-Xe case above, the net gain at $\lambda = 900\text{ nm}$ for $[Li^*]/[Li] = 0.05$ is given in Fig. 5.4. This is almost equal to the Li-Xe gain at the wavelength (Fig. 5.4) in spite of the stronger binding ($\sim 4 kT$) of the Li-Xe A -state. This is a result of a much more repulsive $V(R)$ for Li-He compared to Li-Xe. Since the Li-He system has very slight or no A -state attraction, the molecular state populations will be in equilibrium with the gas temperature under all feasible conditions. Furthermore, all excited atoms can deliver their energy to a very short pulse (no vibrational relaxation is required). This is a very interesting example of an “excimer” laser candidate based on free colliding atoms.

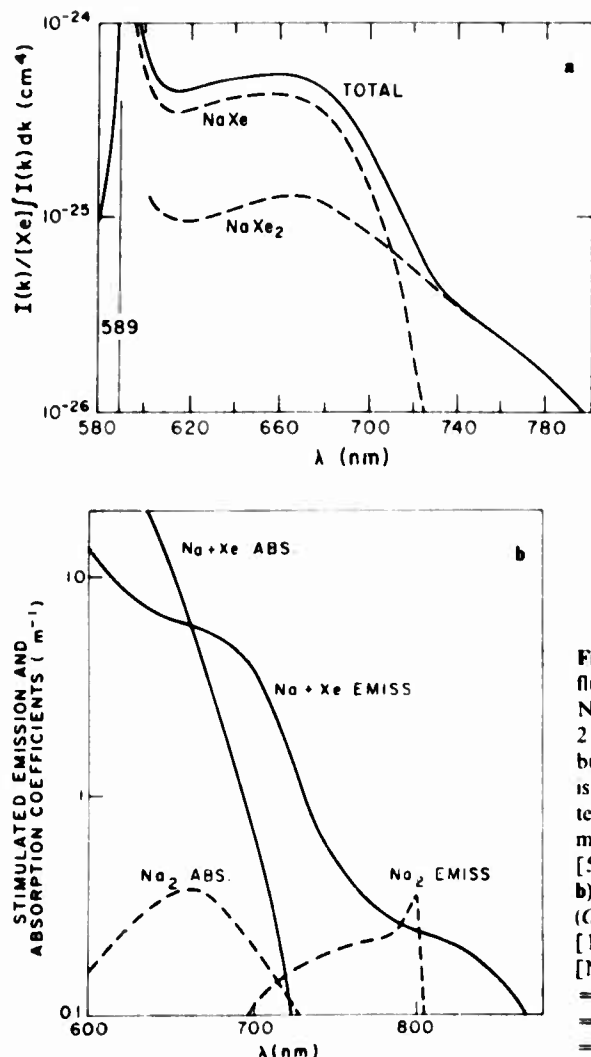


Fig. 5.3. a) The normalized fluorescence from optically thin Na(3P) at 420 K in the presence of $2 \times 10^{20} \text{ cm}^{-3}$ of Xe. The contribution from the NaXe $A-X$ band is indicated, as is the residual intensity which is attributed primarily to the $A-X$ band of NaXe₂ [5.15]. b) Absorption (K_A) and stimulated (G_s) coefficients for $T = 760 \text{ K}$, $[\text{Na}(3S)] = 3.5 \times 10^{16} \text{ cm}^{-3}$, $[\text{Na}(3P)] = 3.5 \times 10^{15} \text{ cm}^{-3}$, $[\text{Xe}] = 2.7 \times 10^{20} \text{ cm}^{-3}$, $[\text{Na}_2(X)] = 10^{14} \text{ cm}^{-3}$, and $[\text{Na}_2(A^1\Sigma)] = 2 \times 10^{13} \text{ cm}^{-3}$ (from [5.12]).

The $A-X$ bands of the other alkali-Xe cases have similar properties except that their bands are at longer wavelengths [5.6, 8, 14]. The $A-\Lambda$ bands are weaker and less extended to the red for lighter noble gases, so that they make less viable excimer laser candidates in spite of the desirability of a smaller noble-gas index of refraction [5.6, 8]. The above Li-He case and to some extent NaHe are the only known exceptions to this rule.

We now discuss other possible absorptions. Absorption from the $[AB^*]$ to a higher electronic states $[AB^{**}]$ will generally be spread across molecular bands of width similar to the $A-X$ band. The same initial-state populations,

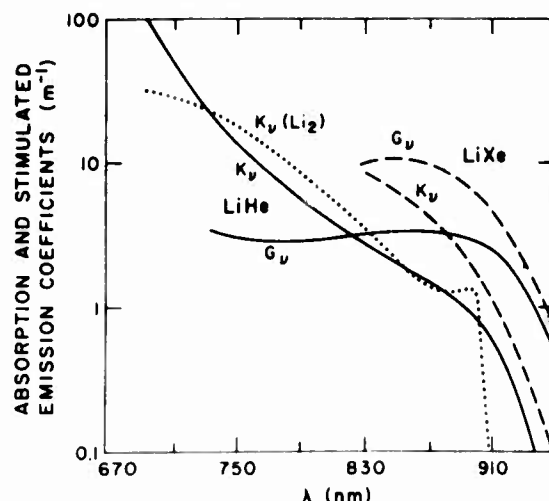


Fig. 5.4. Absorption (K_v) and stimulated emission (G_v) coefficients for $T = 1180\text{ K}$, $[\text{Li}(2S)] = 10^{17}\text{ cm}^{-3}$, $[\text{Li}(2P)] = 5 \times 10^{15}\text{ cm}^{-3}$, $[\text{Li}_2] = 5 \times 10^{15}\text{ cm}^{-3}$, $[\text{Xe}]$ or $[\text{He}] = 2 \times 10^{20}\text{ cm}^{-3}$ (from [5.3, 8]).

[AB^*], contribute to stimulated emission in the $A-X$ band and to the absorption coefficients for upward transitions. The oscillator strength for the alkali $A-X$ band is close to unity, whereas absorption from the A -state should be fairly evenly distributed across many bands and the ionization continuum (based on the alkali-atom oscillator strengths and sum rules). Therefore, only the relatively rare coincidence of a particularly strong absorption band bunched into a critical wavelength range can cause difficulties.

The most serious absorption source we are aware of is the $A-X$ band of the alkali dimers. The alkali dimers are typically bound by $\sim 0.4\text{ eV}$, their $A-X$ bands are in the same spectral regions as the metal-noble gas $A-X$ bands, and the dimer $A-X$ band has a large oscillator strength. This absorption has been discussed in detail by York and Gallagher [5.3]. As an example, the Na_2 absorption is shown in Fig. 5.3b for $[\text{Na}_2]$ calculated to occur in a high-power discharge [5.12]. Of key importance is the fact that the alkali-dimer absorption has a red edge, or satellite, beyond which absorption decreases rapidly. Thus, the net optical gain in longer wavelength portions of alkali-noble gas $A-X$ bands is not affected. In addition to the LiHe and LiXe cases described above, with $A-X$ bands extending past the Li satellite, the NaXe_2 $A-X$ band extends far past the Na_2 satellite [5.15], although the gain coefficients at $[\text{Xe}] = 2 \times 10^{20}\text{ cm}^{-3}$ are rather small (Fig. 5.3b). There are good reasons to expect this type of three-body excimer spectrum for many excimers. The Li_2 absorption spectrum in the presence of high pressure Xe is unknown, but unlikely to cause any unexpected problems as the area $\int K_v dv$ must be the same as that in Fig. 5.4.

Another important factor in the alkali-dimer absorption is that the alkali-dimers are bound by many kT (e.g., $11 kT$ for Na_2 at 750 K), so that their collisional dissociation by gas collision is relatively slow and expo-

nentially dependent on the gas temperature. Their density and absorption thus decrease rapidly with increasing gas temperature above that corresponding to the alkali equilibrium vapor pressure. Part of this gas temperature rise could be deliberately imposed externally, but the gas heating associated with the excitation of the medium also causes it. Furthermore, if discharges or e -beam excitation is used, the electron collisions with the dimers cause dissociation and thereby depletion of the dimer concentration. As an example, the $[Na_2]$ used for Fig. 5.3a is a factor of 15 less than the equilibrium value, as was obtained from discharge modeling [5.12]. If wide-band optical pumping is used, the alkali-dimer $A\ X$ and $B\ X$ bands absorb the pumping light across many hundreds of nanometers, so that the X state will again be severely depleted. In essence, the strong dimer absorption under equilibrium conditions is due to the relatively strong binding of the A_2 molecules, but they are not formed very rapidly by $A + A + Xe \rightarrow A_2 + Xe$ collisions due to the low A density. Thus any depletion mechanism, even an excimer-laser field itself, can be effective at depleting the dimer concentration. By comparison, the AB^* excimers associated with the excimer gain are only bound by a few kT and the process $A^* + Xe + Xe \rightarrow AXe^* + Xe$ is proportional to $[Xe]^2$ rather than $[A][Xe]$ for the dimer formation process. Thus dimers are depleted long before excimers are.

Collision-Induced Excimer Bands

Collision-induced absorption and emission in the wings of forbidden atomic lines has been studied for many years. However, only in the past two years was it discovered that the strong excimer bands occur very far from the forbidden atomic lines. The Columbia group of *Tam, Moe, Happer*, and associates discovered and have now measured absorption and emission by many of the bands associated with the transition to the first excited S and D states of the alkalis perturbed by noble gases [5.13]. More recently *Sayer et al.* [5.17], *Gauthier et al.* [5.18], and *Eden et al.* [5.19] have also measured properties of these bands. The bands associated with the D state appear to the blue side of the atomic transition energy, so the exponential factor of (5.6) favors absorption over emission and they are not viable excimer-laser candidates. (This occurs because the excited state is more repulsive than the ground state.) The bands associated with the $n^2S_{1/2}$ (ground state) to $(n+1)^2S_{1/2}$ transitions are to the red of the atomic transition wavelength $\lambda_0 = k_0^{-1}$, so they are potential excimer-laser candidates.

For the Rb and Cs-noble gas cases, the $nS \rightleftharpoons (n+1)S$ bands have a strong peak at the furthest red shift (k_s), indicating a "satellite" or that a minimum occurs in $V^*(R) - V(R)$ [5.2]. The frequency shift $hc(k_s - k_0)$ is greatest for Xe, but even in this case the $\exp[-hc(k_s - k_0)]$ factor of (5.6) that enhances G_v/K_v is only 10 at the temperatures necessary for a reasonable alkali density and gain coefficient. [The $V^*(R)$ binding is weak enough that (5.6) rather than (5.6a) is appropriate here.] Thus, net gain requires $[Cs(7^2S)]/[Cs(6^2S)] \geq 0.1$ and

equivalently for Rb, and this only appears feasible with laser pumping. We conclude that the Rb and Cs-Xe bands might be used as gaseous dyes for tuneable frequency conversion in the 500–700 nm region, but they do not appear to be viable candidates for flash lamp, e-beam, or discharge pumping. The absorption coefficient at these band peaks has been measured [5.13] to be typically $K_v/[Xe][A] \approx 10^{-38} \text{ cm}^5$, from which it follows that $G_v/[Xe][A^*] \approx 10^{-37} \text{ cm}^5$. Thus at $[Xe] = 10^{20} \text{ cm}^{-3}$, $[A] = 7 \times 10^{16} \text{ cm}^{-3}$, $[A^*] = 3 \times 10^{16} \text{ cm}^{-3}$ due to strong laser pumping, $K_v = 0.07 \text{ cm}^{-1}$ and $G_v = 0.3 \text{ cm}^{-1}$ might result. Some of the general properties of such “gaseous dye lasers” are discussed further in Sect. 5.3.

As the lighter alkalis are used, the $nS \rightleftharpoons (n+1)S$ excimer bands broaden, indicating the absence of a satellite, and they shift further from the atomic transition energy, again with largest shifts for Xe [5.13]. Consequently, the exponential factor in (5.6) more strongly favors G_v versus K_v and these systems become viable excimer-laser candidates. In addition, the theoretical potentials of Pascale and Vandeplaque [5.14], which disagreed sharply with the Cs and Rb-noble gas data, appear to give excellent predictions for K-Ar, Kr, Xe and Na-Ar, Kr, Xe [5.13]. The Na-Xe potentials in Fig. 5.2 include the “ $4S\Sigma$ ” state associated with $\text{Na}(4^2S_{1/2}) + \text{Xe}$. This potential is essentially that given by Pascale and Vandeplaque [5.14], except that we have lowered it 400 cm^{-1} at the minimum to conform better to the spectroscopic data of Tam et al. [5.13], who observed an $\sim 20 \text{ nm}$ wide emission band centered at 440 nm.

From (5.2) the spontaneous emission power reported in [5.13] can be multiplied by λ^3 to obtain the shape of $G_v/[Xe][\text{Na}^*]$ at the same temperature. Then from (5.6), $K_v/[Xe][\text{Na}]$ is obtained. Both G_v and K_v are then in the same units, but these are relative units since neither has been measured in absolute units for NaXe. At the center of the band the $\exp[-h(v-v_0)/kT]$ factor of (5.6) is ~ 200 , yielding net gain for 0.5% excitation fraction. (At this $[Xe]$, and for the $4S\Sigma$ potential in Fig. 5.2, $K_{eq}[\text{Xe}] \approx 0.15$ and these relations in terms of atomic populations are accurate to $\sim 10\%$.) We have estimated the magnitude of G_v and K_v for Na-Xe by comparing to the Cs-Xe and Rb-Xe cases for which K_v has been measured [5.13]. For this comparison we use (5.13), assume that the $A(R)$ are proportional to the square of the alkali atomic size, and evaluate the effective dv/dR at a satellite in terms of the area under the peak [5.6]. The dominant difference is about a factor of 10 reduction of G_v from Cs-Xe to Na-Xe, since the latter band does not have a satellite and is more spread out. The result is then, at $T=810 \text{ K}$ corresponding to $[\text{Na}] = 10^{17} \text{ cm}^{-3}$, $G_v(440 \text{ nm})/[\text{Na}(4S)][\text{Xe}] \approx 10^{-38} \text{ cm}^5$. It appears that this G_v magnitude estimate should be a lower bound, since NaXe is much more strongly bound than CsXe and one might expect the induced transition moment to be also stronger than for CsXe. The resulting G_v and K_v for $[\text{Na}] = 10^{17} \text{ cm}^{-3}$, $\text{Na}^*(4S) = 10^{15} \text{ cm}^{-3}$, and $[\text{Xe}] = 10^{20} \text{ cm}^{-3}$, are given in Fig. 5.5. The excitation fraction of $\text{Na}^*(4S)/\text{Na}(3S) = 0.01$ was arbitrarily chosen. The possibility of obtaining this excitation fraction in discharge, flashlamp or e-beam excitation has been neither modeled nor measured.

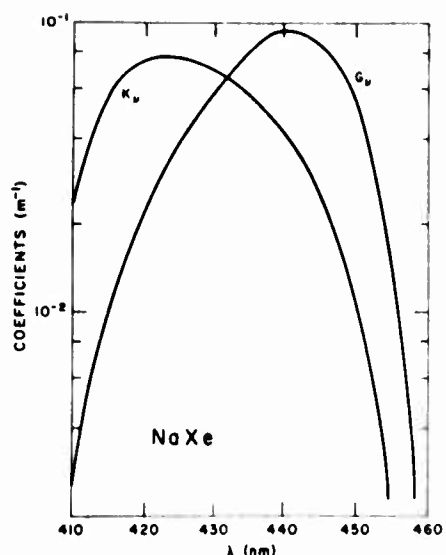


Fig. 5.5. Absorption (K_v) and stimulated emission (G_v) coefficients for the $4S\Sigma-X^2\Sigma$ band of NaXe , from analysis of the data in [5.13]. The absolute scale is estimated and 1% of the Na is assumed to be in the $4S$ state

It appears highly probable that the alkali dimers have absorption bands in the same spectral regions as these bands, since there will also be dimer states of $\text{Na}(4S)\text{Na}(3S)$ parentage. However, the same dimer depletion arguments discussed above in connection with the $A-X$ bands hold here; these dimer absorptions might not be a problem in a high-power system.

5.2.2 Group II-VIII Excimers

In contrast to the I-VIII excimers, for which the $A-X$ bands and potentials of most pairs have been thoroughly characterized, the only II-VIII band that has ever been observed is that of Hg-Xe . The broadening and shift of many Group II lines, due to noble-gas collisions, have been measured [5.5], but these relate only to very long-range interactions and are of no help in predicting excimer bands. We will thus discuss only Hg-Xe below, after a few general comments applicable to all of the Group II elements.

Visible and uv excimer bands associated with the n^3P and $n^1P \rightarrow n^1S$ (ground state) transition may be viable excimer laser candidates, and even the near infrared $n^3P \rightarrow (n-1)^3D$ and $n^1P \rightarrow (n-1)^1D$ transitions might be of interest for Ca, Sr, and Ba. Generalization of the Baylis models [5.20] for alkali-noble gas potentials argues that Xe should produce the strongest binding to Group II excited states, but that these will still be weakly bound ($< 10 kT$). Possible rapid predissociation of n^3P or n^1P excimers to repulsive excimer states associated with $(n-1)^1D$ and $(n-1)^3D$ levels could be serious for Ca, Sr, and Ba. The rate of energy transfer via $AB^* + A \rightarrow A^* + B$ is expected to be 10^6 – 10^7 s^{-1} at typical $[A] \sim 10^{16}$ – 10^{17} cm^{-3} , and this could be a significant

$[AB^*(n^3P)]$ depletion mechanism. (It is a source term for the buffered A_2^* excimer bands described in the Group II-II section.) The bands associated with the $n^3P \rightarrow n^1S_0$ transition will have small transition probabilities, probably similar to the atomic values as the same spin-orbit perturbation is involved. Thus any excited-state absorption bands that occurred in the same wavelength regions as these excimer bands would probably eliminate gain at these wavelengths. The $n^1P \rightarrow n^1S_0$ atomic-line radiation is trapped, but the far line wings which include the excimer bands will escape. The result is typically an effective radiative loss rate of $0.05 - 0.2 \Gamma_{\text{Atomic}} \cong 10^7 - 10^8 \text{ s}^{-1}$ for the total $A^*(n^1P) + AB^*(n^1P)$ population. It is clear that rapid, high-power pumping is necessary. Excited-state absorption should be negligible compared to these strongly allowed resonance-line bands, but $AB^*(n^1P)$ might be predissociated or collisionally transferred to n^3P , particularly for the heavier Group II elements for which the triplet singlet mixing is greatest.

The Hg-Xe excimer bands as well as the fluorescence yields and excited state kinetics were studied with e beam excitation by Gutcheck et al. [5.21]. Two uv bands were reported, each $\sim 30 \text{ nm}$ wide and centered at about 220 and 270 nm. The shapes of these two bands and their fluorescence yields for Hg-Ar, Kr, Xe, using e -beam excitation, have recently been reported by Woodworth [5.22]. In both studies the energy radiated in each band is typically $\sim 1\%$ of the e beam energy deposited in the gas. The shorter wavelength band is on the red wing of the 185 nm $6^1P_1 - 6^1S_0$ transition and clearly is the associated $A-X$ band; the longer wavelength transition comes from the 6^3P excimer manifold. The shape of the 270 nm Hg-Xe band has also been reported by Oldenberg [5.23], Freeman et al. [5.24], Nikoforov et al. [5.25], and others, using 6^3P_1 optical excitation. The band has a similar but significantly different shape than that observed in the e beam excitation experiments. The binding of the HgXe^* state associated with the 270 nm band, which we will label $\text{HgXe}^*(6^3P_1)$, is estimated as 1300 cm^{-1} relative to 6^3P_1 by Gutcheck et al. [5.21], 1560 cm^{-1} by Strausz et al. [5.26], and 600 cm^{-1} by Kielkopf and Miller [5.27]. The ground-state interactions have been determined from atomic beam scattering data [5.28]. Nothing else is known of the Hg-noble gas excited-state potentials, but there should be no strongly bound nonradiative HgXe^* reservoir states to compete for the excited-state population (see Hg_2^*). However, the 6^3P_0 level is $\sim 1800 \text{ cm}^{-1}$ below 6^3P_1 and could act as such a reservoir. It is discussed in the following paragraph. The data of Gutcheck et al. [5.21] also yield $\Gamma K_{\text{eq}} = 2 \times 10^{-14} \text{ cm}^3 \text{ s}^{-1}$, where $K_{\text{eq}} = [\text{HgXe}^*(6^3P_1)] / [\text{Hg}(6^3P_1)][\text{Xe}]$ and Γ is the effective radiative rate for $\text{HgXe}^*(6^3P_1)$ excimers. For the expected $\Gamma_1 \cong \Gamma_0 \cong 10^7 \text{ s}^{-1}$, this yields $K_{\text{eq}} = 2 \times 10^{-21} \text{ cm}^3$, a reasonable value for an excimer bound by $\sim 1300 \text{ cm}^{-1}$ or $3-4kT$.

Since $kT \cong 300 \text{ cm}^{-1}$ at temperatures corresponding to $[\text{Hg}] = 10^{16} - 10^{17} \text{ cm}^{-3}$, any of the above binding energies are less than $6kT$ and an equilibrated distribution of $[\text{HgXe}^*]/[\text{Hg}^*(6^3P_1)]$ is expected. Thus, the net gain criteria of Sect. 5.2 can be applied, and at 270 nm yields the requirement $[\text{Hg}(6^3P_1)] / [\text{Hg}(6^1S_0)] > 3 \exp(-2400 \text{ cm}^{-1} / 300 \text{ cm}^{-1}) = 10^{-3}$.

The gain coefficient at 270 nm assuming $\Gamma = 10^7 \text{ s}^{-1}$ and 300 cm^{-1} binding, is $G_v[\text{Hg}(6^3P_1)][\text{Xe}] \geq 2 \times 10^{-38} \text{ cm}^5$, yielding $K_v = 0.02 \text{ m}^{-1}$, $G_v = 0.2 \text{ m}^{-1}$ at $[\text{Hg}] = 10^{17} \text{ cm}^{-3}$, $[\text{Hg}(6^3P_1)] = 10^{15} \text{ cm}^{-3}$, $[\text{Ne}] = 10^{26} \text{ cm}^{-3}$. If $\text{Hg}(6^3P_1) + \text{Xe} \rightarrow \text{Hg}(6^3P_0) + \text{Xe}$ (excitation transfer) were a rapid process, it would be very difficult to achieve this 6^3P_1 state density as a large nonradiative 6^3P_0 population would lose excited-state energy via electron quenching or $^3P_0 - ^3P_0$ collisions. However, an upper limit to the rate coefficient of $10^{-14} \text{ cm}^3 \text{ s}^{-1}$ [5.29] has been measured for this excitation transfer and, therefore, in an e -beam afterglow or discharge the electrons may keep 6^3P_1 and 6^3P_0 in about a statistical ratio. Due to the shallow binding and resulting rapid Xe induced dissociation of the $\text{HgXe}^*(6^3P_1)$, electrons will not readily change the $[\text{HgXe}^*(6^3P_1)]/[\text{Hg}(6^3P_1)]$ ratio. Consequently, we conclude that this system could be a good excimer laser candidate, probably with higher efficiency in a discharge than in the above e -beam experiment. The low gain coefficient per $\text{Hg}(6^3P_1)$ can be compensated by increasing $[\text{Hg}]$, presumably at constant excitation fraction, until collisions between excited states represent a significant loss. Excited state absorption could, of course, destroy net medium gain at any density.

The $\text{Hg}(6^1P_1)$ excimer bands are also viable laser candidates. Assuming weakly bound $\text{Hg}(6^1P_1)-\text{Xe}$, the net gain criteria of (5.6) becomes at 215 nm $[\text{Hg}(6^1P_1)]/\text{Hg}(6^1S_0)] = 3 \exp(-7500 \text{ cm}^{-1} 300 \text{ cm}^{-1}) \geq 10^{-10}$. The 215 nm stimulated emission coefficient, from (5.13), is $\Gamma_0 = 8 \times 10^8 \text{ s}^{-1}$ [5.30], and assuming $\sim 600 \text{ cm}^{-1}$ binding in the 6^1P_1 state, $G_v[\text{Hg}(6^1P_1)][\text{Xe}] = 10^{-37} \text{ cm}^5$. For example, if $[\text{Xe}] = 10^{20} \text{ cm}^{-3}$, $[\text{Hg}] = 10^{18} \text{ cm}^{-3}$, and $[\text{Hg}(6^1P_1)] = 10^{15} \text{ cm}^{-3}$, we find that $G_v \approx 1 \text{ m}^{-1}$ and $K_v \geq 10^{-7} \text{ m}^{-1}$ at 215 nm. No studies of the feasibility of obtaining such 6^1P densities in e -beam, discharge, or optically pumped Hg-Xe vapor have been reported, but such a low excitation fraction is required that this appears as a fairly promising laser candidate.

5.2.3 Group III-VIII Excimers

The Group III metals attain equilibrium vapor densities appropriate for excimer lasers ($\geq 10^{16} \text{ cm}^{-3}$) at temperatures of 800–2000 °C, but they are generally nonreactive with window and containment materials. Their resonance lines are in the 250–530 nm region so that the red-wing excimer bands occur in the 250–700 nm regions. The only III–VIII excimers that have been studied experimentally are those of Tl, the most volatile member in the group, so the remainder of this discussion will concentrate on Tl.

Thallium has a $6^2P_{1/2}$ ground state and a metastable $6^2P_{3/2}$ state separated by 1 eV fine structure. Transitions from these states to the $7^2S_{1/2}$ and 6^2D states have large oscillator strengths, so Tl has four strong resonance lines occurring at 277, 353, 378, and 535 nm. The red-wing excimer bands associated with each of these lines are viable excimer laser candidates, so they encompass much of the

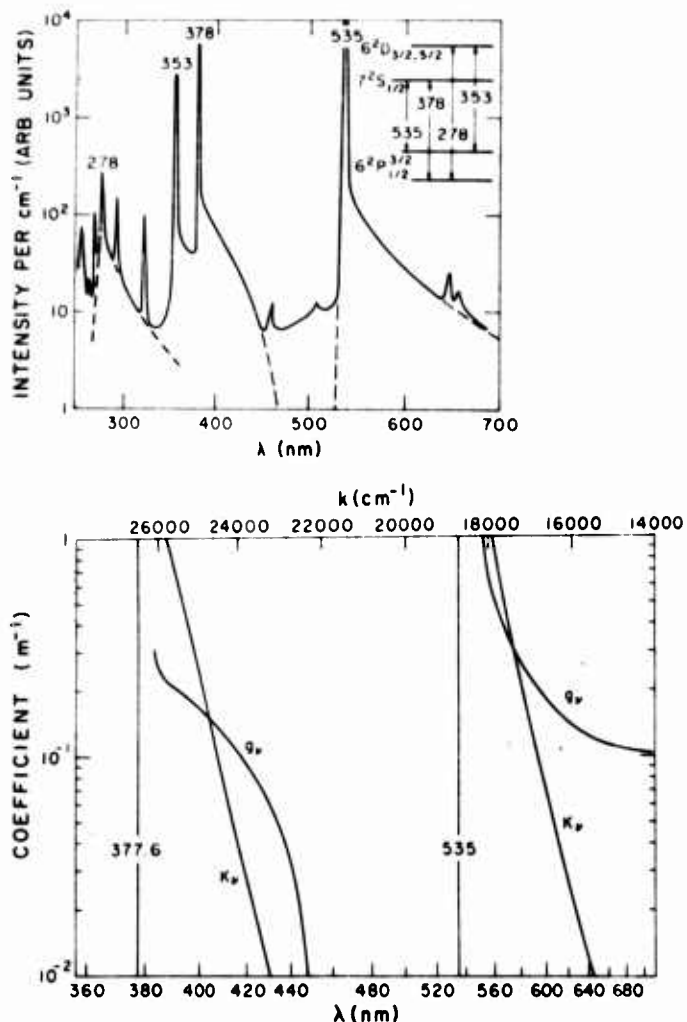


Fig. 5.6. a) Spontaneous emission from a discharge in TlXe for $T = 1020\text{ K}$, $[\text{Tl}] = 3 \times 10^{15}\text{ cm}^{-3}$ and $[\text{Xe}] = 3 \times 10^{19}\text{ cm}^{-3}$ (from [5.32]). The excimer bands are indicated by dashed lines.
b) Absorption (K_ν) and stimulated emission (G_ν) coefficients for TlXe at $T = 1090\text{ K}$, $[\text{Tl}(6^2P_{1/2})] = [\text{Tl}(6^2P_{3/2})] = 5 \times 10^{15}\text{ cm}^{-3}$, $[\text{Tl}(7^2S_{1/2})] = 2 \times 10^{14}\text{ cm}^{-3}$, $[\text{Xe}] = 2.7 \times 10^{20}\text{ cm}^{-3}$ (from [5.31])

near uv and visible spectrum. As with the I-VIII excimers, Xe produces the strongest and widest excimer bands, and is, from the discussion above, selected as the best laser candidate [5.31]. The relevant Tl energy levels and the Tl-Xe excimer emission spectrum from a weak discharge in $[\text{Tl}] \approx 10^{16}\text{ cm}^{-3}$ and $[\text{Xe}] \approx 10^{20}\text{ cm}^{-3}$ are shown in Fig. 5.6a [5.32]. The temperature dependence of the two visible band intensities associated with the $7^2S_{1/2} - 6^2P_{1/2, 3/2}$ transitions has been measured, and interpreted to yield the Tl-Xe excimer

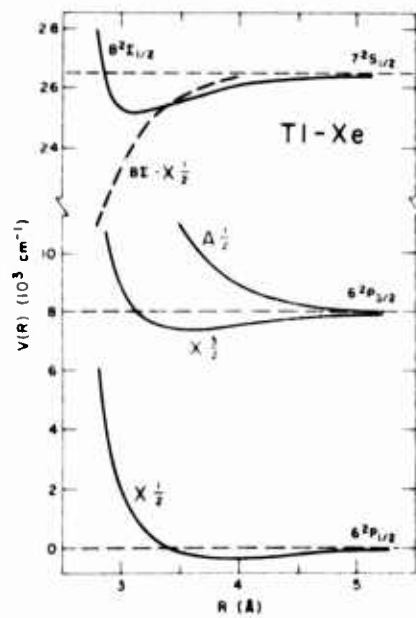


Fig. 5.7. Experimental Tl-Xe potentials (from [5.31])

potentials [5.31] shown in Fig. 5.7. From (5.2) and (5.6), these normalized spontaneous emission intensities have been converted into the G_v and K_v in Fig. 5.6b. The conditions assumed for this figure are [Tl] and [Xe] appropriate for a high-power excimer laser, with 2% excited Tl(7^2S) and the remainder divided equally between the $6^2P_{1/2} + 6^2P_{3/2}$ states. This $7^2S_{1/2}$ excitation fraction corresponds to an electron temperature $T_e \sim 1\text{ eV}$ in (5.7). Studies of its feasibility are underway in the author's laboratories. The 278-310 and 353-378 nm bands in Fig. 5.6a are associated with the $6^2D - 6^2P$ transitions. These have not been studied in normalized fluorescence, so the excimer potentials associated with the 6^2D states and the gain coefficient as a function of [Tl(6^2D)] have not been determined. Nonetheless, based on the intensity of these bands in the discharge spectrum they are expected to be as good an excimer laser candidate as the visible bands.

Tl is essentially a one-electron atom, and the oscillator strengths of the above four resonance lines add up to 0.95 with about 1/3 of this in the $6P \rightarrow 7S$ transition [5.33]. Therefore the arguments applied to alkali-noble gas absorption from excited states apply here as well, although it is somewhat weaker for the $6P \rightarrow 7S$ bands due to their smaller oscillator strengths. It is possible for absorption in strongly allowed Tl-Xe bands out of the 7^2S or 6^2D levels to exceed the stimulated emission in the $7^2S \rightarrow 6^2P$ or $6^2D \rightarrow 6^2P$ bands, but the oscillator strengths of the latter bands are large enough that it is extremely unlikely these excited state absorptions could eliminate net gain in all regions of the bands. The other potential absorption, by Tl_2 , is difficult to evaluate due to

minimal knowledge of the Tl_2 binding energy. Tl_2 is known to have several absorption bands in the 400–440 nm region [5.34], and by inference from emission bands there should also be absorption bands in the 620–650 nm region from $Tl(6^2P_{3/2})$ parentage states. The Tl_2 binding energy is unknown, although it has been estimated as ~ 0.6 eV [5.35]. Anything in excess of 0.75 eV would cause serious absorption if Tl_2 occurred in an equilibrium concentration. However, just as in the Na_2 case above, severe Tl_2 depletion can be expected to occur due to gas heating and electron collisional dissociation in high-power discharges, e beams, or optical pumping schemes.

The Group III elements share a potentially useful feature with many other metals; they are much more volatile as halogenated compounds. This has been used to advantage in arc lamps [5.36] and tested under excimer laser conditions [5.37]. It could be valuable for many metal-based excimer lasers. Relatively high densities of metal vapors can thereby be obtained at moderate temperatures, with the compounds dissociated in the discharges but recombining in cold outer zones to prevent metal condensation on relatively cold walls. In addition to allowing the use of many otherwise intractable metals, the exponential Boltzmann factors in G_v and G_v/K , of Sect. 5.2 show that much larger gain coefficients and inversions can be attained if temperatures can be lowered. Other compounds besides halogens can be considered, of course, particularly as the residual halogens could have a deleterious effect on discharge stability.

5.2.4 Group I-II Excimers

The existence of low-lying 1D and 3D excited states of Ca , Sr , and Ba combined with the causticity and low vapor pressures of these elements make them poor candidates for replacing the noble gas in excimer molecules. Mg , Zn , Cd , and Hg are reasonable candidates for use with elements of equal or lesser excitation energies, but to obtain the necessary $\geq 10^{19} \text{ cm}^{-3}$ densities requires 900–1000 °C for Mg , Zn , and Cd . Thus, due to its volatility and relatively mild chemical behavior Hg is clearly the most practical and frequently studied substitute for noble gases. In the remainder of this section and most of the following two sections we will discuss only such A–Hg type excimers.

The interaction potentials of alkali–Hg molecules have been studied by *Duren*, both experimentally through atomic beam scattering and theoretically [5.38] using the method developed by *Baylis* [5.20] for alkali–noble gas molecules. As an example these calculated Na–Hg potentials are shown in Fig. 5.8 and the G_v and K , for the $A-X$ band which these yield from (5.13) for typical laser-model conditions are shown in Fig. 5.9. The only spectroscopic data available for these alkali–Hg molecules are those of *Drummond* [5.39], who measured the $A-X$ band shapes, but not in absolute units. The shape of G_v corresponding to Drummond's spontaneous-emission band shape is shown in Fig. 5.9 for comparison. The extent of the agreement between these theoretical

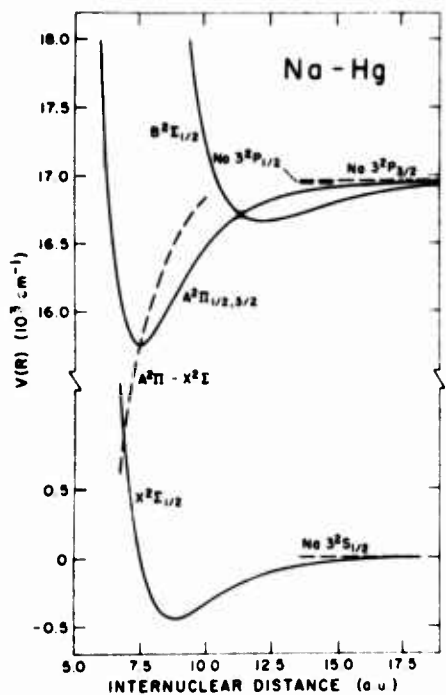


Fig. 5.8. Theoretical NaHg potentials (from [5.38])

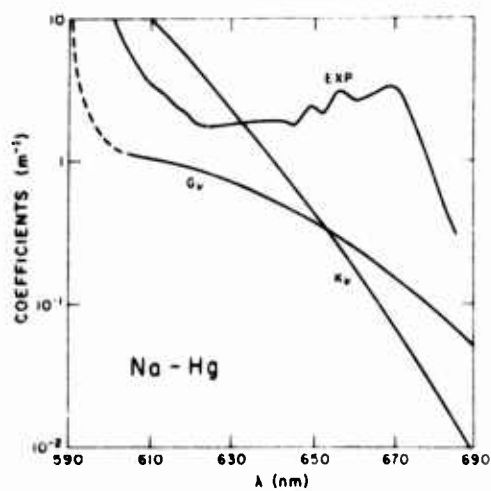


Fig. 5.9. Absorption (K_A) and stimulated emission (G_A) coefficients for NaHg, deduced from the potentials in Fig. 5.8, for conditions of $T = 690$ K, $[Na(3S)] = 10^{16} \text{ cm}^{-3}$, $[Na(3P)] = 10^{15} \text{ cm}^{-3}$, and $[Hg] = 10^{14} \text{ cm}^{-3}$. The experimental line is the measured shape of G_A obtained from the measured fluorescence spectrum of [5.39]. This experimental curve is arbitrarily normalized

and experimental band shapes is typical of that seen between measurements and Baylis-type potential calculations for the alkali-noble gas molecules [5.7, 8, 13]. The d^3R/dv term in (5.13) is very sensitive to $V^*(R) - V(R)$, so that a very accurate set of $V(R)$ is necessary to produce the $A X$ band intensity distribution.

As this NaHg band does not extend as far to the red as the NaXe band, there is little to recommend NaHg in place of NaXe unless the gain coefficient for NaHg is much larger (due to stronger NaHg* binding), or higher excitation efficiency were feasible. Duren's theoretical potentials predict alkali-Hg $A-X$ bands of strength similar to those of alkali-Xe, so on this basis the alkali-Hg molecules would not be very interesting excimer-laser candidates if these potentials were correct. But in view of the very stringent requirements on the accuracy of the potentials, this is still an unsettled question.

5.2.5 Group II-II Excimers

Most excimer-laser related studies in this class have concentrated on Hg as the "noble gas", with most of this attention placed on the 330 and 480 nm bands from pure Hg vapor. The exception is some models and measurements [5.40] reported for Cd-Hg. Very little is known about any other atom pairs, with the exception of Mg₂ [5.41]. The Mg₂ A and X -state potentials are well known [5.41-43], and allow its amplification characteristics to be modeled using (5.13). As these characteristics are fairly interesting, we will include them below before discussing the Cd-Hg and pure Hg vapor work.

Mg₂

Balfour and Douglas [5.41] have measured the bound-bound spectrum of the $A^1\Sigma_u^+ - X^1\Sigma_g^+$ system of Mg₂, which connects to the $3^1P_1 - 3^1S_0$ resonance

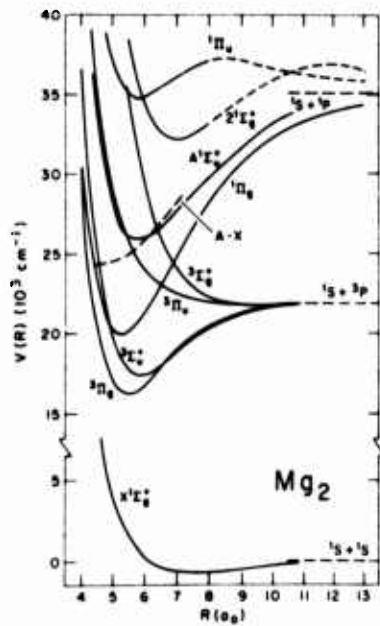


Fig. 5.10. Mg₂ potentials. The $A^1\Sigma_u^+$ and $X^1\Sigma_g^+$ potentials are from spectroscopic data [5.41] and the rest are theoretical [5.44]

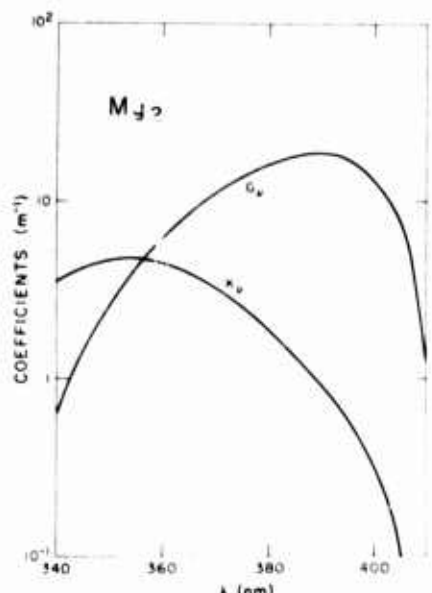


Fig. 5.11. Absorption (K_v) and stimulated emission (G_v) coefficients for Mg_2 for $T=1150\text{ K}$, $[Mg]=10^{18}\text{ cm}^{-3}$, $[Mg_2(A^1\Sigma^+)] = 10^{15}\text{ cm}^{-3}$

transition of Mg. Their initial analysis to obtain the potentials has been extended by *Li* and *Stwalley* [5.42] and by *Vidal* and *Scheingraber* [5.43] to accurately determine dissociation limits and many higher-order Dunham coefficients. These potentials [5.43] are given in Fig. 5.10, along with other potentials calculated by *Stevens* and *Krauss* [5.44]. A -state predissociation into the triplet manifold was also observed in [5.43], but lifetimes are not given. The difference between the A and X -state potentials is also plotted in Fig. 5.10, so that the small slope at $R \sim 5.5 a_0$ is apparent. This helps concentrate the band and yields a large G_v at $\lambda \approx 390\text{ nm}$. The absorption and gain coefficients for $[Mg]=10^{16}\text{ cm}^{-3}$ at $T=870\text{ K}$, $Mg_2^*(A^1\Sigma)=10^{14}\text{ cm}^{-3}$, and $F_0=3.5 \times 10^8\text{ s}^{-1}$ [5.45] in (5.13, 13a) are shown in Fig. 5.11. This is shown to indicate the possibilities as a high-power laser in a buffered system. However, the feasibility of obtaining a vibrationally thermalized or partially thermalized A -state population of this magnitude has not been investigated. In particular, predissociation to repulsive triplet states and gas collisional conversion of $A^1\Sigma$ into nonradiative $^1\Pi_g$ molecules could be very fast and eliminate the possibility of obtaining such $A^1\Sigma$ state populations. Absorptions out of large triplet and $^1\Pi_g$ populations could also be a serious problem.

Cd-Hg

The excimer bands associated with $Cd(5^3P)-Hg$, have been reported by *McGeoch* et al. [5.40] as a $\sim 100\text{ nm}$ wide continuum centered at $\sim 470\text{ nm}$. *McGeoch* and *Fournier* [5.40] have also reported $0.4\% \text{ cm}^{-1}$ gain at 488 nm in

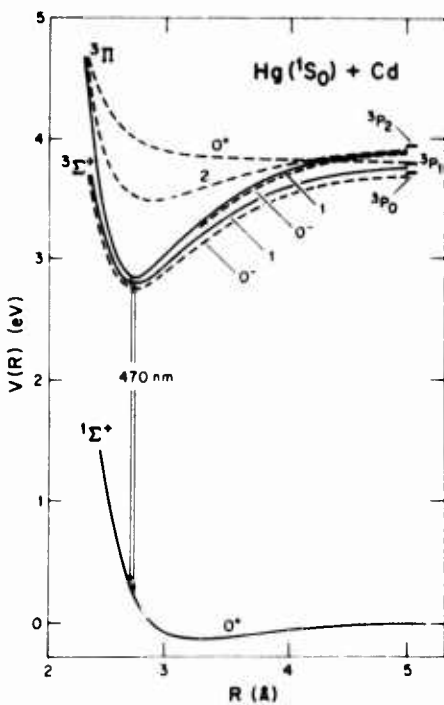


Fig. 5.12. HgCd potentials, from [5.40]. The explanation of the 470 nm band is indicated

flashlamp excited vapor of $[Cd] = 3 \times 10^{15} \text{ cm}^{-3}$, $[Hg] = 2 \times 10^{18} \text{ cm}^{-3}$. However, recent investigations at LLL have failed to show gain in a nearly equivalent experiment [5.46]. The potentials proposed by these authors are given in Fig. 5.12; they assign radiative lifetimes of $\sim 3 \mu\text{s}$ to the two levels associated with the excited 3P states. As in the Hg_2 case which follows, this may be an effective radiative rate due to an excited population distributed thermally between the 31 and $^3O^-$ states, with the latter metastable. However, the gain coefficient per total $Hg Cd^*$ density is still given by $(\lambda^2/8\pi)\Gamma_{eff}/\Delta v$ where Γ_{eff} is this effective radiative rate and Δv is the width of the band. In view of this very small Γ_{eff} (an effective oscillator strength of $\sim 10^{-3}$), excited state absorption could be a very serious issue in this molecule.

Hg_2

Due to the ease of handling Hg vapor and its importance in lighting and electrical equipment, the kinetics, spectra and discharge properties of Hg vapor have been studied extensively [5.47]. In spite of this, many of the properties which determine the viability and efficiency of potential Hg_2 excimer lasers have only been determined very recently if at all. Studies by Hill et al. [5.48], and by Schlie et al. [5.49] indicated potential optical properties in e -beam excited Hg vapor, but only the recent very thorough experimental studies by

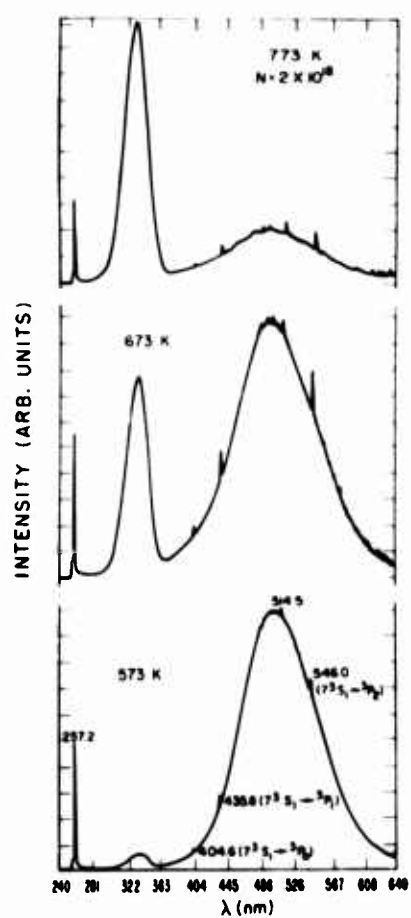


Fig. 5.13. Fluorescence spectrum from optically excited Hg vapor at $[Hg] = 2 \times 10^{18} \text{ cm}^{-3}$ and the indicated temperatures (from [5.50])

Drullinger et al. [5.50] combined with theoretical potentials by Stevens and Krauss [5.44] have finally yielded a fairly complete picture of the Hg_2 energy levels and radiative properties as well as the heavy particle kinetics associated with the $Hg(6^3P)$ states and connected Hg_2^* levels. Some calculations [5.51, 52] and measurements [5.4, 53] on Hg discharges have elucidated aspects of high-power discharges in high pressure Hg vapor, as appropriate for excimer lasers. These are discussed in Sect. 5.3; we summarize the Drullinger et al. [5.50] picture for Hg_2 potentials and Hg vapor kinetics in the following paragraphs.

Temperature dependent emission spectra of optically excited Hg vapor are shown in Fig. 5.13, and a set of Hg_2 potentials is shown in Fig. 5.14. The R scale is not well determined by the theory or data, so is left arbitrary in the figure; this uncertainty is not important for laser modeling. These potentials were derived by adjusting theoretical potentials from Stevens and Krauss to match experimental data, where available. The Hg_2 radiative transition

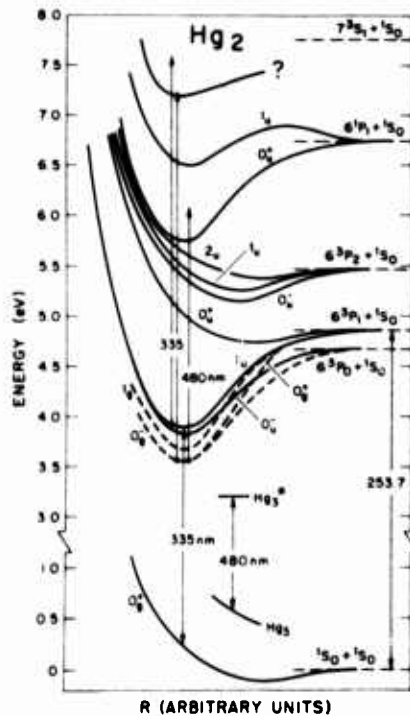


Fig. 5.14. Hg_2 potentials and the effective position of the Hg_3 levels responsible for the 480 nm band, from [5.50]. These were constructed by adjusting the results of Mg_2 ab initio calculations to fit expected Hg_2 behavior and known spectroscopic data. We have added the (?) potential associated with the 7^3S state, whose shape is unknown

associated with the 335 nm band is indicated, as is the effective energy position of the Hg_3^* and Hg_3 levels which the authors associate with the 480 nm band. The experimental observations indicate that the nonradiative O_u^- , O_g^- , and O_g^+ states act like an effective reservoir (Res) for most of the Hg_2^* population that is $\sim 2700 \text{ cm}^{-1}$ below the minimum of the radiative 1_u state, which has a band-averaged radiative rate $\Gamma_1 \approx 10^6 \text{ s}^{-1}$. Another 3800 cm^{-1} below this effective Hg_2 reservoir is the average position of the Hg_3^* population responsible for the 480 nm band. At densities $[\text{Hg}] > 10^{18} \text{ cm}^{-3}$ appropriate for high-power excimer lasers, and without electron collisions, the population of this Hg_3^* state is in equilibrium with the Hg_2^* reservoir, so that $[\text{Hg}_3^*]/[\text{Hg}_2^*(\text{Res})] = [\text{Hg}]K_3 \exp(3800 \text{ cm}^{-1}/kT)$. Similarly, the Hg_2^* populations come to an equilibrium ratio $[\text{Hg}_2^*(1_u)]/[\text{Hg}_2^*(\text{Res})] = (Z_{1u}/Z_{\text{Res}}) \exp(-2700 \text{ cm}^{-1}/kT)$, where the partition functions should satisfy $Z_{1u}/Z_{\text{Res}} \sim 1$. Thus if the band-average radiative rate of Hg_3^* is Γ_3 , the ratio of the bands in fluorescence is

$$\frac{I_{335}}{I_{485}} = \frac{\Gamma_1 \exp(-6500 \text{ cm}^{-1}/kT)}{[\text{Hg}]K_3 \Gamma_3} \quad (5.14)$$

Measurements have determined that $\Gamma_1/K_3 \Gamma_3 = 4.5 \times 10^{23} \text{ cm}^{-3}$. If one estimates $K_3 \sim 10^{-22} \text{ cm}^3$, then $\Gamma_3 \sim \Gamma_1/50 \sim 2 \times 10^4 \text{ s}^{-1}$, corresponding to an

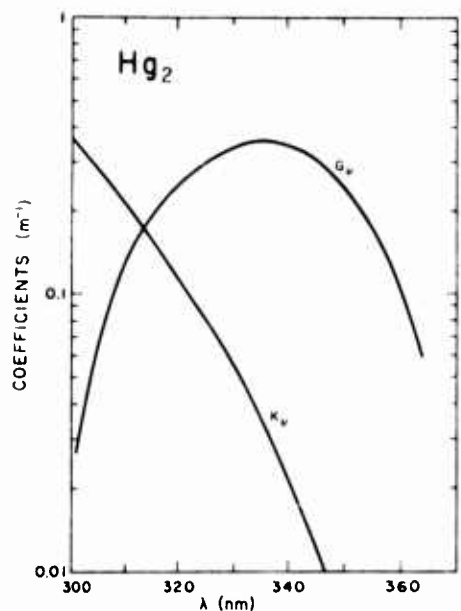


Fig. 5.15. Absorption (K_v) and stimulated emission (G_v) coefficients for Hg vapor at $T = 1300\text{ K}$, $[\text{Hg}] = 10^{19}\text{ cm}^{-3}$, $[\text{Hg}_2^*] = 1017\text{ cm}^{-3}$, where Hg_2^* refers to the 35-4.0 eV excimer states in Fig. 5.14

oscillator strength of about 10^{-4} at 480 nm. These results, the shape of the 1_u potential, and the $1_u \rightarrow O_g^+$ (ground state) transition moment variations were deduced from analysis of the temperature and time dependence of the band intensities and shapes, following optical excitation.

Due to the $\exp(-2700/kT)$ ratio of $[\text{Hg}_2^*(1_u)]/[\text{Hg}_2^*(\text{Res})]$, the 330 nm band gain can be greatly enhanced by overheating the vapor relative to the equilibrium density. Figure 5.15 shows the 330 nm band gain and absorption for $T = 1300\text{ K}$ and $[\text{Hg}_2^*(\text{Total})]/[\text{Hg}] = 1\%$, where total refers to the 1_u and reservoir states. At this temperature about 7% of the total Hg_2^* is in the radiating state, so that raising T further could enhance $G_v/[\text{Hg}_2^*(\text{Total})]$ by as much as a factor of five. The other effects of such gas heating would be to spread the band slightly and to increase K_v , although by a smaller factor than the G_v increase. In a discharge or e -beam excited vapor, electron collisions will tend to raise the $[\text{Hg}_2^*(1_u)]/[\text{Hg}_2^*(\text{Res})]$ ratio above the gas temperature, thereby increasing the gain coefficient per unit of total $[\text{Hg}_2^*]$ density.

The stimulated emission coefficients for these bands are very weak when expressed as a function of the total Hg_2^* density, e.g., it is $\sim 4 \times 10^{-20}\text{ cm}^2$ at 335 nm and $T = 1300\text{ K}$ (Fig. 5.15). Therefore, absorption from Hg_2^* in allowed bands, particularly from the reservoir states which contain most of the population, will be $\sim 10^3$ stronger and will destroy the medium gain if they occur in the same wavelength regions as the excimer bands. Estimates of some higher excited Hg_2^* states which could cause such absorptions, by Stevens and Krauss, are shown in Fig. 5.14. Arrows of length corresponding to 335 nm and

480 nm are drawn upwards from the O_u^- , O_g^+ , and O_g^- reservoir states and from the 1_u state to indicate where these absorptions would be expected to go, although it is not necessary that they start at the potential minimum. Hill et al. [5.48] measured almost a constant absorption from 390–515 nm in *e*-beam pumped Hg vapor, and attributed this to absorption by the Hg_2^* states associated with $Hg(6^3P) - Hg$ to repulsive upper levels of Hg_2 . Drullinger et al. [5.50] also measured absorption at 488 nm from the equilibrated population of optically excited $Hg(6^3P) - Hg$ states. These absorptions very likely occur from the reservoir states to the 1_u and O_u^- repulsive states which dissociate to 6^3P_2 ; these might be more repulsive than indicated in Fig. 5.14. Although the 480 nm band gain per Hg_2^* might be improved somewhat over the value in the Hill et al. [5.48] study (e.g., using lower temperatures), the effective stimulated coefficient per Hg_2^* is quite small and the dipole-allowed Hg_2^* absorption within the triplet manifold will probably be stronger under most realizable conditions.

Hg_2^* absorption in the region of the 335 nm band would be very strong if sufficiently attractive states associated with $Hg(7^3S) - Hg$ occur (e.g., the state with question mark in Fig. 5.14). Stevens [5.54] suggests that Rydberg-like states should occur about as indicated in Fig. 5.14, although no detailed calculations have been made. This absorption coefficient per Hg_2^* is of course given by (5.13) where V refer to the potentials of the Hg_2^* states and V^* to those of the $Hg(7^3S) - Hg$ state. Thus, if $V^*(R) - V(R)$ traverses the 335 nm band photon energies anywhere in the 2.7–3.5 Å region, very strong absorption bands will obscure the excimer-band gain. York et al. [5.53] have measured typically 10% net absorption in a discharge afterglow at a number of wavelengths in the 335 nm band, and Byer et al. [5.55] have measured absorption at 325 nm from strongly optically pumped Hg vapor. Drullinger et al. [5.50] obtained an upper limit of $\sim 3 \times 10^{-18} \text{ cm}^2$ for 325 nm absorption per total Hg_2^* in their weakly excited vapor with $[Hg^*] \geq 10^{12} \text{ cm}^{-3}$. This limit is large enough to allow the above measured absorptions to be due to $Hg_2^*(\text{Res} + 1_u)$. However, the absorptions in the strongly excited vapors could also be due to populations of Hg_2 in higher excited states with strong absorptions from these. For this absorption to show the same time dependence as fluorescence it would, of course, be necessary for these higher Hg_2^{**} state populations to follow the same decay curve as the Hg_2^* emission, but this is not unreasonable if the decay rates were predominantly due to net energy flow out of many strongly coupled levels. The coupling can occur through the $Hg_2^* - Hg_2^*$ collisions, radiative and collisional cascading following recombination, electron collisions, and other possibilities. In fact the fluorescence observed from these and *e*-beam excited vapors may also have major fluorescence bands due to more highly excited excimer states; the fact that an apparent single decay rate is observed is not proof that a single, closely grouped, excited-state manifold is the source of all the bands. But returning to the Hg_2 335 nm band, it requires strong excitation to obtain useful excimer gain levels, so that absorption under these conditions is the crucial test. These measurements indicate that net gain of significant size cannot be obtained on

the 335 nm band with strong pumping, unless index of refraction variation or some other loss process is being misinterpreted as Hg_2^* absorption. On the other hand, if excited-state absorption could be overcome the 335 nm excimer band itself has excellent gain characteristics (Fig. 5.11). It appears reasonable to expect that a large concentration of Hg_2^* excimers might be achievable, subject to the limitations discussed in Sect. 5.3, and this is generally considered to be an attractive candidate for high-energy, subnanosecond pulses.

The excited-state absorption issue is a serious consideration for all excimer bands with low gain coefficients. Discharges and e^- beams populate many high-excited levels, and there may be no net medium gain until these higher levels are largely emptied, hopefully long before the desired lowest excimer states are emptied.

5.2.6 Group III-II Excimers

In this group, Hg is the most tractable Group II replacement for the noble gas, although densities of 10^{19} cm^{-3} of Cd, Zn, or Mg are feasible at 800–1100 °C. Temperatures in this range are necessary as well to obtain appropriate Group III vapor densities. As with all the metal-based excimers, the substitution of Hg for Xe offers the possibility of stronger excited-state binding and thereby larger gain coefficients due to the exponential factor in (5.13a). But whereas this may be a vain hope for the alkali Hg excimers, it is astonishingly successful for Tl-Hg. *Drummond and Schlie* [5.56] have shown that Tl-Hg has relatively narrow excimer emission bands with gain coefficients to per $[\text{Tl}^*(7^2S)]$ that are 10–100 times larger than for Tl-Xe. It is likely that similarly strong bands occur in other visible wavelength regions when other Group III elements are substituted for Tl. *Santaran et al.* [5.57] have studied the bands of TlHg , TlCd , TlZn , InHg , and InZn , and obtained some portions of the potentials. Since Tl-Hg has been studied as an excimer laser candidate by *Drummond and Schlie*, and it is a very promising candidate, we will discuss this case below.

The Tl-Hg potentials, from [5.56], are shown in Fig. 5.16. These have a similar appearance to the Tl-Xe potentials in Fig. 5.7, but there are two important and major differences. It is instructive to compare the optical consequences of these differences from the standpoint of (5.13). First the B -state of Tl-Hg is bound by 4100 cm^{-1} , compared 1300 cm^{-1} for Tl-Xe, so that the $\exp(-AV^*/kT)$ population factor in (5.13a) is $\sim \exp(5.4)$ for Tl-Hg and $\sim \exp(1.7)$ for Tl-Xe at $T = 1100 \text{ K}$ corresponding to $[\text{Tl}] \sim 10^{16} \text{ cm}^{-3}$. Due to this, $G_v/[\text{Tl}^*][\text{Hg}]$ in the center of the Tl-Hg emission bands is ~ 50 times greater than $G_v/[\text{Tl}^*][\text{Xe}]$ in the center of its bands. In either case, at high enough $[\text{Hg}]$ or $[\text{Xe}]$ most of the $[\text{Tl}^*(7^2S)]$ is in molecular form and most of the emission is in the molecular band (5.13a), but the Tl-Hg band is still narrower due to the larger exponential population factor. This factor concentrates the emission band in the wavelength region corresponding to the potential minimum. If the gain coefficient per excimer molecule is approxi-

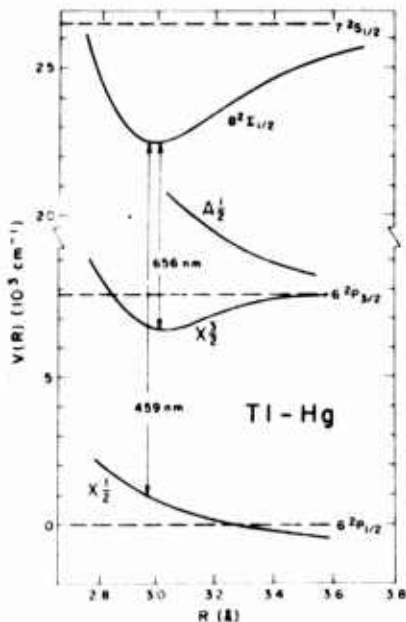


Fig. 5.16. TI-Hg potentials and origins of the 656 and 459 nm bands, from [5.56]. The $A_{1/2}$ state is not known, but is expected to be quite repulsive as shown

mated as in (5.12) one can see that this decreased Δv_{Band} results in a higher gain coefficient. This effect is greatly enhanced by the second important difference between the TI-Hg and TI-Xe potentials: $V^*(R) - V(R)$ goes through a minimum for TI-Hg near 3.1 Å. This results in the "head of band-heads" or "satellite" seen in the TI-Hg bands in Fig. 5.17. (These TI-Hg potentials were in fact constructed by Drummond and Schlie [5.56] to match this measured effect.) This further narrows the effective Δv_{Band} to $\sim 500 \text{ cm}^{-1}$, compared to 5000 cm^{-1} for the TI-Xe bands. This is in fact the same effect that is responsible for the narrowness of the halogen-noble gas uv excimer bands. In the present context, it results in the large gain coefficients shown in Fig. 5.17 for the assumed TI, Hg, and TI^* densities, which have been obtained here by applying (5.2) and (5.6) to the fluorescence data in [5.56]. Comparison to Fig. 5.6 shows that even for $[\text{Xe}]/[\text{Hg}] \leq 0$, the TI-Hg gain exceeds that of TI-Xe by a factor of ~ 5 . Furthermore, as noted in [5.56] this [Hg] or lower values can be used with a He buffer so that the index of refraction effects will be less severe.

These comparisons between TI-Hg and TI-Xe have been made to demonstrate the sensitivity of the optical properties to the features of the potentials. It should be apparent that the TI-Hg potentials are characteristic of an ideal excimer-laser candidate. The excited state has enough binding ($\sim 5 kT$) to concentrate the emission band at moderate "noble gas" densities, yet it is shallow enough to allow rapid relaxation from initially excited free $\text{TI}^*(7^2S)$ into the several lowest vibrational states responsible for the band peak. (This three-body association rate constant is $3 \times 10^{-31} \text{ cm}^6 \text{ s}^{-1}$ [5.56].) A minimum occurs in $V^* - V$ at an R near the V^* potential minimum. This causes a

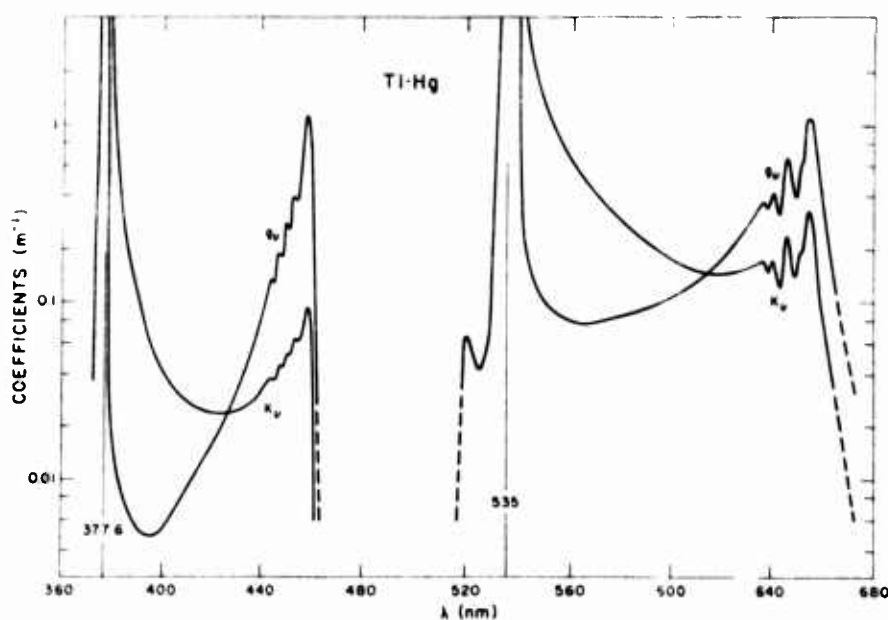


Fig. 5.17. Absorption (K_v) and stimulated emission (G_v) coefficients for the Ti-Hg excimer bands of Fig. 5.15, from data in [5.56]. The conditions are $[Tl(6^2P_{1/2})]=[Tl(6^2P_{3/2})]=5 \times 10^{15} \text{ cm}^{-3}$, $[Tl(7^2S)]=2 \times 10^{14} \text{ cm}^{-3}$, $[Hg]=3 \times 10^{14} \text{ cm}^{-3}$, $T=820^\circ\text{C}$

convergence of bands, so that a number of low-lying vibrational states [in $V^*(R)$] radiate predominantly at the same wavelength. The resulting high gain coefficient and homogeneous broadening make this the best known candidate for a visible metal-vapor excimer laser. The lower gain-coefficient Tl Xe system is much more difficult to achieve laser action in, although it could attain higher power and energy densities without superfluorescence losses if successful.

Hg_2 absorption is negligible in the 450 and 650 nm regions where the peak G_v of the Tl Hg bands occur. Absorption by Tl_2 might occur in these regions, but is very unlikely to match the Tl Hg* gain at the peak G_v wavelengths. Of course, Tl_2 would also be severely depleted in any high-power pumping scheme. Strong absorption by Tl Hg excimers to higher states is extremely unlikely to occur in the precise λ regions of 450–460 and 620–650 nm with sufficient strength to decrease these G_v significantly.

5.3 Excitation Methods and Efficiency

The potential efficiency of these molecular lasers depends on the excitation method as well as on the molecular properties discussed in Sect. 5.2. We will discuss four excitation schemes, in order of increasing potential efficiency.

These excimers can easily be used as *laser-pumped tunable lasers* if desired. Simple considerations lead to a typical single pass gain $G \sim (\lambda^2/8\pi)P/\Delta\nu_{\text{Band}}$ for such a laser, where P is the pump power in photons $\text{cm}^{-2}\text{s}^{-1}$ and $\Delta\nu_{\text{Band}}$ is the width of the excimer emission band. For a 1000 Å wide visible excimer band and a 10 W Ar⁺ pump laser with a 20 μm waist, $G \geq 0.05$. This is very similar to existing dye lasers, as indeed these considerations apply equally to them. A variety of issues such as index of refraction variations, band shapes, and flow turbulence enter into the determination of relative values for different tuneable media. These will not be discussed here, since the present work is concerned instead with efficient, high-power excimer lasers.

If flashlamps are used to excite the excimers, only radiation in the wings of the resonance lines, where the absorption coefficient is 0.1–10 cm⁻¹, is useful. These wavelength regions are usually relatively narrow, typically filling less than 1% of the visible continuum. Thus, although the laser energy might be a large fraction of the absorbed light, the latter will normally be a very small fraction of the total flashlamp radiation. The flashlamp spectral match to the absorption could be improved somewhat by filling it with the same excimer vapor species as the gain tube, but we still would not expect high efficiencies or scalable, high powers by this method. It may be easier to achieve gain in flashlamp pumped rather than electrically excited systems due to the absence of undesired electron collision processes, but their potential efficiencies appear to be much lower than if the discharge is applied directly to the laser medium.

High energy electron beam (e -beam) excitation occurs predominantly via recombination and excited state relaxation following ion-pair formation. Ion-pair energies are typically ~1.7 times ionization energies, and generally only one excimer is formed per ion pair. Under these circumstances the maximum efficiency is given by the excimer-band photon energies divided by the ion-pair energy. Excimer states with large ratios of excitation energy to ionization energy, as in the noble-gas dimers, are, therefore, the most efficient for e -beam pumping. The optimum e -beam excimer pumping efficiencies predicted for these cases by current models are about 40–50% relative to the energy deposited in the gas (Chap. 3). Foil losses, beam spreading, and other problems limit the actual overall efficiencies to significantly lower values. For excimer lasers based on a small fraction of metal atoms in a high pressure Group II or Group VIII vapor, e beam excitation would primarily ionize the major constituent, requiring typically 10–20 times the metal-excimer photon energy. Thus maximum efficiencies would be 5–10% relative to the energy deposited in the gas if each ionization event produced only one visible photon. No modeling or experiments have been reported and this may be an overly pessimistic assumption, but the potential efficiencies in these metal-doped noble gases do appear to be much greater for discharges. In addition to their use as the entire energy source, electron beams are of value as preionizers, sustainers, and diagnostics. Cases in which a larger metal fraction and, therefore, a larger potential efficiency is possible are Hg noble gas and Hg₂. These have been studied with e beam excitation; $HgXe$ by Gutcheck et al. [5.21] and by

Woodworth [5.22]; Hg₂ by Hill et al. [5.48] and by Schlie et al. [5.49]. Gutchek et al. [5.21] reported a maximum fluorescence energy efficiency of ~0.5% relative to the energy deposited in the gas for the 270 nm band associated with Hg(6³P)–Xe. Woodworth also reported ~0.5% fluorescence efficiency for this band and about 3 times as much in the 200 nm band associated with Hg(6¹P₁)–Xe. Hill et al. [5.48] and Schlie et al. [5.49] have not reported efficiencies.

The metal-atom excitations desired for this type of excimer laser have two basic features that contribute to a potentially high laser efficiency with *discharge excitation*. First, the excited atomic state responsible for the laser transition (A^*) is the lowest excited state so that its excitation is the first inelastic process available to the accelerating electrons. [Vibrational and rotational excitation of excited molecular states occurs, but densities of these states are low and this is not a significant energy drain except at large molecular ion and electron (n_e) densities.] Second, the excitation energy is a relatively small fraction of the ionization energy. For n_e less than about 10^{14} cm^{-3} the electron energy loss in a discharge from this $A \rightarrow A^*$ excitation causes a rapid decrease in the electron energy distribution with increasing energy above the inelastic threshold. This attenuates ionization of the metal atoms and greatly reduces the excitation of the "noble gas", even though its density is typically at 10^4 greater than that of the metal vapor. Since the A^* energy is less than half of the ionization energy, the electrons (predominantly with energies below the first inelastic threshold) will generally be more efficient at exciting A to A^* than at further ionizing the A^* . This situation is in contrast to the noble-gas excimers for which the excitation energy is a large fraction of the ionization energy. In this case the electrons with energies below the inelastic threshold are very effective at ionizing the noble-gas excimers and excited atoms. For $n_e > 10^{14} \text{ cm}^{-3}$ electron-electron collisions tend to thermalize the electron energy distribution, and multiple-step ionization of A^* occurs rapidly. This situation is discussed below for the Na–Xe example.

Discharge modeling at power levels appropriate for excimer lasers has been carried out only for Hg vapor and alkali-noble gas mixtures. No measurements have yet been compared to these although some observations of general discharge behavior in these systems has been reported. Therefore, the discussions following will concentrate on the pure Hg and alkali-noble gas cases.

Glow and arc discharges in Hg vapor have been studied for several decades on account of their importance in lighting and electrical switching [5.47]. Neither discharge is appropriate for lasers, as they are cw discharges and the atomic level populations, gas temperature, electron density, and effective electron temperature are all approximately in equilibrium. The first attempt at a pulsed, high power discharge in Hg vapor to obtain gain was by Carbone and Litvak [5.4], who studied the Hg₃ 480 nm band emission in a pulsed, longitudinal arc in $\sim 10^{18} \text{ cm}^{-3}$ of Hg. Electrical energy deposition rates up to $\sim 10 \text{ W cm}^{-3}$ for $\sim 1 \mu\text{s}$ were achieved without developing nonuniformity or

instabilities, while the effective electron temperature was estimated at ~ 0.6 eV. Although the 480 nm band gain calculated from the observed emission was too small to be useful, this magnitude of energy deposition is sufficient for most potential metal-vapor excimer lasers.

More recently the Boltzmann equation has been solved in Hg vapor by Rockwood [5.51], Masek and Vokaty [5.58], and by Judd [5.52]; but none of the investigations looked into the effect of excited state ionization or superelastic collisions on discharge stability. Moshburg and Witke [5.59] have measured the Hg_2 excimer vibrational temperature in Hg discharges, thereby inferring the effective vibrational excitation plus excimer quenching rates by electrons. York and Carbone [5.53] recently operated a transverse pulsed discharge in $\sim 10^{19} \text{ cm}^{-3}$ of Hg, and obtained homogeneous discharges of $\sim 10 \text{ J l}^{-1}$ energy deposition following uv preionization. From the excimer fluorescence intensity they inferred that $\sim 2\%$ net gain should occur on the 320 nm excimer band for their 10 cm discharge length. A measurement at 325 nm, however, indicated a net loss in transmission during the discharge pulse. Although this was reported in York et al. [5.53] as preliminary and inconclusive, later measurements at 325 nm and other, nearby wavelengths also indicated net attenuation (private communication with G. York). It has been suggested that these observations might be reconciled with the net gain at 325 nm observed with *e*-beam pumping [5.49] if the higher Hg_2^* states associated with $\text{Hg}(7^3S) + \text{Hg}$ had a larger population in the *e*-beam case. Thus, net gain might occur on these bands, associated with the $7^3S - 6^3P$ transition, for *e*-beam excitation while net absorption might occur in a discharge.

Discharge excitation of alkali-noble gas mixtures has also been studied for many years in relation to metal vapor lamps [5.47]. As noted above these essentially cw discharges are not very relevant to laser discharges. High power discharge excitation in cold, non-LTE gas was first modeled by Palmer [5.10] using a thermal electron energy distribution $f(u)$ with a limited number of metal-atom states and collision processes. His results indicated the possibility of reasonably efficiency excitation and net gain in the K-Xe excimer bands, but the effect of the expected non-Boltzmann character of $f(u)$ and of additional states and collision processes remained unclear. Schlie [5.60] solved the Boltzmann equation for $f(u)$ in typical laser mixtures of Na and Xe ($1:10^3 - 1:10^4$) without excited states. His results indicated a very rapid drop in $f(u)$ above the first alkali inelastic threshold. More recently, Shuker et al. [5.12] investigated the effect of excited Na states on $f(u)$ in Na-Xe and self-consistently solved the Boltzmann equation for $f(u)$ and the population rate equations for the excited state and electron densities. The results of this calculation and the general characteristics of this system will now be explored.

In the absence of excited Na, about 90% of the electrical energy goes into the desired $\text{Na}(3S) \rightarrow \text{Na}(3P)$ excitation for a wide range of E/N . The remaining energy goes primarily into Xe elastic recoil at the lower E/N values and into ionization and undesired excitation at higher E/N . The overall efficiency for discharge operation in Ne-Xe mixtures is additionally limited by the typical

0.75 factor in the ratio $h\nu_{\text{laser}}/\Delta E_{\text{exc}}$, which is a fundamental consequence of the red-shift between excimer absorption and emission bands.

Quenching of Na(3P) by the low-energy electrons is an important decay mechanism at the excitation fractions and electron densities appropriate for high-power discharge operation [5.2, 3, 12]. This is not a net energy loss mechanism, but it limits the $[\text{Na}^*]/[\text{Na}]$ fraction to $R_{\text{exc}}/(R_q + \Gamma_{\text{eff}})$, where R_{exc} and R_q are the electron excitation and quenching rates and Γ_{eff} is the effective Na^{*} spontaneous radiative loss plus stimulated emission rates. The spontaneous emission loss rate is roughly equal to $\Gamma_0 [\text{Na}^*]/[\text{Na}]$ where Γ_0 is the natural atomic radiative rate. For a useful net gain the E/N must be high enough to keep $[\text{Na}^*]/[\text{Na}]$ above typically 0.05. This excitation fraction has not been achieved in preliminary high- n_e discharge experiments [5.32], although the models of these systems [5.12] do yield it under appropriate assumptions.

If the excited Na(3P) fraction builds up to the ~5% levels appropriate for appreciable optical gain, the Na(3P) excitation efficiency drops due to ionization of excited states. The calculations indicate that typically 20–50% of the electrical energy might nonetheless be extracted as laser power, with the remainder going primarily into gas heating. Most of this heating is attributed to rotational and vibrational excitation of molecular ions, momentum transfer collisions with Xe, and A^* multiple-step ionization followed by recombination. These calculations also indicate that Na₂, with its associated deleterious absorption, is severely depleted by electron collisional dissociation, and would be further depleted by gas heating and laser-field bleaching. Electron densities of 10^{15} – 10^{16} cm^{-3} , $E/[\text{Xe}] \sim 10^{-17}$ – 10^{-16} V cm^2 at typical $[\text{Na}] \geq 3 \times 10^{16}$, $[\text{Xe}] \geq 3 \times 10^{20} \text{ cm}^{-3}$, and current densities of 10 – 100 A cm^{-2} result from the calculations. At these power depositions of 10^2 – 10^3 MW l^{-1} , the gas heating rate is 10 – $100 \text{ }^\circ\text{C } \mu\text{s}^{-1}$. If total gas heating of $100 \text{ }^\circ\text{C}$ could be tolerated during an excitation pulse, about 10^3 J l^{-1} , would be deposited in the gas, conceivably with 20–50% convertible into laser power. These calculations are obviously very speculative and the actual situation will be less favorable, but this at least indicates the sizes of the laser power, efficiency, and pulse energies under consideration.

One major question that is not addressed by these homogeneous discharge models is the time for growth of an arc instability in this high-pressure mixture. Various uniform preionization schemes are available, but preliminary investigations by *Drummond* [5.61] and by *Rothwell* et al. [5.32] are very encouraging, as they indicate that these metal-doped noble gas mixtures are much more stable against arcing than the pure noble gases.

Another potential major problem is cavity quality deterioration due to index of refraction variations, i.e., loss of medium homogeneity. Xe at 10^{20} cm^{-3} has an index of refraction $n - 1 \geq 2.4 \times 10^{-3}$, and an expected 10% temperature rise due to the excitation pulse will cause variations of ~10% of this. If this index gradient occurs nonuniformly, it could severely distort the laser beam. As an example, if an index variation $n - 1 = 2 \times 10^{-4}(y^2/y_0^2)$ occurred uniformly along a laser Z axis of length L , then in the $L < f$ limit the

medium would look like a negative cylindrical lens of focal length $f = y_0^2/(4 \times 10^{-4} L)$. If, for example, $y_0 = 1$ cm and $L = 25$ cm, $f = 100$ cm results. A distribution of many small-scale density variations due to nonuniform temperatures could be even more serious. During a short excitation pulse the gas will not move very far and the index changes will be smaller. Nonetheless, it is essential to deposit the pump energy uniformly and to maintain highly isothermal initial temperatures. The temperatures gradient to room temperature at the end of heat pipes make their value for lasers highly uncertain [5.62].

We conclude this section on metal vapor systems by noting that this class of systems offers a variety of choices of excimer species which radiate in the visible and ultraviolet region.

Acknowledgements. This work was supported in part by the Air Force Weapons Laboratory under grant no. AFWL 77010, and in part by the Advanced Research Projects Agency of the Department of Defense, monitored on ONR under Contract No. N00014-76-C-0123.

References

- 5.1 See, for example, I.Procaccia, R.D.Levine: *J. Chem. Phys.* **63**, 4261 (1975) and references therein
- 5.2 A.V.Phelps: "Tunable Gas Lasers Utilizing Ground State Dissociation", JILA Rpt. 110, University of Colorado, Boulder, Colo. (1972)
- 5.3 G.York, A.Gallagher: "High Power Gas Lasers on Alkali-Dimer $A-X$ Band Radiation", JILA Rpt. 114, University of Colorado, Boulder, Colo. (1974)
- 5.4 R.J.Carbone, M.M.Litvak: *J. Appl. Phys.* **39**, 2413 (1968)
- 5.5 S.Y.Chen, M.Takeo: *Rev. Mod. Phys.* **29**, 20 (1957)
A.Jablonski: *Phys. Rev.* **68**, 78 (1945)
- 5.6 R.F.M.Hedges, D.L.Drummond, A.Gallagher: *Phys. Rev. A6*, 1519 (1972)
- 5.7 G.York, R.Scheps, A.Gallagher: *J. Chem. Phys.* **63**, 1052 (1975). The conditions for Fig. 11 are $[Xe] = 2 \times 10^{20} \text{ cm}^3$, $[Na] = 10^{17} \text{ cm}^3$, $[Na^+]/[Na] = 0.05$, $T = 810 \text{ K}$
R.Scheps, Ch.Ottinger, G.York, A.Gallagher: *J. Chem. Phys.* **63**, 2581 (1975)
- 5.8 D.L.Drummond, A.Gallagher: *J. Chem. Phys.* **60**, 3426 (1974)
- 5.9 R.B.Bernstein, J.T.Muckerman: *Advances in Chemical Physics*, Vol. 12, ed. by J.O.Hirschfelder (Wiley and Sons, New York 1967) p. 389
- 5.10 A.J.Palmer: *J. Appl. Phys.* **47**, 3088 (1976)
A.J.Palmer, L.D.Hess, Semiannual Rpt. #1, 2 (1975) #3 (1976) Hughes Res. Lab., Malibu, Calif.
A.J.Palmer, L.D.Hess, Semiannual Rpt. Hughes Res. Lab., Malibu, Calif. #1, 2 (1975) #3 (1976)
- 5.11 L.A.Schlie: *J. Appl. Phys.* **47**, 1397 (1976)
- 5.12 R.Shuker, L.Morgan, A.Gallagher, A.V.Phelps: To be published
- 5.13 A.Tam, G.Moe, W.Park, W.Happer: *Phys. Rev. Lett.* **35**, 85 (1975)
A.Tam, G.Moe, B.Bulos, W.Happer: *Opt. Commun.* **16**, 376 (1976)
G.Moe, A.Tam, W.Happer: *Phys. Rev. A14*, 349 (1976)
W.Happer, G.Moe, A.C.Tam: *Phys. Lett.* **54A**, 405 (1975)
- 5.14 J.Pascale, J.Vandeplanque: *J. Chem. Phys.* **60**, 2278 (1974)
- 5.15 W.P.West, P.Shuker, A.Gallagher: To be published

- 5.16 R.Scheps, A.Gallagher: J. Chem. Phys. **65**, 859 (1976)
 5.17 B.Sayer, M.Ferray, J.Lozingot, J.Berlande: J. Phys. **B9**, L293 (1976)
 5.18 J.C.Gauthier, F.Devos, J.-F.Delpech: Phys. Rev. **14**, 2346 (1976)
 5.19 J.C.Eden, B.F.Cherington, J.T.Verdeyen: IEEE J. QE-**12**, 698 (1976)
 5.20 W.F.Baylis: J. Chem. Phys. **51**, 2665 (1969)
 5.21 R.A.Gutcheck, R.M.Hill, D.L.Huestis, D.C.Lorentz, M.V.McCusker: Stanford Res. Inst. Rpt. MP75-43, Menlo Park, Calif. (1975)
 5.22 J.R.Woodworth: J. Chem. Phys. **66**, 754 (1977)
 5.23 O.Oldenberg: Z. Phys. **47**, 184 (1928), **51**, 605 (1928), **55**, 1 (1929)
 5.24 C.G.Freeman, M.J.Mcfwan, R.Claridge, L.F.Phillips: Chem. Phys. Lett. **6**, 482 (1970)
 5.25 E.V.Nikoforov, L.I.Plimck, Y.B.Predtechenskin, L.D.Shererha: Opt. Spektrosk. **41**, 339 (1976). [English transl.: Opt. Spectrosc. **41**, 195 (1976)]
 5.26 O.P.Strausz, J.M.Campbell, S.DePauli, H.S.Sandhu, H.E.Gunning: J. Am. Chem. Soc. **95**, 732 (1973)
 5.27 J.T.Kielkopf, R.A.Miller: J. Chem. Phys. **61**, 3304 (1974)
 5.28 J.R.Powers, R.J.Cross, Jr.: J. Chem. Phys. **56**, 3181 (1972)
 5.29 J.S.Deech, J.Pitre, L.Krause: Can. J. Phys. **49**, 1976 (1971)
 5.30 A.Lurio: Phys. Rev. **140A**, 1505 (1965)
 5.31 B.Cheron, R.Scheps, A.Gallagher: J. Chem. Phys. **65**, 326 (1976)
 5.32 H.Rothwell, D.Leep, A.Gallagher: Bull. Am. Phys. Soc. **23**, 142 (1978)
 5.33 A.Gallagher, A.Lurio: Phys. Rev. **136A**, 87 (1964)
 5.34 D.S.Ginter, M.L.Ginter, K.K.Innes: J. Phys. Chem. **69**, 2480 (1965)
 5.35 J.Drowthart, R.F.Honig: J. Phys. Chem. **61**, 980 (1957)
 5.36 For example, J.F.Waymouth: Proc. IEEE **59**, 629 (1971)
 C.S.Lin, R.J.Zollweg: J. Chem. Phys. **60**, 2384 (1974)
 J.J.DeGrout, A.G.Jack: J. Phys. **D6**, 1477 (1973)
 5.37 D.Drummond, L.A.Schlie: Private communication
 5.38 R.Duren: Chem. Phys. Lett. **39**, 481 (1976)
 5.39 D.Drummond: Private communication
 5.40 M.W.McGeoch, G.R.Fournier, P.Ewart: J. Phys. **B9**, L121 (1976)
 G.R.Fournier, W.M.McGeoch: "Kinetics of Proposed Cd-Hg Excimer Lasers", Int. Conf. on Quantum Electron., Amsterdam (1976)
 M.W.McGeoch, G.R.Fournier: J. Appl. Phys. (in press)
 5.41 W.Balfour, A.L.Douglas: Can. J. Phys. **48**, 901 (1970)
 5.42 K.C.Li, W.C.Stwalley: J. Chem. Phys. **59**, 4432 (1973)
 5.43 C.R.Vidal, H.Scheingraber: J. Mol. Spectrosc. **65**, 46 (1977)
 5.44 W.J.Stevens, M.Krauss: J. Chem. Phys. **67**, 1977 (1977)
 5.45 W.L.Wiese, M.W.Smith, B.M.Miles: *Atomic Transition Probabilities, Vol. II Na-Ca*, NSRDS-NBS22 (U.S. GPO, Washington, D.C. 1969)
 5.46 L.Pleasance: Private communication
 5.47 W.Elenbaas: *The High Pressure Mercury Vapor Discharge* (North-Holland, Amsterdam 1951)
 W.Elenbaas: *Light Sources* (McMillan, London 1972)
 J.F.Waymouth: *Electric Discharge Lamps* (MIT, Cambridge, Mass. 1971)
 5.48 R.M.Hill, D.J.Eckstrom, D.C.Lorentz, H.H.Nakano: Appl. Phys. Lett. **23**, 373 (1973)
 D.Eckstrom, R.M.Hill, D.C.Lorentz, H.H.Nakano: Chem. Phys. Lett. **23**, 112 (1973)
 5.49 L.A.Schlie, B.D.Guenther, R.D.Rathge: Appl. Phys. Lett. **28**, 393 (1976)
 L.A.Schlie, B.D.Guenther, D.L.Drummond: Chem. Phys. Lett. **34**, 258 (1975)
 5.50 R.E.Drullinger, M.M.Hessel, E.W.Smith: NBS Monograph 143, Natl. Bur. Stand. (U.S.) (1974)
 M.Stock, R.E.Drullinger, M.H.Hessel: Chem. Phys. Lett. **45**, 592 (1977)
 E.W.Smith, R.E.Drullinger, M.M.Hessel, J.Cooper: J. Chem. Phys. **66**, 5667 (1977) (Theory)
 R.E.Drullinger, M.M.Hessel, E.W.Smith: J. Chem. Phys. **66**, 5656 (1977) (Experiment)
 M.Stock, E.W.Smith, R.E.Drullinger, M.M.Hessel: J. Chem. Phys. **67**, 2463 (1977)
 5.51 S.D.Rockwood: Phys. Rev. **A8**, 2348 (1973)
 5.52 O.Judd: J. Appl. Phys. **47**, 5297 (1976)

- 5.53 G.York, J.Carbone: "Electrical and Optical Properties of a High Pressure Transverse Hg Discharge", Abstract in *Electronic Transition Lasers II*, ed. by L.Wilson, S.Suchard, J.Steinfeld (MIT Cambridge, Mass. 1977)
- 5.54 W.Stevens: Private communication
- 5.55 K.Komine, R.L.Byer: *J. Appl. Phys.* **48**, 2505 (1977)
- 5.56 D.Drummond, L.A.Schlie: *J. Chem. Phys.* **65**, 3454 (1976). The intensity scale of the reported fluorescence has been revised slightly (private communication)
- 5.57 C.Santaran, V.K.Vaidyan, J.G.Winans: *J. Phys.* **B4**, 133 (1971) and references therein
- 5.58 K.Masek, E.Vokaty: *Czech. J. Phys.* **B24**, 267 (1974)
- 5.59 E.Mosburg,Jr., M.Witke: To be published
- 5.60 L.A.Schlie: *Bull. Am. Phys. Soc.* **21**, 172 (1976)
- 5.61 D.Drummond: Private communication
- 5.62 J.E.Deverall: "Gas-Interface Studies in Large Horizontal Heat Pipes", Los Alamos Rpt. LA-6646-MS (1977)

Na 3^2P - 3^2D LINE BROADENING BY Ne, Ar, AND Xe

D. W. WILDMAN, L. W. SCHUMANN, and A. C. GALLAGHER†

Joint Institute for Laboratory Astrophysics, University of Colorado and National Bureau of Standards,
Boulder, CO 80309, U.S.A.

(Received 2 October 1979)

Abstract—The normalized emission intensity in the wings of the optically thin Na 3^1P - 3^2D lines broadened by Ne, Ar, and Xe has been measured in emission from a high-pressure discharge. A blended satellite occurs about 80 cm^{-1} into the Na-Xe red wing and a progression of increasing red wing intensity from Ne to Ar to Xe is observed. Xe densities of 2.5 and $9.1 \times 10^{19}\text{ cm}^{-3}$ were used, and the pressure dependence of the NaXe line shape indicates that multiple perturber interactions are important in the far wing at the higher noble gas densities.

EXPERIMENTAL

Noble gas broadening of Na lines is often used as a test of line broadening theory and of interaction potentials. Due in part to the ease with which the resonance transition (3^2S - 3^2P) can be optically excited, most work has been concerned with this transition. The present results for transitions between higher states are made possible by operating a stable, pulsed electric-discharge in high pressure noble gas.¹ This is only achieved without arcing instability when the inert gas is doped with $\sim 10^{13}\text{ cm}^{-3}$ or more of metal vapor. We have now operated such discharges in Na, Tl, and Mg doped inert gases,¹⁻³ so that this appears to be a feasible source for obtaining collisional lineshapes of many metal vapors.

Numerous experiments and calculations on Na have examined inert gas broadening of the Lorentzian, line-core region, which is sensitive to the long-range interactions.⁴⁻⁸ The normalized emission in the far wings of the Na resonance lines⁹ and the bound-bound spectra of supercooled nozzle beams of NaAr¹⁰ have been interpreted to yield close range interactions. The effects of multiple inert gas interactions in the far wings of the resonance lines¹¹ and collision induced bands¹² have also been demonstrated at high noble gas densities. Here we present data showing the far wing broadening of the higher excited state (3^2P - 3^2D) transitions by Ne, Ar, and Xe, for inert gas densities that yield predominately single-perturber interactions. The normalized emission intensity $I_N(k)$ was measured for the wings of the Na($3^2P_{1/2}$ - $3^2D_{3/2}$) (818.326 nm) line and the unresolved Na($3^2P_{3/2}$ - $3^2D_{5/2}$) (819.482 nm) and Na($3^2P_{3/2}$ - $3^2D_{3/2}$) (819.479 nm) lines for noble gas densities of 2.5 - $9.1 \times 10^{19}\text{ cm}^{-3}$. $I_N(k)$ is defined as the intensity radiated per wave number, $I(k)$, divided by the total integrated intensity of the three lines and the noble gas density N :

$$I_N(k) = \frac{I(k)}{N \int I(k) dk}$$

The integral is taken over all three lines since the far wings are related to the entire multiplet. The densities of the $3^2D_{3/2}$ and $3^2D_{5/2}$ states responsible for the emission are expected to be in a statistical ratio owing to rapid collisional mixing at the high gas densities of these experiments.

The emission line shapes from a pulsed, high pressure Na doped-noble gas discharge were measured. The discharge cell was similar to one previously described¹ with the Na density 10^{-3} - 10^{-4} times the noble gas density so that the (non-resonant) broadening by Na was negligible compared to noble gas broadening. Spectra were taken on a 0.5 m scanning monochromator equipped with a photomultiplier having a GaAs photocathode. A gated sample and hold circuit was used to measure the fluorescence intensity during the discharge current pulse. A filter transmitting $\lambda > 5400\text{ \AA}$ was placed in front of the monochromator entrance slit to block higher order wavelengths. The relative spectral response of the optical system was measured using a calibrated tungsten iodide lamp illuminating a barium sulfate diffusing screen. The

†Staff Member, Quantum Physics Division, National Bureau of Standards.

instrument resolution was varied from approx. 2 cm^{-1} for the $|\Delta k| < 20\text{ cm}^{-1}$ data to 8 cm^{-1} for $|\Delta k| > 100\text{ cm}^{-1}$.

The data taken at a temperature $T = 673^\circ\text{K}$, corresponding to a Na density¹³ of $5.5 \times 10^{15}\text{ cm}^{-3}$, were obtained from a $4\text{ }\mu\text{s}$ pulsed discharge with a diameter of $\sim 3\text{ mm}$ and a current density $J \sim 200\text{ A cm}^{-2}$. From measurements of the electric field across the discharge and the electron mobility in xenon, the electron density was calculated to be $n_e = 4 \times 10^{15}\text{ cm}^{-3}$. This electron density is expected to produce a Stark broadened FWHM of $\sim 0.27\text{ cm}^{-1}$ ¹⁴ which is much less than that due to the noble gas (see Fig. 1). The emission spectra reported here are

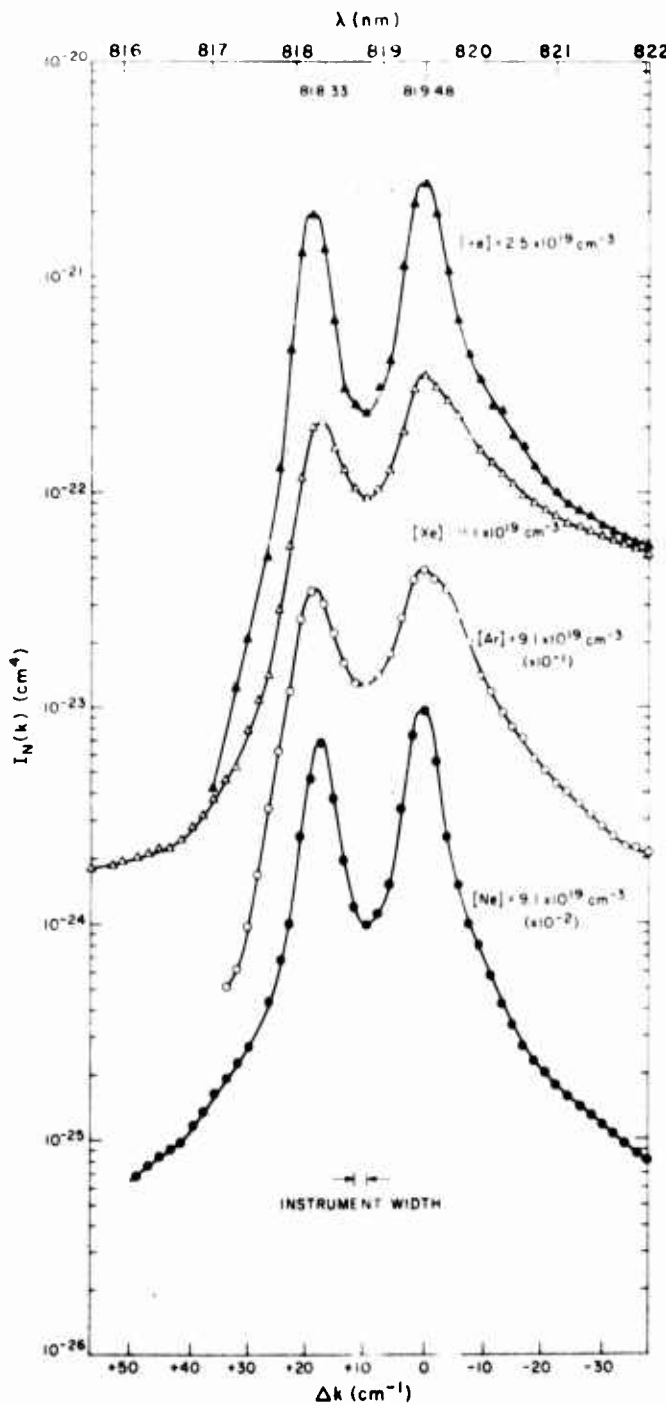


Fig. 1. Normalized emission intensity of the Na 3P-3D transitions broadened by Xe, Ar, and Ne at $T = 673^\circ\text{K}$ and $[\text{Na}] = 5.5 \times 10^{15}\text{ cm}^{-3}$. The Ar and Ne data have been shifted by factors of 10 and 100 respectively.

within the impact region for electron broadening, so that the electron-broadened wings are expected to decrease as Δk^{-2} . The reported Ne, Ar, and Xe broadened wings decrease less rapidly, so that the reported wing intensities are essentially all due to noble gas broadening. The higher temperature data ($[Xe] = 9.1 \times 10^{19} \text{ cm}^{-3}$, $T = 773^\circ\text{K}$, $[Na] = 5 \cdot 10^{16} \text{ cm}^{-3}$) were taken with a 50 ns current pulse of $J \sim 10^4 \text{ A cm}^{-2}$, yielding an electron density $n_e = 2 \times 10^{16} \text{ cm}^{-3}$. Since both n_e and $[Xe]$ are larger in this case, this wing is also due to only Xe broadening.

The Na density $[Na]$, was varied from $10^{14} - 5 \times 10^{16} \text{ cm}^{-3}$ in order to obtain $I_N(k)$ in the limit of zero Na($3P$) density, for which the $3D$ - $3P$ emission is optically thin. The Na($3P$) density was also measured from absorption profiles, similar to those described in Ref. 1, verifying the low optical depths obtained at the lower $[Na]$. From these $[Na] \rightarrow 0$ extrapolations it was determined that emission for $T = 673^\circ\text{K}$ and $[Na] = 5.5 \times 10^{15} \text{ cm}^{-3}$ was optically thin, with the exception of the $[Xe] = 2.5 \times 10^{19} \text{ cm}^{-3}$ data for which the line center optical depth was ~ 3 . The far wing line-shape data (from -20 to 400 cm^{-1}) for this optically thick case were normalized at $\Delta k = -20 \text{ cm}^{-1}$ to the optically-thin line-core $I_N(k)$, obtained at $T \approx 620^\circ\text{K}$.

The Na(3^2P - 3^2D) line shapes broadened by Ne, Ar, and Xe at $T = 673^\circ\text{K}$ are shown in Fig. 1. An approximate broadened line width can be inferred from these data, but at these present inert gas densities this broadening does not correspond to the Lorentzian, impact-region of the line. For this reason we have not attempted to analyze the observed line shape in terms of instrumental and collisional broadening, nor do we report broadening coefficients. The shift of the line core has been reported in Ref. 1.

As has been described previously,¹⁵ it is not necessary to resolve the line core to obtain $I_N(k)$ in the far wings. The measured red wing $I_N(k)$ for $|\Delta k| > 10 \text{ cm}^{-1}$ are shown in Fig. 2. (Values of $I_N(k)$ could not be accurately determined on the blue wing due to overlap with Na₂ A-X band emission.^{1,16}) Continuum emission obscured by the four Xe emission lines at 823.2, 828.0, 834.7, and 840.9 nm is shown as a dashed line for the open triangle case in Fig. 1. These regions are deleted in the other NaXe spectra, as is the Na-Ar data near the Ar 826.5 nm line. Minor fluctuations, typically $\sim 5\%$, about smooth lines through the data in Fig. 2 are not deemed significant. Our ability to measure values of $I_N(k)$ below $\sim 5 \times 10^{-25} \text{ cm}^4$ is limited by a broad continuum from the discharge that underlies the entire spectrum. This continuum emission was also observed with a 0.75 m double grating monochromator which would have eliminated any spurious signals from scattered light.

The temperature dependence of the NaXe line shape was investigated by raising the cell temperature T from 673 to 773°K . Since the Na reservoir was located in the cell, this temperature increase also raised the Na vapor pressure from $5.5 \times 10^{15} \text{ cm}^{-3}$ to a density of $5 \times 10^{16} \text{ cm}^{-3}$, but this should not have any effect on these normalized emission data. The higher temperature data (\times) in Fig. 2 are seen to follow the lower temperature data (Δ) for $|\Delta k| < 200 \text{ cm}^{-1}$ but fall about 20% below the lower temperature results for $300-400 \text{ cm}^{-1}$ frequency shifts.

These wing emissions result from transitions between essentially five different molecular potentials originating in the 3^2D state and three in the 3^2P state. It is not possible to infer these various potentials from temperature-dependent $I_N(k)$ as the resulting bands overlap. However, these data provide a stringent test of theoretical potentials. We are aware of only one published set of potentials for these states, that of Pascale and Vandeplanque.¹⁷ The increase in the magnitude of $I_N(k)$ from Ne to Ar to Xe is consistent with these theoretical potentials, which predict increasing 3^2D binding as the mass of the inert gas increases. Also, the order of magnitude of the $I_N(k)$ obtained using these theoretical potentials in the quasi-static theory¹⁵ is similar to that observed. However, the detailed shapes and magnitudes are not in agreement. As an example we show the $I_N(k)$ for NaXe obtained from the theoretical potentials and the assumption of a constant transition moment between each pair of potentials. Whereas the data indicate a severely broadened satellite with a red "edge" near 75 cm^{-1} , the theory produces a satellite at 150 cm^{-1} . (The latter will be somewhat smeared out in a more exact theory.¹⁸) Also, at $|\Delta\nu| > 200 \text{ cm}^{-1}$ the theory predicts much more intensity than is observed. The temperature dependence at the larger $|\Delta\nu|$ is due to the Boltzmann factor $\exp\{(V^*(\infty) - V^*(R))/kT\}$ in the quasistatic theory, where $V^*(R)$ is the upper-state potential.¹⁵ The theory predicts $\sim 15\%$ change in $I_N(k)$ in the $(\Delta k) = 300-400 \text{ cm}^{-1}$ region, which results from three overlapping bands.

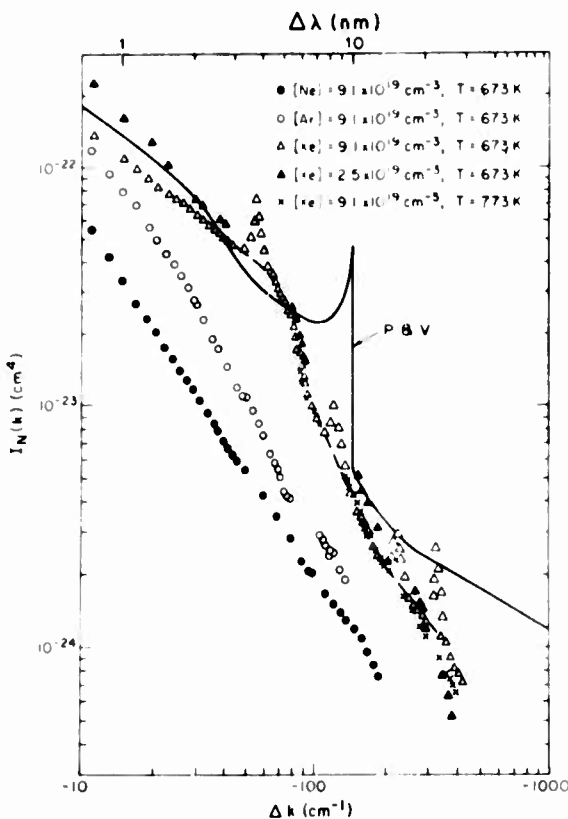


Fig. 2. Normalized emission intensity on the red wing of the Na 3D-3P transitions broadened by Xe, Ar, and Ne. The shifts $\Delta\lambda$ and Δk are measured from 819.48 nm. The actual data, including overlying Xe lines, are shown for the Δ case, where dashed lines show the underlying continuum. For the other Xe cases and the Ar case near an 826.5 nm line this portion of the data is deleted. The $I_N(k)$ which results from using the potentials of Pascal and Vandeplanque (Ref. 17) in the quasistatic theory (Ref. 15) is labeled P & V.

The experiment obtained $\sim 25\%$ change in this region, indicating larger excited-state binding at the appropriate R .

One of these NaXe potentials responsible for these data, the attractive $A^2\pi$ state originating in 3^2P , is known experimentally.⁹ The Pascale and Vandeplanque potential does not agree at all well with this known $V(R)$, and it appears unlikely that this theory could be any more accurate for the other potentials of importance here. Thus the above poor quantitative agreement is hardly surprising.

MULTIPLE-PERTURBER INTERACTIONS

The effects of multiple perturber interactions can also be seen in Fig. 2 where $I_N(k)$ for NaXe is plotted for densities of $[\text{Xe}] = 2.5 \times 10^{19} \text{ cm}^{-3}$ and $9.1 \times 10^{19} \text{ cm}^{-3}$ (open and closed triangles). The high Xe pressure data are seen to be above the lower pressure line shape for $|\Delta k| > 300 \text{ cm}^{-1}$ and below the low pressure results for $|\Delta k| > 300 \text{ cm}^{-1}$. As reported in Refs. 11 and 19, this type of behavior is predicted by multi-perturber interactions which decrease $I_N(k)$ in those portions of the far-wing spectrum dominated by diatomic NaXe emission and increase $I_N(k)$ for those regions at larger frequency shifts where $\text{NaXe}_{2,3\dots}$ emission predominates. Following this interpretation, the region $|\Delta k| < 300 \text{ cm}^{-1}$ is primarily due to diatomic NaXe molecules; and the region $|\Delta k| > 300 \text{ cm}^{-1}$ is primarily due to NaXe_2 .

Acknowledgements—We wish to thank A. V. Phelps and Jinx Cooper for valuable discussions. This work was supported in part by the Advanced Research Projects Agency of the Department of Defense and was monitored by ONR under Contract No. NO0014-76-C-0123.

REFERENCES

1. H. L. Rothwell, D. Leep, and A. Gallagher, *J. Appl. Phys.* **49**, 4396 (1978).
2. D. Wildman, L. Schumann and A. Gallagher, *J. Appl. Phys.* (Nov. 1979).
3. L. Schumann, D. W. Wildman, and A. Gallagher, *J. Chem. Phys.* in press.

4. J. F. Kielkopf and R. B. Knollenberg, *Phys. Rev. A* **12**, 559 (1975).
5. N. Lwin, D. G. McCartan and E. J. Lewis, *J. Phys. B9*, L161 (1976).
6. D. G. McCartan and J. M. Farr, *J. Phys. B9*, 985 (1976).
7. D. Kunth, F. Masnou-Seeuws, F. Rostas, and E. Roueff, *J. Phys. B* **8**, 203 (1975).
8. W. P. West and A. Gallagher, *Phys. Rev. A* **17**, 1431 (1978).
9. G. York, R. Scheps, and A. Gallagher, *J. Chem. Phys.* **63**, 1052 (1975).
10. R. Smalley, D. Aurbach, P. Fitch, and D. Levy, *J. Chem. Phys.* **66**, 3778 (1977).
11. W. P. West, P. Shuker, and A. Gallagher, *J. Chem. Phys.* **68**, 3864 (1978).
12. A. Tam, T. Yabuzaki, S. Curry, and W. Happer, *Phys. Rev.* **18**, 196 (1978).
13. A. N. Nesmeyanov, *Vapor Pressure of the Chemical Elements*. Elsevier, New York (1963).
14. H. R. Griem, *Plasma Spectroscopy*. McGraw-Hill, New York (1964).
15. R. E. M. Hedges, D. Drummond, and A. Gallagher, *Phys. Rev. A* **6**, 1519 (1972); D. L. Drummond and A. Gallagher, *J. Chem. Phys.* **60**, 3426 (1974).
16. L. K. Lam, A. Gallagher and M. M. Hessel, *J. Chem. Phys.* **66**, 3550 (1977).
17. J. Pascale and J. Vandeplanque, *J. Chem. Phys.* **60**, 2278 (1974); J. Pascale and J. Vandeplanque, Centre d'Etudes Nucléaires de Saclay Reports 1974 (unpublished).
18. K. M. Sando and J. C. Wormhoudt, *Phys. Rev. A* **7**, 1889 (1973).
19. T. Yabuzaki, A. C. Tam, S. M. Curry, and W. Happer, *Phys. Rev. Lett.* **41**, 543 (1978).

Models of high-power discharges for metal-Xe excimer lasers

R. Shuker,^{a)} A. Gallagher,^{b)} and A. V. Phelps^{b)}

Joint Institute for Laboratory Astrophysics, University of Colorado and National Bureau of Standards,
Boulder, Colorado 80309

(Received 20 August 1979; accepted for publication 28 September 1979)

High-power ($\sim 10^8$ W/l) discharges in metal-doped Xe are modeled for typical metal atom densities of 10^{15} – 10^{17} cm⁻³ and Xe densities of $\sim 10^{20}$ cm⁻³, and electron densities of 10^{14} – 10^{17} cm⁻³ as appropriate for proposed excimer lasers. Na is used as a prototype species, while its properties are varied to indicate some of the changes that could result from the use of different metals. The model includes sixteen excited levels of Na, three ionic species, the excimer levels of NaXe, and Na₂. The degree of ionization is determined by collisional multistep excitation and ionization of excited atoms versus dissociative recombination of electrons with Na₂⁺. Steady-state conditions in the positive column are calculated for typical gas temperatures of ~ 0.06 eV and electron temperatures T_e of 0.3–0.5 eV. The Na population distribution is largely Boltzmann at the electron temperature and the electron density is close to the Saha equilibrium value except at low electron temperatures and very high extracted laser powers. Useful gain and extracted powers of ~ 10 MW/cm² are predicted for the higher T_e and Na densities, with the pulse width limited to $\sim 10^{-7}$ sec by gas heating. The model indicates that a metal which produces a deeply bound product state via dissociative recombination could yield a very efficient high-power laser or gain cell.

PACS numbers: 42.55.Hq, 52.80. — s

I. INTRODUCTION

Metal-noble gas (or Hg) excimers are candidates for high-power tunable laser.¹ Due to small stimulated emission coefficients, large excited-state (excimer molecule) densities, high gas densities, and high excitation powers are required for such lasers. Because of the well-known arcing instability of high-pressure gases, most excimer lasers have utilized a high-energy electron beam for initiating or sustaining the discharge. Exceptions are laser action that has recently been achieved in short uv preionized discharges² in KrF and halogen-Hg vapor. Pure discharges are much simpler and are expected to be more efficient and reliable if arcing instabilities can be avoided. We have found experimentally³ that several metal-doped noble gases do yield stable homogeneous discharges even without preionization. The n_e in these discharges are very high (10^{14} – 10^{16} cm⁻³). As a consequence, the density of the 3p state of Na is maintained at near its equilibrium value by electron collisions, and the NaXe(A³) excimer level, which is nearly in collisional equilibrium with the Na(3p) level through Xe collisions, is rapidly refilled. Very large extracted laser powers are thus feasible in short pulses. These very high power pulsed discharges in high-pressure nonequilibrated gases are unusual in many other regards as well, so that it is desirable to build an understanding of the most important controlling factors. Finally, our experiments³ were carried out in a small volume cell under a limited range of conditions that were not optimized for excimer gain. The present model is thereby used to investigate the possible gain and efficiency of excimer lasers based on these discharges, but under a wide operating range of conditions (primarily higher gas densities and current densi-

ties). The present work thus extends the analysis of electrons in Na-Xe mixtures by Schlie⁴ to higher degrees of excitation, i.e., to higher discharge power densities. Very recently, related experimental studies of metal vapor Hg discharges, i.e., Tl-Hg, have been reported by Hamil *et al.*⁵ Our present analysis does not extend to the low-power densities of the recent models⁶ of mercury and rare-gas-based laser discharges.

Discharges in metal-doped noble gas and/or Hg mixtures at high pressures have been studied extensively for many years due to their use in lighting.⁷ These lamps differ in three major respects from the present discharges: they are operated with either dc or low-frequency excitation rather than for short pulses, their power densities are typically 10^{-3} times smaller, and the gas temperature is the same as the electron temperature. Due to the high gas temperature, the fractional concentrations of excimer molecules and molecular ions are small, whereas they are large and important here. Metal-doped flashlamps⁸ operate at conditions closer to the present case, but they have not been characterized or analyzed sufficiently to allow useful comparisons with the present results.

The species, their optical and collisional properties, and the discharge model used in the present calculations are described in Sec. II. The results, in the form of excited-state and species densities and their dependence on the discharge parameters, are given in Sec. III A. The optical gain and efficiency are discussed in Sec. III B. Other possible energy-loss mechanisms not included in the computer model are discussed in Sec. IV. The consequences of assuming a Saha-Boltzman relation, as expected at high electron temperatures, is considered in Sec. V, and overall conclusions are given in Sec. VI.

II. THE MODEL

We have chosen to use Na and Xe as the specific case to

^{a)}Present address: Department of Physics, Ben-Gurion University of the Negev, Beer Sheba, Israel.

^{b)}Staff member, Quantum Physics Division, National Bureau of Standards.

model, but we have varied several of their parameters in order to investigate possible behavior of other metal-inert gas mixtures. It is believed that many of the properties of these particular species should be characteristic of other mixtures, as long as the ionization energy of the dopant is below the first excited state of the noble gas, and the electron affinity of the dopant is small enough that negative ion densities are insignificant.

A. Discharge conditions

The pulsed discharges under consideration typically occur in Xe at densities of $[Xe] = 10^{19}\text{--}10^{20} \text{ cm}^{-3}$ doped with Na at densities of $[Na] = 10^{15}\text{--}3 \times 10^{17} \text{ cm}^{-3}$. The electron densities (n_e) are typically $10^{14}\text{--}10^{17} \text{ cm}^{-3}$, the electric field to total gas density ratios E/N are in the $10^{16}\text{--}10^{17} \text{ V cm}^{-2}$ range, the electron temperature T_e is $0.3\text{--}0.5 \text{ eV}$, and the gas temperature $T \approx 800 \text{ K}$, so that $kT \approx 0.07 \text{ eV}$. Here and throughout this paper, electron temperatures are expressed in eV. Typical modeled discharge power densities are $10\text{--}10^4 \text{ MW/l}$. It is assumed that quasi-steady-state discharges will be terminated before excessive ($\sim 300^\circ \text{C}$) gas heating occurs. The present models thereby emphasize steady-state constant gas temperature conditions. Results in Sec. III are obtained by integration of nonlinear time-dependent rate equations, and in Sec. V by use of a two-temperature approximation. The near-uniform cylindrical spatial character of the discharge under consideration is described in Ref. 3.

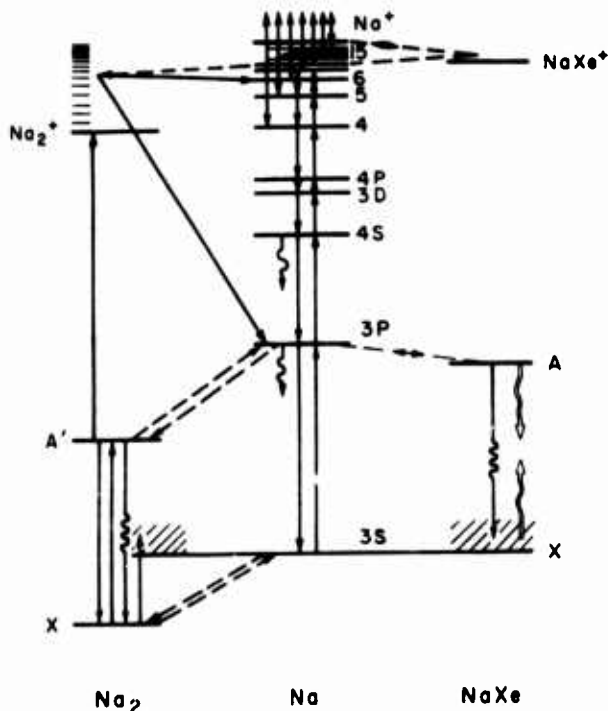


FIG. 1. Energy levels and radiative and collisional processes used in the model. Dashed lines are due to gas collision processes, solid line to electron collisions, single wavy lines to spontaneous emission, and double wavy lines to absorption and stimulated emission. Ionization from and inverse ionization to all Na levels are included in the model, although only those to higher levels are indicated here. Some vibrational levels of Na_2^+ are indicated, although Na_2^+ is treated as a single state in the calculations. Fig. 1 shows the alternate paths for electron- Na_2^+ dissociative recombination leading to Na atoms in the $3p$ or $n = 6$ levels.

Here we consider only a uniformly excited region in the positive column of the discharge.

We initially treated only a few Na excited states in the model and calculated the electron energy distribution from the Boltzmann equation.⁹ However, at the high-power densities necessary for the desired $[\text{Na}(3p)]/[\text{Na}(3s)]$ excitation fraction, both the experiments and theory indicated that higher excited states were playing an important role in the discharge. Also, the fractional ionization is high enough so that electron-electron collisions could be expected to largely Maxwellianize the electron energy distribution.⁴ Thus, the calculations presented here utilize Maxwellian electron energy distributions and Na excited states up to an effective quantum number of 15.

B. Atomic states

An $\text{Na}(3p)/\text{Na}(3s)$ fraction of ~ 0.05 , which is equivalent to an $\sim 0.5\text{-eV}$ excitation temperature, is desired for efficient laser action. [As another example, $\text{Ti}(7s)/\text{Ti}(6p_{1/2}) \approx 0.02$ equivalent to $T_e \approx 0.85 \text{ eV}$ is desired for a Ti-Xe excimer laser.³] If this excitation temperature results from a balance between electron excitation and deexcitation of $\text{Na}(3p)$, then an electron temperature T_e of $\sim 0.5 \text{ eV}$ is necessary. Electron collisions with $\text{Na}(3p)$ atoms will then tend to produce a similar excitation temperature between $\text{Na}(3p)$ and higher excited states. Radiation will lower the excited state populations, but at the electron densities in these discharges this is a minor effect. If the excited Na densities are characterized by an excitation temperature in this 0.5-eV range, then the electron collisional excitation and ionization rates out of excited levels increase with increasing excitation energy of the level. Thus, highly excited states must be considered in the ionization balance. We have included Na states with an effective principal quantum number n up to 15 in the present model, and we allow for the effect of still higher levels through the collisional rate coefficients assigned to this terminal $n = 15$ level.

The highly excited Na states are strongly mixed by electron collisions, so that most of the population resides in the high angular momentum states. These states are very hydrogenic and very nearly degenerate at integral n values. Consequently, we have simplified the level structure by grouping all states above $4p$ into 11 hydrogenic levels, $n = 4\text{--}15$, as shown in Fig. 1. This also allows the use of hydrogenic cross sections for electron collisions with highly excited states. Tests of the validity of this approximation are discussed in Appendix A. We have included the lowest excited states of Xe as a single Xe^* , and the processes $e + \text{Xe}^* \rightleftharpoons 2e + \text{Xe}^*$. In fact, the Xe^* ions are rapidly converted into Xe_2^* ions, which undergo dissociative recombination to form Xe^* . For the T_e considered here, the densities of Xe^* and Xe_2^* are much lower than Na^* and Na_2^* , and they do not significantly influence the kinetics.

C. Molecular species

The lower energy levels and ionic forms of Na, Na_2 , and NaXe are shown in Fig. 2. The $A\text{-}X$ band of the NaXe excimer is a broad continuum extending from the 590-nm Na

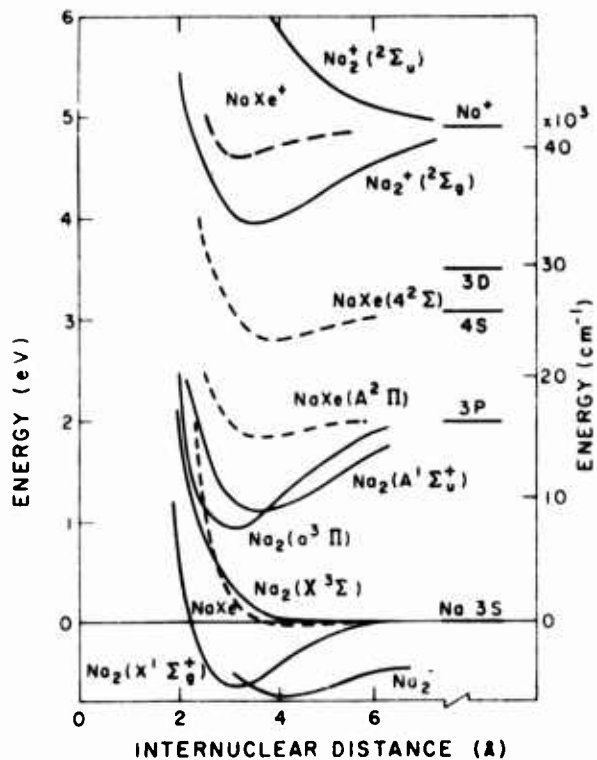


FIG. 2. Electronic energies of various NaXe, Na₂, and Na states. The Na₂, Na₂⁺, and Na₂⁺ potentials are from Ref. 14, NaXe^{*} from Ref. 12, NaXe and NaXe(A²Π) from Ref. 10, and NaXe(A²Σ) from Ref. 11.

resonance line to ~ 720 nm; the 700-nm region of this band is the most favorable region for excimer laser action.¹⁰ The *B* state of NaXe, not shown in Fig. 2, is a repulsive state correlating asymptotically with Na(3p) and Xe(¹S₀). The *B-X* band of NaXe extending from 560–590 nm is very weak and from thermodynamic arguments is not expected to exhibit net gain.¹ The 4sΣ state radiates a 4sΣ-XΣ band¹¹ which could have net gain in the present discharges if sufficiently high excitation temperatures are obtained. Higher levels of NaXe are not shown, but they are expected to exhibit a Rydberg-like shape, approximately paralleling the NaXe^{*} potential.¹²

At the typical Na densities of 10^{15} – 10^{17} cm⁻³ under consideration, a few percent of the Na is bound as Na₂. The associated *A-X* (560–800 nm) and *B-X* (450–500 nm) bands of Na₂ can cause severe absorption, although the *A-X* band may also be capable of yielding net gain in a discharge.¹³ The radiative lifetimes of the Na₂ *A* and *B* states are about 10 nsec. The *A*¹Σ_u⁺, *a*¹Π_u, and *X*¹Σ_g⁺ states of Na₂ are strongly bound¹⁴ so that the Xe-induced collisional dissociation rate coefficient is very small. The relative populations of the *A* and *a* states are expected to be maintained in approximate statistical equilibrium and are represented in the model by an *A'* state. Since Na₂ molecules are depleted by electron-induced dissociative excitation, the Na₂ states are expected to be present at much less than their equilibrium fractions. In order to evaluate this effect, the *A'* and *X* states of Na₂ are included in the calculation, although they are minor constituents.

The NaXe(*A*) state is bound by only a few kT , so that the Na(3p) and NaXe(*A*) densities are maintained at their

gas temperature equilibrium ratio, typically 10% as molecules for [Xe] = 2.7×10^{20} cm⁻³, by rapid association and dissociation, i.e., we assume equilibrium for the reaction



The dissociation rate per NaXe(*A*) molecule is about 10^{10} sec⁻¹ at typical [Xe] = 10^{20} cm⁻³, so that the equilibrium ratio of [NaXe(*A*)]/[Na(3p)][Xe] = K_{eq}^{-1} is maintained as long as the destruction of NaXe(*A*) as the result of deexcitation by stimulated emission and of dissociation and deexcitation by electrons is slower than 10^{10} sec⁻¹. This is expected to hold at the ratio $n_e/[Xe] < 10^{-3}$ and the incident optical intensities considered here. Vibrational and rotational excitation of NaXe *A*-state molecules by electrons is expected to be slow compared to vibrational and rotational relaxation by Xe so that these electron collisions can be ignored. The observation in Ref. 3 of a nearly thermal excimer band shape, corresponding to a vibrational temperature at the gas temperature *T*, also supports these expectations. In the present calculation we therefore include only molecular states connecting to the Na(3p) states, with the implicit assumption that the equilibrium portion of this is in the form of NaXe *A*-state molecules. Thus, all inelastic collision cross sections of electrons with the molecules are effectively assumed to be identical to those for the parent Na state.

The Na(3p) states radiate with a lifetime of 16 nsec while the NaXe *A* and *B* states have slightly longer and shorter radiative lifetimes, respectively. Therefore, the combined Na(3p) + NaXe(*B*) + NaXe(*A*) population radiates with an effective lifetime near 16 nsec. From the normalized emission spectrum of this composite population, and the absorption coefficient derived therefrom,¹⁰ one finds about a 10% probability that a photon is emitted in an optically-thin portion of the spectrum (for a 0.2-cm escape distance and [Xe] $\sim 10^{20}$ cm⁻³), i.e., the effective radiative lifetime for this combined population is about 160 nsec. This effective radiative rate constant is not very sensitive to [Na] and it scales linearly with [Xe] for values below 10^{21} cm⁻³. The stimulated emission coefficient at 700 nm is $\sim 10^{-16}$ cm² per NaXe(*A*) molecule, and thus is $\sim 10^{-17}$ cm² per total Na(3p) population (bound and free) at [Xe] = 10^{20} cm⁻³. Some of the transitions from higher Na states to Na(3p) are also slightly optically thick, but since their radiative rates are much smaller than their electron collisional rates, this is ignored in the calculations.

The NaXe^{*} molecular ion is structurally an Na⁺-Xe molecule whose potential (Fig. 2) we take to have an ~ 0.3 eV binding and $R_e \sim 3.2$ Å from experiments and theory.¹² (We have no information about TlXe^{*}.) The fact that only one molecular ground state results from this interaction between closed shell (¹S₀) monomers has a profound effect on its collisional and optical properties. Thus, NaXe^{*} cannot absorb in the visible, and the highly excited states of Na⁺-Xe will all nearly parallel the single Na⁺-Xe potential. The latter property yields the expectation that Xe collisions will not efficiently quench highly-excited Na⁺ atoms or bound Na⁺-Xe molecules and, as discussed further below, that dissociative recombination with NaXe^{*} will have a small rate coefficient.¹⁵ The reactions Na⁺ + 2Xe \rightleftharpoons NaXe^{*} + Xe will be very

fast¹² at high [Xe], yielding a ratio of $[NaXe^+]/[Na^+][Xe]$ very close to the equilibrium ratio K_{eq}^{+} at all n_e considered here. As discussed in Sec. III, the size of K_{eq}^{+} is very important in determining the effective rate of electron recombination in the discharge.

The Na_2^+ molecular ion potentials, from Ref. 14, are shown in Fig. 2. Under the conditions considered below, Na_2^+ is a minor constituent in the discharge, so that absorption by Na_2^+ (see Ref. 16) and emission from excited states of Na_2^+ are expected to be negligible. However, $e + Na_2^+ \rightarrow Na^* + Na$ is the dominant electron recombination mechanism in our model. Na_2^+ will be formed by the exchange reaction $Na \rightarrow NaXe^+ \rightarrow Na_2^+ + Xe$. Due to the low $[Na]/[Xe]$ ratio, the equilibrium ratio of $[Na_2^+]/[NaXe^+]$ is typically on the order of 1; rapid dissociative recombination of Na_2^+ normally makes this ratio much smaller.

The highly excited states of Na are expected to have associated $NaXe$ states with binding energies about equal to that of $NaXe^+$. If predissociation of lower excited states of $NaXe$ occurs to form excited Na, the loss of $NaXe^+$ will cause a net downward flow of excitation in the molecular excited state ladder and produce departures of the Na^* populations from Boltzmann equilibrium in the same manner as dissociative recombination of electrons with $NaXe^+$. However, as discussed in Sec. III, the experimental lower excited state population data seem to show that departures from the Boltzmann plot are small. The contribution of this process to the energy balance is evaluated in Appendix B.

D. Electrons

At the typical ionization fraction of interest to us, i.e., $n_e/[Xe] \sim 10^{-4}$, energy exchange by electron-electron collisions is much more rapid than energy loss by recoil of Xe. Inelastic and superelastic collisions with Na^* are largely in balance so that the net energy transfer rate between electrons and Na^* is much smaller than between free electrons. Therefore, the electron energy distribution is expected to be very nearly Maxwellian at a temperature T_e . The range of validity of this assumption for the higher excited state densities is being investigated separately.¹⁷

E. Collision rate coefficients

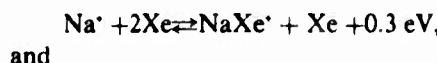
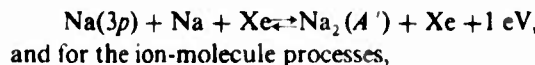
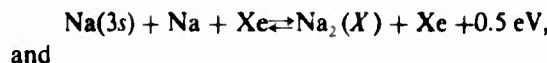
The simplified model used considers the states shown in Fig. 1, plus Xe^* , Xe^+ , and Xe_2^+ . In addition to $Na_2(X)$, $Na_2(A)$, Na^+ , $NaXe^+$, and Na_2^+ , hydrogenic levels of Na from $n = 4-15$ and the $3s$, $3p$, $4s$, $3d$, and $4p$ levels of Na are included. Electron collision rate coefficients between $n = 4$ and $n = 15$ levels and for ionization of these levels are calculated from the hydrogenic cross sections of Johnson,¹⁸ by integrating over the assumed Maxwellian energy distribution. Additional details for these and other rate coefficients are given in Appendix A. Calculations by Moores *et al.*¹⁹ are used for cross sections within the five lower Na levels, and scaling and detailed balance arguments are used for rate coefficients between the five lower Na and the $n = 4-15$ levels, as described in Appendix A. In order to account for the $n > 15$ levels that are neglected, we give the $n = 15$ level an ionization rate coefficient equal to about one-third the rate

for the $n = 15$ to $n = 16$ step. This is about $20 \times$ the direct ionization rate coefficient and is close to the effective multi-step ionization rate coefficient.²⁰ The $n = 14$ ionization rate coefficient is interpolated between this and the $n = 13$ value. Since the electron energy distribution is Maxwellian, all $i \rightarrow j$ rate coefficients k_{ij} are related by the thermodynamic ratio $k_{ij}/k_{ii} = (g_i/g_j) \exp[(E_j - E_i)/kT_e]$. The thermodynamic (Saha) equilibrium condition is also used to relate ionization and inverse ionization rate coefficients. This condition is usually written as

$$\frac{n_e}{g_e} \frac{[Na^+]}{g_+} = \frac{[Na(n)]}{g_n} \left(\frac{2\pi m k T_e}{h^2} \right)^{3/2} \times \exp[-E_i(n)/kT_e], \quad (1)$$

where $E_i(n)$ is the ionization potential of the n th level. The statistical weights are $g_e = 2$ for the electrons and $g_+ = 1$ for Na^+ . The g_n vary from 2 for the $3s$ level to $2n^2$ for the hydrogenic levels.

The only heavy particle collision rates entering the rate equations are those for $Na_2(X)$ and $Na_2(A)$ association and dissociation¹³ [as noted above, the $NaXe(A)/Na(3p)$ ratio is assumed in equilibrium], i.e.,



We assume that all molecules are in an equilibrated vibrational and rotational distribution at T , and the ratio of forward to backward rate coefficients is given by equilibrium relations at the gas temperature T ; these rate coefficients are given in Appendix A.

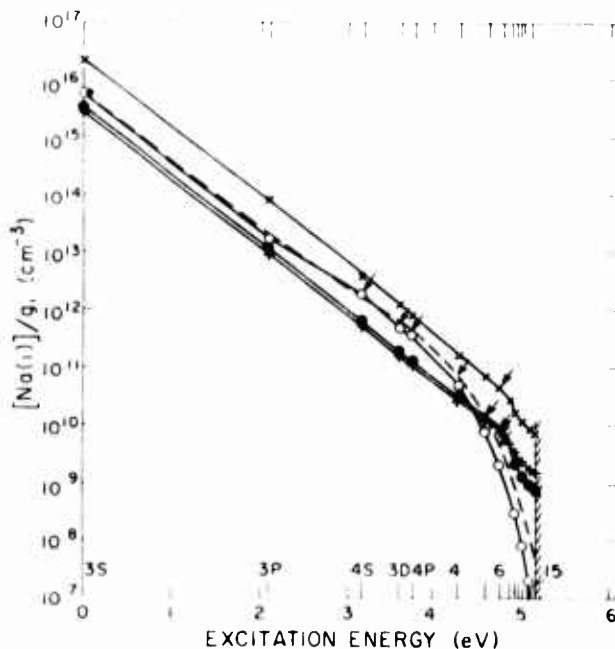
One of the most important processes controlling the behavior of these discharges, in which most of the ions are molecular and $T < T_e$, is dissociative recombination of electrons with the molecular ions. Dissociative recombination is generally described²¹ in terms of a curve crossing of the dissociative diatomic state (AB^+) with the molecular ion state (AB'). In homonuclear diatomics such crossings always occur because symmetry considerations lead to a repulsive as well as an attractive molecular-ion state; thus some of the Rydberg-like A_2^+ states will parallel this repulsive state and cross the (attractive) A_2^+ state. This situation applies to Na_2^+ dissociative recombination, so that we expect it to have the typical large rate coefficient observed for the heavier inert gas diatomics,²² e.g., $2 \times 10^{-7}(0.026/T_e)^{1/2} \text{ cm}^3/\text{sec}$. For $NaXe^+$, on the other hand, only one attractive state occurs and the Rydberg-like $NaXe^+$ states will not cross this ion state. The rate coefficient for $NaXe^+$ dissociative recombination is thereby expected¹³ to be much smaller than the Na_2^+ value. Including $NaXe_n^+$ clusters does not modify this conclusion. For the same reasons, associative ionization to form $NaXe^+$ is assumed not to occur. Consequently, we have taken $\alpha(NaXe^+) = 0$ in most of the calculations. Unless the rate coefficient for $Na^+ + Na + Xe \rightarrow Na_2^+ + Xe$ were usually

large, e.g., $10^{-28} \text{ cm}^3/\text{sec}^{-1}$, the Na_2^+ is formed predominantly from NaXe^* through the $\text{NaXe}^* + \text{Na} \rightarrow \text{Na}_2^+ + \text{Xe}$ ion exchange process. Due to the low Na density, this process is usually the rate-limiting step that determines the electron-ion loss rate in the discharge. For this ion exchange rate coefficient k_e , we use a Langevin rate coefficient, and believe that this should be fairly accurate. However, the final Na^+ product state of the Na_2^+ dissociative recombination must be estimated by fitting the model to the experiments.

The curve-crossing model predicts that the final state products of Na_2^+ dissociative recombination

$[\text{Na}_2^+ + e \rightarrow \text{Na}(n_R) + \text{Na}]$ will be an atomic state bound by about 2.3 eV, which is the vertical dissociation energy of Na_2^+ . This would apply to Na_2^+ in the ground vibrational state, whereas the same model would predict that an excited vibrational state would dissociate to less strongly bound Na^+ states. Thus, we expect a distribution of final states labeled by principal quantum numbers n_R , with the mean values of n_R increasing with Na_2^+ vibrational temperature. For convenience we often use a single n_R , representing the effective value of this distribution.

Destruction of excited Na in collision with Na, by associative ionization to form $\text{Na}_2^+ + e$, occurs with a typical gas



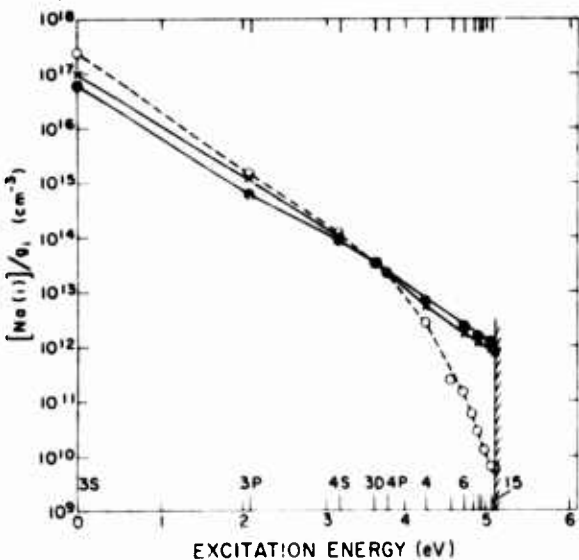


FIG. 5. Same quantities as in Fig. 3 as a function of 700-nm radiation intensity I , with $[Na]_0 = 2.7 \times 10^{17} \text{ cm}^{-3}$, $[Xe] = 2.7 \times 10^{20} \text{ cm}^{-3}$, $T_e = 0.52 \text{ eV}$, and $n_R = 3p$. The closed circles are for $I = 0$, the \times for $I = 320 \text{ MW/cm}^2$, and the open circles for $I = 560 \text{ MW/cm}^2$; the corresponding values of n_e are 2.0×10^{17} , 1.65×10^{17} , and $1.4 \times 10^{16} \text{ cm}^{-3}$, respectively.

operate during the relatively long steady-state portion of the discharge. This is due to the energy initially required to ionize a major fraction of the Na atoms. The data in Ref. 3, to which we will compare, also represent steady-state conditions. Consequently, we will concentrate here on the calculated steady-state densities of the 17 Na states in the model, and of the ion and electron densities. The calculations were made for fixed electron temperatures. As expected, there is an exponential buildup of n_e from the assumed starting electron density of 10^{10} cm^{-3} , an increasing rate of ionization as n_e increases, and once n_e exceeds about 10^{14} cm^{-3} , there is convergence to the steady-state conditions within a few nanoseconds. In cases where the neutral Na density is severely depleted at steady state, the excited-state densities are larger during the rapid ionization transient than for steady-state conditions.

The excited state and ion densities in the steady-state positive column depend on T_e , n_R , and the effective dissociative recombination rate per Na⁺ ion. The latter rate depends on the $[NaXe^+]/[Na^+]$ ratio, which is assumed in equilibrium at the gas temperature. Since Na₂⁺ is formed by NaXe⁺ + Na → Na₂⁺ + Xe, with rate coefficient k_a , the effective Na₂⁺ dissociative recombination rate per Na⁺ is proportional to $k_a [NaXe^+]$. The actual ratio $[NaXe^+]/[Na^+] = K_{eq}^+ [Xe]$ is < 0.5 at the $[Xe] < 4.5 \times 10^{19}$ considered in Ref. 3(a), and as a result the effective dissociative recombination rate is too small to significantly perturb the $[Na^+]$ and $[Na^{\cdot}]$ densities, i.e., these densities relative to [Na] are very close to the Saha ratios at T_e , in agreement with the Na-Xe discharge data in Ref. 3(a). The laser gain which results from this limit is considered in Sec. V.

In contrast to the Na-Xe case, the Tl-Xe discharge data of Ref. 3(b) does not fit the Saha relation for the higher n . This implies a more rapid dissociative recombination and thus larger values of $K_{eq}^+ [Xe]$ and/or a much lower energy

for the atomic level resulting from dissociative recombination. In order to investigate this type of behavior, we have used all other cross sections as appropriate to Na and Xe, but increased K_{eq}^+ by a factor of 10–20, corresponding to 0.45 eV rather than 0.30 eV of molecular ion binding, i.e., $[NaXe^+] \approx n_e$. We have then systematically varied T_e , n_R , and k_a . We will illustrate the effect of these parameters, and of including NaXe⁺ dissociative recombination in the examples shown in Figs. 3 and 4. The effects of variations in the stimulated emission rate caused by external radiation are shown in Fig. 5 for the case of $n_R = 3p$. The calculated values of extracted power densities and laser amplifier efficiency for the $n_R = 6$ (Saha) case and for $n_R = 3p$ are shown in Fig. 6. Detailed discussions of these results are presented in the Secs. IIIA and IIIB.

A. Excited state densities

In Figs. 3–5 we show results of our calculations in the form of plots of the log of $[Na(i)/g_i]$ versus excitation energy. We use $2I_e + 1$ for the statistical weight, neglecting the alkali spin, since the actual ground state Na density then appears on the abscissa. An excited state distribution at the electron temperature (Saha condition) would appear as a straight line in Figs. 3–5. In all the cases in Figs. 3 and 4 the electron densities are high enough so that Na radiative rates are much slower than electron collisional rates and the

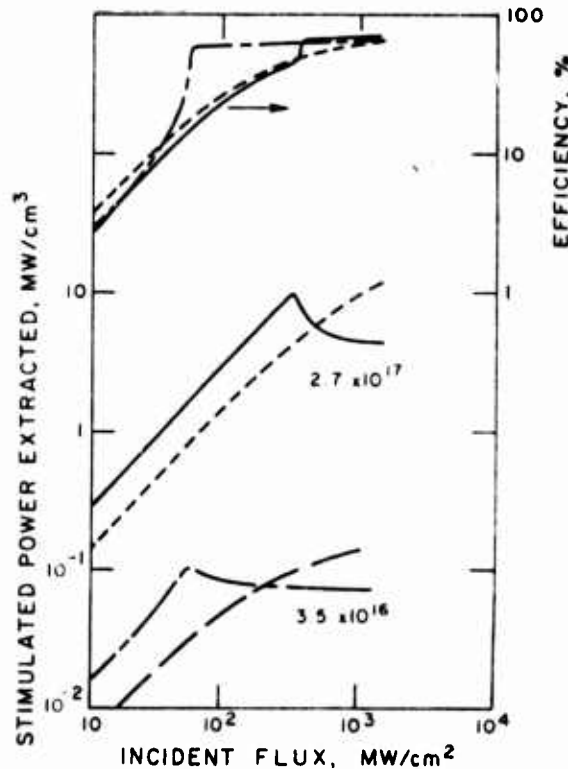


FIG. 6. Stimulated radiative power extracted from the discharge (lower four curves) and laser amplifier efficiency (upper three curves) as a function of incident optical power at 700 nm. The solid curves are for the conditions of Fig. 5. The chain (—·—) curves are for $[Na]_0 = 3.5 \times 10^{16} \text{ cm}^{-3}$ and $n_R = 3p$. The long and short dashed curves are for $n_R = 6$ and for $[Na]_0 = 3.5 \times 10^{16}$ and $2.7 \times 10^{17} \text{ cm}^{-3}$, respectively, conditions which result in near Saha values for n_e and all $[Na^{\cdot}]$.

$[\text{Na}(i)/g_i]$ for the lower energy states do nearly fit a straight line at the electron temperature. However, above the terminal Na^* state of recombination n_R , the population distribution frequently falls below such a straight line. In this region of excited state energies, electron collisions are exciting Na^* up a ladder of increasing n and then ionizing the higher n levels. The resulting Na^* forms NaXe^* and Na_2^+ , which then dissociatively recombine to $\text{Na}(n_R) + \text{Na}(3s)$ to complete the cycle (see Fig. 1). Thus, competition between excitation and ionization by electrons and recombination on Na_2^+ results in population ratios $[\text{Na}(n+1)/g_{n+1}]/[\text{Na}(n)/g_n]$ for $n > n_R$ whose average behavior is characterized by an excitation temperature between T_e and T . Using predicted scaling based on the Bates' approximation,²⁰ we find that at $n_e^2/[\text{Na}][\text{Xe}] > 10^{-4}$ (for the $n_R = 6$, $T_e = 0.3\text{-}0.5\text{-eV}$ case) this excitation temperature approaches T_e ; at much lower $n_e^2/[\text{Na}][\text{Xe}]$ it should approach T . In a gas discharge near equilibrium, such as a high-pressure arc with $T = T_e$, inverse ionization of Na^* and dissociative recombination of Na_2^+ would be balanced by the processes of Na excited-state ionization and $\text{Na}^* + \text{Na}$ associative ionization. However, in the present discharges in cold gas the Na_2^+ density builds up so that additional dissociative recombination occurs and drives the net ionization below the Saha value appropriate to T_e .

In Fig. 3 we show the effect of varying k_a and n_R at a fixed $T_e = 0.38\text{-eV}$. The values $[\text{Na}]_0 = 6.3 \times 10^{15} \text{ cm}^{-3}$ and $[\text{Xe}] = 4.5 \times 10^{19} \text{ cm}^{-3}$ are used for the four lower curves in Fig. 3; these values are representative of the densities used in the experiments of Refs. 3(a) and 3(b). In the lowest (+) curve, $n_R = 6$ and $k_a = 1 \times 10^{-9} \text{ cm}^3 \text{ s}^{-1}$; the n_R value is indicated by an arrow. Note that the densities follow a $T_e = 0.38\text{-eV}$ straight line for $n < 6$ and dip slightly below this for $n > n_R$. In the next higher (-) case, k_a is increased to $2 \times 10^{-9} \text{ cm}^3 \text{ s}^{-1}$. The dip below a $T_e = 0.38\text{-eV}$ line for $n > 6$ is more pronounced than in the first case because of the faster rate of Na_2^+ formation and dissociative recombination. The effect of changing n_R can be seen as follows. The dashed line results from distributing the dissociative recombination equally between $n_R = 3d, 4p, 4, 5$, and 6 states, with $k_a = 1 \times 10^{-9} \text{ cm}^3 \text{ s}^{-1}$. Note that the increased difficulty of laddering upward from these levels has caused a major drop in n_e and the density of high n states. In the (0) case, $k_a = 1 \times 10^{-9} \text{ cm}^3 \text{ s}^{-1}$ and $n_R = 4s$ is still more strongly bound, causing n_e and the densities of states with high n to drop still further.

To indicate density dependences, the top (\times) curve in Fig. 3 again has $n_R = 6$ and $k_a = 1 \times 10^{-9} \text{ cm}^3 \text{ s}^{-1}$ as for the lowest (+) curve, but both $[\text{Na}]_0$ and $[\text{Xe}]$ have been increased by about a factor of 6. These two $n_R = 6$ cases dip below the Saha (straight) line by about the same amount, indicating that there the density dependence is relatively minor (at constant $[\text{Na}]_0/[\text{Xe}]$). This is due to a balance between the effective recombination rate (proportional to $[\text{Xe}]$) and the effective ionization rate (roughly proportional to n_e , which varies as $[\text{Na}]_0$).

The Na_2^+ dissociative recombination rate coefficient k_{DR} was varied slightly in the different cases in Fig. 3, but the consequences are minor since the $\text{NaXe}^* \rightarrow \text{Na}_2^+$ ion ex-

change is the primary recombination rate limiting step. The value $k_{DR} = 2 \times 10^{-7} (0.026/T_e)^{1/2}$ was used for the cross and plus cases in Fig. 3, $k_{DR} = 1 \times 10^{-7} (0.026/T_e)^{1/2}$ for the open circle case, $k_{DR} = 5 \times 10^{-8} (0.026/T_e)^{1/2}$ for the solid circle case, and $k_{DR} = 2 \times 10^{-8} (0.026/T_e)^{1/2}$ to each state from 3d to 6 for the dashed-line case.

In Fig. 4 we show T_e dependence, for $[\text{Na}]_0 = 3.5 \times 10^{16} \text{ cm}^{-3}$ and $[\text{Xe}] = 2.7 \times 10^{20} \text{ cm}^{-3}$ as would be appropriate for excimer laser. We have used $n_R = 3p$ examples to illustrate departures from the Boltzmann equilibrium for higher T_e , i.e., for $n_R > 3d$ the densities would satisfy a Boltzmann equilibrium at all n in the $T_e = 0.52\text{-eV}$ case. In the $n_R = 3p$, $T_e = 0.52\text{-eV}$ case (open circles in Fig. 4), the Na^* densities fall about a decade below the Saha limit at high n , while in the $T_e = 0.43\text{-eV}$ case they drop about five decades below this limit. This abrupt change from near Saha equilibrium to severely depleted $[\text{Na}^*]$ occurs for any n_R ; for higher n_R the critical T_e is lower. The abruptness of this change is due to strong positive feedback: an increase in the laddering-ionization rate coefficient with T_e raises n_e , which further enhances the ionization rate. In the final example in Fig. 4 (∇), we have added rapid NaXe^* dissociative recombination to show the major effect this has. Since in this case the recombination does not proceed via the relatively slow $\text{NaXe}^* + \text{Na} \rightarrow \text{Na}_2^+ + \text{Xe}$ process, it very effectively depresses n_e and the $[\text{Na}^*]$ at high n values.

The relative Na^* densities for $n = 12\text{-}15$ in our model are normally (for $n_e > 10^{15} \text{ cm}^{-3}$) determined by T_e , since the $n \rightarrow n+1$ collisional mixing rates increase rapidly with increasing n , and greatly exceed the dissociative recombination flux for $n > 10$. Thus all states above $n = 12$ closely follow a T_e slope. From the Saha condition, which must hold for the very high n , we have from Eq. (1)

$$[\text{Na}^*/g^*]_\infty = (2\pi m k T_e / h^2)^{3/2} [\text{Na}^*] n_e / 2g^*, \quad (2)$$

where $[\text{Na}^*/g^*]_\infty$ is the $n \rightarrow \infty$ limit of $[\text{Na}(n)]/g_n$ and $g^* = 1$ is the Na^* statistical weight. Thus, the calculated n_e and $[\text{Na}^*]$ should yield a $[\text{Na}^*/g^*]_\infty$ from Eq. (2) that is consistent with the $n = 12\text{-}15$ values of $[\text{Na}(n)]/g_n$. Using Eq. (2) we have calculated the $[\text{Na}^*/g^*]_\infty$ points at the Na ionization limit in Figs. 3 and 4, and it can be seen that these fit an extrapolation of the $n = 10\text{-}15$ densities.

One can also use the experimental n_e from Refs. 3 and a calculated $[\text{Na}^*]/n_e$ value to obtain an experimental value of $[\text{Na}^*/g^*]_\infty$ from Eq. (1). For the $[\text{Na}]_0 = 6.3 \times 10^{15} \text{ cm}^{-3}$ and $[\text{Xe}] = 4.5 \times 10^{19} \text{ cm}^{-3}$ case, the ratio $[\text{NaXe}^*]/[\text{Na}^*]$ is expected to be near the equilibrium value of $K_{eq} [\text{Xe}] \approx 0.4$ and $[\text{Na}_2^+] \ll n_e$, so that $[\text{Na}^*] + [\text{NaXe}^*] + [\text{Na}_2^+] = n_e$ yields $[\text{Na}^*] \approx n_e/1.4$. Using this relation in Eq. (2) with the experimental n_e yields an experimental point at the Na ionization limit. (The n_e are calculated in Refs. 3 from measured current densities and E/N values and calculated electron mobilities.²⁷) For the data in Fig. 5 of Ref. 3(a), $n_e = 2 \times 10^{15} \text{ cm}^{-3}$ and $3.5 \times 10^{14} \text{ cm}^{-3}$, respectively, for the 0.38 and 0.33-eV cases. The resulting ionization-limit points at 5.14 eV are $\sim 4 \times 10^9 \text{ cm}^{-3}$ for the $T_e = 0.38\text{-eV}$ case and $\sim 2 \times 10^8 \text{ cm}^{-3}$ for the 0.33-eV case, i.e., the 0.38-eV point falls slightly below the extrapolation of the 0.38-eV Saha line

in the figure of Ref. 3(a), while the 0.33-eV point falls about a factor of 4 below the 0.33-eV Saha line.

In the Tl case, we do not have even an estimate of K_{eq}^+ for $TlXe'$, although the rapid decrease in $[Tl^*/g^*]$ above 4.5 eV in Fig. 8 of Ref. 3(b) suggests that K_{eq}^+ is much larger than for $NaXe'$ and the effective energies of the $Tl^*(n_R)$ states are near 4.5 eV. Since n_e is an upper limit for $[Tl^*]$, one can still obtain an upper limit to $[Tl^*/g^*]_u$ using $[Tl^*] = n_e$ and the experimental n_e in Eq. (2). This has been done in Fig. 8 of Ref. 3(b), where it can be seen that it confirms the existence of a major falloff of the high n densities relative to the Saha condition. These Tl data bear considerable resemblance to some of the calculated curves in Figs. 3 and 4.

B. Stimulated emission and efficiency

For metal-excimer laser operation, one would like to obtain a large population in the first excited state, corresponding to a high excitation temperature, i.e., $T_e > 0.5$ eV for the Na case. If the higher levels are also at T_e , however, most of the neutral metal atoms will be ionized. One solution to this problem is to increase $[Na]_0$; then the Saha relation [Eq. (2)] forces the ionization balance toward a smaller fractional ionization. The medium gain in the Saha limit is considered in Sec. V. Another possible solution occurs if the high n levels are depressed, relative to Boltzmann equilibrium at T_e , by dissociative recombination, as in some cases in Figs. 3 and 4. In order to explore this latter possibility in detail we have included stimulated emission in the model. We continue to use a K_{eq}^+ of ~ 10 times the value for $NaXe'$ in order to represent systems in which dissociative recombination can drive the high Na^* and n_e below the Boltzmann equilibrium values. The expected n_R are of course unknown, but states bound by up to 2.5 eV are expected in the Na case and the following results are not very sensitive to the choice of $n_R = 3p$ (bound by 3 eV) and $4s$ (bound by 2 eV). Thus we use $n_R = 3p$ in the following illustrative example.

In the two-temperature model with weakly bound excimers,¹ the ratio of excimer band stimulated emission cross section $\sigma_s = g_s/[Na(3p)]$ to absorption cross section $\sigma_a = k_s/[Na(3s)]$ is given by $(1/3) \exp [h(v_0 - v)/kT]$, where v_0 is the atomic transition frequency. The open circle case of Fig. 5 involves high laser powers, where the absorption and stimulated emission rates are almost equal. For this condition, $[Na(3s)]/[Na(3p)]$ is driven to the above ratio, which corresponds to an $Na(3p)$ excitation temperature of $T v_0 / (v_0 - v)$. For 700-cm radiation and $T = 750$ K the quantity $T v_0 / (v_0 - v)$ is ~ 0.40 eV. We use $T_e = 0.52$ eV in the examples to be given, so the laser-induced transition between $3s$ and $3p$ drives the $[Na(3p)]/[Na(3s)]$ population temperature from 0.52 eV toward 0.4 eV, thereby extracting power from the medium. This transition in the population ratio occurs when the stimulated emission rate equals or exceeds the electron quenching rate for $Na(3p)$ atoms. One can thus estimate the maximum power available for extraction as being about equal to that going into $3p$ quenching by electrons; the following calculations confirm this expected behavior.

We have calculated excited state densities and excimer-band stimulated and absorbed power densities as a function

of incident Flux I for a 700 nm wavelength, $T_e = 0.52$ eV, and $[Xe] = 2.7 \times 10^{20}$ cm⁻³ using gain and absorption coefficients $g_s/[Na(3p)] = 5 \times 10^{-38}$ cm⁵ and $k_s/[Na(3s)] = 7.5 \times 10^{-40}$ cm⁵ from Ref. 7 for $T = 750$ K. For $[Na]_0 = 2.7 \times 10^{17}$ cm⁻³, the resulting Na^* population distributions are given in Fig. 5 while the output powers and efficiencies are given as a function of incident radiation power by the solid curves in Fig. 6. (This incident power would be intercavity power in a self-oscillator.) The sharp peaks in the stimulated power and the abrupt increases in efficiency in the $n_R = 3p$ cases in Fig. 6 are due to a sudden drop in n_e by about an order of magnitude, as seen in Fig. 5. This occurs because the $[Na(3p)]/[Na(3s)]$ ratio is lowered by the laser power. Since ionization occurs by multistep excitation from $Na(3p)$, n_e is therefore forced to decrease, and this also makes the multistep ionization less rapid, which further decreases n_e . At fixed T_e the discharge can thus undergo a type of phase transition from highly ionized Na and large n_e to slightly ionized Na and low n_e . In the $[Na]_0 = 3.5 \times 10^{16}$ cm⁻³ case, also shown in Fig. 6, this transition to low n_e occurs at a lower incident radiation field. Thus far, our models have examined this effect only at a fixed T_e corresponding approximately to a fixed discharge voltage. If the power supply had an internal impedance comparable to or greater than the discharge impedance, the discharge voltage would rise, causing an increase in T_e and tending to maintain n_e near a constant value. The net gain, extracted power, and efficiency should then be larger than indicated in Fig. 6. The maximum net gain coefficient in Fig. 6 is $g_s - k_s \approx 0.03$ cm⁻¹ with $g_s \approx 0.05$ cm⁻¹ for $[Na]_0 = 2.7 \times 10^{17}$ cm⁻³. It is important to note that each excimer emission event transfers a fraction $(v_0 - v)/v \approx 0.19$ of the photon energy into gas heating, whereas an absorption event causes an equal amount of gas cooling. Therefore, the efficiency is not very sensitive to the amount of net stimulated emission in the excimer band.

For comparison, we have also indicated in Fig. 6 (short-and long-dashed curves) the stimulated power that would be extracted if $n_R = 6$, still with the larger K_{eq}^+ . In this case, n_e and all $[Na^*]$ are very near the Saha values. These stimulated powers rise smoothly with increasing incident flux as n_e is nearly constant. At low fluxes, net gains are approximately 0.015 and 0.006 cm⁻¹ for $[Na]_0$ values of 3.5×10^{16} and 2.7×10^{17} cm⁻³. At high incident fluxes the calculated discharge efficiency approaches about 60%, with the energy lost primarily by thermalization of the X and A states of $NaXe$ following stimulated emission and by electron excitation of molecular ions (see Appendix B).

The maximum efficiency for extracted power in the $n_R = 3p$ cases of Fig. 6 also $\sim 60\%$, with 19% going into gas heating during rethermalization of the $NaXe$ molecules and with the remaining $\sim 20\%$ going primarily into dissociative recombination of electrons and Na_2^+ ions. This large efficiency is the result of the large rates of $Na(3p)$ deexcitation collisions and of the consequent large rate of saturated stimulated emission compared to the effective rate of ionization for $Na(3p)$ atoms. The maximum extracted power at ~ 350 MW/cm² incident laser flux is ~ 10 MW/cm³ or 10^3 J/l in a 0.1-μsec pulse. (The pulse length is limited to ~ 0.1 μsec by

gas heating.) We must reemphasize that this model applies to a hypothetical excimer with $K_{eq} > 10^{-19} \text{ cm}^2$ and in which the equivalent of $e + \text{Na}_2^+ \rightarrow \text{Na}(3p) + \text{Na}(3s)$ occurs. Furthermore, as discussed in Sec. IV, the model does not contain an unknown process that is responsible for approximately 75% of the discharge energy reported in the measurements of Ref. 3.

IV. DISCHARGE ENERGY BALANCE AND V-/CURVES

Once the kinetics have been established (see Sec. III), one expects to be able to write down the energy balance for the metal-rare gas discharge. In principle the energy balance can be used to derive volt-ampere curves for the discharge. However, we will show that the energy loss processes considered in our model do not add up to the experimental energy input so that there must be energy loss mechanisms that we have not considered. Only the dominant energy loss processes are discussed here; additional mechanisms are discussed in Appendix B.

The electron energy balance equation relevant to the present problem is

$$JE = \sum h\nu R_v + v_u k(T_e - T)n_e + (\epsilon_R + 3kT_e/2)\alpha_{DR} \\ \times n_e [\text{Na}_2^+] + (\epsilon'_R + 3kT_e/2)\alpha'_{DR} n_e [\text{NaXe}^+] \\ + \sum \epsilon_{ij} k_{ij} n_e [\text{NaXe}^*]. \quad (3)$$

Here, the power input to the electrons is JE , where J is the current density and E is the electric field. The first term on the right-hand side is the net radiative energy loss, the second term is due to elastic recoil of Xe atoms, the third and fourth terms are due to dissociative recombination of Na_2^+ and NaXe^* , and the last term represents vibrational and rotational excitation of NaXe^* . R_v is the rate ($\text{cm}^{-3} \text{s}^{-1}$) of escape of photons of energy $h\nu$ and v_u is the frequency of energy exchange collisions of electrons of temperature T_e with the neutral atoms of temperature T . Also, ϵ_R and ϵ'_R are the average ionization energies of excited atoms produced by dissociative recombination of electrons and Na_2^+ and NaXe^* ions, respectively, with rate coefficients α_{DR} and α'_{DR} respectively. ϵ_{ij} and k_{ij} are the energy transferred and rate coefficient associated with electron impact excitation of NaXe^* from vibrational-rotational level i to level j . Note that the first, third, and fourth terms on the right-hand side of Eq. (3) replace the large number of terms representing the electron energy loss and gain in excitation and deexcitation collisions with metal atoms.

The radiative loss term in Eq. (3) includes spontaneous emission and stimulated emission and absorption via the excimer band. Since we have assumed that the upper and lower molecular states of the excimer transition are maintained in thermal equilibrium with the respective atomic states, the energy supplied by the electrons per excimer photon emitted is equal to the excitation energy of the atomic resonance state. Experiments³ and our calculations show that the contribution of spontaneous radiation for wavelengths between 200 and 800 nm is only a few percent of the discharge power, and we believe that radiative losses are still negligible when

shorter and longer wavelengths are included. As noted in Sec. III B, for Na the net gas heating is 19% of the optical energy extracted at 700 nm.

The frequency v_u as in Eq. (3) for energy exchange collisions in Eq. (3) is roughly equal to $(2m/M)\langle\sigma_m v\rangle[\text{Xe}]$ for electron temperatures of interest in this paper, i.e., the electrons lose energy by elastic recoil of the Xe atoms. Here, m and M are the electron and Xe atom masses and $\langle\sigma_m v\rangle[\text{Xe}]$ is the average frequency of momentum transfer collisions of electrons with Xe atoms. Using the cross-section data from Ref. 27, we obtain a normalized energy exchange collision frequency $v_u/[\text{Xe}] = 1.5 \times 10^{-12}(T_e)^{1/6} \text{ cm}^3/\text{sec}^{-1}$ for T_e between 0.3 and 1 eV. We then find that for the experimental $n_e = 2 \times 10^{15} \text{ cm}^{-3}$ of the 0.38-eV case in Ref. 3(a), the energy lost by elastic recoil is about 10% of the experimental power input of about 16 kW/cm².

Since the Na_2^+ dissociative recombination rate is limited by the ion exchange rate k_a , the contribution of dissociative recombination to the energy balance can be estimated as $k_a[\text{Na}][\text{NaXe}]\Delta E$, where the energy loss per recombination $\Delta E = 3kT_e/2 + \epsilon_R$, i.e.,

$$\alpha_{DR} n_e [\text{Na}_2^+] = k_a [\text{Na}(3s)][\text{NaXe}^*]. \quad (4)$$

Using a mean value of ~ 1 eV for ϵ_R ,

$[\text{NaXe}^*] = n_e K_{eq}^+ [\text{Xe}] / (1 + K_{eq}^+ [\text{Xe}])$, and $k_a = 10^9 \text{ cm}^3 \text{ s}^{-1}$ yields recombination energy losses which are typically about 4% of the experimental energy input for the 0.38-eV data of Ref. 3(a). [In the limit of $K_{eq}^+ [\text{Xe}] \gg 1$, where K_{eq}^+ refers to TiXe^+ , the recombination energy loss is about 20% of the total energy input for the Ti-Xe discharge data of Ref. 3(b).] If NaXe^* dissociative recombination to a high n_R (e.g., 8) is added, the energy loss via dissociative recombination is increased by a large factor without significantly changing n_e or the measured Na^* values. Thus, adding NaXe^* recombination at high n , typically with a rate coefficient α_{DR} of about half the Na_2^+ value, is one way to explain the measured powers. However, as indicated in Sec. II, theoretical arguments predict α_{DR} of NaXe^* to be much smaller and this contribution to the energy balance to be negligible. (This also applies to Ti-Xe and to any metal whose ionization energy is less than the Xe excitation potential.)

Based on arguments in Appendix B, rotational and vibrational excitation of the dominant molecular ion NaXe^* appear to be a small ($\sim 2\%$) but not negligible energy drain. Other energy loss processes considered but rejected as too small to be of importance in Eq. (3) were (a) collisions between two excited atoms; (b) inverse ionization and collisional deexcitation down the NaXe molecular excited state ladder to the $\text{NaXe}(A^2\Sigma)$ state followed by dissociation and then by electron induced excitation and ionization up the atomic excited state ladder; (c) quenching of Na^* states due to Xe collisions with a rate coefficient of about $10^{-10} \text{ cm}^3/\text{sec}^{-1}$; (d) dissociation of molecules by electron impact; and (e) free-free radiation, which has been calculated²⁸ and also could be detected at wavelengths below 1 μm if it were large enough to yield a significant energy loss. We therefore calculate a total energy loss rate for the $T_e = 0.38 \text{ eV}$ case of Ref. 3(a) of less than 25% of the measured power input. A similar discrepancy is found for the $T_e = 0.33 \text{ eV}$ case. Oth-

er processes considered in Appendix B that could make major contributions to the energy balance are Eqs. (B6)–(B9) and possible molecular impurities. However, the rate coefficients for Eqs. (B6)–(B9) are unknown and the impurity densities are expected to be small, so that these contributions are highly uncertain.

An alternative means of examining the energy balance is to derive an expression for the electric field versus current density, or more commonly, the volt-ampere curve for the discharge. We first note that the current density is given by the relation ($N = [\text{Xe}]$)

$$J = e\mu_e N(E/N), \quad (5)$$

where $\mu_e N$ is the electron mobility normalized to unit density. When Eqs. (4) and (5) are substituted in Eq. (3), with radiation neglected, one obtains the equation

$$\begin{aligned} & e\mu_e N(E/N)^2 \\ &= (\epsilon_K + 3kT_e/2) k_a [\text{Na}(3s)]/N + (\nu_u/N) \\ &\quad \times k(T_e - T) + [(\epsilon'_K + 3kT_e/2)\alpha_{DR} + \sum \epsilon_y k_y] \\ &\quad \times (J/N)[e\mu_e N(E/N)]^{-1}. \end{aligned} \quad (6)$$

From Eq. (6) one sees that when the energy loss is due only to Na_2^+ dissociative recombination and Xe elastic recoil [first two terms on the right side of Eq. (6)], E/N depends on the discharge current density only through the rather slow changes in electron temperature with J . Experimental measurements³ show that E/N increases much more rapidly with J than predicted from the temperature increase of these terms. When the last term in Eq. (6) dominates, the E/N varies approximately with $(J/N)^{1/3}$. Approximate agreement in magnitude and J/N variation with the initial voltage-current data, before measurements of cathode fall, led us to the no-longer-tenable hypothesis⁹ that dissociative recombination of electrons with NaXe^+ was the dominant energy loss mechanism in the experimental discharges. However, this now appears to be very unlikely as are other possible causes we have investigated, such as rotational and vibrational excitation of NaXe^+ . See Appendix B for an evaluation of these other energy losses.

V. GAIN COEFFICIENT IN THE SAHA-BOLTZMAN LIMIT

The primary objective of Sec. V is to explore the consequences of assuming that $[\text{Na}^+]$, n_e , $[\text{Na}]$, and all $[\text{Na}^*]$ are in Saha-Boltzmann equilibrium ratios at temperature T_e . As in Secs. I–IV, we assume that atomic translation and molecular vibration temperatures are at the gas temperature T , so that gain in the excimer band results at a sufficient excited state density, as in the two-temperature model of Ref. 1. As suggested in Sec. III, a rapid improvement in laser gain with increasing $[\text{Na}]_0$ is predicted. In the Tl-Xe case, the data indicate that less ionization actually occurs, perhaps due to a larger binding of TlXe^+ compared to NaXe^+ . A modification of this simple two-temperature model for this case will be discussed at the end of Sec. V.

As was found in the detailed model, we assume that $\text{Na}^+ + 2\text{Xe} \rightleftharpoons \text{NaXe}^+ + \text{Xe}$ is in equilibrium at the gas temperature,

$$\frac{[\text{NaXe}^+]}{[\text{Na}^+]} = [\text{Xe}] K_{eq}^+(\mathcal{T}), \quad (7)$$

where we use $K_{eq}^+(\mathcal{T}) = 6 \times 10^{-3} (T/670 \text{ K})^{1/2} \exp(-0.3 \text{ eV}/kT) \text{ cm}^{-3}$. From the calculations of Sec. III we find that $[\text{Na}_2^+]/[\text{Na}^+] \ll 1$, as expected due to slow formation and rapid depletion of Na_2^+ at $n_e > 10^{15} \text{ cm}^{-3}$. Thus, using Eq. (7),

$$\begin{aligned} n_e &= [\text{Na}^+] + [\text{Xe}] K_{eq}^+(\mathcal{T}) + [\text{Na}_2^+] \\ &\approx [\text{Na}^+] \{1 + [\text{Xe}] K_{eq}^+(\mathcal{T})\}. \end{aligned} \quad (8)$$

Combining Eqs. (1) and (8), we obtain

$$\begin{aligned} n_e^2 &\approx \{1 + [\text{Xe}] K_{eq}^+(\mathcal{T})\} [\text{Na}(3s)] \\ &\quad \times (2\pi m k T_e/h^2)^{3/2} \exp(-E_i/kT_e) \end{aligned} \quad (9)$$

If we take into account neutral depletion, i.e., $[\text{Na}(3s)] \approx [\text{Na}]_0 - n_e - [\text{Na}_2^+] \approx [\text{Na}]_0 - n_e$, then the electron temperature is given approximately by the solution of the relation

$$\begin{aligned} \exp(-E_i/kT_e) \\ = \frac{n_e^2 / ([\text{Na}]_0 - n_e)}{(2\pi k T_e/h^2)^{3/2} \{1 + [\text{Xe}] K_{eq}^+(\mathcal{T})\}}. \end{aligned} \quad (10)$$

Assuming equilibrium between the $\text{Na}(3p)$ and $\text{Na}(3s)$ densities at T_e , we see that the $[\text{Na}(3p)]$ density can then be expressed as

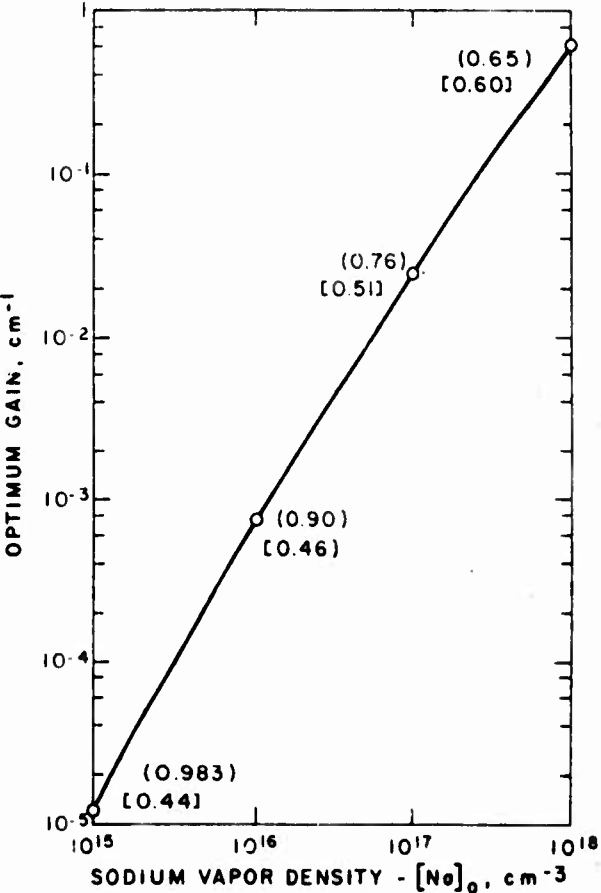


FIG. 7. Maximum net gain versus initial sodium density $[\text{Na}]_0$. The numbers in square brackets are the electron temperatures in eV and the numbers in parentheses are the ratios of n_e to $[\text{Na}]_0$.

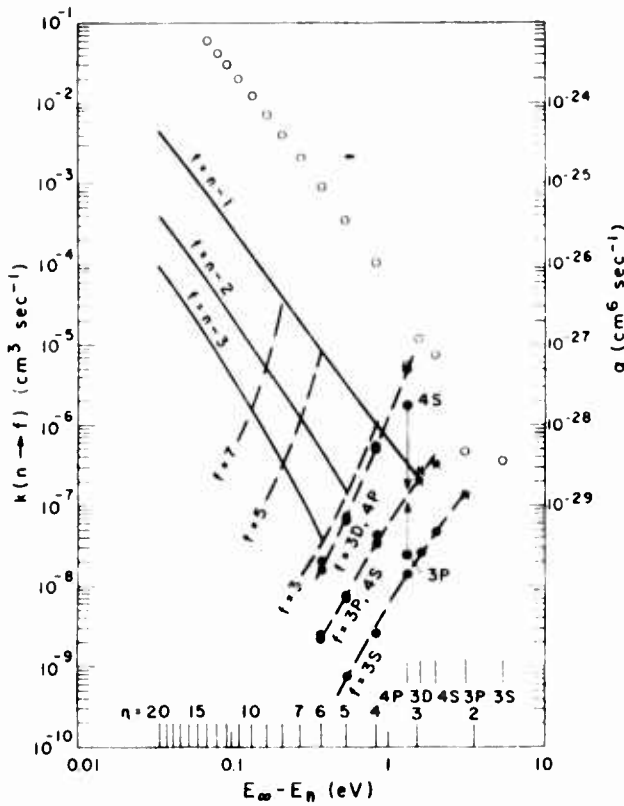


FIG. 8. Deexcitation and inverse ionization rate coefficients used for various states of Na for $T_e = 0.38$ eV. Excited states above Na(4p) are replaced by hydrogenic equivalents. The sources of these values are discussed in Appendix B.

$$\frac{[\text{Na}(3p)]}{3([\text{Na}]_0 - n_e)} = \exp[-E(3p)/kT_c] \\ = [\exp(-E_i/kT_c)]^{2.1 \text{ eV}/5.14 \text{ eV}}. \quad (11)$$

When Eq. (11) is substituted into the expression for the net gain, i.e., $G = \sigma_s [\text{Na}(3p)] - \sigma_a [\text{Na}(3s)]$, we obtain the relation

$$\frac{G}{\sigma_i} = [\text{Na}]_0(1-\chi) \left(\frac{B_i^{2a}}{(1-\chi)^a} - \frac{\sigma_a}{\sigma_i} \right), \quad (12)$$

where $\chi = n_e / [\text{Na}]_0$, $B = 3[\text{Na}]_0^{\alpha} [(2\pi m k T_e / h^2)^{1/2} \times (1 + [\text{Xe}] K_{eq})]^{-1}$, and $\alpha = 2.1/5.14 = 0.41$. Since B varies slowly with T_e , most of the variation in gain with electron temperature has been absorbed into the variation with electron density. We therefore maximize the gain in Eq. (12) with respect to electron density at constant B to obtain the maximum gain values shown in Fig. 7. Note that n_e is a controllable experimental parameter determined primarily by the discharge current density. At high radiative fluxes the Na(3p) and Na(3s) densities are no longer in equilibrium and one must use a more detailed model, such as that of Sec. III.

Figure 7 indicates that very large gain coefficients might be achieved at higher Na densities than those investigated in Ref. 3 (10^{15} - 10^{16} cm $^{-3}$). However, two major problems with the higher density regime are the rapid gas heating and the low discharge impedance. Using the relations given in Sec. IV for the energy dissipation and the conditions given in Fig. 7 for an optical gain of 0.02 cm $^{-1}$, we calculate rates of rise of gas temperature of about 2000 K/ μ sec. The corresponding discharge resistivity is 0.07 Ω cm. Because of the

unexplained excess energy losses in the experimental discharges³ discussed in Sec. IV, the actual rate of rise of gas temperature and the discharge impedance could be significantly larger than these values. Thus, while the gain and excitation temperature are very favorable at

$n_e \approx [Na] \approx 10^{17} \text{ cm}^{-3}$, the power dissipation would limit the discharge pulse length to about 100 nsec. Of course, this is just a statement of a universal problem: any device with an efficiency ϵ for laser power extraction and an allowable gas heating of ΔT will be limited to pulse energy densities of $c_p N \Delta T$ and extracted energy densities of $\epsilon c_p N \Delta T$, where c_p is the specific heat and N is the density of the gas.

The Tl doped-Xe experiment in Ref. 3(b) indicated that $[Tl^+]$ and the higher $[Tl^{*}]$ are below the Saha or equilibrium values at T_e [see Ref. 3(b), Fig. 8]. According to our model this indicates that $K_{eq}^{+} [Xe] > 1$ for $TlXe^+$. This reduction of $[Tl^+]$ below the Saha value by a factor $F < 1$ can be accounted for in Eqs. (1) and (7)–(11) by multiplying the right side of Eq. (1) by F . The quantity $(1 + K_{eq}^{+} [Xe])$ in Eqs. (9), (10), and (12) is then multiplied by F . In Sec. III we tested for the effect of such an increase in K_{eq}^{+} by increasing that for $NaXe^+$ by a factor of 10–20. Some reduction in $F(1 + K_{eq}^{+})[Xe])$ did occur, but the consequence in Eq. (12) was less than 50% reduction in the gain shown in Fig. 7. This is in part because increasing K_{eq}^{+} increased the effective dissociative recombination rate and thereby decreased F . Thus the optimum gain appears to be almost independent of the size of K_{eq}^{+} , although the energy dissipated in the ionization-recombination loop is directly proportional to K_{eq}^{+} .

VI. CONCLUSIONS

We have modeled a very high power density electric discharge in a nonequilibrated vapor consisting of low ionization-potentials atoms (Na or Tl) doped into a high ionization-potential atomic gas (Xe). It was necessary to include a large number of excited-state species, plus several ion and molecular species. At the lower T_e considered, the principal mechanism controlling the discharge impedance is multistep ionization from a state of principal quantum number n_R , followed by molecular ion formation and dissociative recombination back to n_R . Comparison to Tl excited-state densities in a Tl-doped Xe discharge indicates that n_R values as low as 3 occur for this case. In the Na-Xe discharge case it is not possible to infer n_R because the small K_{eq}^+ causes relatively small departures from Saha densities at T_e . In the Na case the measured discharge power typically exceeds that in the model by a factor of 4. Electron-Xe elastic recoil, Na_2^+ dissociative recombination, radiation, quenching of excited Na and NaXe states, and rotational and vibrational excitation of NaXe^* were considered. As yet we have no explanation for this extra power dissipation.

At the $T_e > 0.5$ eV appropriate for NaXe excimer laser operation, the densities of n_e and all Na states are very nearly in Saha equilibrium at T_e , regardless of n_R . Reasonable gain coefficients and efficiencies can be obtained at high $[Na]_0$ under these circumstances, e.g., for $[Na]_0 = 2.7 \times 10^{17} \text{ cm}^{-3}$ and $[Xe] = 2.7 \times 10^{20} \text{ cm}^{-3}$ a maximum gain of 0.03 cm^{-1} and delivered power of 10 MW/cm^3 at an incident radiative flux of 350 MW/cm^2 and an electron density of 10^{17} cm^{-3} . A 10

cm length of such a medium could readily yield a self-excited oscillator, although the power buildup e-folding time of ~ 1 nsec in this low-gain medium must be considered. This conclusion does not depend on an understanding of all the energy-loss mechanisms in the discharge, but the efficiency does. The calculated maximum efficiencies of $\sim 60\%$ are probably at least a factor of 3 too high, but as we have not identified the dominant energy-loss mechanism or its dependence on n_e and T_e , we cannot reliably estimate the efficiency. The scaling of this gain and power output with $[Na]_0$ and other parameters allows predictions of operating conditions for maximum gain to be made rather simply.

By considering the case of a large K_{eq} value and dissociative recombination of Na_2^+ to product $Na(3p)$ atoms, we have identified an interesting sort of phase transition in which n_e decreases and $[Na]$ increase by about an order of magnitude at a critical laser power. In addition to raising the discharge impedance, this lower n_e condition would probably yield higher efficiency in a real case since experimental data indicate that the unknown energy-loss mechanism scales as a fairly high power of n_e . These results point to the desirability of finding a metal species M with relatively strong $M-Xe^+$ binding for which the dimer ion dissociatively recombines into a strongly-bound excited atom and a ground state atom.

ACKNOWLEDGMENTS

This work was supported by the Advanced Research Projects Agency through the Office of Naval Research (Contract N00014-76-C0123) and the Air Force Weapons Laboratory (Agreement 78-036). Initial phases were supported by the Energy Research and Development Administration under Agreement EA-77-A-01-6010. We wish to thank W.L. Morgan, G. Victor, and L. Vriens for valuable suggestions.

APPENDIX A: RATE COEFFICIENTS

The superelastic electron Na collision rate coefficients in our model are given Fig. 8 for $T_e = 0.38$ eV. Only the superelastic (deexcitation) rate coefficients are shown since they increase slowly with increasing T_e , typically by a factor of ~ 1.5 from $T_e = 0.3-0.6$ eV, and the reverse (excitation) rate coefficients are related by detailed balance. The solid lines in Fig. 8 are rate coefficients from Ref. 18 for hydrogenic $n \rightarrow f$ transitions; these have been used for transitions between the $n = 4-15$ states. Dashed lines indicate $k(n \rightarrow f)$ for a constant final state f . The rate coefficients for transitions between these $n = 4-15$ states and the five Na states are indicated as solid circles and are connected by dashed lines corresponding to a common lower state. Note that the $k(n \rightarrow f)$ summed over $f = 3d$ and $4p$ add up to the hydrogenic $k(n \rightarrow 3)$, and that the $3d$ and $4p$ states are energetically close to $n = 3$. We have applied similar effective quantum number and statistical weight arguments to hydrogenic cross sections to obtain the $k(n \rightarrow f)$ where $f = 3s, 3p$, and $4s$ for $n > 4$. Rate coefficients for the $3p \rightarrow 3s$, $3d \rightarrow 3p$, $3d \rightarrow 4s$, and $4s \rightarrow 3p$ transitions (* points in Fig. 8) are most easily obtained by passing a typical deexcitation cross-section en-

ergy dependence through the calculated points of Ref. 19. The remaining $k(n \rightarrow f)$ for the five Na levels (solid points in Fig. 8) are then obtained by connecting the * points to the hydrogenic $k(n \rightarrow n^*)$ points, as indicated by the dashed lines in Fig. 8. The exceptions to this are the $4p \rightarrow 4s$ case, which is a large allowed cross section, and the $4p \rightarrow 3p$ case, which is optically forbidden and taken much smaller. Note that the resulting pattern of rate coefficients is quite systematic, and that $k(3d \rightarrow 3p)$ inferred from Ref. 15 is consistent with the hydrogenic $k(3 \rightarrow 2)$.

The rate coefficients $\alpha(n)$ for inverse ionization [$2e + Na^+ \rightarrow e + Na(n)$] are plotted as open circles versus n in Fig. 8 for $T_e = 0.38$ eV. For $n = 4-13$ these $\alpha(n)$ are from Ref. 18; they decrease by $\sim 25\%$ at $T_e = 0.52$ eV. The assumed rate coefficients for $n = 4p, 3d, 4s, 3p$, and $3s$ are also indicated in Fig. 8. The calculations of Sec. III show that the rates of excited atom ionization via this single step process are slow compared to the rates of ionization by the multistep processes, i.e., by ladder climbing.

The momentum transfer cross section for electrons in Xe used to calculate the electron mobility and the energy loss by elastic recoil are taken from analyses of electron transport data.²⁷ Momentum transfer in electron collisions with Na is an insignificant energy-loss mechanism in the discharge. Such collisions lower the electron mobility by less than 10% for $[Na]/[Xe] < 10^{-3}$. Because of the Rainsauer minimum in the electron-Xe momentum transfer cross section,²⁷ electron-positive ion collisions²⁹ become important for $n_e/[Xe]$ values greater than about 10^{-4} . Thus, for $n_e/[Xe] = 10^{-4}$ at $T_e = 0.4$ eV, the mobility is reduced and the elastic recoil energy loss is increased by about 30% relative to the values in the absence of electron-ion collisions.

The Na_2 excited states are greatly simplified; we use an A' state that is an admixture of $A' \Sigma_u^+ + a^3\Pi_u$ in a $1 : 6$ statistical ratio¹³ and neglect the other excited states. The rate coefficients for $e + Na_2(A') \rightarrow e + Na_2(X^1\Sigma)$ are taken equal to the $e + Na(3p) \rightarrow e + Na(3s)$ rate coefficient. The dissociation rate coefficients $e + Na_2(X^1\Sigma) \rightarrow 2Na(3s) + e$ and $e + Na_2(A') \rightarrow Na(3s) + Na(3p) + e$ are taken as 8.3×10^{-8} and $1.6 \times 10^{-7} \text{ cm}^3 \text{ sec}^{-1}$, respectively; the reverse processes are neglected. The first rate coefficient is obtained by scaling H_2 X -state data by ΔE^{-2} , where ΔE is the threshold dissociation energy; the second is a rough estimate.

The necessary electron-ion rate coefficients for dissociative recombination and rotational-vibrational heating have not been measured. Based on Refs. 15, 21, and 22 we have generally used $k = 2 \times 10^{-7} (0.026/T_e)^{1/2} \text{ cm}^3 \text{ sec}^{-1}$ for $e + Na_2^+ \rightarrow Na^*(n_R) + Na$ and $k = 0$ for $e + NaXe^+ \rightarrow Na^*(n_R) + Xe$. Any different rate coefficients are noted in the text. The rate coefficients for vibrational and rotational excitation of $NaXe^+$ by electrons are discussed in Appendix B.

All heavy particle collisions are assumed to be characterized by the gas temperature T . The most important heavy-particle rate coefficient is the ion exchange reaction $NaXe^+ + Na \rightarrow Na_2^+ + Xe^- + 0.7 \text{ eV}$, for which we normally use about one-half the Langevin rate coefficient³⁰ for Na, i.e., $10^{-9} \text{ cm}^3 \text{ sec}^{-1}$. The factor of 1/2 accounts for the probability that Na^+ and Na interact in the attractive rather than the

repulsive Na_2^+ state. The reverse reaction is assumed negligible due to the ~ 0.7 -eV exothermicity and rapid depletion of Na_2^+ by dissociative recombination. The effects of possible vibration excitation of the Na_2^+ are neglected since they are unknown. For the reactions $\text{Na}^+ + 2 \text{Xe} \rightarrow \text{NaXe}^+ + \text{Xe}$ $+ 0.3$ eV, we use $3 \times 10^{-31} \text{ cm}^6 \text{ sec}^{-1}$. For the reverse dissociation reaction we have used $1.2 \times 10^{-12} \text{ cm}^3 \text{ sec}^{-1}$ for the $[\text{Na}]_0 = 6.3 \times 10^{15} \text{ cm}^{-3}$ (lower T) case and about one-half that value for the $[\text{Na}]_0 = 3.5 \times 10^{16} \text{ cm}^{-3}$ (higher T) case. These dissociation rates yield K_{eq}^+ of ~ 10 times the actual NaXe^+ value. We use $k_d = 2 \times 10^{-14} \text{ cm}^3 \text{ sec}^{-1}$ and $k_f = 10^{-31} \text{ cm}^6 \text{ sec}^{-1}$ for $2\text{Na}(3s) + \text{Xe} \rightleftharpoons \text{Na}_2(X) + \text{Xe}$, and we use $k_d = 3 \times 10^{-15} \text{ cm}^3 \text{ sec}^{-1}$ and $k_f = 10^{-30} \text{ cm}^6 \text{ sec}^{-1}$ for $\text{Na}(3s) + \text{Na}(3p) + \text{Xe} \rightleftharpoons \text{Na}_2(A') + \text{Xe}$. These rate coefficients are for $T = 760$ K. Since our calculations and the simple model²⁰ show that the departure of $[\text{Na}^*/g^*]B$ from the Saha equilibrium value is proportional to $k_a K_{eq}^+$, an error in our value of K_{eq}^+ would require a corresponding change in the value of k_a derived from the experiment in Sec. III A. In view of the uncertainty in the binding energy and structure of NaXe^+ , we estimate the uncertainty in our value of K_{eq}^+ , and therefore of k_a , to be a factor of 2.

The Xe metastable (Xe^*) quenching rate coefficient by electrons is not very important but is taken as $1 \times 10^{-9} \text{ cm}^3 \text{ sec}^{-1}$. Penning ionization in $\text{Xe}^* + \text{Na}$ and $\text{Xe}^* - \text{Xe}^*$ collisions, $e + \text{Xe}^* \rightleftharpoons \text{Xe}^- + 2e$, and $\text{Xe}^* + \text{Xe}$ quenching are included in the calculation, but as Xe^* is a minor constituent these are not significant processes.

A number of tests have been made of the effects of changes in the excited state model. For example, a model utilizing all Na excited states with energies up to that of the 8s level was used to show that the use of a hydrogenic model beginning at $n = 4$ gives a good representation of the overall excited state population distribution. This test is most sensitive to states with ionization potentials greater than about the electron temperature, i.e., to states in the "bottleneck" region of collisional-radiative recombination theory.²⁰ This calculation demonstrated that the principal net flow is from the state(s) produced by dissociative recombination to nearby states of large angular momentum and then via these nearly hydrogenic levels to Na^+ . In a second test, made under the conditions of the upper curve for $T_e = 0.52$ eV in Fig. 3, electron excitation and deexcitation rate coefficients for states with $n > 4$ for which $|\Delta n| > 1$ were set equal to zero. Although some of the excited state densities (with $n \sim 5$) change by almost a factor of 2, the resultant electron, ion, and lower excited state densities changed by less than 10% for this case of a large flow of excitation up the excited state ladder. Although further tests are desirable, the success of this $\Delta n = \pm 1$ model of excited state behavior encourages us to proceed with simple models of metal vapor-rare gas discharges.²⁰

APPENDIX B: ENERGY LOSS PROCESSES

In this appendix we estimate some of the energy loss rate coefficients and rates of energy loss discussed in Sec. IV. We are particularly interested in energy loss resulting from collisions between electrons and ions since Eq. (6) shows that such processes lead to a positive volt-ampere characteristic,

such as is observed experimentally. The contribution of Na_2^+ dissociative recombination to the energy dissipation is discussed in Sec. IV. Two other processes for which we are able to make estimates are the excitation of rotation and vibrational levels of the NaXe^+ molecule. Finally, we will make rough estimates of the effects of electron collisions which excite and deexcite the highly excited states of NaXe^+ and of electron collisions which dissociate Na_2 .

According to Boikova and Obeydkov,³¹ the cross section for rotational excitation of a polar molecule in the Coulomb-Born approximation is

$$\frac{\sigma(J, J+1)}{\pi a_0^2} = \frac{4(J+1)}{3(2J+1)} D^2 \frac{Ry}{\Delta\epsilon_J} \sigma_0 \left(\frac{\Delta\epsilon_J}{2Ry}, \frac{\epsilon}{\Delta\epsilon_J} \right). \quad (\text{B1})$$

Here a_0 is the Bohr radius, D is the dipole moment of the molecular ion in units of ea_0 , Ry is the Rydberg, $\Delta\epsilon_J = (2J+2)B_0$ is the energy loss in the transition from the J to the $J+1$ rotational state, B_0 is the rotational energy constant, and σ_0 is a function given by Gailitis.³² For $2 < \epsilon/\Delta\epsilon < 10^3$ and $\Delta\epsilon_J/Ry \gg 0$, σ_0 can be approximated to better than 15% by

$$\sigma_0 = 2.65(\Delta\epsilon/\epsilon)^{0.75}. \quad (\text{B2})$$

This is the same power law dependence on the electron energy as that used by Hake and Phelps³³ to approximate the cross section for rotational excitation of a neutral dipole. Using their "continuous" approximation to rotational excitation and assuming a Maxwellian electron energy distribution, we find that the power loss per electron and ion is

$$\frac{P_r}{n_e [\text{NaXe}^+]} = \frac{2.65}{4} \frac{\Gamma(15/8)\Gamma(5/4)}{\Gamma(3/2)} \times \left(\frac{kT_e}{kT_g} \right)^{1/8} \left(\frac{2B_0}{kT_e} \right)^{7/8} \left(\frac{2kT_e}{m} \right)^{1/2} \frac{Ry}{8\pi_0^2 D^2}. \quad (\text{B3})$$

Here the ratio of $2.65/4$ is the ratio of the magnitudes of the high-energy approximation for electron excitation of rotational states of ionic and of neutral molecules with the same dipole moment and B_0 value.

We will estimate the dipole moment of XeNa^+ using theoretical calculations¹² of the equilibrium internuclear separation of various rare-gas alkali ions and assume that the ionic charge is unity and is centered at the Na nucleus. The product of the distance from the center of mass and the unit charge gives $D = 4.7 ea_0$. This model gives a rotational constant of $B_0 = 0.10 \text{ cm}^{-1}$. Substitution of these values along with $kT_e = 0.38 \text{ eV}$, $kT_g = 0.06 \text{ eV}$, and an upper limit of $n_e = [\text{XeNa}^+] = 2 \times 10^{15} \text{ cm}^{-3}$ yields a value of $P_r = 0.4 \text{ kW/cm}^3$. This value is only 2.5% of the measured power input.¹

Boikova and Obeydkov also give formulas for the cross section for the vibrational excitation by electrons of an ion in the harmonic oscillator and Coulomb-Born approximation. The cross section is

$$Q(v, v+1) = \frac{1}{2} \pi a_0^2 \left(\frac{Ry}{\Delta\epsilon} \right)^2 \left(\frac{dD}{dR} \right)^2 \frac{m_e}{\mu} (v+1) \times \sigma_0 \left(\frac{\Delta\epsilon}{2Ry}, \frac{\epsilon}{\Delta\epsilon} \right), \quad (\text{B4})$$

where v is the initial vibrational quantum number, μ is the reduced mass of the molecule, and dD/dR is the rate of change of the dipole moment with internuclear separation and is in units of the electronic charge. In this approximation all excitation thresholds are the same and the rate of power loss due to vibrational excitation can be written as

$$\frac{P_v}{n_e [\text{NaXe}']} \approx \Gamma(\frac{1}{2}) \left(\frac{8kT_e}{\pi m} \right)^{1/2} Q_{01}(kT_e) \left(\frac{T_e - T_k}{T_e} \right), \quad (\text{B5})$$

where $\Delta\epsilon$ is the separation in energy of the vibrational levels and is assumed small compared to kT_e and kT_k . Q_{01} is the cross section for excitation of the $v = 0$ and $v = 1$ transition. We have calculated dD/dR assuming that the charge coincides with the Na nucleus as the internuclear separation changes, i.e., $dD/dR = 0.85 e$. The vibrational spacing of 0.010 eV is obtained by fitting a parabola to the estimated potential energy curve for NaXe' . With these approximations and the experimental conditions of $T_e = 0.38$ eV, $T_k = 0.06$ eV, and $n_e = [\text{NaXe}'] = 2 \times 10^{15} \text{ cm}^{-3}$, we find $P_v = 0.17 \text{ kW/cm}^3$ or about 1% of the measured power input. By using the harmonic oscillator model we effectively assume that the effects of $|\Delta v| > 1$ transitions and of the decrease in vibrational level spacing are small. Note that the absence of NaXe potential energy curves crossing that of the ground state of NaXe' prevents resonance vibrational excitation³⁴ as well as dissociative recombination.

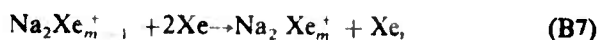
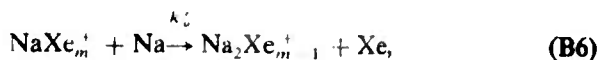
In order to obtain an estimate of an upper limit to the power loss as the result of electron collisional coupling of the excited states of NaXe , we will assume that, contrary to theory,¹⁵ there is no predissociation of these excited states into Xe and excited Na. As in Sec. III we assume that the populations of the $A(^2\Pi)$ molecular state of NaXe and the ground state of NaXe' are in equilibrium with their dissociated atoms. For the sake of simplicity we assume that the excited state populations for NaXe are distributed according to the Boltzmann law at the electron temperature as discussed in Sec. III. If the ionization potential of the $\text{NaXe}(A^2\Sigma)$ state were the same as that of the $\text{Na}(3^2P)$ state, these assumptions would lead to a Boltzmann equilibrium among the excited state of Na at the electron temperature. However, since the estimated ionization potential of $\text{NaXe}(A^2\Sigma)$ is about 0.2 eV smaller than that of $\text{Na}(3^2P)$, this model leads to a circulating flux of excitation down the molecular ladder and up the atomic ladder with a net transfer of energy from the free electrons to the kinetic motion of the gas. An upper limit to the magnitude of this flux is equal to the product of the density of atoms in the $3p$ state and the sum of the rate coefficients for electron excitation of the $3p$ state to higher states and the electron density. This flux times the difference in ionization potentials yields the power loss. For the experimental conditions cited in the preceding calculations of P_v and P_e , the calculated upper limit to the power loss is 0.015 kW/cm^3 or 0.1% of the measured value. Note that according to this model one would expect the integrated intensity of molecular radiation to be comparable with the integrated intensity of atomic radiation and, therefore, to be only a few percent of the discharge power.

Next we note that flux down the molecular ladder followed by rapid predissociation of excited NaXe to

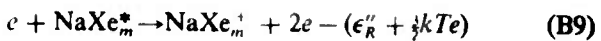
$\text{Na}(n_K) + \text{Xe}$ would have the overall effect of $e + \text{NaXe}' \rightarrow \text{Na}^*(n_K) + \text{Xe}$. This process, which required favorable curve crossings, does not occur for higher excited NaXe but cannot be ruled out for NaXe states with > 1 -eV binding energy.³⁵ The effective recombination coefficient³⁶ for this process would be limited by the rate coefficients for deexcitation of the higher molecular states and would be given by the "collision-radiative" rate coefficient for the predissociating state,²⁰ i.e., roughly $10^{-24} n_e^2 [\text{NaXe}']$. If we associate a 1-eV energy loss with this predissociation we obtain an upper limit to the power loss of 0.7 kW/cm^3 or about 4% of the measured power input for $[\text{NaXe}'] \approx n_e$. If this process were as rapid as assumed here one should have observed significant departures of the normalized populations from the Boltzmann line for Na^* states above $\text{Na}(n_R)$.

The energy loss caused by electron impact dissociation of Na₂ is expected to be limited by the rate of association, e.g., by $2\text{Na} + \text{Xe} \rightarrow \text{Na}_2(X) + \text{Xe}$. Assuming an association rate coefficient of $3 \times 10^{-31} \text{ cm}^3 \text{ sec}^{-1}$, we see that the power loss for our experimental conditions of $[\text{Na}]_0 = 6.3 \times 10^{14} \text{ cm}^{-3}$, $[\text{Xe}] = 4.5 \times 10^{19} \text{ cm}^{-3}$, and $n_e = 2 \times 10^{15} \text{ cm}^{-3}$, is 0.1 kW cm^{-3} and negligible. Similar considerations for dissociation of $\text{NaXe}^* A$ state by $A \rightarrow B$ state excitation yield similar or smaller numbers. Any dissociation of Na_2^+ would compete with dissociative recombination. This rate would also be limited by the ion transfer rate and is expected to yield a comparably small energy loss.

Our model has neglected the possible role of cluster ions, such as the structural forms $\text{Na}_2^+ \text{Xe}_m$ and $\text{Na}^* \text{Xe}_m$ for $m > 1$. Ion-molecule reaction experiments suggest that once a diatomic ion is formed, the cluster ions would rapidly grow to an equilibrium distribution of bound Xe atoms. Since we are unable to observe these ions, we can only speculate as to their role in the dissociative recombination-collisional ionization loop. Thus, the energy loss in the reaction sequence



and



could be several times that deduced from coefficients derived in Sec. III. If reactions (B6)–(B9) were the dominant energy loss loop, then the populations of the highly excited NaXe_m molecules would deviate from their Boltzmann plot more than that shown in Fig. 4 for the atomic states. In this case the non-Boltzmann behavior of the atomic states could be the result of collisional dissociation of excited NaXe , i.e., $\text{NaXe}^* + \text{Xe} \rightarrow \text{Na}(n=6) + 2\text{Xe}$. Here it is not clear why dissociation should not occur more readily for the lower energy but higher density and more weakly bound excited states of NaXe . The maximum increase in energy loss via dissociative recombination for sequence (B6)–(B9) is roughly equal to the increase in $k'_a \epsilon_R''$ over $k_a \epsilon_R'$. Using estimated limiting values of $k'_a = 2.5 \times 10^{-9} \text{ cm}^3 \text{ s}^{-1}$ and $\epsilon_R'' = 2 \text{ eV}$ one predicts a maximum contribution to the energy loss for the

$T_e = 0.38$ -eV case of about 40% of the measured loss and a total predicted energy loss of about one-half the measured value. Note that the addition of these processes points to the possibility of population inversion among the intermediate excited levels of, for example, NaXe.

Finally we note that vibrational excitation of molecular impurities, if present, could make a significant contribution to the rate of energy loss in the experimental discharges. Thus, either about 3% N₂ or 0.02% CO₂ would have a large enough energy exchange collision frequency^{33,37} ν_v to account for the observed discrepancy.³ Such large concentrations of molecular impurities appear very unlikely in view of the gas purification procedure used. Also, if N₂ were present at the 3% level we would expect quenching³⁸ by N₂ to produce a significant depression of the [Na(3p)]/[Na(3s)] ratio below the level set by the electron temperature. The 0.02% CO₂ would not cause significant quenching of Na(3p).

³⁴A.V. Phelps, Joint Institute for Laboratory Astrophysics, Report No. 110, University of Colorado, Boulder, Colorado, 1972; A. Gallagher, in *Topics in Applied Physics*, edited by Ch K. Rhodes (Springer, Berlin, 1979), Vol. 30, pp. 135-174.

³⁵See for example, R.C. Sze and T.R. Lorec, *IEEE J. Quantum. Electron. QE-14*, 944 (1978); C.J. Schmidtschek and J.E. Celio, *Optics Lett.* **2**, 64 (1978).

³⁶H. Rothwell, D. Leep, and A. Gallagher, *J. Appl. Phys.* **4**, 4396 (1978).

³⁷L.W. Schuman, D.W. Wildman, and A. Gallagher (unpublished).

³⁸L.A. Schlie, *J. Appl. Phys.* **47**, 1397 (1976).

³⁹R.A. Hamil, D.L. Drummond, L.A. Schlie, and R.P. Benedict, *J. Appl. Phys.* **50**, 637 (1979).

⁴⁰For recent discussions of excited state effects in laser discharges see B.N. Srivastava, J.H. Jacob, J.A. Mangan, and R. Rokni, *Appl. Phys. Lett.* **32**, 705 (1978); W.L. Nighan, *IEEE Quantum Electron. QE-4*, 464 (1978).

⁴¹J.J. de Groot, J.A.J.M. Van Vliet, and J.H. Waszink, *Philips Tech. Rev.* **35**, 334 (1975); J.F. Waymouth, *Electric Discharge Lamps* (MIT, Cambridge, Mass., 1971).

⁴²W.F. Hug, C.M. Hains, and C.J. Marlett, *J. Opt. Soc. Am.* **68**, 62 (1978).

⁴³R. Shuker, A.V. Phelps, and A.C. Gallagher, in *Electronics Transition Lasers II*, edited by L.E. Wilson, S.N. Suchard, and J.I. Steinfeld (MIT, Cambridge, Mass., 1977), p. 208. For details see Final Report for ERDA Contract No. E(49-1)-3800, February, 1977 (unpublished).

⁴⁴G. York, R. Scheps, and A. Gallagher, *J. Chem. Phys.* **63**, 1052 (1975). The conditions in Fig. 11 are [Xe] = 2×10^{20} cm⁻³, [Na(3s)] = 10^{17} cm⁻³, [Na(3p)] = 5×10^{15} cm⁻³, $T_e = 810$ K.

⁴⁵A.C. Tam, C. Moe, B.R. Bulos, and W. Happer, *Opt. Commun.* **16**, 376 (1976); A.C. Tam, T. Yabuzaki, S.M. Curry, and W. Happer, *Phys. Rev. A* **18**, 196 (1978).

⁴⁶The NaXe' potential is estimated from the following references: T.R. Powers and R.J. Cross, Jr., *J. Chem. Phys.* **58**, 626 (1973); F.E. Budenholzer, E.A. Gisason, and A.D. Jorgensen, *J. Chem. Phys.* **66**, 4832

(1977); F.A. Gianturco, *J. Chem. Phys.* **64**, 1973 (1976); Y.S. Kim and R.G. Gordou, *J. Chem. Phys.* **61**, 1 (1974). Rate coefficients for the formation and dissociation of the similar molecule KAr' have been measured by G.E. Keller, R.A. Beyer, and L.M. Colonna-Romano, *Phys. Rev. A* **8**, 1446 (1973).

⁴⁷G. York and Gallagher, 114, Joint Institute for Laboratory Astrophysics, Report No. 114 University of Colorado, Boulder, Colorado, 1974. For laser operation on the *B-X* band of Na, see B. Welleghausen, S. Shahdin, D. Friede, and H. Wellig, *Appl. Phys.* **13**, 97 (1977).

⁴⁸J.N. Burdsey, B.R. Junker, and D.W. Norcross, *Chem. Phys. Lett.* **37**, 502 (1976).

⁴⁹M.A. Biondi (private communication). For a concurrent recognition of the absence of dissociative recombination for asymmetry diatomic molecules such as HeH', see M.I. Chibisov and S.I. Yakovlenko, *Zh. Eksp. Teor. Fiz.* **73**, 43 (1977) [Sov. Phys. JETP **46**, 21 (1977)].

⁵⁰D.E. Nitz, P.B. Hogan, L.D. Schearer, and S.J. Smith, *J. Phys. B* **12**, L103 (1979); T. Uzer and A. Dalgarno (unpublished).

⁵¹W.L. Morgan and A.V. Phelps (private communication). See also L. Vriens and F.A.S. Lighthart, *Philips Res. Rep.* **32**, 1 (1977).

⁵²L.C. Johnson, *Astrophys. J.* **174**, 227 (1972).

⁵³D.L. Moores, D.W. Norcross, and V.B. Sheorey, *J. Phys. B* **7**, 371 (1974). See also, D.F. Korf, S. Chung, and C.C. Lin, *Phys. Rev. A* **7**, 545 (1973).

⁵⁴A.V. Phelps, D. Leep, and A. Gallagher, *Bull. Am. Phys. Soc.* **23**, 141 (1978). For discussions of simplified models of electron-excited state processes in low density gases see, for example, D.R. Bates, *Proc. R. Soc. London Ser. A* **337**, 15 (1974) and L.M. Biberman, V.S. Vorob'ev, and I.T. Yakubov, *Usp. Fiz. Nauk.* **107**, 353 (1972) [Sov. Phys. Usp. **15**, 375 (1973)].

⁵⁵J.N. Burdsey and M.A. Biondi, *Adv. At. Mol. Phys.* **6**, 1 (1970).

⁵⁶Y. Shiu, M.A. Biondi, and D.P. Sipler, *Phys. Rev. A* **15**, 494 (1977).

⁵⁷Y.-T. Lee and B.H. Mahan, *J. Chem. Phys.* **42**, 2893 (1965). See also A. Klucharev, V. Sepman, and S. Vajnovic, *J. Phys. B* **10**, 715 (1972).

⁵⁸M.R. Flannery, *Ann. Phys. Leipzig* **61**, 465 (1970).

⁵⁹T.F. Gallagher and W.E. Cooke, *Phys. Rev. A* **19**, 2161 (1979).

⁶⁰A.C. Hindmarsh, Lawrence Livermore Laboratory Report No. UCID-30001 (1972).

⁶¹L.S. Frost and A.V. Phelps, *Phys. Rev. A* **136**, 1538 (1964).

⁶²S. Geltman, *J. Quant. Spectrosc. Radiat. Transfer* **13**, 601 (1978).

⁶³G.S. Argyropoulos and M.A. Casteel, *J. Appl. Phys.* **41**, 4162 (1970).

⁶⁴E.W. McDaniel, *Collision Phenomena in Ionized Gases* (Wiley, New York, 1964), Chaps. 3 and 6.

⁶⁵R.F. Boikova and V.D. Obeydkov, *Zh. Eksp. Teor. Fiz.* **54**, 1439 (1968) [Sov. Phys. JETP **27**, 772 (1968)]. See also S.-I. Chu and A. Dalgarno, *Phys. Rev. A* **10**, 788 (1974); A.S. Dickinson and J.M. Munoz, *J. Phys. B* **10**, 3151 (1977).

⁶⁶M.K. Gailitis, *Atomic Collisions* (AN Latv SSR, Riga, 1963), p. 93.

⁶⁷R.D. Hake, Jr. and A.V. Phelps, *Phys. Rev.* **158**, 70 (1967). See footnote 58 of this reference.

⁶⁸G.J. Schulz, *Rev. Mod. Phys.* **45**, 423 (1973).

⁶⁹J. Pascale and J. Vandéplanque, *J. Chem. Phys.* **60**, 2278 (1974).

⁷⁰C.B. Collins, *Phys. Rev.* **140**, A1850 (1965).

⁷¹A.G. Engelhardt, A.V. Phelps, and C.G. Risk, *Phys. Rev.* **135**, A1566 (1964).

⁷²J.R. Barker and R.E. Weston, Jr., *J. Chem. Phys.* **65**, 1427 (1976).

Emission of Mg-Xe discharge and the MgXe excimer band

L. Schumann, D. Wildman, and A. Gallagher^{a)}

Joint Institute for Laboratory Astrophysics, University of Colorado and National Bureau of Standards,
Boulder, Colorado 80309

(Received 28 December 1979; accepted 15 February 1980)

The emission intensities and excited state densities of a Mg-doped high-pressure Xe discharge are reported. The normalized emission of the MgXe excimer band associated with the Mg $3^1P_1-3^1S_0$ resonance transition is obtained from the data, as well as a 320–380 nm band attributed to XeMg⁺. The Mg, A-X band is not seen in emission under any discharge conditions in Mg doped Xe or Ne. This Mg-Xe mixture does not appear to be a reasonable candidate for a discharge-excited excimer laser due to the large excitation energies associated with the Mg and Mg⁺ resonance transitions.

Discharges in metal-doped inert gases are of interest in lighting¹ and laser applications,^{2,3} as well as for studies of discharge characteristics and of metal-inert-gas interactions. They are particularly well suited to optical diagnostics, since they radiate profusely in the visible. In the case of Mg, the strong lines and bands of the ion as well as the neutral are in the visible and near UV, providing an unusual amount of information. The particular choice of Xe in the present experiments results from our interest in the excimer bands for possible excimer lasers; the Xe induced bands are generally the best candidates.³ Also with this application in mind, we have studied pulsed, high power discharges in high pressure Xe, typically at 1–5 atm.

We have measured the emission from the positive column of the discharge with calibrated detectors, and the densities of various Mg, Mg⁺, and Xe excited states are obtained from atomic line intensities. We have also measured the electric field in the positive column, for use in comparing to discharge models. The MgXe excimer band associated with the $3^1P_1-3^1S_0$ transition in Mg dominates in the UV, and the normalized emission of the band, per Mg(3^1P_1) and Xe density, is obtained from the data. Another strong band is observed in the UV region of the spectrum at high discharge currents, when the Mg⁺ density is comparable to the Mg density. We believe this band is due to the transition from the ground to first excited state of XeMg⁺, i.e., the XeMg⁺ states associated with the 3^2S and 3^2P states of Mg⁺.

The discharges reported here are in a Xe density [Xe] of $2.5 \times 10^{19} \text{ cm}^{-3}$ and in magnesium densities [Mg] of $10^{14}-10^{16} \text{ cm}^{-3}$. Stable, steady-state pulsed discharges of several microseconds duration and 1–20 A current and cw discharges of a few milliamperes have been operated in an apparatus that has been described previously.⁴ Figure 1 shows a pulsed, high-current magnesium–xenon discharge spectrum (upper spectrum) in $[\text{Mg}] \approx 10^{16} \text{ cm}^{-3}$ with most of the lines identified. As described below, the excitation temperature is ~0.48 eV for this discharge. The bands centered at 480, 517.5, and 555 nm have been identified by their rotational structure as due to MgH(A $1\Pi^2-X^2\Sigma^+$) with $v', v''=1, 0; 0, 0$;

and 0, 1 respectively.⁵ Estimates indicate that the ground state MgH density (due to impurities) necessary to produce the observed emission intensity is about $10^{12}/\text{cm}^3$. The lower, incomplete spectrum in Fig. 1 is for similar Mg and Xe densities but for a much smaller discharge current that yields a much lower excitation temperature, as described below. Under these conditions the excimer band, connected with the lowest strongly radiating state of Mg, is expected to dominate the spectrum. Thus we identify the 285–375 nm continuum band in this spectrum as originating from the $3^1P_1-3^1S_0$ (285.3 nm) resonance transition in Mg. Essentially identical MgXe excimer band shapes are observed in the 280–375 nm region for a range of low excitation temperatures, verifying the identification and that the band shape is accurately represented by the lower spectrum in Fig. 1 after the 309.3 and 333.2 nm lines from higher states are removed.

The dashed line in the high-current spectrum of Fig. 1 indicates the continuation of the MgXe excimer band, which dominates in the 280–300 nm region, to longer wavelengths in accordance with band shape in the low-current data. The additional intensity in the 300–380 nm region of the high-current spectrum is attributed to the XeMg⁺ band associated with the Mg⁺ resonance transitions (3^2P-3^2S) at 280 nm. The regular structure in this band is characteristic of bound-bound bands of heavy diatomic molecules.⁶ This identification is in part due to the absence of this band from discharges in similar Mg densities with a low density of Xe or with $2.5 \times 10^{19} \text{ cm}^{-3}$ of Ne. Also, this band increased with increasing Mg⁺ density [Mg⁺], e.g., in the high current discharge of Fig. 1 $[\text{Mg}^+] \approx 0.1[\text{Mg}]$, whereas in the low-current discharge the excitation temperature is much lower and $[\text{Mg}^+]/[\text{Mg}] \ll 1$. A weaker, structured continuum also occurs in the 435 and 600 nm regions; these may be due to bound-bound MgXe bands associated with the $3^3D-3^3P^0$ and $4^3S-3^3P^0$ transitions in Mg.

A Boltzmann plot of the atomic excited state densities obtained from the line emission intensities and transition probabilities^{7,8} is shown in Fig. 2. The discharge conditions are about the same as for the high-current case in Fig. 1. The densities of the 3^1S_0 , 3^3P , and 4^3S states nearly fit a straight line, corresponding to an electronic excitation temperature of 0.48 eV. The Xe excitation

^{a)}Staff Member, Quantum Physics Division, National Bureau of Standards.

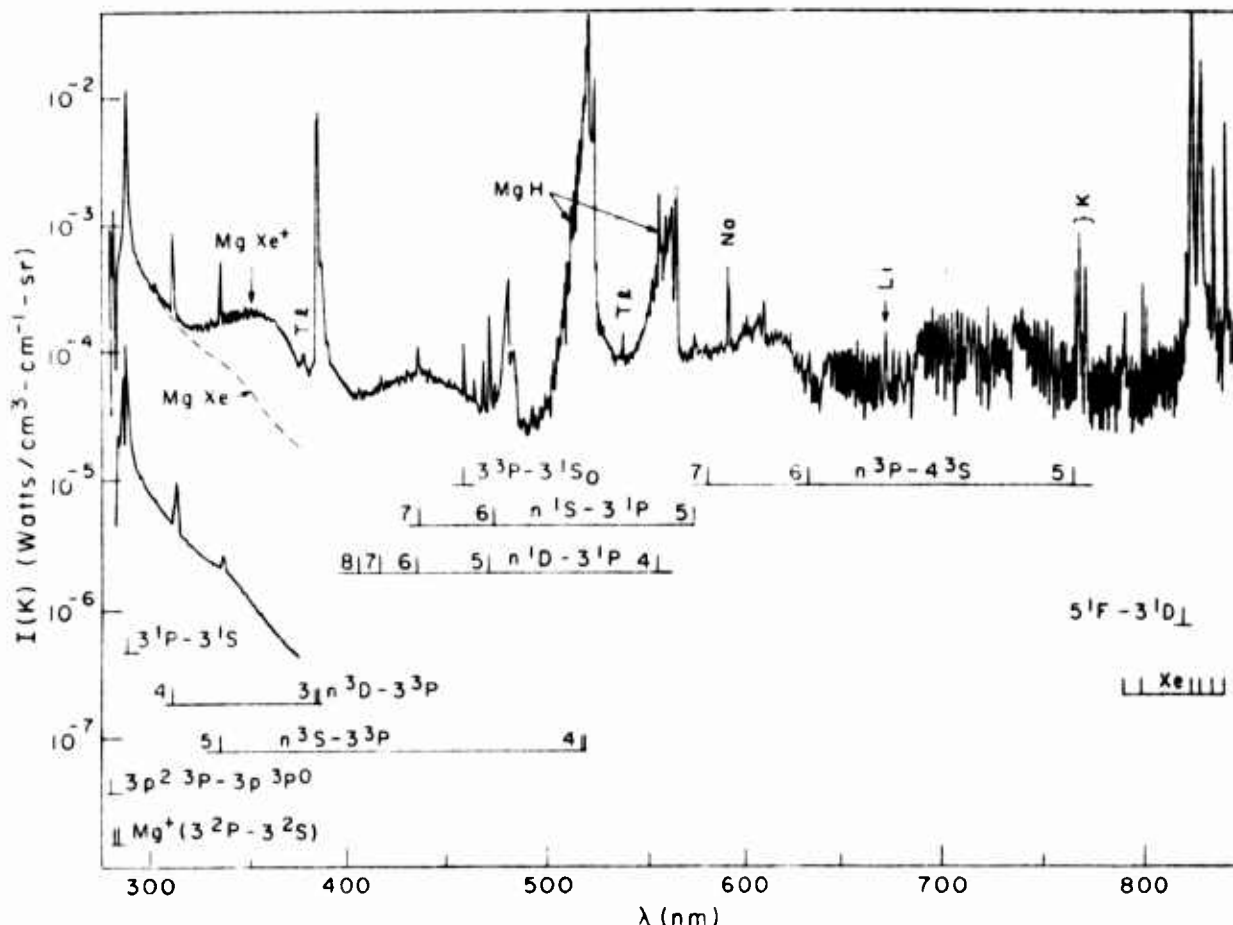


FIG. 1. Magnesium-xenon discharge spectrum for $[Mg] = 7.3 \times 10^{15} \text{ cm}^{-3}$, and $[Xe] = 2.53 \times 10^{19} \text{ cm}^{-3}$. For the upper spectrum $J = 100 \text{ A/cm}^2$, $n_e = 8.4 \times 10^{14} \text{ cm}^{-3}$, $E/N = 6.3 \times 10^{-18} \text{ V cm}^2$. For the lower spectrum $J = 0.05 \text{ A/cm}^2$ and $n_e \approx 10^{11} \text{ cm}^{-3}$.

temperature of about 0.51 eV is obtained from the 800 nm region lines emanating from states near 10 eV. The open square point at the Mg ionization limit is the Mg^*/g^* density obtained from the Saha equation (g =statistical weight)

$$\left(\frac{[\text{Mg}^*]}{g^*}\right)_{\text{limit}} = \frac{[\text{Mg}^*]}{g^*} \frac{n_e}{g_a} \left(\frac{2\pi n k T}{h^2}\right)^{3/2}, \quad (1)$$

with $[Mg^*] = n_e$ and $n_e = 8.5 \times 10^{14}/cm^3$ obtained from measured current density and electron mobilities in Xe.⁹ Since an unknown amount of $XeMg^*$ and Mg_2^+ may occur, this $[Mg^*] = n_e$ case is actually an upper limit to $[Mg^*]$. Another value for $[Mg^*]$ can be obtained from the intensities of the $Mg^* 3^2P-3^2S$ lines at 279.6 and 280.3 nm. After correcting for self-absorption these yield the $Mg^* 3^2P$ state densities and assuming the ~ 0.48 eV electron temperature also fixes the ratio of $Mg^*(3^2P)$ to $Mg^*(3^2S)$ densities, this yields $[Mg^*]$. These ion densities are plotted as open circles at the equivalent neutral density given by the Saha relation;

$$\left(\frac{\text{Mg}^*(i)}{g_i} \right)_{\text{plotted}} = \left(\frac{\text{Mg}^*(i)}{g_i} \right)_{\text{measured}} \cdot \frac{n_e}{g_e} \left(\frac{2\pi m k T}{h^2} \right)^{-3/2} . \quad (2)$$

The self-absorption correction, for this case of optical depth ~ 15 at the center of the $P_{3/2}$ line, raises

$[\text{Mg}^*(3P_{3/2})]$ by about a factor of 4 relative to what would be obtained by assuming the line is optically thin. This correction,¹⁰ which depends on the unknown Xe broadening of the lines, is uncertain to perhaps a factor of 2, so the resulting $[\text{Mg}^*]$ and $[\text{Mg}(3^2P)^*]$ are equally uncertain. Nonetheless, a major decrease in the actual $[\text{Mg}^*]$ and high $[\text{Mg}^*]$ densities relative to 0.48 eV equilibrium values (an extension of the 0.48 eV line above 5 eV) is unmistakable. This is attributed to¹¹ excited-state quenching by Xe and dissociative recombination of Mg $_2^*$.

Some Mg* densities are also shown in Fig. 2 for a low current, cw discharge in which $j \geq 0.05$ A/cm² and $\mu_e \geq 7 \times 10^{10}$ cm⁻³. Here the 3³P₁ density should be determined by electron collisional excitation and deexcitation, so that its excitation temperature of ~0.32 eV should be representative of the electron temperature. The higher-state densities and the ionization limit point from Eq. (1) are far below an 0.32 eV excitation temperature. This is attributed primarily to radiation and Xe quenching collisions.

For the high-current data in Fig. 2, the fit (within experimental accuracy) of all the Mg excited state densities below 5 eV and the Xe excited states below 10 eV to a single excitation temperature is attributed to electron collision dominated populations,¹¹ with the electron temperature essentially equal to the observed population

temperature. In essence, electron collisional rates are faster than radiative and inelastic gas collisional rates. As a consequence, the Mg 3^1P_1 density can be determined from this ~ 0.48 eV excitation temperature, as indicated by the arrow at the 3^1P_1 energy in Fig. 2. This density has then been used to determine the normalized emission intensity of the excimer band, even though the observed $3^1P_1 - 3^1S_0$ line is severely weakened by self-absorption. Specifically, since the atomic line emission dominates the total emission from Mg(3^1P_1),

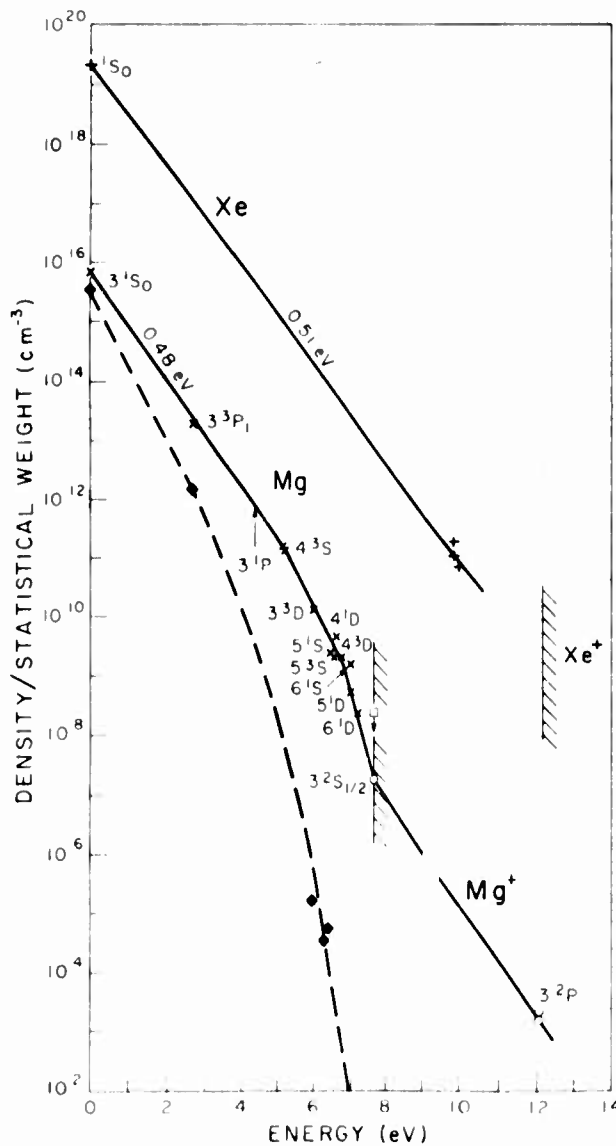


FIG. 2. Upper set of data is a Boltzmann plot of excited state densities for $[Mg]_0 = 7.3 \times 10^{15} / \text{cm}^3$, $[Xe] = 2.4 \times 10^{19} / \text{cm}^3$, $n_e = 8 \times 10^{14} / \text{cm}^3$, $E/N = 6.6 \times 10^{-18} \text{ V cm}^2$, $J = 110 \text{ A/cm}^2$ in the pulsed discharge. The Mg excited state densities obtained from line intensities are indicated by \times , the Mg^* $3^2P_{1/2,3/2}$ densities by \square , and the Xe excited state densities from the 823.2, 828.2, and 840.9 nm lines as $+$. A radiation trapping correction, typically a factor of ~ 4 , has been applied to the Mg^* lines and the Mg 4^3S and 3^3D lines which are optically thick at the line center. The Mg^{*} densities are plotted as equivalent neutral densities, as given by Eq. (2). The lower set of data (dashed line and \dagger) is for $[Mg]_0 = 3.5 \times 10^{15} \text{ cm}^{-3}$, $[Xe] = 1.9 \times 10^{19} \text{ cm}^{-3}$, $n_e = 7 \times 10^{14} \text{ cm}^{-3}$, and $j = 0.05 \text{ A cm}^{-2}$ in a cw discharge. The point at the Mg^* ionization limit corresponding to $[Mg] = n_e$ in Eq. (1) is off the graph at 5 cm^{-3} .

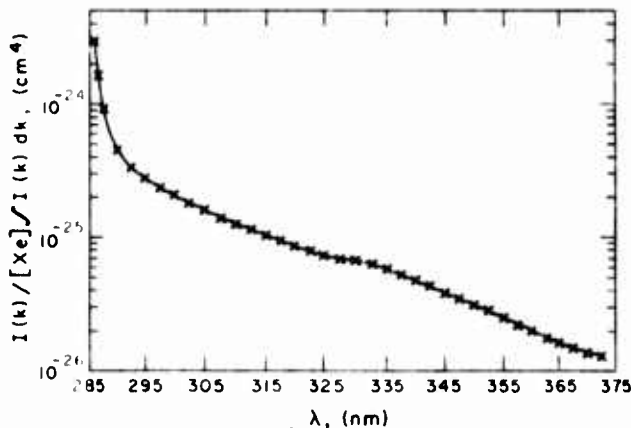


FIG. 3. Normalized excimer band of $Mg(3^1P_1 - 3^1S_0)Xe$ with $[Xe] = 2.41 \times 10^{19} / \text{cm}^3$ and $T = 853^\circ\text{K}$.

$\int I(k) dk$ per steradian across the line is equal, in the absence of self-absorption, to $[Mg(3^1P_1)]A\hbar\nu z/4\pi$, where A is the atomic radiation rate of $4.7 \times 10^8 \text{ sec}^{-1}$, z is the discharge diameter, and $\hbar\nu$ the 285 nm photon energy. The resulting normalized emission spectrum of the MgXe excimer band is shown in Fig. 3. The crosses represent the observed intensity from the low-current discharge in Fig. 1, properly normalized and with overlapping lines removed. The accuracy of the normalization of this band is estimated as about 40%. A direct measurement of the normalized emission at $[Mg] = 10^{13} \text{ cm}^{-3}$, where the resonance-transition line-center optical depth was ~ 10 , yielded a value about three times as large for $I_N(k)$, consistent with the values in Fig. 3 and the expectation¹⁰ of about a $\sqrt{10}$ correction for this much radiation trapping of the resonance transition.

The UV band attributed to $XeMg^*$ is shown in Fig. 4, after averaging through the vibrational structure seen in Fig. 1. It was taken from the upper discharge spectrum in Fig. 1 after subtracting the MgXe($3^1P_1 - 3^1S_0$) radiation (dashed line). This $XeMg^*$ band has been normalized to $\int I(k) dk$ across both of the $Mg^*(3^2P_{1/2,3/2} - 3^2S_{1/2})$ atomic lines after making the correction for radiation trapping described below Eq. (1). As noted

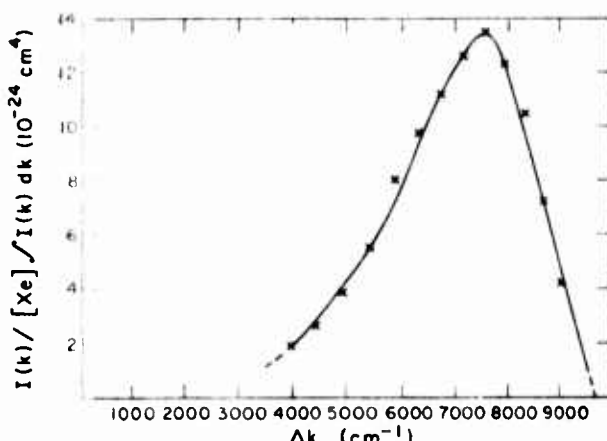


FIG. 4. Normalized excimer band of $Mg^*(3^2P_{1/2,3/2} - 3^2S_{1/2})Xe$ vs the frequency shift in cm^{-1} from the ion resonance lines. $[Xe] = 2.53 \times 10^{19} / \text{cm}^3$ and $T = 853^\circ\text{K}$.

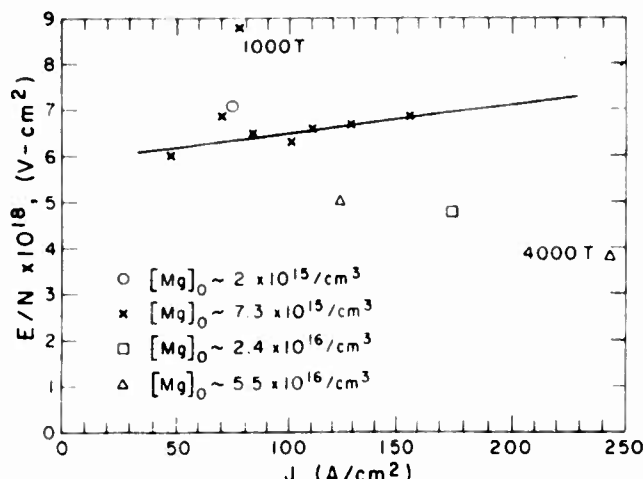


FIG. 5. Electric field E in the positive column divided by $[Xe]$ vs J at different magnesium densities. The Xe pressure is 2000 Torr except for the two points marked 1000 Torr and 4000 Torr.

above, this normalization is uncertain to at least a factor of 2. It is nonetheless useful as it indicates that the magnitude of the equilibrium constant of $XeMg^*(3^2P)$ relative to the $Mg^*(3^2P)$ levels is $\sim 2 \times 10^{-20} \text{ cm}^3$ and the binding is probably about 0.5 eV.

For the purpose of comparison to models, we also include electric field data in Fig. 5.

Because of the large red shifts from the parent atomic line ($\sim 7000 \text{ cm}^{-1}$), the MgXe band is expected to exhibit gain in the discharge. The $XeMg^*$ band will also probably exhibit gain on its long-wavelength side if not everywhere. The maximum possible gain from both bands at 350 nm can be calculated from the fluorescent intensity of the discharge P_s by assuming that there is no absorption ($\text{gain}/\text{cm} = P_s \lambda^3 / 8\pi hc^2$). P_s in our discharge is $2.5 \times 10^{-3} \text{ W/cm}^3 \text{ cm}^{-1}$ at 350 nm, mostly from $XeMg^*$, and this gives a gain of $7.2 \times 10^{-6}/\text{cm}$ for our conditions of $[Xe] = 2.5 \times 10^{19}/\text{cm}^3$, $[Mg^*] = 7 \times 10^{15}/\text{cm}^3$, $T_e = 0.48 \text{ eV}$, $T_i = 853 \text{ K}$, and $J \approx 100 \text{ A/cm}^2$. This is far too

small to be useful, so that much higher $[\text{Mg}]$, $[\text{Mg}^*]$, and $[\text{Xe}]$ are necessary for useful gains. However, if either the magnesium density or the xenon density is increased, the power input must be increased as well or the electron temperature decreases due to the added power going into exciting and ionizing these gases.¹⁰ Since the Mg and Mg^* resonance transitions are more energetic than for the alkalis, the problem of obtaining sufficient excited state density and gain in these resonance transitions is also more severe than for the alkalis.

ACKNOWLEDGMENTS

We wish to thank A. V. Phelps for many valuable discussions and suggestions. This work was supported in part by the Advanced Research Projects Agency of the Department of Defense and was monitored by ONR under Contract No. N00014-76-C-0123.

- ¹J. F. Waymouth, *Electric Discharge Lamps* (MIT, Cambridge, Mass., 1971).
- ²A. V. Phelps, Joint Institute for Laboratory Astrophysics Report 110, 1972 (unpublished).
- ³A. Gallagher, in *Metal Excimers*, Vol. 30 of *Topics in Applied Physics*, edited by C. K. Rhodes (Springer-Verlag, Berlin, 1979), pp. 135-174.
- ⁴H. Rothwell, D. Leep, and A. Gallagher, *J. Appl. Phys.* **49**, 4396 (1978).
- ⁵G. Herzberg, *Spectra of Diatomic Molecules* (Van Nostrand, New York, 1950).
- ⁶L. Lam, A. Gallagher, and M. Hessel, *J. Chem. Phys.* **66**, 3550 (1977).
- ⁷W. L. Wiese, M. W. Smith, and B. M. Miles, *Atomic Transition Probabilities*, NSRDS-NBS 22 (U.S. GPO, Washington, D.C., 1969).
- ⁸G. A. Victor, R. F. Stewart, and C. Laughlin, *Astrophys. J. Suppl.* **31**, 237 (1976).
- ⁹A. V. Phelps (private communication).
- ¹⁰T. Holstein, *Phys. Rev.* **83**, 1159 (1951).
- ¹¹R. Shuker, A. Gallagher, and A. V. Phelps, *J. Appl. Phys.* (in press).

Submitted to Physical Review A

Nonradiative transport of atomic excitation in Na vapor

Arthur G. Zajonc^{a)} and A. V. Phelps^{b)}

Joint Institute for Laboratory Astrophysics

University of Colorado and National Bureau of Standards

Boulder, Colorado 80309

Received: _____

Abstract

Measurements are reported which show the effect of nonradiative losses at a gas/window interface on the backscattered fluorescence intensity for Na vapor at frequencies in the vicinity of the resonance lines near 589 nm. The Na $3P_{1/2,3/2}$ states are excited with a low-intensity, single-mode, tunable dye-laser at high Na densities and the frequency integral of the backscattered fluorescence intensity in the D1 and D2 lines is measured. As the laser is tuned through resonance, the loss of atomic excitation to the window appears as a sharp decrease in the frequency-integrated fluorescence intensity. For example, at 7×10^{20} atoms m^{-3} the fluorescence intensity decreases by a factor of 4 in a frequency interval of 4 GHz. Measured absolute fluorescence intensities versus laser frequency are compared with predictions made using the theory of Hummer and Kunasz which includes both radiative and nonradiative transport processes. The agreement between theory and experiment is remarkably good when one considers that the theory contains only one unknown coefficient, i.e., the reflection coefficient for excited atoms at the windows. In our case the excited atoms are assumed to be completely destroyed at the window.

I. INTRODUCTION

In this paper we report the results of an experimental study of excited state losses in sodium vapor due to collisions of the excited atoms with a boundary. An early experimental study of resonance fluorescence in Hg vapor by Hansen and Webb¹ has been interpreted by Phelps and Chen² as showing that the collisions of excited mercury atoms with the window determine the magnitude of the diffusely emitted fluorescence when the excited atoms are produced close to the window as occurs when the gas density is high and when resonance line excitation is used. Evidence for the deexcitation of excited atoms on collision with the windows has also been obtained from studies of the specular reflection of laser radiation at a glass-sodium vapor interface⁵ and from VUV absorption spectra in high density xenon.⁶ Conflicting results as to the importance of excited atom-window collisions have been obtained using the Hanle-effect.⁷ However, backscattered fluorescence experiments by Heering³ and by Fujimoto and Phelps⁴ using broad band excitation and low resolution measurements of fluorescence showed a relatively small effect caused by nonradiative transport. We show in this paper that using laser excitation allows separation of the effects of radiative and nonradiative transport of resonance radiation in such fluorescence experiments.

The theory of radiative transfer⁸⁻¹⁰ normally applied to the transport of resonance excitation neglects excited atom diffusion, i.e. the motion of the excited atoms is neglected except as it affects the absorption and emission profile through the Doppler effect. Formalisms have recently been developed^{2,11-15} which include the diffusion of excited atoms as a means of nonradiative excited-atom transport. These theories predict an excited-atom population density orders of magnitude smaller near a boundary than do the purely radiative treatments. The present experiments test the ability of these theories to predict the absolute intensities of scattered radiation in

a situation where losses to a boundary are significant. We make a detailed comparison between experimental results and the solution of the transport equations given by Hummer and Kunasz¹² as formulated in the computer program developed by Kunasz and Kunasz for a three-level system.¹³

Section II contains a summary of the recent theoretical treatments of the combined radiative and nonradiative transport of the excitation associated with the resonance states of atoms. In Sec. III we discuss the experimental apparatus while in Sec. IV we present the results of the experiment. The results are compared with theory in Sec. V.

II. THEORY OF EXPERIMENT

The treatments of the transport of low intensity resonance radiation by Kenty,¹⁶ by Holstein⁸ and by Biberman⁹ showed that, although this problem cannot be solved by ordinary diffusion theory, reasonably simple solutions of the transport equation are possible. In these papers atomic motion entered in only through line shape effects and the absorption and emission profiles were assumed to be identical, i.e., complete redistribution of the radiation was assumed to occur at each absorption event. In treating radiative processes ahead of a shockwave, Biberman and Veklenko¹⁷ presented a transport equation which included the mass flow of excited atoms. McIntyre and Fowler attempted to model the effects of the diffusion of excited atoms and incomplete frequency redistribution in infinite parallel plane geometry.¹⁸ Phelps and McCoubrey¹⁹ and Phelps and Chen² extended the work of Holstein and Biberman to include diffusion of excited atoms by adding a diffusion loss term to the rate equation for the excited atoms. For two-level atoms located between infinite parallel plane boundaries (actually windows) their equation describing the

production and loss of excited atoms of density $n(z)$ is

$$F(\omega_L)k(\omega_L) \exp[-k(\omega_L)z/\cos \theta]$$

$$= An(z) - A \int_0^d n(z')K(|z'-z|)dz' - D \frac{d^2 n(z)}{dz^2} + C_{21}n(z) . \quad (1)$$

According to the left-hand side of Eq. (1), excited-state atoms are created by the laser incident at an angle θ to the normal and of photon flux $F(\omega_L)$. The absorption coefficient at the laser frequency is $k(\omega_L)$. At the low intensities of these experiments $k(\omega_L)$ and the ground state density N are independent of position. The first term on the right-hand side of Eq. (1) is the rate of loss due to spontaneous decay, where A is the Einstein coefficient for spontaneous radiation and $n(z)$ is the excited-state population density as a function of the depth z , into the cell. The second term on the right-hand side is the Holstein-Biberman term which describes the excited atom production resulting from the absorption of resonance radition. The kernel $K(|z'-z|)$ is the probability that a photon emitted at z' will be absorbed at z . Thus, the first two terms on the right-hand side of Eq. (1) represent the radiative transport of the energy of the excited atoms.

The next to last term on the of Eq. (1) is the diffusive term in which we are particularly interested. To a good approximation the diffusion coefficient is given by the expression¹⁹

$$D = \frac{kT}{M\langle\sigma v\rangle N} , \quad (2)$$

where k is the Boltzmann's constant, T is the vapor temperature and M is the atomic mass. Here $\langle\sigma v\rangle$ is the rate coefficient for momentum transfer collisions of the excited atoms with ground state atoms and is taken to be equal to twice the rate coefficient for excitation transfer collisions^{8,19,20} between excited

and ground state atoms. This theory shows that $\langle \sigma v \rangle$ is independent of the gas temperature. The factor of two in $\langle \sigma v \rangle$ takes into account the fact that to a good approximation these excitation transfer collisions are equivalent to 180° scattering collisions in the center of mass frame. Because of the large values of $\langle \sigma v \rangle$ for resonance states the diffusion coefficients calculated using this relation are typically several hundred times smaller than the usual gas-kinetic diffusion coefficients such as used by some authors^{3,14,18,21} in estimating the importance of this process. The last term in Eq. (1) represents the quenching of the excited atoms, for example by Na₂ molecules, with a rate coefficient C₂₁ as measured by Lam *et al.*²² Collision excitation of resonance atoms is neglected in the two-level model described by Eq. (1). The assumptions, such as complete frequency redistribution and isotropic scattering, made in deriving the radiative terms in Eq. (1) are discussed in detail by Holstein⁸ and Biberman.⁹ The assumptions are expected to be valid at the high gas densities of the present experiments.

The very approximate solutions of Eq. (1) obtained by Phelps and Chen² gave very good agreement with experiment¹ and so served to demonstrate the importance of nonradiative transport in Hg vapor.

Lagarkov and Medvedera¹¹ derive an equation essentially the same as Eq. (1) but modified to include gas-flow and diffusion terms of interest for shockwave experiments. In their first paper analytic solutions for the excited atom density are found for distances exceeding one effective mean free path away from the surface bounding the excited volume. Their second paper presents analytic solutions near the boundary which show that for a non-reflecting boundary the excited-atom densities are orders of magnitude lower than those determined by the Holstein-Biberman equation which omits the diffusion term in Eq. (1). Numerical solutions of the equivalent of Eq. (1)

have been obtained by Düchs et al.¹⁴ for the case of the emission of resonance radiation from a plasma. However, since these authors assume complete reflection of excited atoms at the boundary they find that the effect of adding diffusion is to increase the excited atom density at the boundary and so to increase the fluorescence at line center. This is just the opposite of the result obtained for a boundary which does not reflect the excited atoms.

The approach used by Hummer and Kunasz¹² is to write separate equations for radiative transport and for the transport of excited atoms. For a two-level atom these equations are:

$$\mu \frac{d}{d\tau} I_p(x, \mu, \tau) = \phi(x) [I_p(x, \mu, \tau) - \frac{An(\tau)}{B_{12}N}] \quad (3)$$

and

$$v_0 \mu k \frac{d}{d\tau} I_n(\mu, \tau) = (A + C_{21} + N<\sigma v>) I_n(\mu, \tau) - \frac{N<\sigma v>n(\tau)}{4\pi} - \frac{N(B_{12}\bar{J} + C_{12})}{4\pi} \quad (4)$$

Here

$$n(\tau) = 2\pi \int_{-1}^1 I_n(\mu, \tau) d\mu \quad (5)$$

is the excited atom density at an optical depth $\tau = kz$, while I_n is the particle intensity of excited atoms at that depth moving in the direction θ measured relative to the outward normal at the entrance window and $\mu = \cos \theta$. Similarly, the mean radiation intensity $\bar{J}(\tau)$ is related to the normalized line profile $\phi(x)$ and the photon intensity $I_p(x, \mu, \tau)$ by

$$\bar{J}(\tau) = \frac{1}{2} \int_{-1}^1 d\mu \int_{-\infty}^{\infty} dx \phi(x) I_p(x, \mu, \tau) \quad (6)$$

The line profile $\phi(x)$ used is the Voigt profile, i.e., it includes both Doppler

and collision broadening. Here x is the normalized frequency measured from line center. Equation (3) relates the spatial attenuation of the radiative intensity to the difference between the photon absorption by ground state atoms and the photon production by spontaneous emission of the excited atoms. Stimulated emission can be neglected at the low laser intensities of our experiment. Equation (4) relates the attenuation of the intensity of excited atoms to the loss by radiation and deexcitation, the net scattering by collisions, the production by photon absorption and reradiation and the production by collisional excitation. In Eqs. (3) and (4), B_{12} is the Einstein coefficient for absorption, $v_0 = (2 kT/M)^{1/2}$ is the single atomic speed used to characterize the motion of the excited atoms, and C_{12} is the rate coefficient for thermal excitation of the ground state atoms to the resonance state. These authors also discuss the boundary conditions appropriate to Eqs. (3) and (4) and the method of including the incident radiation. It should be noted²³ that when the angular distributions of the photon and particle intensities can be represented using the first two terms of a spherical harmonic expansion Eqs. (3) and (4) can be reduced to the equivalent Eq. (1). This point brings out one of the advantages of the Hummer and Kunasz solution relative to earlier work, i.e. the more accurate treatment of highly anisotropic angular distributions of radiant and particle intensities, such as found near an absorbing boundary.

Cipolla and Morse¹⁵ have also presented treatments of the coupled radiative and nonradiative transfer problem using kinetic theory. Their treatment differs from that of Hummer and Kunasz in that they solve for the velocity distribution of the atoms. However they consider conditions for which radiative decay occurs sufficiently more frequently than excitation

transfer collisions so that they can neglect collisions. The Na densities in the experiment reported in this paper are high enough so that excitation transfer collisions occur more frequently than does spontaneous emission so that the Hummer and Kunasz theory is appropriate for our purposes.

In order to investigate the effects of nonradiative transport we take advantage of the variation of absorption length, $1/k(\omega_L)$, as a function of detuning from the resonance frequency. As can be seen from the left-hand side of Eq. (1), the depth of laser penetration is determined by the exponential term with $k(\omega_L)$ varying with the laser frequency. As we tune away from line center the laser radiation penetrates deeper into the cell creating excited-state sodium atoms far away from the window. One may therefore expect the losses due to collisions with the window will be largest for zero detuning where the radiation is absorbed near the window. Such losses should become increasingly less significant as the laser is tuned further and further from resonance. This effect is responsible for the observation that excited atom destruction at the window is relatively difficult to detect when "white" light excitation is used.⁴

The theoretical results with which our experimental data are compared were obtained using the extension of Eqs. (3) and (4) reported by Kunasz and Kunasz.¹³ Their solution (designated SLAB3) treats a three-level atom, e.g., the $3^2P_{3/2}$ and $3^2P_{1/2}$ excited states and the $3^2S_{1/2}$ ground state of Na. Their program has been further modified by Fujimoto and Phelps⁴ to take account of the 1.77 GHz hyperfine splitting (HFS) of the ground state of sodium and by us to include partial redistribution of the incident photon in the first scattering event. The latter modification, which made use of multiple scattering theory,²³ had little effect on the calculated results and will not be considered further. The coefficients used in the comparison with experiment are

listed in Table I. Resonance broadening coefficients are approximately the mean of the experimental values of Niemax and Pichler²⁴ and the theoretical values of Carrington, Stacey and Cooper.²⁵ Excitation transfer rate coefficients were scaled from line broadening data using ratios of these coefficients from Carrington, Stacey and Cooper.²⁵ The cross sections for collisional transfer of excitation between the $P_{3/2}$ and $P_{1/2}$ fine structure components were taken from Pitre and Krause.²⁶ Finally, quenching coefficients for excited Na by Na_2 molecules C_{21} and C_{31} were determined from the experimental work of Lam et al.,²² including approximate allowance for backfeeding from the $a^3\Pi$ state and radiative decay of $a^3\Pi$ atoms to the $X^1\Sigma$ state.

In order to show the general behavior predicted by the theory, we first show predictions made using the program of Kunasz and Kunasz¹³ as modified to include hyperfine structure. The calculated excited-state populations as a function of distance from the window for detuning of 0 and 4 GHz are shown in Fig. 1. In this case the excited atoms are assumed to be deexcited on striking the window. For line center excitation the excited-state population density is found to peak at 3×10^{-6} m from the boundary. This distance is about equal to the optical depth for absorption at line center. On the other hand, for 4 GHz detuning, the peak in the excited-state population density occurs some 20 times deeper into the cell. Clearly, one expects wall losses to be smaller in this latter case.

Figure 2 shows the calculated variation with laser frequency of the integral of the fluorescence signal over the D2 resonance line. Unless otherwise noted, the coefficients used in these calculations were those of Table I scaled to a sodium density of 10^{21} atoms/m³. This integrated line fluorescence is plotted as a function of laser detuning from the center of the D1 line for a range of diffusion coefficients and boundary conditions. The

solid and dashed curves are for 100% absorption and 100% reflection of excited atoms at the window, respectively. Thus, the dashed curve shows the profile expected if destruction of the excited atoms at the boundaries is negligible. The dip in the dashed curve at line center is the result of the competition between reradiation and excitation transfer between the $^2P_{1/2}$ and $^2P_{3/2}$ states. In the remainder of this paper we assume that the excited atoms are completely deexcited at the window. The only difference in the coefficients used in the calculations for the three solid curves is the value used for the momentum transfer rate coefficient $\langle\sigma v\rangle$, which affects the diffusion coefficient D through Eq. (2) and the excited atom transport through the elastic scattering term in Eq. (4). The profile marked D shows the theoretical predicted behavior, namely increasing fluorescence intensity as one approaches line center and a sharp dip at line center due to nonradiative losses. From these curves it is seen that if the momentum-transfer rate coefficient $\langle\sigma v\rangle$ were smaller by a factor of 100 (multiplying D by 100), the integrated intensity curve shows a slightly deeper and wider dip at zero detuning. At line center this case approaches the conditions for which excited atom-ground state collisions are unimportant as considered by Cipolla and Morse.¹⁵ Conversely, if the momentum-transfer rate coefficient is increased by two orders of magnitude, thereby decreasing the mean-free-path between collisions and therefore decreasing the importance of nonradiative losses to the window, the curve marked Dx.01 is the result. As expected in this instance the dip at zero detuning is much shallower than the previous case. The relatively small change in the minimum when the momentum-transfer rate coefficient is reduced by a large factor (D to $D \times 100$) results from the fact that for our conditions the photon absorption length at line center is roughly equal to the mean-free path of the excited atoms, i.e., increasing the excited atom mean free path

used in the calculations by a factor of 100 does not increase greatly the fraction of the atoms colliding with the window before spontaneous emission. This means that the results presented in this paper are not a sensitive test of the value of $\langle \sigma v \rangle$ used in the calculations.

Figure 3 shows the percent of the incident energy lost via wall quenching as a function of detuning from line center. This calculation was made using the same coefficients as for Fig. 2 and shows that at line center the losses to the window by nonradiative transport are about 65% of the incident energy. Note that the energy lost to the window via the $^2P_{3/2}$ state is much smaller than the loss via the $^2P_{1/2}$ state because of the finite rate of collisional excitation transfer between these states.²⁶

III. EXPERIMENTAL PROCEDURE AND APPARATUS

The schematic diagram of the experimental apparatus is shown in Fig. 4. The sodium cell C shown in Fig. 5 is of a special design which allows operation up to 500°C. The details of its construction are given elsewhere.²⁷ The gap between the front and back sapphire windows was 8.6 mm. The cell and sidearm temperatures could be controlled independently by ovens O1 and O2 and were monitored continuously by several thermocouples. The sodium cell was maintained at a temperature somewhat higher than the sidearm assembly and outer windows were added to avoid condensation of sodium on the cell windows. Before vacuum distilling sodium from the high-purity sodium ampule into the siderarm, the entire assembly was evacuated and baked. A pressure of $\sim 3 \times 10^{-6}$ Pa was obtained.

The source of monochromatic radiation was an argon-ion pumped, cw dye laser operated single mode and tuned electronically with an intracavity

etalon. The spectral line width of the output laser beam was approximately 200 MHz at a power level of 30 mW. The mode structure of the dye laser was continuously monitored by a scanning Fabry-Perot interferometer. Mode hops occurred once every 2 to 4 minutes. The laser beam passed through a neutral density filter of unit optical density, a beam-expanding telescope L1, an iris diaphragm, and a beam splitter before passing into the sodium cell at an angle of 15° to the window normal. The input intensity was continuously monitored by a semiconductor photodiode and was always less than 5 W/m^2 . The fluorescent signal was found to be a linear function of incident intensity²⁸ between 0.5 W/m^2 and 5 W/m^2 . The fluorescence signal emitted normal to the window was focused on the 24 μm entrance slit of a 1-m Czerny-Turner monochromator with f/8.7, a dispersion of 0.83 nm/mm and a limiting spectral resolution of 10^{-2} nm or 9 GHz. The exit slit of the monochromator was opened to approximately 300 μm when integrating the fluorescence intensity over either the D1 or D2 line. The photon flux from the monochromator was measured by a photon counting chain consisting of a multialkali photo-multiplier operated at dry ice temperature, a preamplifier, an amplifier/discriminator and a scalar. Count rates were typically 20,000 counts per second with integration times of 1 sec. Both the laser and the monochromator could be scanned under the control of a minicomputer which also normalized the signal count rate to the laser intensity. The monochromator scan was provided by a stepping motor with 0.01 nm per step increments, whereas the dye-laser scan was performed by the intracavity etalon in 560 MHz steps. The raw data along with the laser input intensities were stored on magnetic tape for later analysis.

Sodium densities were calculated from the data of Nesmeyanov.²⁹ As a check, absorption measurements were made using a white light source T (tungsten-filament-iodine lamp) operated at a color temperature of about 2900 K. The

measured equivalent widths and line broadening data²⁴ for the D1 and D2 lines could then be used to calculate the sodium densities. These two density determinations were within 15% of that calculated from the vapor pressure curve.

The normalization of the radiant intensity scattered by the Na cell to the incident radiative flux was made by placing a mirror M of known reflectivity into the laser beam such that the reflected laser beam was incident on a white surface S in the same geometry as that of the cell.⁴ The white surface was BaSO₄ paint and its scattering efficiency was calibrated using BaSO₄ powder³⁰ stated by the manufacturer to be 99% efficient at the wavelengths of interest when prepared according to instructions. Transmission coefficients of the evacuated quartz-cell windows of the oven, as well as the sapphire input window, were measured and used in the normalization of the data. By this method we were able to determine the ratio of the fluorescent intensity to the intensity of radiation scattered by a perfectly diffuse surface.

IV. RESULTS

Figure 6 shows experimental spectral line profiles obtained for three values of laser detuning from the D1 resonance line at 589.6 nm. In each case the monochromator was scanned from 588.6 to 590.0 nm for a fixed laser detuning. The Na density was 3×10^{21} atoms m⁻³. As can be seen, with excitation at line center the detected line width is essentially determined by the monochromator resolution of 0.02 nm. The middle trace shows that if the laser excitation is detuned approximately 4 GHz into the red wing of the D1 line, the fluorescence line profiles become broader and the D2 line intensity increases while that of the D1 line decreases. The broader line profile results

from the fact that radiation absorbed deep in the vapor must be emitted in the wings of the resonance line in order to reach the window.^{8,9} The deeper penetration of the laser light also increases the mean lifetime of the excited atoms allowing for greater collisional transfer of excitation to the P_{3/2} component. Finally, for a detuning of 27 GHz, or approximately 0.03 nm, the backscattered line profiles become very broad and display self-absorption at line center. These profiles demonstrate that the D1 and D2 lines are well separated and that a 300 μm exit slit setting is sufficient to include essentially all of the scattered intensity in either the D1 or the D2 line.

Scans of the measured fluorescent intensity integrated over the D1 and D2 lines as a function the laser frequency are shown by the points in Figs. 7 and 8. Experimental runs were made at a variety of densities but detailed theoretical comparisons were made only for Na density of 6.9×10^{20} atoms m⁻³ and cell temperature of 705°K. In these runs stray laser light was measured to be less than 0.6% of the maximum signal.

The theoretical results are shown in Figs. 7 and 8 by the solid lines. The data for P_{3/2} excitation in Fig. 7 clearly show a dip near zero detuning which reflects the expected increased in wall losses. As one would expect, the wall losses for P_{1/2} excitation in Fig. 8 appear smaller due to its smaller absorption coefficient. It is also interesting to note the drastic reduction in sensitized fluorescence, i.e. radiation following energy transfer from the initial excited fine structure component to the second component, when the atoms are excited at resonance. This reflects both the increased loss of excited atoms by radiation and the large wall losses which prevail for these conditions. Calculations such as those plotted in Fig. 3 show that the latter effect is dominant. The asymmetry and structure which consistently appear near line center excitation are attributed to the 1.77 GHz hyperfine

splitting of the ground state.

The agreement between theory and experiment is significantly better for $P_{3/2}$ excitation than for $P_{1/2}$ excitation. In the former case the agreement is excellent in all regions except near zero detuning for the $P_{3/2} - P_{3/2}$ curve (Fig. 7, top). It is, of course, just this region which is most sensitive to boundary effects. Both here and for the $P_{1/2} - P_{1/2}$ (Fig. 8, bottom) results, theory overestimates the experimental results by at least 25%. Inclusion of frequency-coherent scattering of the incident radiation at the first scattering event into the model produced a negligible change in the calculated results at this density. One also notes that since our model assumes complete destruction of the excited atoms at the window it is not possible to lower the calculated intensities at line center by changing the reflection coefficient for the excited atoms at the window.

V. SUMMARY

An experiment has been performed which shows the effect on fluorescent intensity of nonradiative excitation transport to a boundary. In particular, losses due to quenching of excited atoms can be an important and even dominant loss mechanism for certain density and excitation conditions. Funding limitations prevented the more extended analysis of these data necessary to clarify the remaining discrepancies between theory and experiment. Future experiments and analysis should consider the effect of this nonradiative loss of excited atoms on the time dependent decay of the excited atoms and on the propagation of intense laser beams in the region near the boundary.

ACKNOWLEDGMENT

We wish to thank Chela and Paul Kunasz for their untiring patience and assistance with the further development and use of SLAB3 and J. L. Hall for advice and assistance in connection with the dye laser. We also wish to thank T. Fujimoto and R. Smick for their contributions through the construction of apparatus and the development of computer programs during earlier projects. Finally a special thanks to all the JILA electronic and instrument shops. This research was supported in part by the Advanced Research Projects Agency and was monitored by the Office of Naval Research under Contract No. N00014-76-C-0123 with the University of Colorado.

REFERENCES

a) Present address: Physics Department, Amherst College, Amherst, MA, 01002.

b) Staff member, Quantum Physics Division, National Bureau of Standards and Lecturer, Department of Physics, University of Colorado.

1. J. M. Hansen and H. W. Webb, Phys. Rev. 72, 332 (1947).

2. A. V. Phelps and C. L. Chen, Bull. Am. Phys. Soc. 15, 428 (1970).

Details are given in the Yearly Summary Technical Reports for Contract No. NR-4725(00), Westinghouse Research Laboratories, June 1969 and September 1970 (unpublished). The approximate theory of these references shows that the effective diffusion coefficient for sodium atoms in the $3P$ state increases as $N^{1/3}$ for N above about $3 \times 10^{24} \text{ m}^{-3}$. This additional transport is estimated assuming stationary atoms and considering only excitation transfer to nearest-neighbor atoms, i.e. transport by "hopping" of the excitation. Presumably exciton behavior becomes important at the higher Na densities.

3. W. Heering, Z. Physik A274, 91 (1975).

4. T. Fujimoto and A. V. Phelps, Bull. Am. Phys. Soc. 21, 173 (1976).

5. M. F. H. Schuurmans, J. Physique 37, 469 (1976); A. L. J. Burgmans and J. P. Woerdman, J. Physique 37, 677 (1976); A. L. J. Burgmans, M. F. H. Schuurmans and B. Bölgger, Phys. Rev. A 16, 2002 (1977).

6. T. D. Bonifield, F. H. K. Rambow, G. K. Walters, M. V. McCusker, D. C. Lorents and R. A. Gutcheck, J. Chem. Phys. 72, 2914 (1980).

7. B. M. Dodsworth, J. C. Gay and A. Omont, J. Phys. (Paris) 33, 65 (1972); A. L. J. Burgmans, Phys. Rev. A 19, 1954 (1979).

8. T. Holstein, Phys. Rev. 72, 1212 (1947); 83, 1159 (1951).

9. L. Biberman, Zh. Eksp. Teor. Fiz. 17, 416 (1947); Dokl. Akad. Nauk. SSSR 59, 659 (1948).

10. D. G. Hummer, J. Quant. Spectrosc. Radiat. Transfer 8, 193 (1968); D. G. Hummer and G. B. Rybicki, Ann. Rev. Astron. Astrophys. 9, 237 (1971); V. V. Ivanov, Transfer of Radiation in Spectral Lines (translation edited by D. G. Hummer), National Bureau of Standards Special Publication 385 (U.S. G.P.O., Washington, D. C. 1973).
11. A. N. Lagarkov and N. A. Medvedeva, J. Quant. Spectrosc. Radiat. Transfer 13, 209 and 225 (1973); 17, 735 (1977).
12. D. G. Hummer and P. B. Kunasz, J. Quant. Spectrosc. Radiat. Transfer 16, 77 (1976).
13. C. V. Kunasz and P. B. Kunasz, Compt. Phys. Comm. 10, 304 (1975).
14. D. F. Düchs and J. Oxenius, Z. Naturforsch. 32a, 156 (1977); D. F. Düchs, S. Rehker and J. Oxenius, Z. Naturforsch. 33a, 124 (1978).
15. J. W. Cipolla, Jr. and T. F. Morse, J. Quant. Spectrosc. Radiat. Transfer 22, 365 (1979).
16. K. Kenty, Phys. Rev. 42, 823 (1932).
17. L. M. Biberman and B. Veklenko, Sov. Phys. JETP 37, 117 (1960).
18. R. G. McIntyre and R. G. Fowler, Astrophys. J. 133, 1055 (1961); R. G. McIntyre and E. M. D'Arcy, J. Appl. Phys. 43, 2251 (1972).
19. A. V. Phelps and A. O. McCoubrey, Phys. Rev. 118, 1561 (1960).
20. W. Fursow and A. Vlassow, Physik. Z. Sowjetunion 10, 378 (1936). The factor of two used to convert excitation transfer rate coefficients to momentum transfer rate coefficients also occurs in symmetric charge transfer theory. See for example A. Dalgarno and M. R. C. McDowell, Proc. Phys. Soc. 69, 615 (1956).
21. R. G. Fowler, in Handbuch der Physik, edited by S. Flügge (Springer-Verlag, Berlin, 1956), p. 226.

22. L. K. Lam, T. Fugimoto, A. C. Gallagher, and M. M. Hessel, *J. Chem. Phys.* 68, 3553 (1978).
23. P. J. Chantry, A. V. Phelps, and G. J. Schulz, *Phys. Rev.* 152, 81 (1966).
24. K. Niemax and G. Pichler, *J. Phys. B* 8, 179 (1975).
25. C. G. Carrington, D. N. Stacey, and J. Cooper, *J. Phys. B* 6, 417 (1973).
26. J. Pitre and L. Krause, *Can. J. Phys.* 46, 125 (1968).
27. A. G. Zajonc, *Rev. Sci. Instrum.*, in press.
28. This linear behavior, i.e., the absence of saturation effects, is in agreement with predictions of the theory as illustrated by the small degree of fractional excitation calculated for the conditions of Fig. 1. Our attempts to experimentally observe the effects of window losses on the threshold for nonlinear propagation of the laser as a function of frequency were unsuccessful.
29. An. N. Nesmeyanov, Vapour Pressure of the Elements, translated by J. I. Carasso (Academic Press, New York, 1963).
30. V. E. Kartachevskaya, H. Korte and A. R. Robertson, *Appl. Opt.* 14, 2694 (1975).

Table I. Parameters used for comparison with experiment.*

Process	Symbol	Value Used	Other Values
Temperature	T	702 K	
Na ground state density	N	$6.9(20)^a \text{ m}^{-3}$	
Spontaneous emission	A_{21}	$6.28(7)^b \text{ sec}^{-1}$	
	A_{31}	$6.30(7)^b \text{ sec}^{-1}$	
Collisional damping coefficient (FWHM)	$\Delta\omega_2$	$4.5(-13) \frac{\text{rad-m}^3}{\text{sec}}$	$5.8(-13)^{24}$ $2.95(-13)^{25}$
	$\Delta\omega_3$	$5.4(-13) \frac{\text{rad-m}^3}{\text{sec}}$	$6.8(-13)^{24}$ $4.79(-13)^{25}$
Voigt damping parameter	a_2	$2.5(-2)^c$	
	a_3	$2.8(-2)^c$	
Excited atom elastic scattering rate coefficient	$\langle\sigma v\rangle_2$	$2.7(-13)^d \text{ m}^3/\text{sec}$	$5.9(-13)^e$
	$\langle\sigma v\rangle_3$	$3.0(-13)^d \text{ m}^3/\text{sec}$	$9.6(-13)^e$
Transfer from $3^2P_{3/2}$ to $3^2P_{1/2}$ and its reverse	C_{32}	$1.4(6)^{26} \text{ sec}^{-1}$	
	C_{23}	$2.7(6)^{26} \text{ sec}^{-1}$	
Collisional quenching	C_{31}	$7.2(3)^{22} \text{ sec}^{-1}$	
	C_{21}	$7.2(3)^{22} \text{ sec}^{-1}$	
Absorption coefficient at line maximum (with HFS)	$k_2(\text{max})$	$1.835(5)^f \text{ m}^{-1}$	
	$k_3(\text{max})$	$3.66(5)^f \text{ m}^{-1}$	
Excited atom reflection coefficient	R	0.	

* As in Ref. 13, the levels $3^2S_{1/2}$, $3^2P_{1/2}$ and $3^2P_{3/2}$ are designated by 1, 2, and 3, respectively.

^a $6.9(20)$ means 6.9×10^{20} .

^bW. L. Wiese, M. W. Smith, and B. M. Miles, Atomic Transition Probabilities II. Sodium through Calcium, National Stand. Ref. Ser., U. S. Nat. Bur. Std. 22, 1969.

^cCalculated using coefficients of this table and formulas of Ref. 12.

^dCalculated by multiplying the coefficients for self broadening (HWHM) of Niemax and Pichler²⁴ by the respective ratios of the coefficient for the transfer of population to that for relaxation of optical coherence from Carrington, Stacey, and Cooper.²⁵ The factor of two discussed in connection with Eq. (2) was inadvertently omitted.

^eThese values are twice the rate coefficients for the transfer of population calculated using the theory of Carrington, Stacey and Cooper.²⁵

^fCalculated using Voigt profiles and including HFS.

FIGURE CAPTIONS

- Fig. 1. Theoretical excited-state densities for two laser detunings as a function of distance from window. Conditions are: Na density of 7×10^{20} atoms m^{-3} , monochromatic excitation of $P_{3/2}$ state. The plotted population is for the $P_{1/2}$ state and an incident flux of about twice the maximum value used in our experiment, i.e., 10 W/m^2 . Hyperfine splitting was included.
- Fig. 2. Theoretical fluorescent intensity profiles. The frequency integrated fluorescence intensity in the Na D2 line emergent in the backward direction relative to that expected for a perfectly diffuse surface is given as a function of laser detuning from the center of the D1 line. The dashed line shows predicted intensities if wall quenching is negligible (unit excited-atom reflection coefficient). Solid lines show the effect of variation of the momentum transfer rate coefficient on the emergent intensity. The Na density was taken as 1×10^{21} atoms m^{-3} . HFS is not included.
- Fig. 3. Nonradiative losses relative to input power calculated from SLAB3 (including HFS) for a Na density of 1×10^{21} atoms m^{-3} . Losses for both the $P_{1/2}$ and $P_{3/2}$ states are shown as a function of laser detuning from line center of the D1 ($P_{1/2} \rightarrow S_{1/2}$) transition.
- Fig. 4. Block diagram of the experiment. The output beam of the single-mode dye laser is expanded by L1 and directed on the entrance window of the sodium cell C. Fluorescent radiation is focused onto the monochromator by lens L2. Oven 1 is the cell oven and oven 2 is the sidearm and reservoir oven.

Fig. 5. Cross section of the Na vapor cell. Cu gaskets (not shown) are placed between the inner Kovar ring and the inside of each window. Carbon-steel bolts maintain the compression necessary for sealing. Thin sapphire "storm-windows" are placed over the main windows to reduce convective cooling and eliminate Na deposition on the windows (see Ref. 27).

Fig. 6. Normalized fluorescent signal profiles for three values of laser detuning Δ from line center excitation of $P_{1/2}$. The Na density was $3 \times 10^{21} \text{ m}^{-3}$. In the lower trace the peak on the long-wavelength side of the D1 line is due to laser light scattered by imperfections in the cell windows. The scattered light signal from the reference white surface has the same frequency dependence as the profiles in the top trace but has unit amplitude.

Fig. 7. Top: Integrated fluorescence intensity from $P_{1/2}$ as a function of detuning from $P_{3/2}$ line center. Bottom: Fluorescence from $P_{3/2}$ level with $P_{3/2}$ excitation. The Na density was $6.9 \times 10^{20} \text{ m}^{-3}$. Solid curve is model predictions. Dots are the measured ratios of the cell fluorescence to the signal scattered by the white surface after correction for window transmission, etc. The experimental data are shifted in frequency for best fit to the theory.

Fig. 8. Same as Fig. 7 but laser excitation of $P_{1/2}$ and detection of $P_{3/2}$ fluorescence (top) and $P_{1/2}$ fluorescence (bottom).

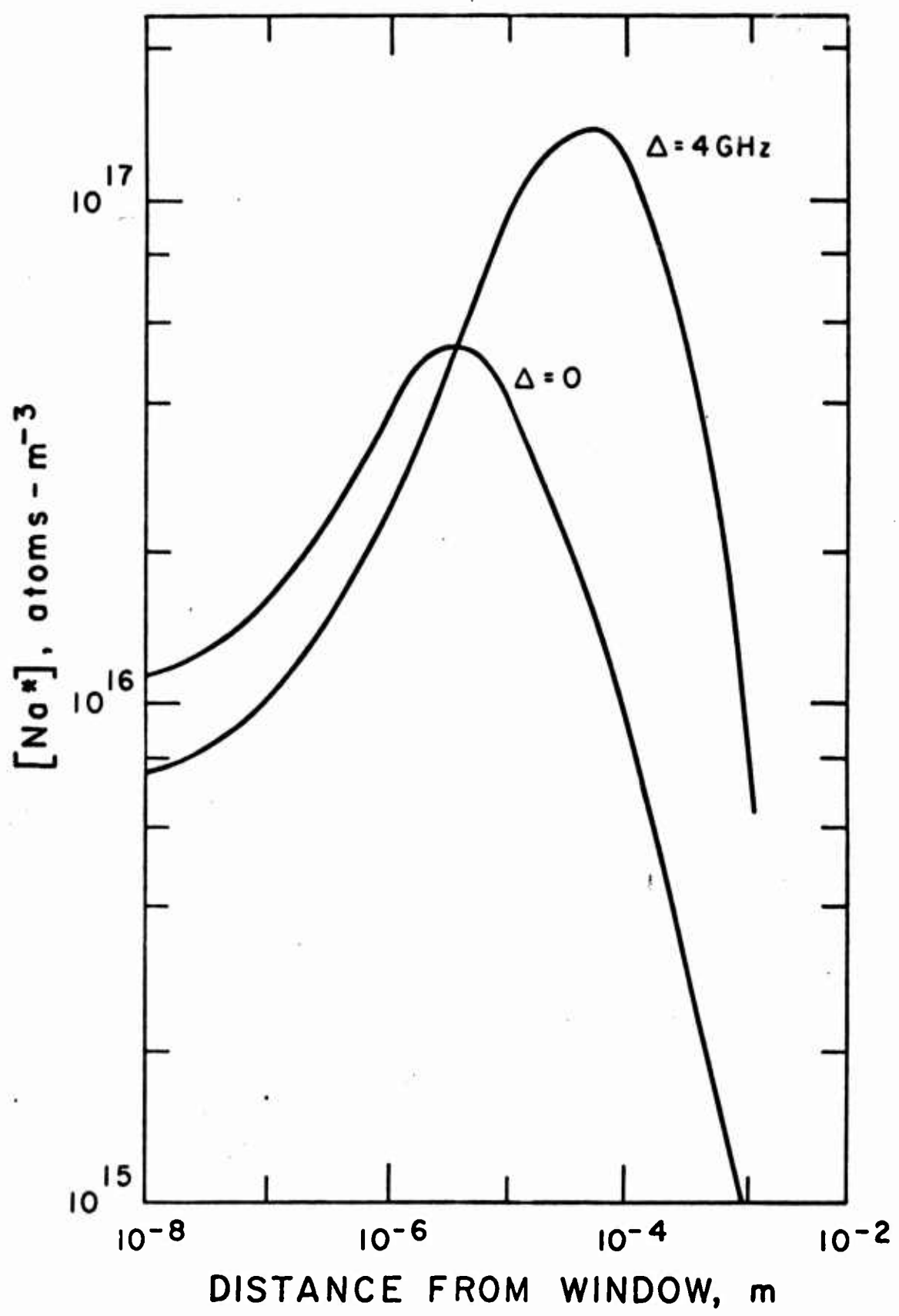


Figure 1

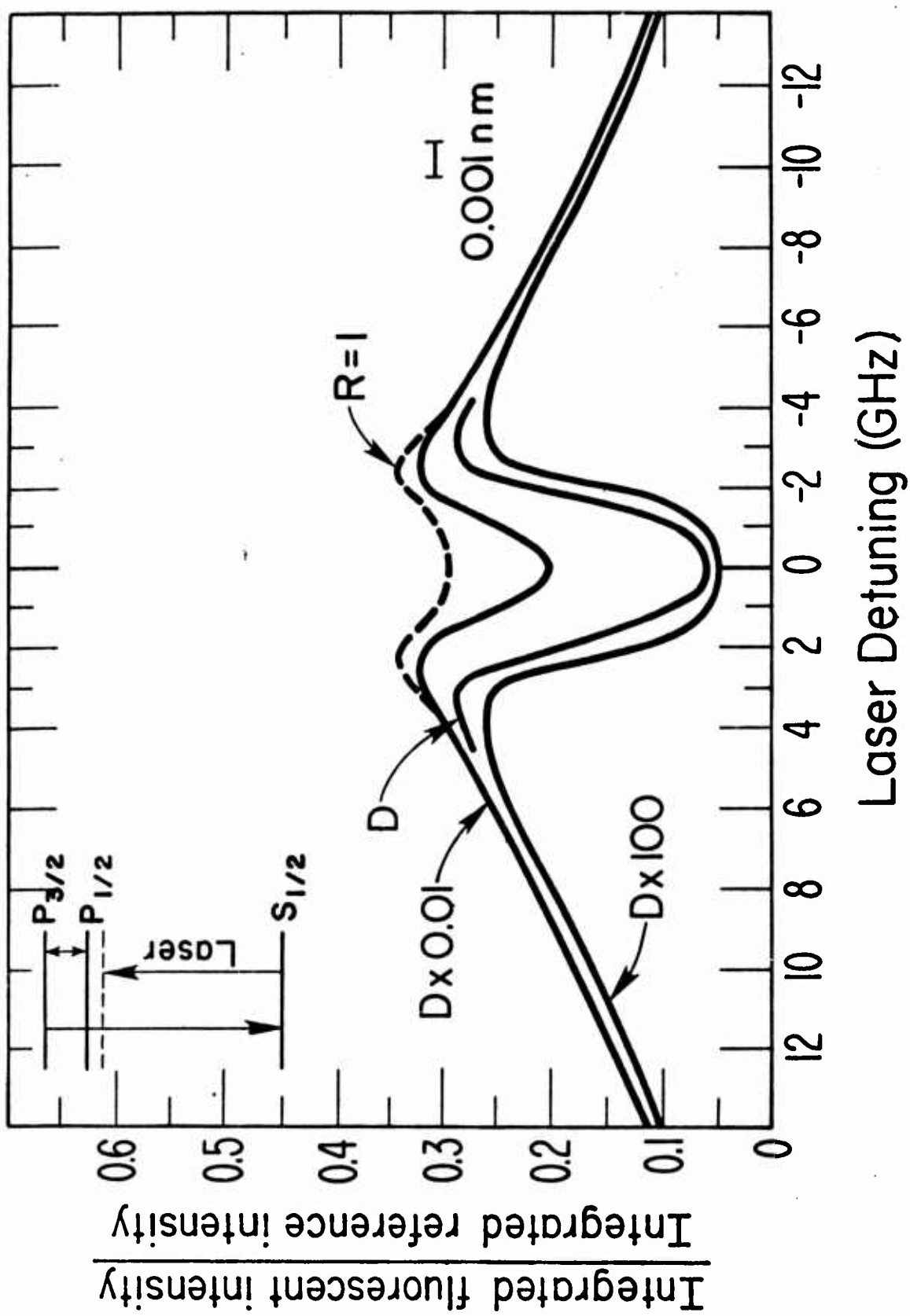


Figure 2

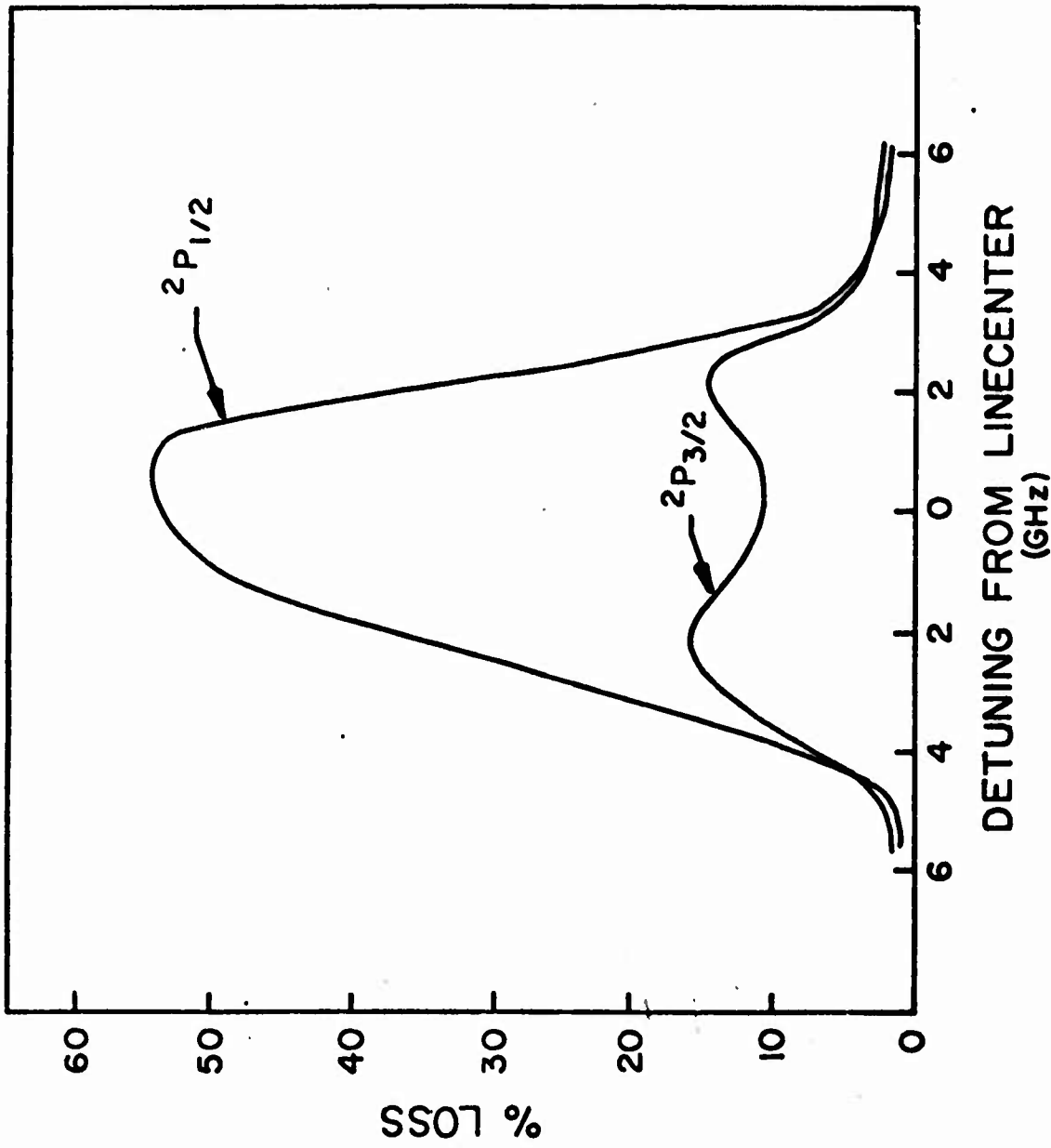


Figure 3

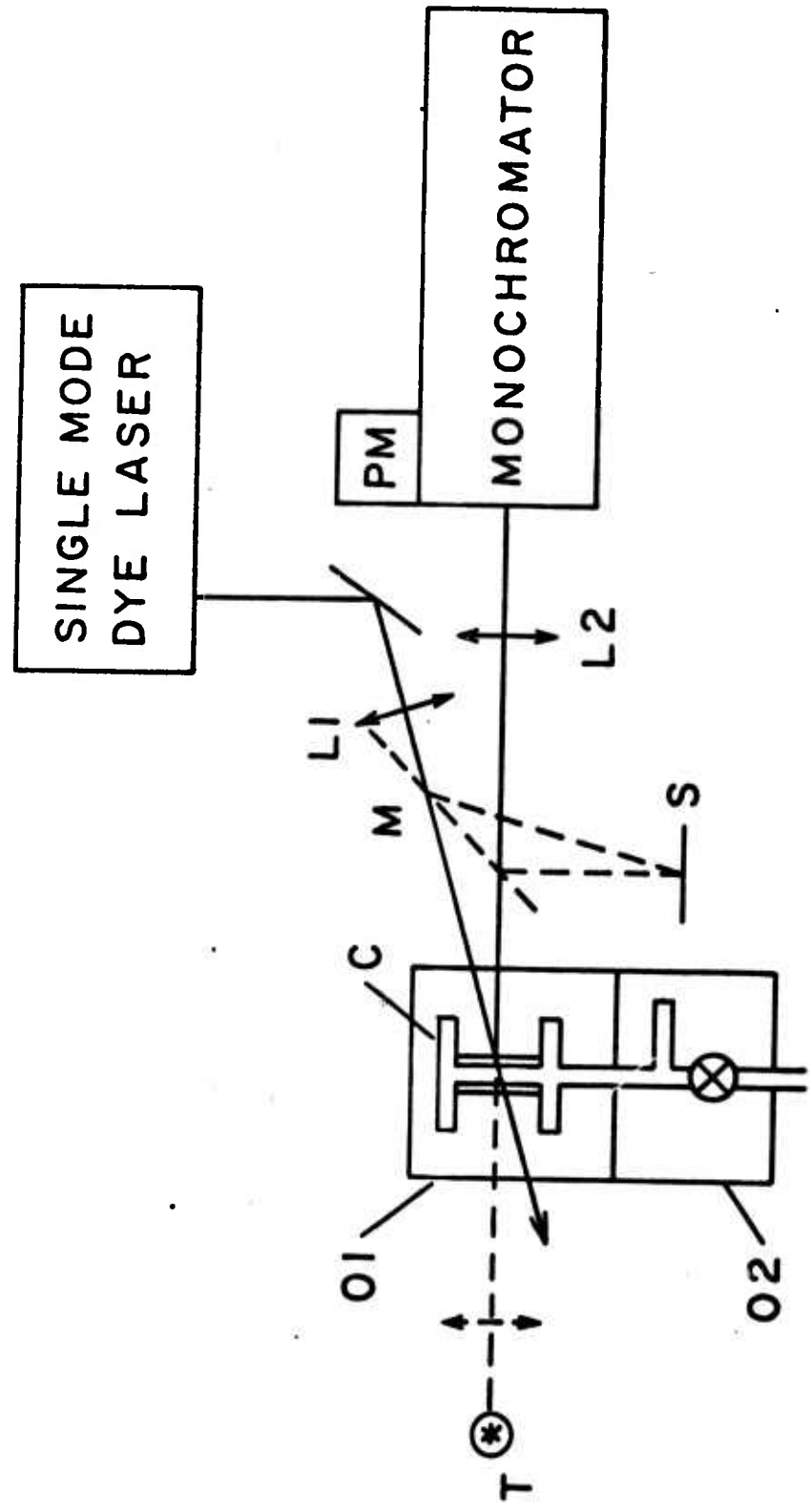


Figure 4

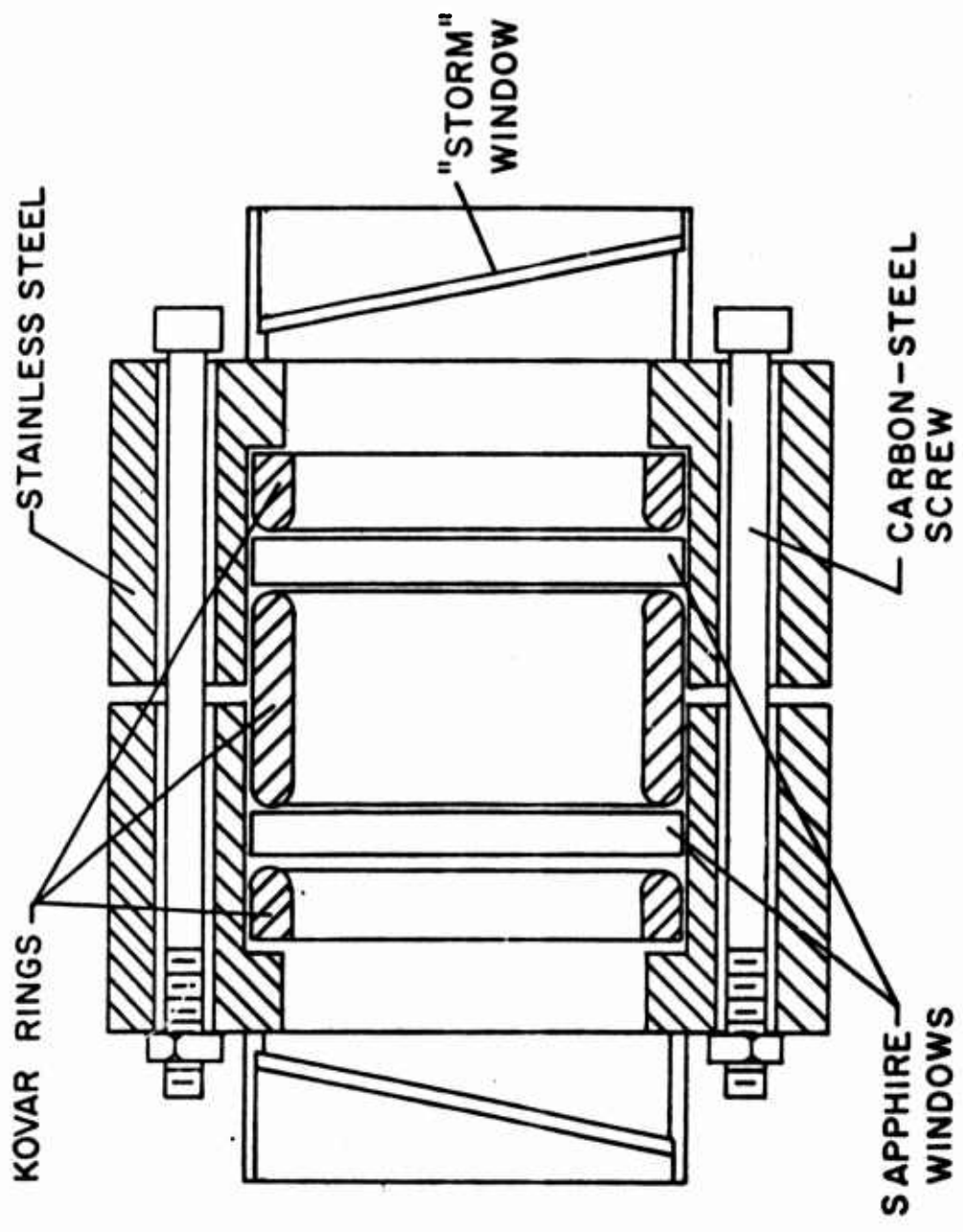


Figure 5

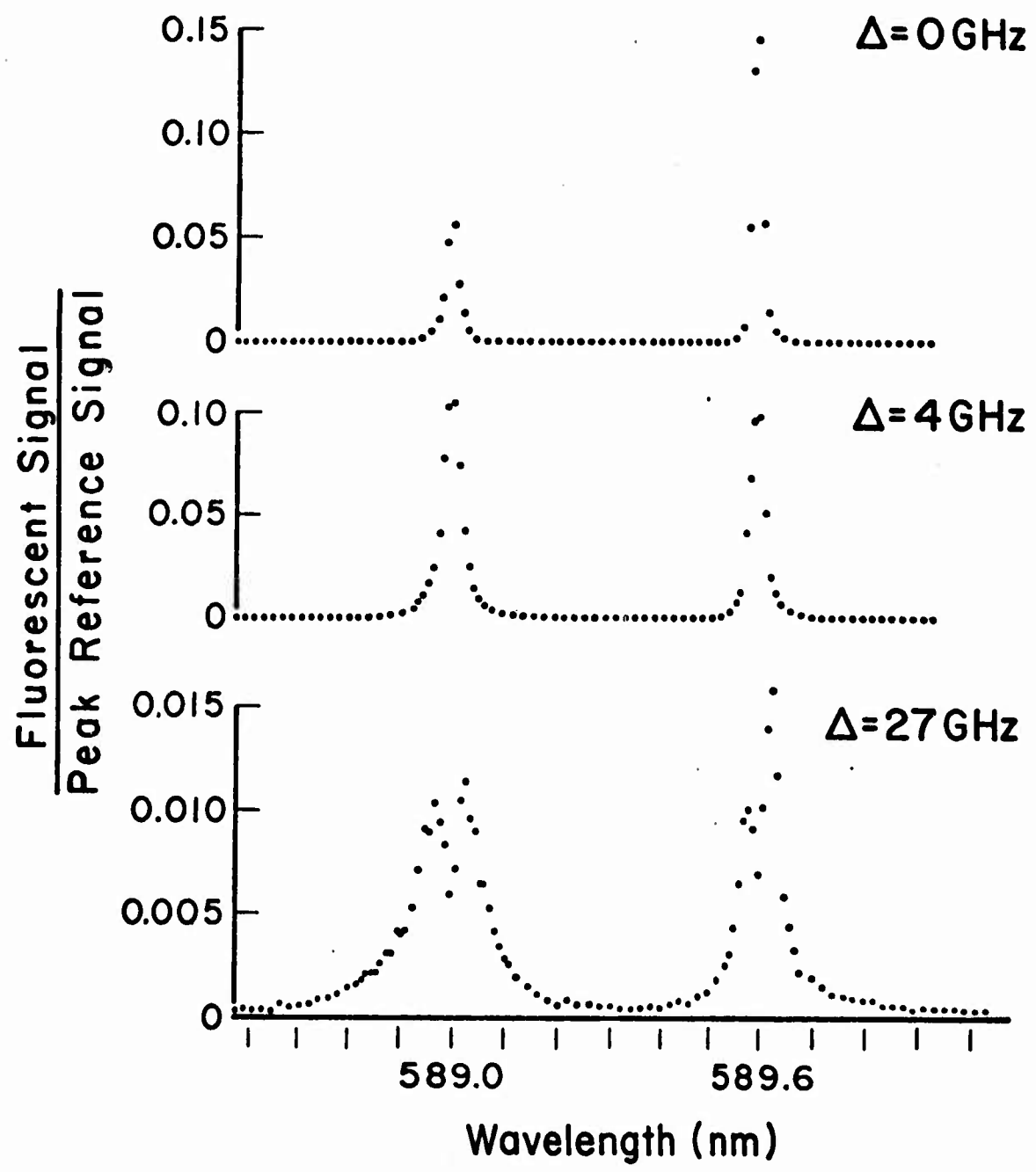


Figure 6

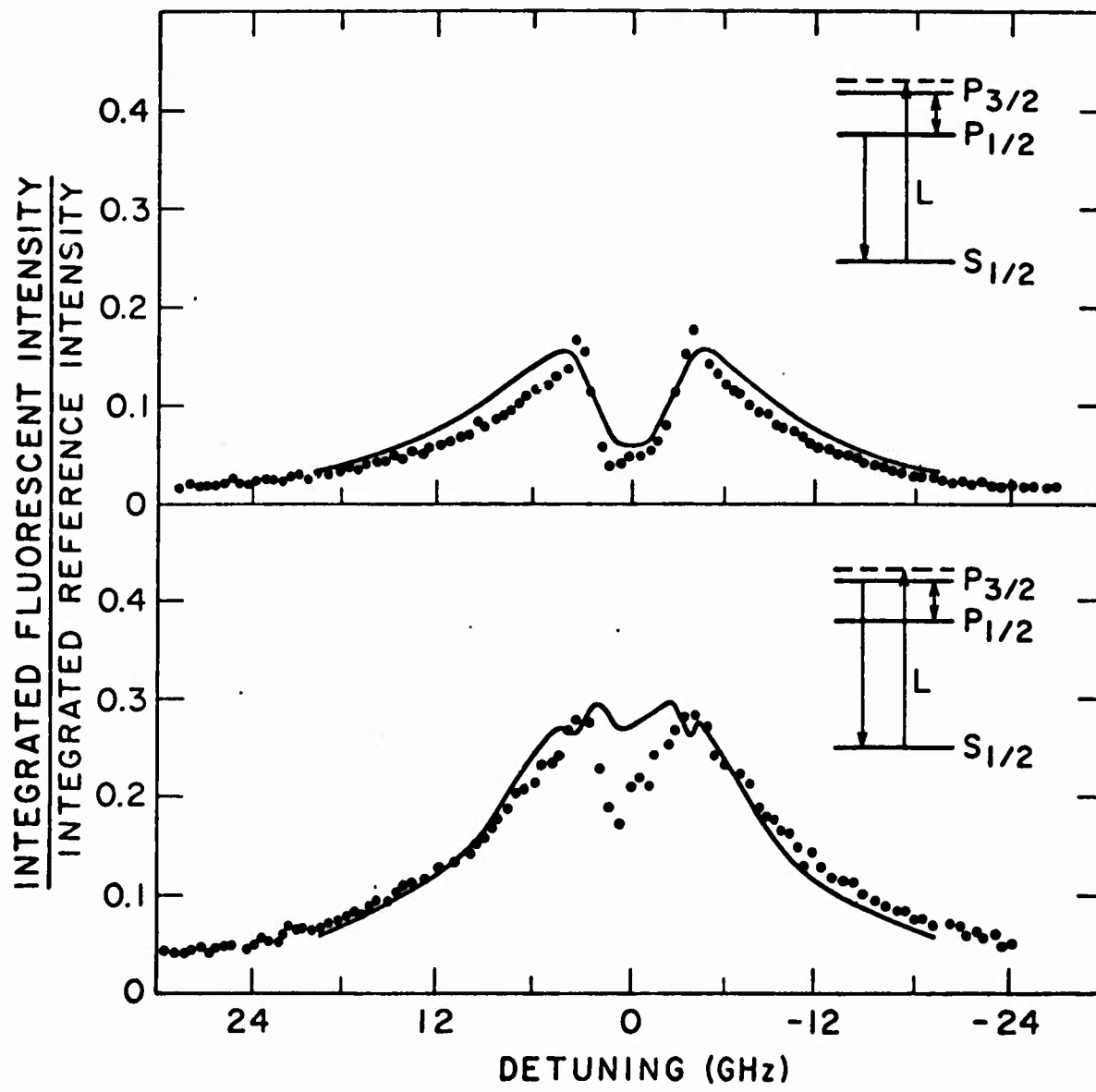


Figure 7

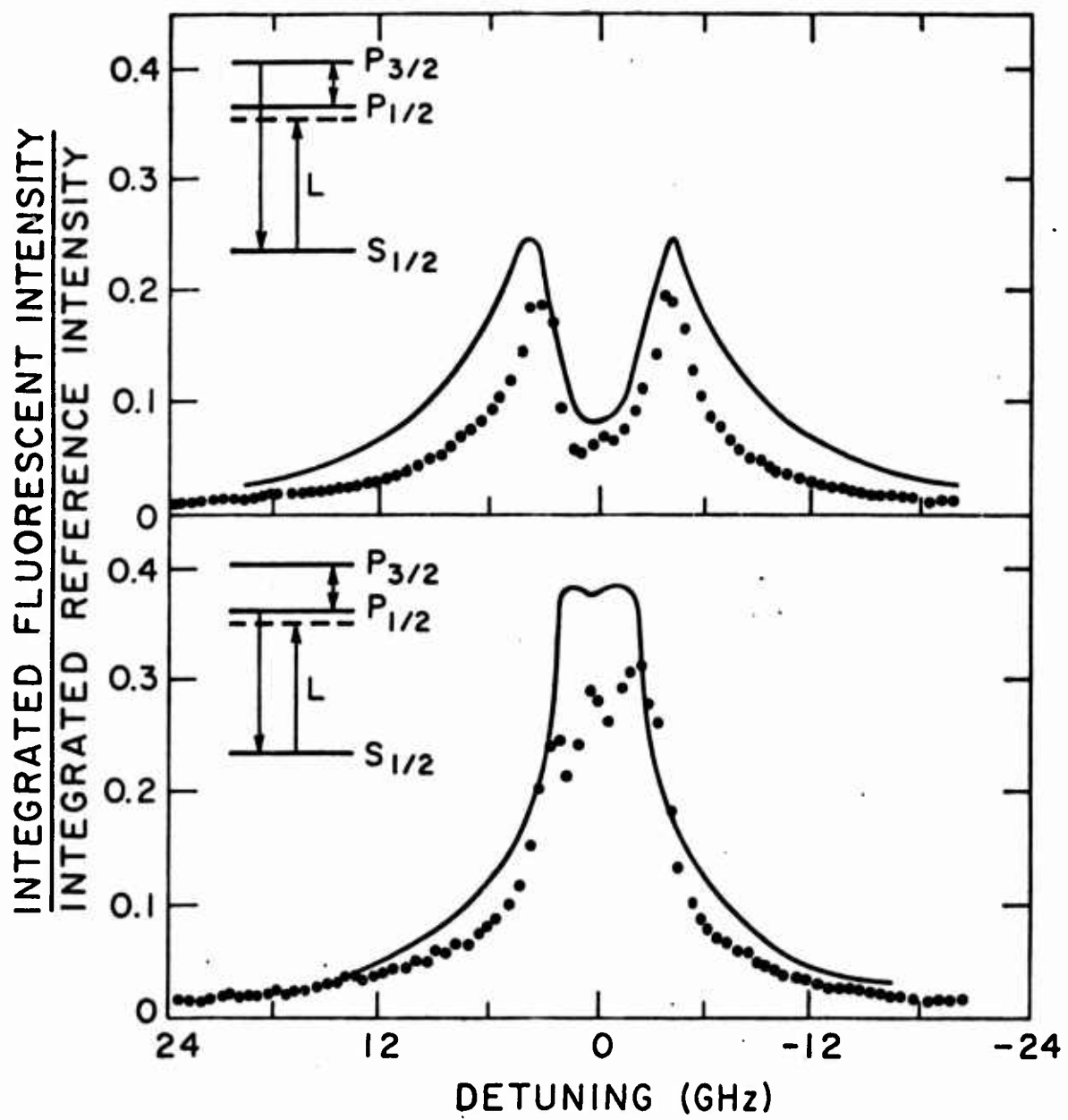


Figure 8